

SOLAR CELLS

INTRODUCTION

As fossil fuels continue to deplete, development and research in sustainable power generation like solar energy has become very important. Even though solar energy is always accessible, challenges arise because the power conversion from solar to electrical energy is not efficient. The energy payback time- that is the time taken for a device to generate as much energy as was needed to fabricate the device should also be acceptable. Above all, production cost should be low. Therefore, technological advancement, improvements in device design and choosing better materials are some ways by which we can reduce the cost of solar cell devices at the same time increasing its efficiency. In this text, operation of solar cells is examined, followed by a brief introduction of 3 interesting papers on solar cell development.

OPERATION OF SOLAR CELL

Solar cell is a photo diode. When light falls on it, electron hole pairs are generated in the n-side, the p-side and the depletion region. Due to the generated carriers, a current flows from n to p region which is I_{op} . As optical generation rate increases this current increases. This current adds

to the normal reverse current of the diode. If we open circuit the photo diode a voltage less than contact potential V_o appears across the pn junction. This is V_{oc} .

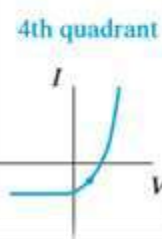
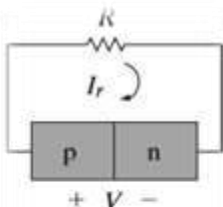


FIGURE 1 VOLTAGE IS POSITIVE, CURRENT IS NEGATIVE, CURRENT FLOWS INTO THE EXTERNAL CIRCUIT

$$I_{op} = qA g_{op}(L_p + L_n + W)$$

$$V_{oc} = \frac{kT}{q} \ln \frac{g_{op}}{g_{th}}$$

Where g_{th} = thermal generation rate and g_{op} = optical generation rate, L_p is diffusion length of holes in n region and L_n is diffusion length of electrons in p region and W is depletion region width.

V_{oc} and I_{op} are important parameters because they give the value of voltage and current obtained from a photo diode. In the 4th quadrant operation of the I-v curve. Applying a positive voltage to the device, we obtain a negative current, that is current is driven towards the load. Hence light energy gets converted to electrical energy. A typical design of a photo diode for a solar cell is as shown in figure 2. The depth d is kept less than L_p , so that holes generated near the surface to diffuse to the junction before they recombine. The area that faces the light is large, for

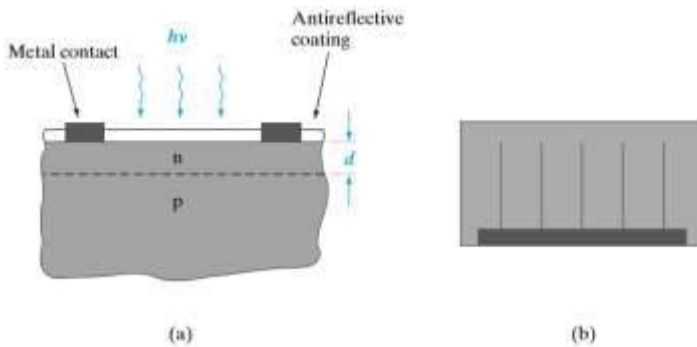


FIGURE 2 A- TYPICAL SOLAR CELL B- TOP VIEW OF N CONTACTS

Even though the currents obtained from a single cell is minimal, many cells add up to give appreciable outputs. Solar cells have established applications in powering satellites, powering remote locations and various consumer products like garden lights.

Fill factor is an important figure of merit for solar cell. The maximum power delivered to a load by the solar cell occurs when the product VI_f is a maximum. Calling these values of voltage and current V_m and I_m , we can see that the maximum delivered power illustrated by the shaded rectangle in Fig. 3 is less than the $I_{sc}V_{oc}$ product. The ratio $I_mV_m / I_{sc}V_{oc}$ is called the fill factor,

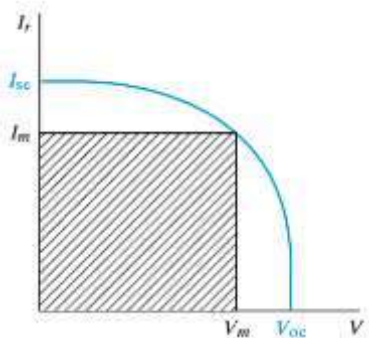


FIGURE 3 FILL FACTOR

PAPER 1 - PEROVSKITE SOLAR CELLS: FROM MATERIALS TO DEVICES

There are two pathways one can take when increasing the productivity in solar cell production. One to manufacture solar cells from highly efficient resources like silicon, with low pay back time and very high cost. Or to compromise a little on efficiency to make cells with lower cost but with high numbers with a different material. Perovskite cell follow the second pathway and have shown superb power conversion efficiency (PCE) along with very low material costs. Solar cell efficiencies of devices using these materials have increased from 3.8% in 2009 to 25.2% in 2020 in single-junction architectures, and in silicon-based tandem cells, to 29.1% exceeding the maximum efficiency achieved in single-junction silicon solar cells. Perovskite solar cells are

maximum exposure to the sun. Metal contacts are designed in such a way that there is minimum ohmic losses. The metal contact on the n region can be distributed like fingers as shown in figure 2 b, to reduce the ohmic loss as well maintain exposure to the light.

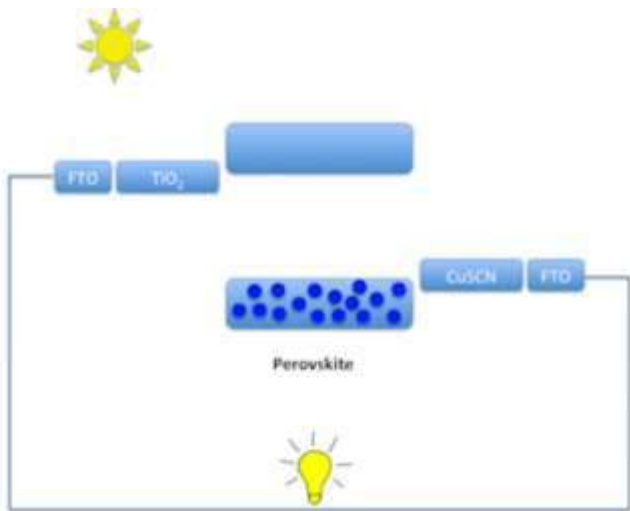


FIGURE 4 WORKING OF THE PEROVSKITE

therefore, currently the fastest-advancing solar technology. The key material for the perovskite solar cell are organometal halides. When sunlight falls on the active perovskite, electron hole pair are generated, electron moves from Titanium oxide to the FTO Anode and holes move from Copper thyocynate to FTO cathode. A big advantage perovskite PVs have over conventional solar technology is that they can react to various different wavelengths of light, which lets them convert more of the sunlight that reaches them into electricity.

Despite all this material has to offer, its commercialization still faces many challenges. The first challenge is toxicity due to PbI_2 – lead iodide, it is one of the breakdown products of perovskite. Long term stability of perovskite solar cells is another big issue. Finding solutions to these problems, would be the concentration of future research studies in this field.

PAPER 2 - SENSITIZATION OF SILICON BY SINGLET EXCITON FISSION IN TETRACENE

The Shockley–Queisser limit refers to the maximum theoretical efficiency of a solar cell using a single p-n junction to collect power from the cell where the only loss mechanism is radiative recombination in the solar cell. It is between 29 and 33 percent depending on how we measure it. This paper details an experiment where solar cells were coated with a thin layer of tetracene, that effectively split incoming photons into two. This process is known as exciton fission and means that the solar cell is able to use high energy photons from the blue-green part of the visible spectrum.

Silicon solar cells generate an electric current by using incoming photons to knock electrons from the silicon into a circuit. Silicon's bandgap corresponds to infrared photons, which carry less energy than photons in the visible part of the electromagnetic spectrum. Photons outside silicon's bandgap essentially go to waste. But here's where tetracene comes in: It splits blue-green photons into two "packets" of energy that are each equivalent to an infrared photon. So rather than each infrared photon knocking free one electron, a single photon in the blue-green spectrum can knock free two electrons. It's essentially getting two photons for the price of one. This new cell represents a fundamentally new approach to a well-known truism in photovoltaics research: If you want to pass the Shockley–Queisser limit, you have to capture energy from a

wider range of solar photons. While none of this is economically viable, the win here is the proof of concept. This is a fundamentally different approach from traditional photovoltaics

PAPER 3 - VERSATILE TERNARY ORGANIC SOLAR CELLS: A CRITICAL REVIEW

This paper presents a critical review of ternary organic cells. The power conversion efficiency (PCE) of organic solar cells (OSC) has increased in the past ten years from 4% up to 11%. Binary OSC and Tandem OSC were first developed. Ternary solar cells developed thereafter, enhancing photon harvesting using an additional layer. This layer can be a donor or acceptor layer. The third component could: (i) be fully embedded in a donor; (ii) be fully embedded in an acceptor; (iii) locate at the donor/acceptor interface; or (iv) form its own channels. This is demonstrated in the figure below.

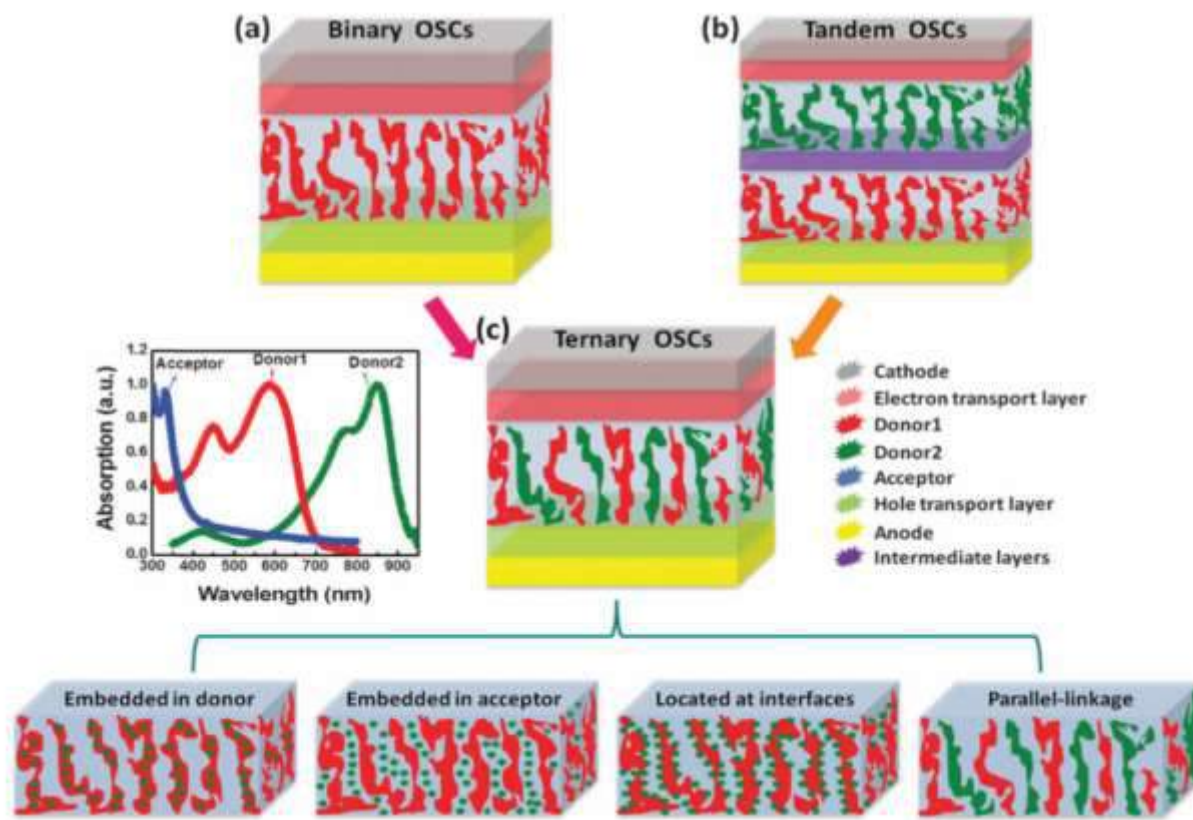


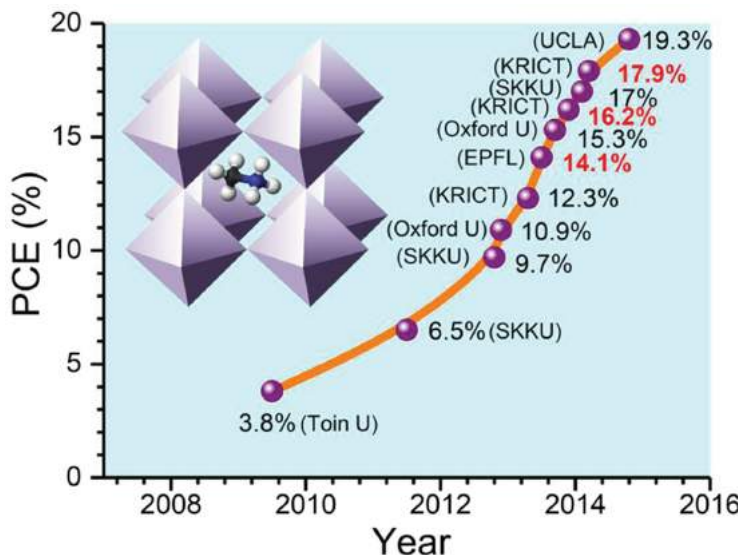
FIGURE 5 DIFFERENT ORGANIC SOLAR CELLS AND TYPES OF TERNARY OSCS BASED ON LOCATION OF THIRD LAYER

The ternary solar cells inherit the major advantages of single junction binary solar cells and tandem configuration solar cells. There are four fundamental principles in ternary solar cells: charge transfer, energy transfer, and parallel-linkage or alloy structure, which are closely related to the location of the third component in the ternary active layer.

This paper describes fundamental physical principles that govern the photovoltaic process in ternary solar cells and the corresponding characterization techniques, such as charge transfer, energy transfer, and parallel-linkage or alloy model. It summarizes the advantages of ternary solar cells, like efficient strategies for enhanced photon harvesting, phase and morphology adjustment, crystallinity forming and device stability. The current challenges and further prospects on ternary solar cells are also briefly analyzed in the last section of this paper.

Perovskite Solar Cells: From Materials to Devices

Hyun Suk Jung* and Nam-Gyu Park*



From the Contents

1. Historical Background of Organometal Halide Perovskites.....11
2. Basic Fundamentals of Organometal Halide Perovskites.....11
3. Working Principle and Device Structures ...13
4. Preparation Methods for High Efficiency Perovskite Solar Cells.....15
5. Photoluminescence and Polarization Characteristics.....18
6. Perovskite Suitable for Flexible Solar Cells21
7. Long-Term Stability22
8. Summary and Outlook.....23

Perovskite solar cells based on organometal halide light absorbers have been considered a promising photovoltaic technology due to their superb power conversion efficiency (PCE) along with very low material costs. Since the first report on a long-term durable solid-state perovskite solar cell with a PCE of 9.7% in 2012, a PCE as high as 19.3% was demonstrated in 2014, and a certified PCE of 17.9% was shown in 2014. Such a high photovoltaic performance is attributed to optically high absorption characteristics and balanced charge transport properties with long diffusion lengths. Nevertheless, there are lots of puzzles to unravel the basis for such high photovoltaic performances. The working principle of perovskite solar cells has not been well established by far, which is the most important thing for understanding perovskite solar cells. In this review, basic fundamentals of perovskite materials including opto-electronic and dielectric properties are described to give a better understanding and insight into high-performing perovskite solar cells. In addition, various fabrication techniques and device structures are described toward the further improvement of perovskite solar cells.

1. Historical Background of Organometal Halide Perovskites

The key material for the perovskite solar cell recently receiving great attention is the organometal halide $\text{CH}_3\text{NH}_3\text{MX}_3$ ($\text{M} = \text{Pb}$ or Sn , $\text{X} = \text{Cl}$, Br or I), whose structure and physical properties were first reported by Weber in 1978.^[1,2] Those Pb- and Sn-based halide perovskite materials were stabilized mostly as cubic perovskite structures at ambient temperature. For $\text{CH}_3\text{NH}_3\text{PbX}_3$, the unit cell parameter a increases from 5.68 to 5.92 and to 6.27 Å as the size of halide increases from $\text{X} = \text{Cl}$ to Br and to I , respectively. Lattice parameters in the cubic phase can be simply tuned by mixing halides; for instance, $\text{CH}_3\text{NH}_3\text{PbBr}_{2.3}\text{Cl}_{0.7}$ showed $a = 5.98$ Å, $\text{CH}_3\text{NH}_3\text{PbBr}_{2.07}\text{I}_{0.93}$ showed $a = 6.03$ Å, and $\text{CH}_3\text{NH}_3\text{PbBr}_{0.45}\text{I}_{2.55}$ showed $a = 6.25$ Å. $\text{CH}_3\text{NH}_3\text{SnBr}_x\text{I}_{3-x}$ ($x = 0$ – 3) crystallized to the cubic perovskite structure with the unit cell parameters $a = 5.89$ Å ($x = 3$), $a = 6.01$ Å ($x = 2$) and $a = 6.24$ Å ($x = 0$). Contrary to Pb-based perovskite materials, some Sn-based perovskite materials exhibited conducting properties.^[2]

Organic-inorganic perovskites have received attention due to their being capable of undergoing a transition from insulator to metal by increasing the number of inorganic layers in the $(\text{C}_4\text{H}_9\text{NH}_3)_2(\text{CH}_3\text{NH}_3)_{n-1}\text{Sn}_n\text{I}_{3n+1}$ layered perovskite.^[3] This result was considered to be an important finding because high-temperature superconductors could be possible from these organic-inorganic perovskite materials. For this reason, little attention has been paid to the photovoltaic ability of the organic-inorganic halide perovskite materials. In 2009, it was first attempted to use $\text{CH}_3\text{NH}_3\text{PbX}_3$ ($\text{X} = \text{Br}$ and I) as a semiconductor sensitizer in dye-sensitized liquid junction-type solar cells.^[4] This attempt led to the power conversion efficiency (PCE) of 3–4%, which was, however, a much low efficiency compared to the conventional Ru-based molecular dyes with PCEs of more than 11%^[5] and even semiconductor quantum dot sensitizers with PCEs of 5–6%.^[6] Thus, little attention has been focused on the methylammonium lead halide perovskite materials due to their low photovoltaic performance and extreme instability to liquid electrolytes. Park's group reported two years later a 6.5% efficient $\text{CH}_3\text{NH}_3\text{PbI}_3$ perovskite solar cell which was slightly more stable in electrolytes.^[7] This result contained more advanced technology, showing how to form the perovskite sensitizer on the thinner TiO_2 film. However, this result was not cited until the development of a long-term stable perovskite solar cell in 2012^[8] due to the dissolution problem of the organic-inorganic halide perovskite in polar liquid electrolytes. Perovskite solar cell research has been triggered by the discovery of the 9.7% solid-state perovskite solar cell with a 500 h confirmed stability.^[8]

2. Basic Fundamentals of Organometal Halide Perovskites

2.1. Madelung Constant and Lattice Energy

The Madelung constant (M) for cubic perovskite $\text{A}^{+1}\text{B}^{+2}(\text{X}^{-1})_3$ was estimated to be related to the Madelung

constant for the CsCl structure and the Cu_2O structure, that is, $M(\text{A}^{+1}\text{B}^{+2}(\text{X}^{-1})_3) = 2M(\text{Cu}_2\text{O}) - 4M(\text{CsCl})$.^[9] The Madelung constant is important in evaluating lattice energy. Based on the knowledge that Madelung constants for Cu_2O and CsCl are 4.4425 and 1.7627, respectively,^[10] the Madelung constant for organometal halide perovskites with cubic structures are calculated to be 1.8342. Since the lattice energy is proportional to the Madelung constant and oxidation numbers (i.e., ionic charges) according to the Born-Lande equation,^[11] the lattice energy can be roughly estimated from those values. For instance, the ratio of lattice energies (E_{lat}) between Cu_2O and CsCl will be $E_{\text{lat}}(\text{Cu}_2\text{O})/E_{\text{lat}}(\text{CsCl}) = 5.0406$, because $E_{\text{lat}}(\text{Cu}_2\text{O}) \propto 4.4425 \times (+1) \times (-2)$ and $E_{\text{lat}}(\text{CsCl}) \propto 1.7627 \times (+1) \times (-1)$, which is consistent with the ratio of 4.9817 calculated from the lattice energies for Cu_2O (3273 kJ/mol) and CsCl (657 kJ/mol), estimated based on the standard thermochemical properties of chemical substances.^[12] Thus the lattice energy of ABX_3 cubic perovskite is expected to be higher than that of CsCl but lower than that of Cu_2O , because $E_{\text{lat}}(\text{ABX}_3) \propto 1.8342 \times (+1) \times (+2) \times (-1)$, from which one can expect that only a low energy is required to separate the perovskite solid into ions and to form the perovskite from ions because of ionic characteristics. In addition, the covalency of the ionic crystal will increase as the lattice energy increases, or iconicity increases as lattice energy decreases.^[13] For instance, the enhanced bond iconicity was found to decrease the lattice energy and thereby improve the dielectric properties.^[13] Thus, organometal halide perovskite tends to possess strong ionic characteristics due to its low lattice energy, which is likely to be sensitive to polarization in an electric field.

2.2. Phase Transition and Its Origin

It is interesting that methylammonium ($\text{MA} = \text{CH}_3\text{NH}_3^+$)-based halide perovskite materials undergo structural phase transitions with temperature, due to the molecular motion of the methylammonium cation along the C–N axis and/or with respect to the crystal axis, as can be seen in Figure 1.^[14] The degree of rotation of CH_3NH_3^+ was investigated using ^1H and ^{14}N NMR spectra, where a rapid rotation was observed at high temperature phases and its rotation was restricted when

H. S. Jung
School of Advanced Materials
Science and Engineering
Sungkyunkwan University (SKKU)
Suwon 440-746, Korea
Tel: 82-31-290-7403
E-mail: hsjung1@skku.edu



N.-G. Park
School of Chemical Engineering and
Department of Energy Science
Sungkyunkwan University (SKKU)
Suwon 440-746, Korea
Tel: 82-31-290-7241
E-mail: npark@skku.edu

DOI: 10.1002/smll.201402767

the temperature was lowered.^[14] The temperature-dependent crystal structure of MAPbX_3 was studied with the powdered samples, where cubic \rightarrow tetragonal \rightarrow orthorhombic phase transitions were detected as the temperature was lowered due to highly ordered organic cations along the C–N axis, via the quenching of molecular motion.^[15]

Recent first principle calculations for $\text{CH}_3\text{NH}_3\text{PbI}_3$ revealed that the C–N bonds of MA ions are arranged in parallel along the *ab* plane that is perpendicular to the *c*-axis, i.e., the (002) or (004) planes in the low-temperature orthorhombic phase, whereas they are distributed vertically and in parallel in the room-temperature tetragonal phase.^[17] The distribution of MA ions does not directly affect the valence band maximum (VBM) and conduction band minimum (CBM), but has an influence on Pb–I bond length, Pb–I–Pb bond angle, and bandgap energy, which indicates that the MA ions play an important role in both the geometry stability and the electronic structure.^[17]

2.3. Band Position and Bandgap Tuning

The absorption coefficient of $\text{CH}_3\text{NH}_3\text{PbI}_3$ was estimated to be $1.5 \times 10^4 \text{ cm}^{-1}$ at 550 nm from a nanocrystalline TiO_2 thin film whose surface was coated with $\text{CH}_3\text{NH}_3\text{PbI}_3$ nanodots,^[7] which indicates that the penetration depth for 550 nm light is only 0.66 μm . The absorption property of a thin $\text{CH}_3\text{NH}_3\text{PbI}_3$ perovskite film was measured and compared to those of conventional photovoltaic materials such as GaAs, CdTe, and CIGS, where the absorption coefficients are as high as 10^4 – 10^5 cm^{-1} and the sharp onset near the bandgap for perovskite was similar to those for the typical photovoltaic materials.^[18] The bandgap of $\text{CH}_3\text{NH}_3\text{PbI}_3$ was evaluated to be 1.50–1.55 eV from UV photoelectron, UV-vis, and incident photon-to-electron efficiency (IPCE) spectra.^[8] However, a bandgap of around 1.55 eV is not enough for panchromatic absorption due to the relatively short absorption wavelength limited to 800 nm. Bandgap tuning is required to extend the absorption to longer wavelengths without sacrificing the absorption coefficient. Replacing MA with other organic cations is one approach, since organic cations in the A site of ABX_3 can tune the bandgap because they modify the M–X–M bond length and angle without affecting the valence band maximum.^[17] For instance, the replacement of MA with formamidinium $\text{HC}(\text{NH}_2)_2^+$ (FA) was found to reduce the bandgap by about 0.07 eV, giving rise to an extension of the absorption wavelength by about 40 nm.^[19] Another approach is the direct modification of M–X bond. For instance, the bandgap decreases from 1.55 eV to 1.17 eV when partially replacing the Pb(2+) in $\text{CH}_3\text{NH}_3\text{PbI}_3$ with Sn(2+).^[20] Thus, the bandgap can be tuned in between 1.55 eV and 1.17 eV by varying the ratio of lead to tin. Moreover, the direct modification of M–X bonds in AMX_3 perovskite will influence the valence band maximum (VBM) and conduction band minimum (CBM), since band edges are determined by the B-site metal orbitals as studied by the first principle calculations.^[21] In $\text{CH}_3\text{NH}_3\text{PbI}_3$, it was estimated that the VBM consisted mainly of the s-antibonding states of Pb 6s



Hyun Suk Jung is an associate professor in the School of Advanced Materials Science & Engineering at Sungkyunkwan University (SKKU). He received his BS, MS, and PhD degrees in materials science and engineering from Seoul National University (SNU), in 1997, 1999, and 2004, respectively. He joined Los Alamos National Laboratory (LANL) as a director's postdoctoral fellow in 2005. He had worked for Kookmin University (KMU) since 2006 and joined SKKU in 2011. He has published over 110 peer-reviewed papers regarding the synthesis of inorganic nanomaterials and dye-sensitized solar cells.

He presently researches perovskite solar cells and flexible solar cells.



Nam-Gyu Park received his BS in chemical education and MS and PhD degrees in chemistry from Seoul National University (SNU) in 1988, 1992, and 1995, respectively. He was at ICMCB-CNRS, France, from 1996 to 1997 and National Renewable Energy Laboratory (NREL), USA, from 1997 to 1999 as a postdoctoral researcher. He worked for the Electronics and Telecommunications Research Institute from 2000 to 2005. He was the director of the solar cell research center at Korea Institute of Science and Technology (KIST) from 2005 to 2009. Since 2009, he joined School of Chemical Engineering of

Sungkyunkwan University (SKKU) as a full professor. He is currently a distinguished professor at SKKU. His research has been focused on dye-sensitized solar cells since 1997, and he is currently devoted to perovskite solar cells since the first report on a solid state perovskite solar cell in 2012 by his group.

and I 5p orbitals, and the CBM was composed primarily of the s-antibonding states of Pb 6p and I 5s orbitals.^[21] It is also obvious that changing the halide in the M–X bond will result in modification of the bandgap. Electronic structures of $\text{CH}_3\text{NH}_3\text{PbX}_3$ ($X = \text{Cl}, \text{Br}$, and I) and $\text{CH}_3\text{NH}_3\text{PbI}_2\text{X}$ were recently studied based on density functional theory (DFT) calculations,^[22] where the calculated bandgaps were in agreement to some extent with the experimentally observed bandgaps for $\text{CH}_3\text{NH}_3\text{PbX}_3$ with tetragonal (1.66 (1.55), 1.83 (1.78), and 1.64 (1.55) eV for $X = \text{I}, \text{Br}$, and Cl , respectively. Parentheses are experimental values.) and cubic (1.57 (1.55), 1.80 (2.00), and 2.34 (3.11) eV for $X = \text{I}, \text{Br}$, and Cl , respectively) structures. **Figure 2** shows the bandgap, VBM, and CBM for ABX_3 ($A = \text{MA}$ and FA, $B = \text{Pb}, \text{Sn}$ or $\text{Sn}_{1-x}\text{Pb}_x$, $X = \text{Cl}, \text{Br}, \text{I}$ or $\text{I}_{1-x}\text{Br}_x$).

Regarding the optical properties of some perovskite materials, Pb-based perovskite materials such as $\text{CH}_3\text{NH}_3\text{PbI}_3$ and $\text{HC}(\text{NH}_2)_2\text{PbI}_3$ exhibit higher absorption coefficients than Sn-based perovskite ones.^[19] However, a contrary result was reported, where the computational calculation based on a GW method incorporating spin-orbit coupling (SOC) showed that the optical absorption of $\text{CH}_3\text{NH}_3\text{SnI}_3$ was higher than that of its Pb-based analogue.^[23] Both the Pb- and Sn-based perovskite materials are promising candidates for high efficiency perovskite solar cells in terms of bandgap and absorption properties.

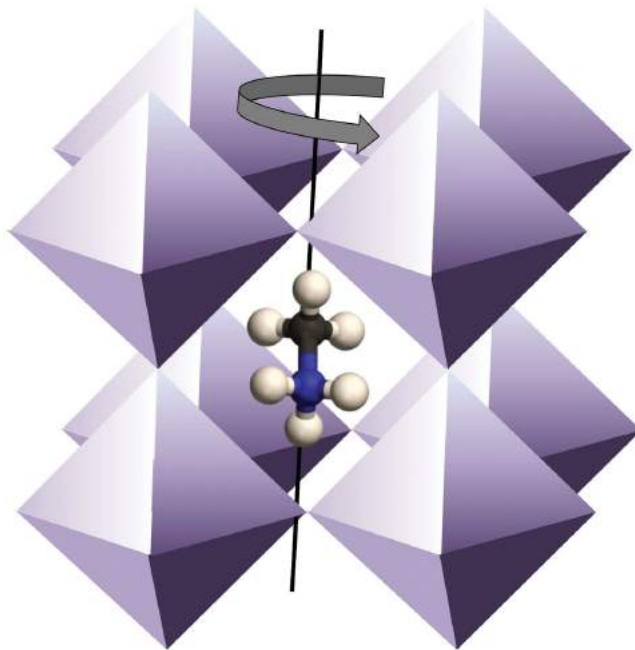


Figure 1. Molecular motion of A-site CH_3NH_3^+ cation in the perovskite $\text{CH}_3\text{NH}_3\text{MX}_3$ (M = divalent metal and X = halogen) unit cell. CH_3NH_3^+ cation can have two types of orientational disorder in the crystal: the orientation of the C–N axis relative to the crystal axis (type A) and the rotation around the C–N axis (type B).^[16]

2.4. Dielectric and Electrical Properties

Heat capacity, dielectric permittivity, AC and DC conductivity, and pressure–temperature phase relations of MAPbX_3 ($\text{X} = \text{Cl}, \text{Br}$ and I) and MASnX_3 ($\text{X} = \text{Br}$ and I) have been studied in detail.^[16,24,25] The data were obtained from single crystals, where an aqueous solution of $\text{Pb}(\text{CH}_3\text{COO})_2$ was added dropwise to an excess quantity of hot aqueous solution of MAX ($\text{X} = \text{Cl}, \text{Br}$, and I), followed by slow cooling to 5 °C for preparing MAPbX_3 ($\text{X} = \text{Cl}, \text{Br}$, and I) crystals. For preparing MASnBr_3 crystals, an anhydrous ethanol solution

of MABr was added dropwise to a boiling ethanol solution of SnBr_2 , which was slowly cooled in a dry N_2 atmosphere. In this case, SnBr_2 was recommended to be purified by sublimation in an evacuated glass tube. The MASnI_3 crystal was grown at 170 °C for 3 days in a glass tube filled with He gas.

The real part of the dielectric permittivity (dielectric constant) ϵ' was investigated with temperature (phase). ϵ' was higher for the tetragonal phase in temperatures ranging from 180 to 300 K, compared to the orthorhombic phase at lower temperature, in which ϵ' increased as the halide anion in MAPbX_3 changed from Cl ($\epsilon' \approx 40$ at 300 K and ≈ 60 at 200 K), to Br ($\epsilon' \approx 50$ at 300 K and ≈ 70 at 200 K) and I ($\epsilon' \approx 60$ at 300 K and ≈ 100 at 200 K) at 100 kHz. In the low-temperature orthorhombic phase, ϵ' was as low as 17, 26, and 36 for Cl, Br and I, respectively, and temperature independent, which indicates that electronic or ionic polarization is expected from the orthorhombic phase. **Figure 3** shows the dielectric constants as a function of frequency,^[12] where electronic polarization arises when the local electronic charges around the nucleus are displaced under the electric field, and ionic polarization results from the displacement of cations and anions in opposite directions under an electric field in ionic materials, whereas orientational polarization can occur in substances with molecules that have permanent electric dipoles. The orientational polarizability (α_{or}) depends on temperature: $\alpha_{\text{or}} = P^2/3kT$ where k is the Boltzmann constant and T temperature. Giant dielectric constants, approaching 10^7 , are observed from perovskites upon illumination especially at low frequencies, as shown in Figure 3b,^[26] which is related to the molecular orientation of A-site CH_3NH_3^+ ions.

Sn-based perovskites such as CsSnBr_3 and $\text{CH}_3\text{NH}_3\text{SnI}_3$ were found to exhibit high electrical conductivity, which might be closely related to the infinite linear –I–Sn–I–Sn– chains formed three-dimensionally in the perovskite lattice.^[28] For the case of Sn-based bromide perovskite materials, the Sn environment coordinated with bromide was found to be critical to determine the electrical properties. According to ^{119}Sn Mössbauer studies on a series of solid solutions, $\text{CH}_3\text{NH}_3\text{Sn}_{1-x}\text{Pb}_x\text{Br}_3$, and CsSnBr_3 , the high electrical conductivity of the CsSnBr_3 (almost metallic) decreased drastically upon replacement of Cs and Sn by CH_3NH_3 and Pb, respectively, due to change in the local octahedral environment of SnBr_6 and the Sn–Br–Sn bond length.^[29]

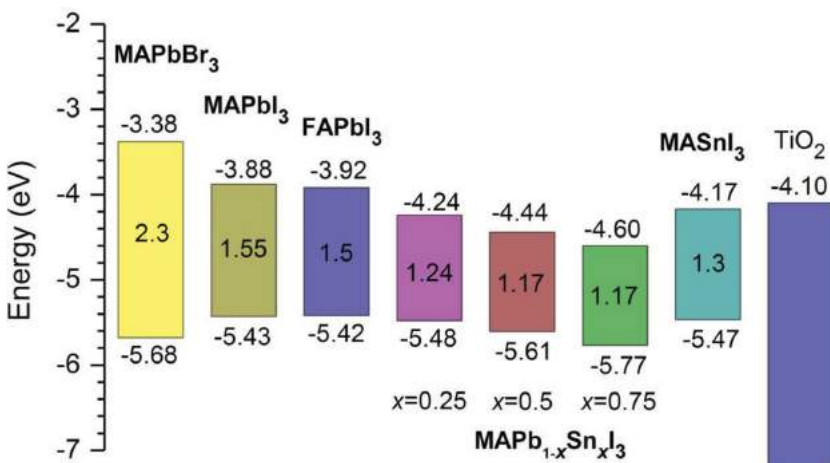


Figure 2. Schematic energy level diagram of MAPbBr_3 , MAPbI_3 , FAPbI_3 , $\text{MAPb}_{1-x}\text{Sn}_x\text{I}_3$, and MASnI_3 along with TiO_2 . MA and FA stand for methylammonium (CH_3NH_3) and formamidinium ($\text{HC}(\text{NH}_2)_2$), respectively. Data for $\text{MAPb}_{1-x}\text{Sn}_x\text{I}_3$ ($x = 0.25, 0.5, 0.75$ and 1) are reproduced with permission.^[20] Copyright 2014, ACS.

3. Working Principle and Device Structures

Light absorption, charge separation, charge transport, and charge collection are general solar cell working processes. In order to construct them, light harvesters should be selected and their opto-electronic properties investigated. For instance, a p-i-n junction is required in case the light harvester is an intrinsic

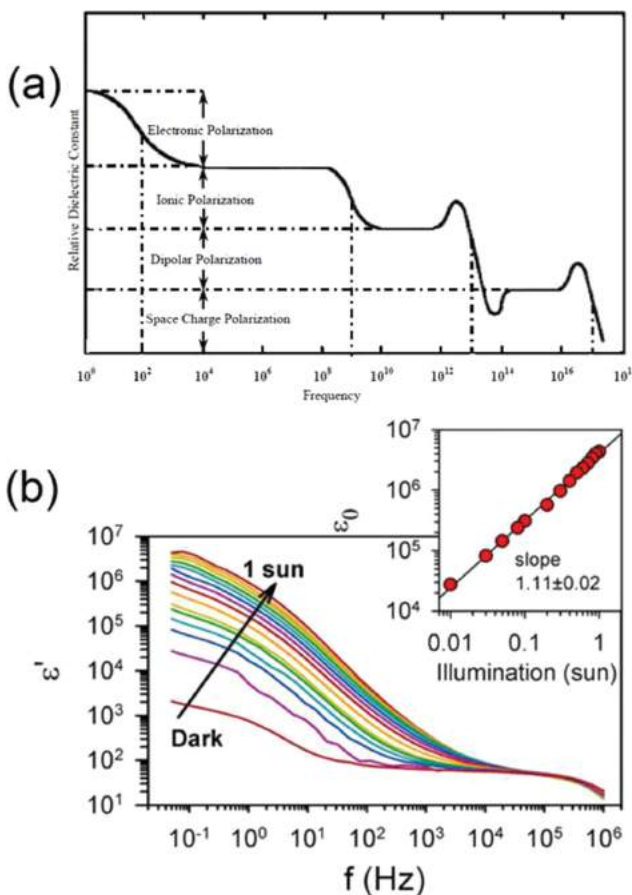


Figure 3. (a) Schematic of different contributions to polarizability as a function of frequency and (b) the real permittivity as a function of frequency for different incident light intensities from dark to 1 sun (100 mW/cm²) for MAPbI_{3-x}Cl_x perovskite (compact TiO₂/MAPbI_{3-x}Cl_x in Al₂O₃ scaffold/spiro-OMeTAD), measured at room temperature and 0 V applied bias. Reproduced with permission.^[27] Inset: linear regression of dielectric constant vs. illumination intensity at $f = 50$ mHz, observing a close-to-linear dependence between ϵ_0 and illumination intensity. Reproduced with permission.^[26] Copyright 2014, ACS.

semiconductor, while a p-n junction is needed if the light harvester possesses an n-type or p-type property, because n- or p-types can transfer electrons or holes to the light harvester. Organometallic perovskite materials can be applied to either p-i-n junction or p-n junction types, since they have balanced charge transport properties. Electron and hole transport properties were reported for CH₃NH₃PbI₃ prepared by different synthetic methods using a CH₃NH₃I + PbI₂ mixture^[30] and a 3CH₃NH₃I+PbCl₂ mixture,^[31] where X-ray diffraction patterns were indexed as tetragonal CH₃NH₃PbI₃ regardless of the preparation method. The electron and hole diffusion lengths were estimated to be ~130 nm and ~100 nm, respectively, for the samples prepared from the former method, while longer diffusion lengths of ~1069 nm for electrons and ~1213 nm for holes were measured for the sample prepared using the latter method. The difference in diffusion length depending on preparation method is likely to be due to quality of the perovskite layer, such as crystallinity or grain size. Electron beam-induced current (EBIC) imaging studies of CH₃NH₃PbI₃ layers prepared from PbI₂ and PbCl₂ sources

revealed that charge diffusion lengths were about 1 μm for both samples, but the diffusion length for holes was longer than that for electrons for the case of CH₃NH₃PbI₃ prepared without a chloride source.^[32] To compensate the shorter electron diffusion length, an electron transport layer with a long diffusion length may be required for CH₃NH₃PbI₃. Electron diffusion lengths of CH₃NH₃PbI₃ solar cells employing mesoporous TiO₂ layers are estimated to exceed 1 μm.^[33] Electron and hole mobilities were found to be as high as 25 cm²/Vs, and the mobilities of both were almost balanced and remained high, on a microsecond time scale, along with a slow microsecond time scale for recombination.^[34] However, the performance may degrade if the mobility of the injected electron in the TiO₂ layer is slower than that of perovskite. Therefore, careful design of oxide layers, taking into account this diffusion length and the mobility of the injected electrons, is important to achieve high efficiency.

Based upon the unique property of the perovskite, two typical structures can be constructed: a mesoscopic nanostructure and a planar structure. Figure 4 shows schematic device structures and energetics. Charge separation by electron injection from perovskite to TiO₂ is obvious in cases where perovskite dots are adsorbed onto the TiO₂ surface.^[8] In this case, the working principle is expected to be similar to dye-sensitized solid state solar cells. However, the working mechanism is different from dye-sensitized solar cells for both mesoscopic nanostructures with perovskite pore fillings (Figure 4a) and planar structures without a mesoporous TiO₂ layer (Figure 4b), because of charge transport^[30,31] and charge accumulation properties in the perovskite.^[35] Carrier transport and recombination were compared for the mesoscopic structure and the planar structure; in this study, the former was lower in efficiency than the latter, and found to be the main factor affecting photovoltaic performance.^[36] The results showed that the transport rate was the same but the recombination rate was higher for the mesoscopic structure. Since the resistances for transport and recombination are related to diffusion length, low performance was ascribed to a low diffusion length associated with a low recombination resistance, accelerating recombination. It was also

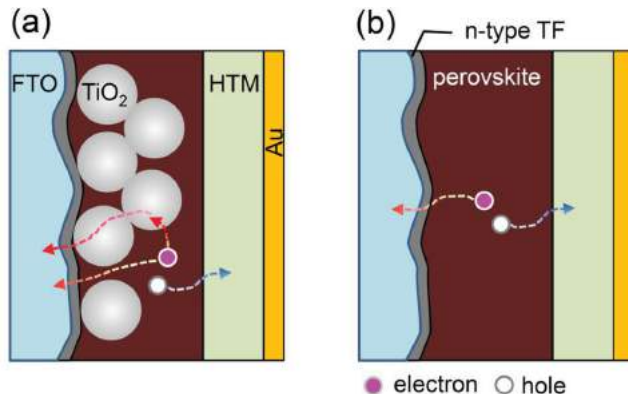


Figure 4. (a) Mesoscopic perovskite solar cell with mesoporous TiO₂ layer and (b) planar structure without a mesoporous TiO₂ layer. Thin film (TF) on fluorine doped tin oxide (FTO) is an n-type semiconductor. HTM stands for hole transporting material. In the mesoscopic structure, electrons can be collected directly and/or via TiO₂ layer.

argued that the dominant transport pathway is the perovskite absorber, even in the mesoscopic structure. However, a different photovoltaic performance was observed from the comparative study on rutile and anatase TiO_2 mesoporous films, which indicates that transport through the mesoporous TiO_2 layer cannot be ruled out.^[37] In the mesoscopic nanostructure, efforts have been made to facilitate charge transport by employing new nanomaterials such as ZnO nanorods, 3D- TiO_2 nanoparticles/ITO nanowire composites, and TiO_2 nanoparticle/graphene composites.^[38–40] The interface engineering of mesoscopic materials is one good way to control charge transport and recombination. Recently, an ultrathin MgO nanolayer was found to retard charge recombination between the electrons injected into TiO_2 nanoparticles and the holes in perovskite materials.^[41] This study demonstrates the importance of interface engineering for improving solar cell performance. Also, in the planar structure, the interface engineering impacts on the charge transport and recombination. Yang's group modified the ITO layer with polyethyleneimine ethoxylate (PEIE) to reduce the work function and increase the carrier density by doping yttrium into the TiO_2 compact layer, thereby improving the electron transport channel in the planar structure perovskite solar cell.^[42] Zhang et al. also inserted polyelectrolyte intermediate layers such as PEIE and P3TMAHT and achieved a high efficiency of 12%, which was attributed to the formation of surface dipoles, thereby reducing the work function of the subsequently deposited metal.^[43] In the planar structure, there are two types of structures, i.e., planar and inverted planar structures. We will discuss this in more detail in Section 6.

Besides the two typical of perovskite solar cell structures depicted in Figure 4, an HTM-free structure is also possible because perovskite possesses hole transporting properties. In the case of hole transport material (HTM)-free perovskite solar cells, a thick perovskite layer with a smooth surface is needed to avoid forming shunt pathways as well as to form a good back contact to achieve high efficiency. The first demonstration of the HTM-free structure with an FTO/2D sheet $\text{TiO}_2/\text{CH}_3\text{NH}_3\text{PbI}_3/\text{Au}$ configuration showed a PCE of 5.5%,^[44] which was improved to 8% after replacing the TiO_2 nanosheet with a thinner TiO_2 nanoparticle film.^[45] The photovoltaic performance of the HTM-free perovskite solar cell was dependent on the depletion layer width at the $\text{TiO}_2\text{-CH}_3\text{NH}_3\text{PbI}_3$ junction, and enlargement of the width by increasing the depleted fraction of TiO_2 led to a PCE of 10.85%.^[46] A triple layer HTM-free perovskite solar cell, composed of a simple mesoscopic $\text{TiO}_2/\text{ZrO}_2/\text{C}$ triple layer, has been exploited by Han et al.^[47] The ZrO_2 layer was found to block the flow of photogenerated electrons to the back contact, retarding recombination with the holes from the perovskite at the back contact. The cell achieved a certified power conversion efficiency of 12.8%.

The studied materials for perovskite solar cells are $\text{CH}_3\text{NH}_3\text{PbI}_3$, $\text{CH}_3\text{NH}_3\text{PbI}_{3-x}\text{Cl}_x$, $\text{CH}_3\text{NH}_3\text{PbBr}_3$, $\text{CH}_3\text{NH}_3\text{Pb}(\text{I}_{1-x}\text{Br}_x)_3$, $\text{HC}(\text{NH}_2)_2\text{PbI}_3$, $\text{HC}(\text{NH}_2)_2\text{Pb}(\text{I}_{1-x}\text{Br}_x)_3$ and $\text{CH}_3\text{NH}_3\text{SnI}_3$. In Table 1, the reported performances are summarized in terms of material and cell configuration. It is noted that most iodide perovskites exhibit an open-circuit

voltage over 1 V and bromide analogues demonstrate higher voltages than iodide ones. This is due to the fact that the bandgap of bromide perovskite is larger than that of iodide. HTM materials are also important for high efficiency perovskite solar cells, where the most studied HTM is spiro-MeOTAD, but polymertic HTMs such as the thiophene derivative P3HT and tryarylamine-based PTAA have also been tested. In addition, inorganic HTMs such as NiO , CuI , and CuSCN are confirmed to be suitable for perovskite solar cells.

4. Preparation Methods for High Efficiency Perovskite Solar Cells

4.1. Solution Process: One-Step Versus Two-Step Coatings

To deposit $\text{CH}_3\text{NH}_3\text{PbI}_3$ perovskite on a substrate, two methods are available, that is, one-step and two-step coating methods. Perovskite forms either by spin-coating a mixed $\text{CH}_3\text{NH}_3\text{I}$ and PbI_2 solution (one-step coating) or by spin-coating $\text{CH}_3\text{NH}_3\text{I}$ after coating with PbI_2 (two-step coating). For the one-step coating method, $\text{CH}_3\text{NH}_3\text{I}$ and PbI_2 are dissolved in an appropriate solvent such as a polar aprotic solvent like *N,N*-dimethylformamide (DMF), gamma-butyrolactone (GBL), or dimethyl sulfoxide (DMSO), and this is used as a coating solution. Drying and annealing processes are followed by spin coating. For the two-step coating method, PbI_2 solution is first coated on the substrate to form a PbI_2 film and then a 2-propanol solution of $\text{CH}_3\text{NH}_3\text{I}$ is spun on the PbI_2 film. Figure 5 shows schematically the procedure for both the one-step and two-step spin-coating methods. In order to prepare high-quality perovskite films, it is important to adjust coating parameters such as spinning rate and time, temperature, solution wettability and viscosity, etc. Compared to one-step spin-coating, two-step spin-coating was found to exhibit better photovoltaic performance due to better morphology and interfaces,^[79] which indicates that morphology control of perovskite film is crucial in achieving high-efficiency perovskite solar cells.

Perovskite prepared by the two-step coating method shows cuboid-like crystals, whereas the one-step method from the dimethyl acetamide (DMA) solution of $\text{CH}_3\text{NH}_3\text{I}$ and PbI_2 produced a shapeless morphology. It was found that the size of $\text{CH}_3\text{NH}_3\text{PbI}_3$ was significantly altered by the concentration of $\text{CH}_3\text{NH}_3\text{I}$ in the second deposition step.^[56] When the concentration of the 2-propanol solution of $\text{CH}_3\text{NH}_3\text{I}$ decreased from 0.063 M to 0.038 M, the average $\text{CH}_3\text{NH}_3\text{PbI}_3$ crystal size increased from about 90 nm to about 700 nm, as shown in Figure 6.

In the case of the methylammonium lead iodide chloride ($\text{CH}_3\text{NH}_3\text{PbI}_2\text{Cl}$) perovskite layer, whose diffusion length is 10 times longer than that of pure $\text{CH}_3\text{NH}_3\text{PbI}_3$, a single-step deposition process using a mixture of $\text{CH}_3\text{NH}_3\text{I}$ and PbCl_2 was adopted due to the poor solubility of PbCl_2 in DMF. Recently, a two-step method was realized using a mixture of PbCl_2 and PbI_2 solution. The solubility of PbCl_2 can be significantly increased in the presence of additives such as PbI_2 due to the common ion effect. Wu et al. successfully dissolved

Table 1. Photovoltaic performance of perovskite solar cells depending on materials and cell configurations. J_{sc} , V_{oc} and FF stand for short-circuit current density, open-circuit voltage, and fill factor, respectively. mp, bl and ETL represent mesoporous, blocking layer and extremely thin layer, respectively.

Materials	Cell configuration	J_{sc} [mA/cm ²]	V_{oc} [V]	FF	PCE [%]	Ref.
MAPbI ₃	mp-TiO ₂ /MAPbI ₃ /spiro-MeOTAD	17.6	0.888	0.62	9.7	[8]
	MAPbI ₃ /PCBM	10.32	0.60	0.63	3.9	[48]
	ZnO nanorod/MAPbI ₃ /spiro-MeOTAD	16.98	1.02	0.51	8.9	[49]
	mp-TiO ₂ /MAPbI ₃ /P3HT-MWNT	14.8	0.76	0.57	6.45	[50]
	rutile TiO ₂ nanorod/MAPbI ₃ /spiro-MeOTAD	15.6	0.955	0.63	9.4	[51]
	mp-TiO ₂ /MAPbI ₃ /PTAA	16.5	0.997	0.727	12	[52]
	mp-TiO ₂ /MAPbI ₃ (2-step)/spiro-MeOTAD	20	0.933	0.73	15	[53]
	mp-ZrO ₂ /MAPbI ₃ /spiro-MeOTAD	17.3	1.07	0.59	10.8	[54]
	mp-TiO ₂ /MAPbI ₃ (Toluene)/PTAA	19.58	1.105	0.76	16.46	[55]
	mp-TiO ₂ /MAPbI ₃ cuboid/spiro-MeOTAD	21.64	1.056	0.741	17.01	[56]
	ZnO nanorod/MAPbI ₃ /spiro-MeOTAD	20.08	0.991	0.56	11.13	[38]
	NiO/MAPbI ₃ /PCBM	13.24	1.040	0.69	9.51	[57]
	polyTPD/MAPbI ₃ /PCBM	16.12	1.05	0.67	12.04	[58]
	ZnO (25 nm)/MAPbI ₃ /spiro-MeOTAD	20.4	1.03	0.749	15.7	[59]
	NiO (45 nm)/MAPbI ₃ /PCBM	16.27	0.882	0.635	9.11	[60]
	mp-TiO ₂ /MAPbI ₃ /CuSCN	19.7	1.016	0.62	12.4	[61]
	mp-TiO ₂ /MAPbI ₃ /Cul	17.8	0.55	0.62	6.0	[62]
MAPbI _{3-x} Cl _x	mp-Al ₂ O ₃ /MAPbI _{3-x} Cl _x /spiro-MeOTAD	17.8	0.98	0.63	10.9	[63]
	MAPbI _{3-x} Cl _x /P3HT	20.8	0.921	0.542	10.4	[64]
	(Al ₂ O ₃ + MAPbI _{3-x} Cl _x)/spiro-MeOTAD at T < 110 °C	12.78	0.925	0.61	7.16	[65]
	MAPbI _{3-x} Cl _x (evap.)/spiro-MeOTAD	21.5	1.07	0.67	15.4	[66]
	bl-Y:TiO ₂ /MAPbI _{3-x} Cl _x (solution)/spiro-MeOTAD	22.75	1.13	0.75	19.3	[42]
MAPbBr ₃	mp-TiO ₂ /MAPbBr ₃ /PCBDPP	4.47	1.16	0.59	3.04	[67]
	mp-Al ₂ O ₃ /MAPbBr ₃ /PDI	1.08	1.30	0.4	0.56	[68]
	mp-TiO ₂ /MAPbBr ₃ /PIF8-TAA	6.1	1.40	0.79	6.7	[69]
	mp-Al ₂ O ₃ /MAPbBr _{3-x} Cl _x /CBP	4.0	1.50	0.46	2.7	[70]
MAPb(I,Br) ₃	mp-TiO ₂ /MAPb(I _{0.8} Br _{0.2}) ₃ /PTAA	19.3	0.91	0.702	12.3	[71]
FAPbI ₃	mp-TiO ₂ /FAPbI ₃ /spiro-MeOTAD	6.45	0.97	0.687	4.3	[72]
	FAPbI ₃ /spiro-MeOTAD	23.3	0.94	0.65	14.2	[73]
	mp-TiO ₂ /FAPbI ₃ /MAPbI ₃ (ETL)/spiro-MeOTAD	20.97	1.032	0.74	16.01	[74]
	mp-TiO ₂ /(MA _{0.6} FA _{0.4})PbI ₃ /spiro-MeOTAD	21.2	1.003	0.7	14.9	[75]
MASnX ₃	mp-TiO ₂ /MASnI ₃ /spiro-MeOTAD	16.8	0.88	0.42	6.4	[76]
	mp-TiO ₂ /MASnI ₃ /spiro-MeOTAD	16.3	0.68	0.48	5.23	[77]
	mp-TiO ₂ /MASnIBr ₂ /spiro-MeOTAD	12.30	0.82	0.57	5.73	[77]
MASn _{0.5} Pb _{0.5} I ₃	mp-TiO ₂ / MASn _x Pb _(1-x) I ₃ /P3HT	20.04	0.42	0.50	4.18	[78]

PbCl₂ salt in DMF with an addition of PbI₂ and then coated the mixture onto the mesoporous TiO₂ layer. After exposing it to CH₃NH₃I solution, finally a CH₃NH₃PbI_{3-x}Cl_x perovskite layer with controlled morphology was successfully obtained.^[80]

It was found that the photovoltaic performance was strongly influenced by the CH₃NH₃I concentration, i.e., the crystal size of CH₃NH₃PbI₃. In Figure 7, photovoltaic parameters are displayed with respect to CH₃NH₃I concentration. For the 0.038 M and 0.05 M cases, the average power conversion efficiencies

(PCE) were around 16.3%, whereas at high concentration of 0.063 M a lower PCE of 13.4% is obtained due to a lower photocurrent density and fill factor. It is noted that large crystals grown from low concentrations show higher J_{sc} than small ones grown from high concentrations, which is due to a higher light harvesting efficiency, as can be seen in Figure 7e, and a better charge-extraction ability, as measured by Photo-CELIV.^[56,81] It is also noticed that V_{oc} would not increase with increasing crystal size. V_{oc} is higher for 0.050 M compared to those for 0.038 M and 0.063 M. It can be explained in connection with

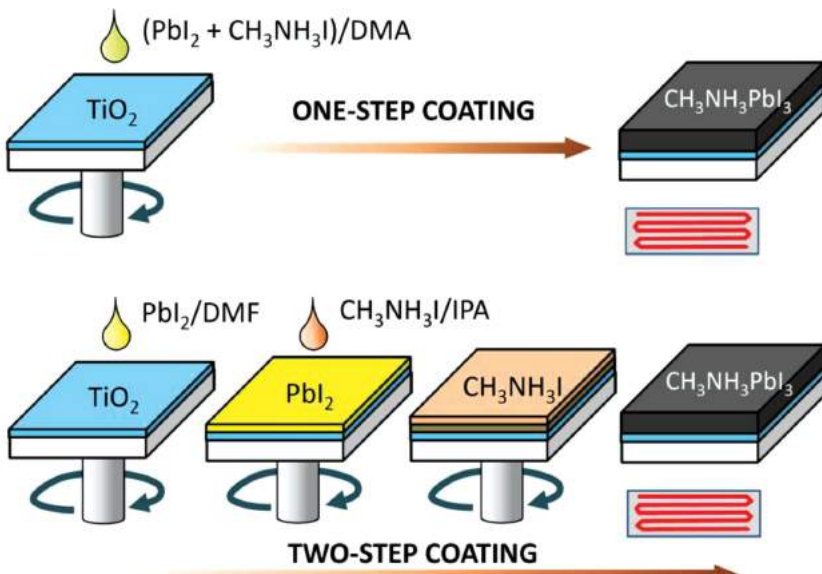


Figure 5. One-step and two-step coating procedures to deposit $\text{CH}_3\text{NH}_3\text{PbI}_3$ perovskite films. DMA, DMF, and IPA represent dimethyl acetamide, dimethyl formamide, and isopropyl alcohol, respectively. Reproduced with permission.^[79] Copyright 2014, AIP.

the Photo-CELIV results, that a change in V_{oc} correlates with the rate of charge-carrier extraction and recombination. A slow hole mobility with high charge extraction characteristics for 0.038 M or a fast hole mobility with low charge extraction characteristics for 0.063 M may not be beneficial to high V_{oc} : a slow hole mobility increases the probability of recombination. Thus, the lowest V_{oc} is observed for the large crystals prepared from the 0.038 M solution. Low charge extraction is likely to lead to not only low photocurrent but also a low Fermi level, which can affect V_{oc} . To realize high V_{oc} the intermediate size with fast mobility, i.e., minimized recombination, and high charge extraction, i.e., maximize the Fermi level, are required. The highest V_{oc} of 1.106 V is observed from the 0.050 M $\text{CH}_3\text{NH}_3\text{I}$ solution.

Recently, solvent engineering enabled the control of morphology of the perovskite layer in solution processes to be comparable with the vacuum process. Cheng et al. reported that a single-step process was capable of fabricating flat and uniform perovskite films by immediately exposing the wet perovskite layer to chlorobenzene, which induced fast crystallization of the perovskite layer.^[82] The role of chlorobenzene is to rapidly reduce the solubility of perovskite materials in the mixed DMF solvent, thereby promoting fast

nucleation and growth of crystals in the film. This technology allowed the reproducible fabrication of high-quality perovskite films. Seok's group also exploited a novel perovskite deposition technique using solvent engineering. They used a mixed solvent of γ -butyrolactone and dimethylsulphoxide (DMSO) followed by toluene drop-casting, which led to extremely uniform and dense perovskite layers.^[55] The role of DMSO was to retard the rapid reaction between PbI_2 and $\text{CH}_3\text{NH}_3\text{I}$, thereby forming a flat film containing an intermediate compound of $\text{CH}_3\text{NH}_3\text{I}\text{-PbI}_2\text{-DMSO}$. The toluene droplet quickly removed excess DMSO solvent from the wet film, which immediately quenched the constituents. Finally, a homogeneous flat perovskite layer was obtained after annealing at 100 °C. The efficiency of these devices was 16.2%, certified by the standardized method in a photovoltaics calibration laboratory. **Figure 8** shows an X-ray diffraction (XRD) pattern of the intermediate and an SEM image of the resulting perovskite layer showing close-packed large grains.

The beauty of solvent engineering was recently verified in the two-step deposition process.^[83] Since the rapid crystallization of PbI_2 induces different crystal sizes on the hole-blocking layer, the resultant perovskite layer possesses inhomogeneity in grain size and stoichiometry. Han et al. used a strong coordinating solvent of DMSO to dissolve PbI_2 and fabricated extremely flat amorphous PbI_2 layers. Consequently, they were able to fabricate a uniform perovskite layer with a small distribution of crystal sizes and a flat surface morphology, which yielded highly reproducible perovskite solar cells with a high efficiency of 13.5%. Effects of additives such as NH_4Cl on the perovskite film were also characterized. Ding and Zuo recorded a 80.11% fill-factor using NH_4Cl additive, which was found to enhance the crystallinity and morphology of perovskite layer.^[84]

4.2. Vacuum Process

Perovskite films can be prepared by the thermal evaporation of chemicals. Co-evaporation of $\text{CH}_3\text{NH}_3\text{I}$ and PbCl_2

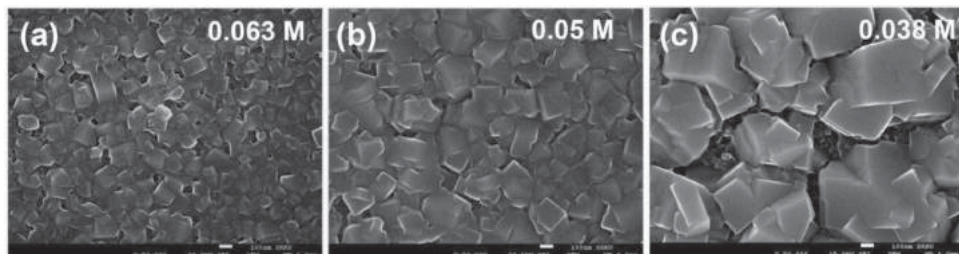


Figure 6. Scanning electron microscopy (SEM) images for $\text{CH}_3\text{NH}_3\text{PbI}_3$ prepared from two-step spin-coating using (a) 0.063 M, (b) 0.05 M and (c) 0.038 M $\text{CH}_3\text{NH}_3\text{I}$ solution. Scale bars represent 100 nm.

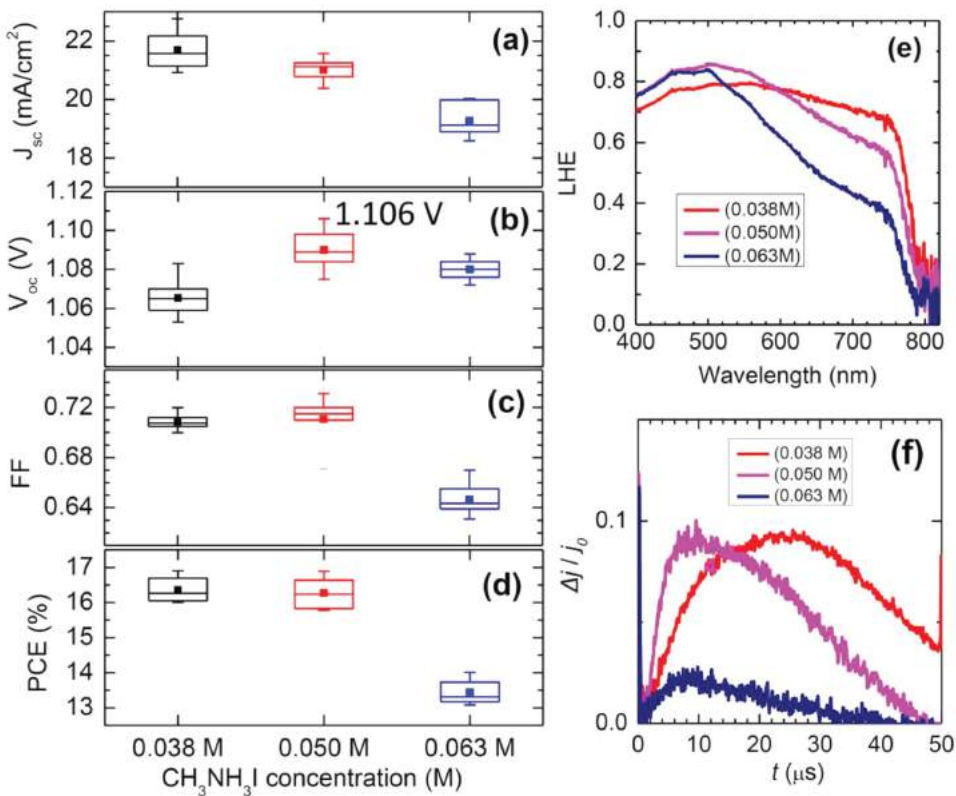


Figure 7. (a–d) Short-circuit current density (J_{sc}), open-circuit voltage (V_{oc}), fill factor (FF) and power conversion efficiency (PCE), depending on the $\text{CH}_3\text{NH}_3\text{I}$ concentration. Error bars in each box represent minimum and maximum values and the middle line in the box represents the median value. Filled squares in the box represent mean values. (e) Light-harvesting efficiency spectra of the $\text{CH}_3\text{NH}_3\text{PbI}_3$ films depending on $\text{CH}_3\text{NH}_3\text{I}$ concentration. (f) Photo-CELIV transients recorded for the devices comprising FTO/bl-Al₂O₃/mp-TiO₂/MAPbI₃/spiro-MeOTAD/Au, depending on the $\text{CH}_3\text{NH}_3\text{I}$ concentration. Reproduced with permission.^[56] Copyright 2014, NPG.

leads to a $\text{CH}_3\text{NH}_3\text{PbI}_3$ phase, and the uniformity of the film was much better than that of the solution-processed films, as shown in **Figure 9**.^[66] The detailed evaporation process is as follows: A dual-source evaporation system with ceramic crucibles was installed in a N_2 -filled glovebox. $\text{CH}_3\text{NH}_3\text{I}$ and PbCl_2 were co-evaporated from separate crucibles at 10^{-5} mbar with an as-deposited molar ratio of 4:1. It was observed that a dark reddish-brown colour appeared immediately after evaporation. Annealing was performed to crystallize the as-deposited perovskite.^[66] The thin perovskite film was prepared by co-evaporation using $\text{CH}_3\text{NH}_3\text{I}$ and PbI_2 , in which the crucible containing $\text{CH}_3\text{NH}_3\text{I}$ was heated to 70 °C and the other containing PbI_2 was heated to 250 °C at 10^{-6} mbar.^[58] The vacuum deposition method seems to be better for thickness control, compared to the solution process.

Thermal evaporation requires high vacuum, which restricts cost effectiveness and mass production. To overcome this problem, a vapor-assisted solution process (VASP), which grows perovskite films via in situ reactions of as-deposited films of PbI_2 with $\text{CH}_3\text{NH}_3\text{I}$ vapor, was developed.^[85] The perovskite film prepared via this method showed a well-defined grain structure with grain sizes up to the microscale, full surface coverage, and small surface roughness.

5. Photoluminescence and Polarization Characteristics

One of the important optical properties when studying photovoltaic materials is photoluminescence (PL), which provides several pieces of information including bandgap, chemical purity, and charge separation. When semiconducting materials absorb photons, electronic excitations occur and then these excitations relax to return to the ground state. Radiative relaxation is called PL. When measuring solid thin films like the organometal halide perovskite films, in contrast to solution samples, careful measurements should be carried out because the angular distribution of the emitted light is highly sensitive to the refractive index of the material and to the orientation of the emitting dipoles within the film.^[86] To minimize the angular distribution, an integrating sphere is recommended to get the absolute PL efficiency of a solid thin film.^[87] However, a conventional set-up may be allowed for comparative studies or relative PL efficiencies. The PL spectra of various organometal halide perovskite materials are collected in **Figure 10**. Lead-based $\text{CH}_3\text{NH}_3\text{PbI}_3$ and $\text{HC}(\text{NH}_2)_2\text{PbI}_3$ show PL values between 750 and 850 nm, where the maximum PL of $\text{HC}(\text{NH}_2)_2\text{PbI}_3$ at around 800 nm is red-shifted compared to that of $\text{CH}_3\text{NH}_3\text{PbI}_3$ at around 775 nm (Figure 10a).^[19] $\text{CH}_3\text{NH}_3\text{SnI}_3$ shows red-shifts of

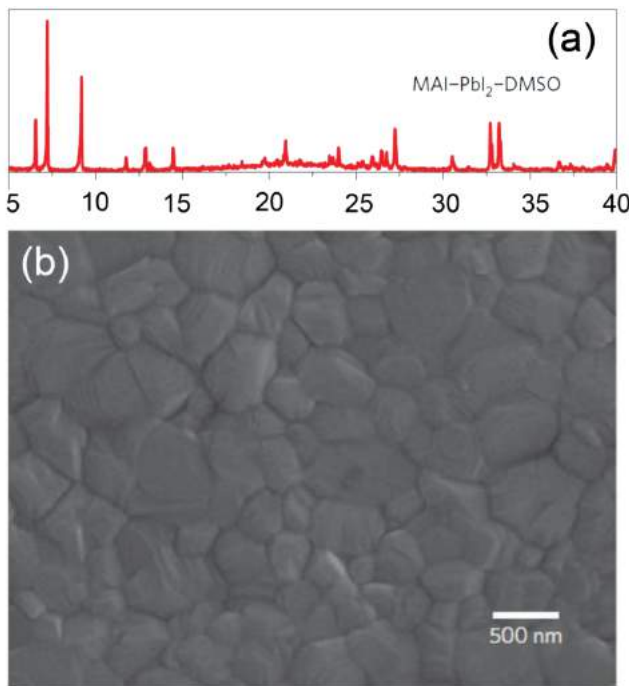


Figure 8. (a) X-ray diffraction pattern of a MAI-PbI₂-DMSO intermediate phase formed by toluene treatment on the film formed by spin-coating of MAI-PbI₂-DMSO-GBL solution. (b) SEM image of the resulting perovskite film via the intermediate phase. Reproduced with permission.^[55] Copyright 2014, NPG.

more than 180 nm and broader PL peaks compared to its lead analogue, as can be seen in Figure 10b,^[76] which is due to its smaller bandgap. Systematic evolution in PL peak shifts is observed upon substitution of methylammonium ($\lambda = 776$ nm) for formamidinium ($\lambda = 776$ nm) in lead iodide perovskite (Figure 10c).^[75] It is noted that PL peaks are broadened upon increasing the formamidinium ratio, which indicates the formation of a solid solution of methylammonium and formamidinium in the perovskite lattice.^[75] In Figure 10d, a gradual blue-shift in PL peaks is observed upon the substitution of iodide for bromide in lead halide perovskite, due to a gradual increase in the bandgap.^[88] The sharp

emission peak for pure iodide broadens as the bromide ratio increases or vice versa, which is indicative of the formation of solid solutions of iodide and bromide in the lattice.

PL quenching measurements are a fast and facile way to investigate charge separation. In the case where perovskite is in contact with an electron acceptor (n-type quencher) or hole acceptor (p-type quencher), PL intensity will be decreased compared to the isolated state due to charge separation by electron or hole injection. From the change in PL intensity, one can evaluate the degree and effectiveness of charge separation. **Figure 11** shows the change in PL intensity for the CH₃NH₃PbI₃ or CH₃NH₃PbI_{3-x}Cl_x perovskites in the absence and presence of n-type or p-type quenchers. A significant decrease in PL intensity is observed when both perovskite materials are in contact with electron-accepting PCBM and hole accepting spiro-MeOTAD, as shown in Figures 11a and b,^[30,31] which is attributed to the injection of electrons and holes. It is also obvious that electrons are injected into mesoporous TiO₂ layers but not into Al₂O₃, because of the higher conduction band position (Figure 11c). However, contrary to the case of spiro-MeOTAD, PL is hardly quenched by PTAA. This suggests that CH₃NH₃PbI₃ can act as a hole-conducting layer.^[52] In the presence of inorganic hole conductors such as NiO and CuSCN, charge separation occurs well, as evidenced by significant PL quenching shown in Figure 11d, where CuSCN is superior to NiO in terms of charge-separation efficiency.^[89] Investigations of PL quenching are thus a useful tool to study charge separation and to get information on interfacial contacts.

Impedance spectroscopic studies on solid-state perovskite solar cells give important insights into carrier transport, recombination, and diffusion length. According to impedance measurements for two different planar and mesoscopic perovskite solar cell structures, it was found that carrier conductivity in both devices was similar but recombination resistance was slightly higher for the planar cell than for the mesoscopic one.^[89] In addition, diffusion length, calculated based on impedance results, was longer for CH₃NH₃PbI_{3-x}Cl_x in the planar structure than for CH₃NH₃PbI₃ in the mesoscopic structure, which is consistent with the diffusion length estimated from time-resolved PL.^[90] The impedance result

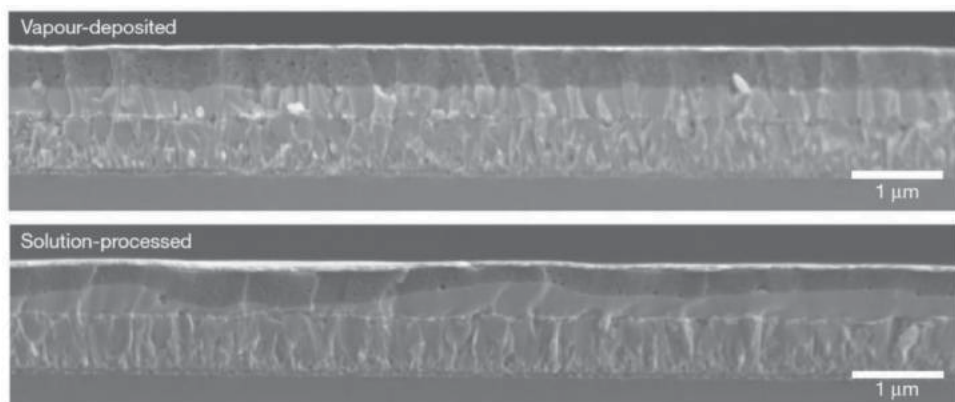


Figure 9. Comparison of the perovskite film uniformity between vapor-deposition and solution-process methods. Reproduced with permission.^[66] Copyright 2013, NPG.

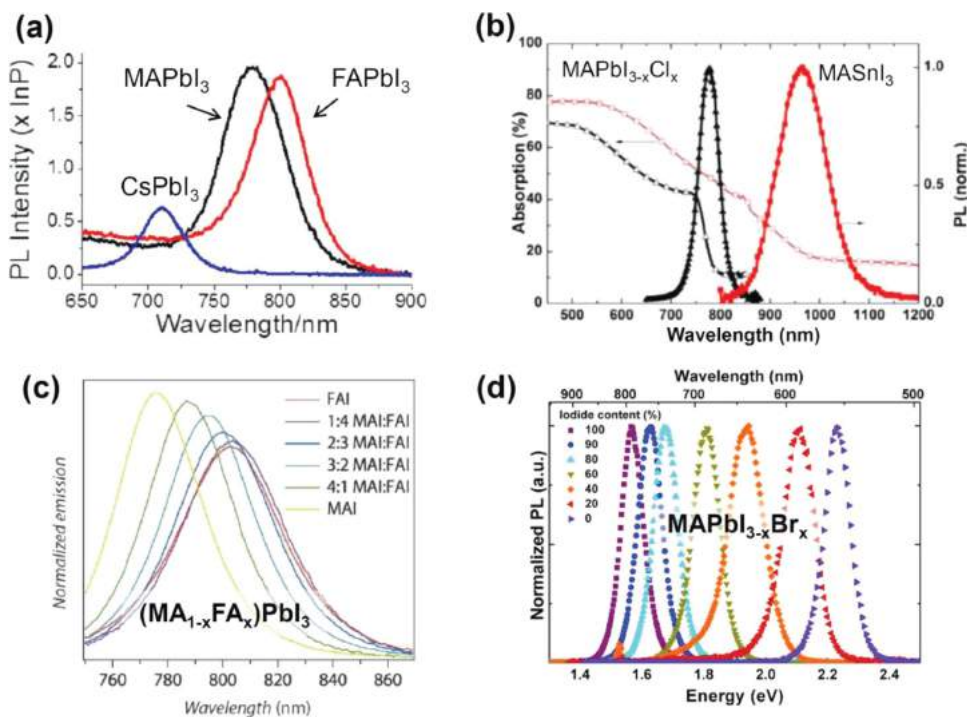


Figure 10. Photoluminescence (PL) characteristics of various organometal halide perovskite materials including (a) lead iodides (Reproduced with permission.^[19] Copyright 2013, NPG.), (b) tin iodide (Reproduced with permission.^[75] Copyright 2014, Wiley.), (c) methylammonium and formamidinium mixed lead iodides (Reproduced with permission.^[76] Copyright 2014, RSC), and (d) iodide and bromide mixed halides (Reproduced with permission.^[88] Copyright 2014, ACS.). PL spectra were obtained by photoexcitation at 532 nm for (a), 500 nm for (b), 460 nm for (c) and 400 nm (3.1 eV) for (d).

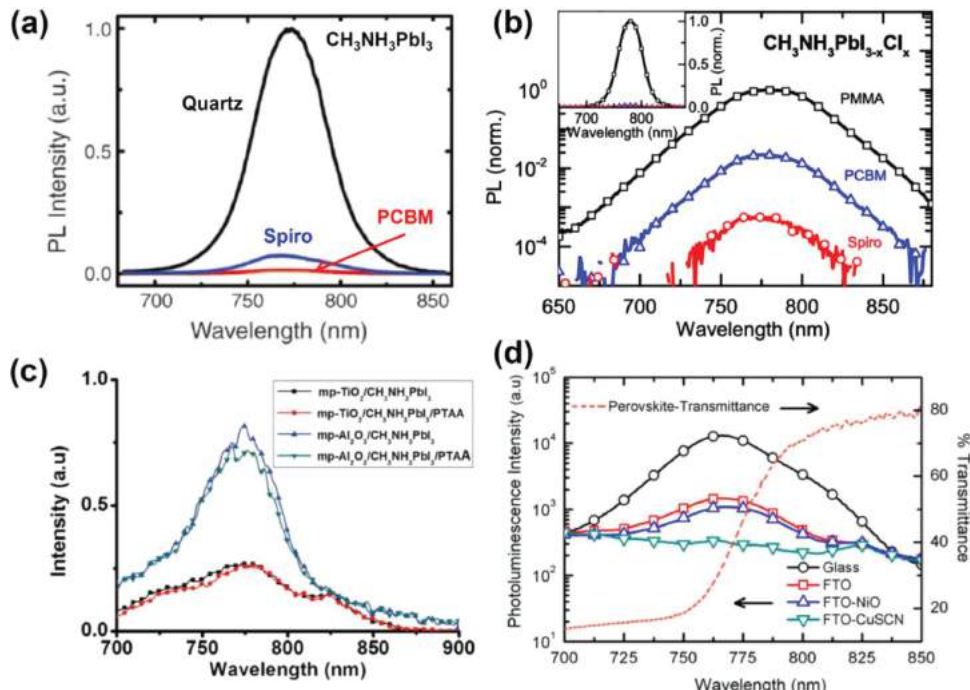


Figure 11. PL quenching behaviors for: (a) CH₃NH₃PbI₃/spiro-MeOTAD system with excitation at 600 nm. Reproduced with permission.^[30] Copyright 2014, AAAS. (b) CH₃NH₃PbI_{3-x}Cl_x/spiro-MeOTAD system with excitation at 507 nm. Reproduced with permission.^[31] Copyright 2014, AAAS. (c) CH₃NH₃PbI₃/PTAA system with excitation at 600 nm. Reproduced with permission.^[52] Copyright 2013, NPG. (d) CH₃NH₃PbI_{3-x}Cl_x/inorganic HTM system with excitation at 530 nm. Reproduced with permission.^[89] Copyright 2014, ACS. Note that (a) and (c) are linear scales but (b) and (d) are log scales. Inset in (b) shows a linear scale.

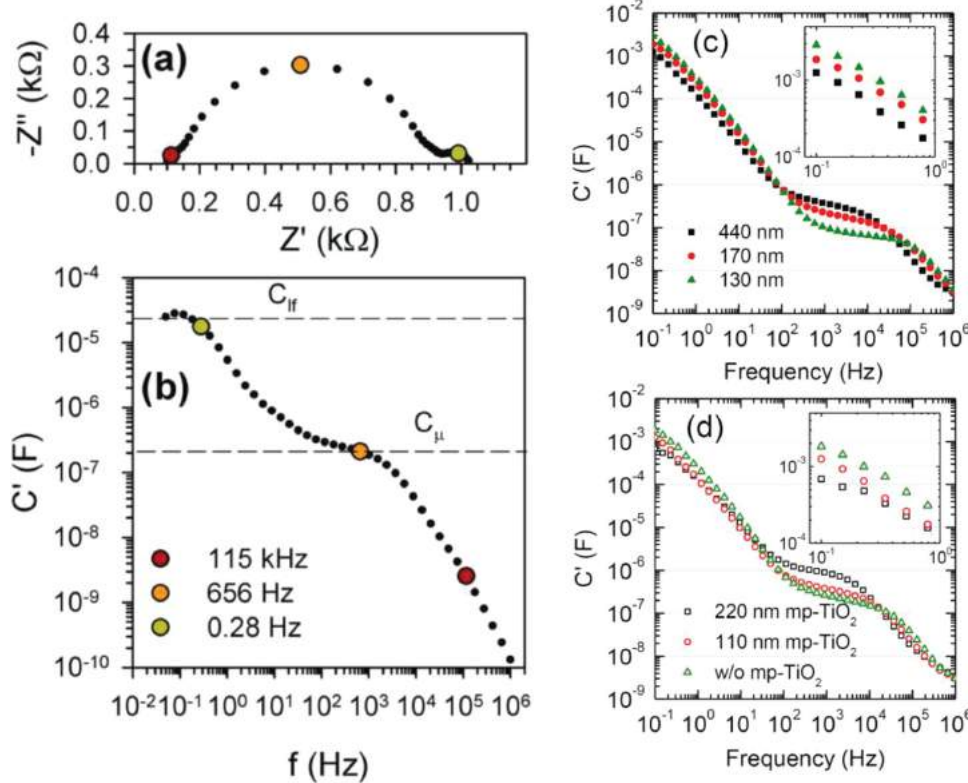


Figure 12. (a) A typical impedance plot (imaginary part of the impedance Z'' versus the real part Z') and (b) Bode plot of the real part of the capacitance C' obtained under dark conditions at 0.9 V applied DC bias. Three frequencies are highlighted to distinguish low, intermediate, and high-frequency regions. Reproduced with permission.^[91] Copyright 2014, ACS. Bode plots of the real part of the capacitance obtained from impedance spectroscopy measured under one sun illumination at the applied voltage of 0.8 V for the devices (c) with different $\text{CH}_3\text{NH}_3\text{PbI}_3$ crystal size and (d) in the absence and presence of a mp-TiO₂ layer. Inset shows the capacitance at low frequencies (10^{-1} to 10^2 Hz). Reproduced with permission.^[93] Copyright 2014, ACS.

indicates that the perovskite light absorber plays a central role in perovskite solar cell performance, regardless of differences between the samples in terms of preparation method and cell configuration. Moreover, impedance measurements can provide information on the polarization of the perovskite material. As can be seen in Figure 12, there are three arcs in a complex impedance plot at low, intermediate, and high frequencies. The high-frequency arc is associated with selective contacts, the intermediate-frequency arc is associated with the chemical capacitance, and the low-frequency arc is related to the polarization created by aligning dipoles or dipolar domains to the external electrical field.^[91] The basis for the interpretation of polarization being at the low-frequency capacitance is because the rearrangement of the overall orientation in response to any external perturbation will occur over slow time dynamics.^[91] The polarization phenomenon in perovskite materials probably causes current-voltage hysteresis. Anomalous I-V hysteresis, differences in I-V curves depending on scan direction, was observed from $\text{CH}_3\text{NH}_3\text{PbI}_{3-x}\text{Cl}_x$ ^[92] and $\text{CH}_3\text{NH}_3\text{PbI}_3$.^[93] Such I-V hysteresis was found to be strongly dependent on perovskite crystal size and the presence of a mp-TiO₂ film, where large-sized perovskite and the presence of mp-TiO₂ would suppress I-V hysteresis.^[93] The degree of I-V hysteresis was found to correlate with low-frequency capacitance, that is, the low-frequency capacitance decreased as the crystal size of

$\text{CH}_3\text{NH}_3\text{PbI}_3$ increased, and also in the presence of mp-TiO₂ (Figures 12c and d), which indicates that polarizability is closely related to I-V hysteresis and large crystals and/or the inclusion of mp-TiO₂ is beneficial to its suppression.

6. Perovskite Suitable for Flexible Solar Cells

Flexible thin film solar cells are open to various potential applications such as portable electronic chargers, bendable display devices, and wearable electronic textiles due to their light weight, bendability, and easy shape changeability.^[94,95] Perovskite solar cells are fairly attractive as flexible solar cells due to the low temperature processing (below ~ 150 °C), all-solid-state nature of the thin films, and high efficiency. Flexible perovskite solar cells are now at a beginning stage, which implies that there is much room for innovation.

Flexible perovskite solar cells have been realized by employing two types of structures, i.e., n-i-p and p-i-n junctions, containing electron transport materials (ETM)/perovskite/HTM and HTM/perovskite/ETM architectures, respectively. Since conventional process for the fabrication of ETM such as a TiO₂ compact layer needs a high temperature (over ~ 400 °C), most flexible perovskite solar cells on ITO-coated poly(ethylene terephthalate) (PET) substrates

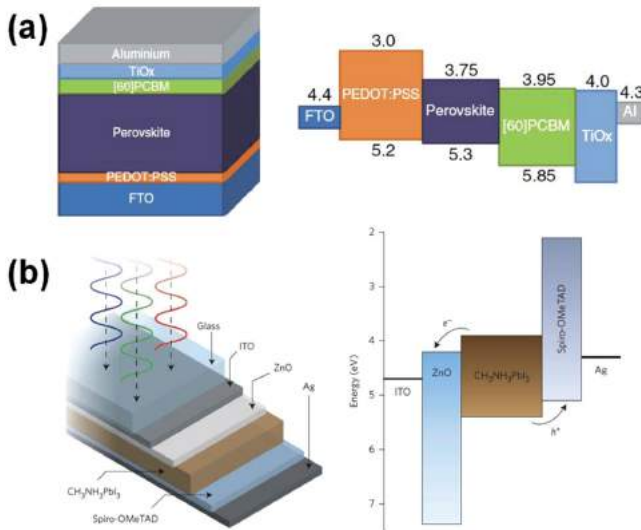


Figure 13. (a) A typical p-i-n device configuration and schematic band diagram of the fabricated solar cell and (b) a typical n-i-p device configuration and schematic band diagram of the fabricated solar cell. Reproduced with permission.^[96,59] Copyright 2013, 2014 NPG.

have adopted p-i-n structures (or inverted planar structures) composed of PEDOT:PSS/perovskite/PCBM architectures (**Figure 13(a)**).^[96–98] These materials are able to be deposited at a low temperature (below 150 °C), which is suitable for the fabrication of flexible solar cells based on PET substrates. Also, flexible perovskite solar cells composed of n-i-p structures (planar structures) were realized by depositing ZnO ETM at a low temperature (Figure 13(b)).^[42,54] ZnO nanomaterials have also been known to be deposited at below 150 °C. Kelly et al. reported an n-i-p structured flexible

perovskite solar cell whose power conversion efficiency (PCE) was 10.2%.^[59]

Recently, a high efficiency flexible perovskite solar cell whose PCE is over 12% was created by employing a TiO_x compact layer deposited using atomic layer deposition (ALD) (**Figure 14(a)**).^[99] As shown in Figure 14(b), this solar cell shows superior mechanical endurance properties, i.e., its energy conversion efficiency does not change after 1000 cycles of bending tests under conditions of a bending radius of 10 mm, demonstrating that the flexible perovskite solar cells are potentially usable as a power solution for future wearable devices.

7. Long-Term Stability

The long-term stability of perovskite solar cells is another big issue. The degradation mechanism of perovskite materials is not clearly understood. An understanding of the degradation mechanism will be helpful to enhance the long-term stability, which will be a significant criterion for the commercialization of perovskite solar cells. Recently, remarkable efforts on improving long-term stability have been made, although it has been not under active research. Snaith's group employed P3HT/single-walled carbon nanotubes (SWCNT)-PMMA double layer as a HTM.^[100] The perovskite solar cell demonstrated remarkable thermal and moisture stability. The P3HT polymer-based HTM showed superior temperature stability compared with the single-molecule based spiro-OMeTAD. The PCE dropped to 20% of initial efficiency after heating the cell at 80 °C for 20 min, which exhibited a temperature coefficient of ~0.33%/°C. This result is similar to that of the copper indium gallium (di)selenide (CIGS) solar cell. The

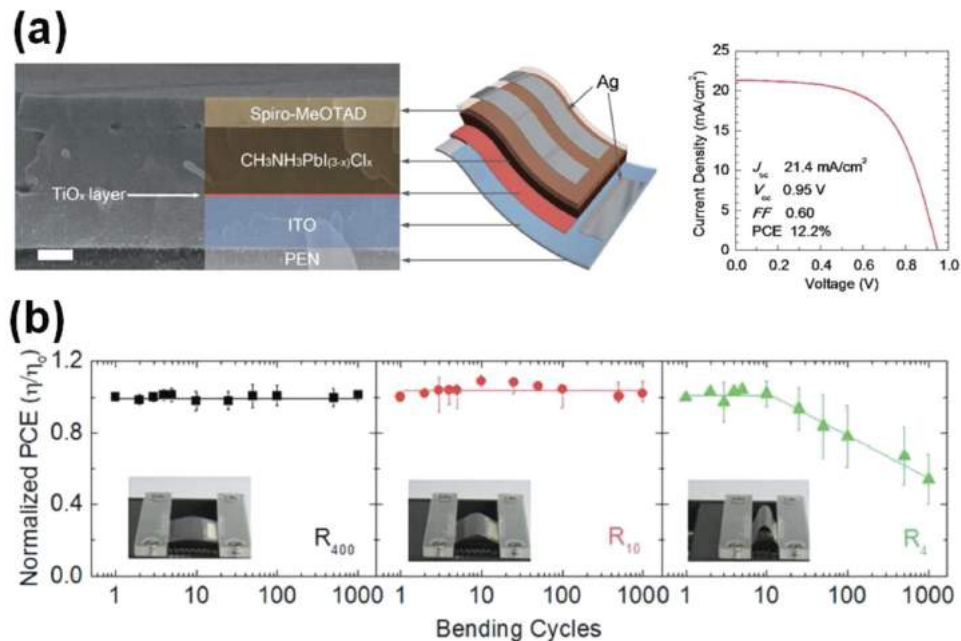


Figure 14. (a) Cross-sectional SEM image of inorganic–organic halide perovskite planar heterojunction flexible solar cell and schematic of flexible device structure. Scale bar: 200 nm and I–V characteristics measured under the simulated solar light (100 mW/cm² AM 1.5G) and (b) normalized PCE of flexible perovskite devices as a function of bending cycles with different radii of 400, 10, and 4 mm. Inset show the real images taken during the bending tests. Reproduced with permission.^[99] Copyright 2014, RSC.

hydrophobic PMMA showed a significant waterproof property, which retarded decomposition of the perovskite layer by water vapor. Han et al. reported remarkable progress regarding this stability issue:^[47] they fabricated a HTM-free and triple layer-based perovskite solar cell, composed of a simple mesoscopic $\text{TiO}_2/\text{ZrO}_2/\text{C}$ triple layer as a scaffold to host the perovskite absorber. The 10 μm thick carbon back contact layer played an important role in resistance to water. This cell exhibited excellent stability under AM 1.5 conditions over 1008 h.

8. Summary and Outlook

In this review article, we have given an overview of the historical progress in perovskite solar cells and revisited the fundamentals of organometal halide perovskite materials from a viewpoint of optical absorption and charge transport properties. Photoluminescence and impedance analysis were described to be important tools which characterized the charge separation, carrier transport, recombination, and diffusion length in perovskite solar cells. Moreover, the correlation between dielectric properties and the chemical bonding nature in ionic crystals with molecular organic ions was also discussed, which is also of great importance to understand the photovoltaic properties of organometal halide perovskite materials. Fabrication methods, including solution and vacuum processes, were shown to influence crystal growth and the morphologies of perovskite materials, thereby impacting on the resultant energy conversion efficiency. Also, recent progress underlying solution engineering exhibited the capability of controlling the morphology of perovskite materials for maximizing the energy conversion efficiency. In particular, the potential of perovskite solar cells for use as flexible solar cells was discussed in terms of low temperature processing (below ~150 °C), all-solid-state thin film nature, and high efficiency. The flexible perovskite solar cell showed an extraordinary bending durable property, fairly suitable for being used as a power solution for future wearable devices.

The high-efficiency and cost-effective materials and processes for perovskite solar cells make them economically viable for commercialization. Theoretically calculated maximum efficiencies for perovskite solar cell are reported by Yan et al.^[101] Based on considerations of the optical absorption coefficient and thickness of the light absorber, the theoretical maximum efficiency for a 1 μm -thick perovskite solar cell composed of $\text{CH}_3\text{NH}_3\text{PbI}_3$ (phase with $P_{m\bar{3}m}$ symmetry) is 26%, which is much higher than the efficiency of a GaAs solar cell with the same thickness. This result indicates that the perovskite solar cells are economically viable from a viewpoint of efficiency. However, commercialization is still challenging because of (1) the toxicity of Pb atoms, (2) long-term stability, and (3) cost-effectiveness. So far, the champion cells have been based on Pb-based perovskite materials. However, the utilization of Pb-based materials has been restricted due to their intrinsic toxicity. Future research directions are going to be finding Pb-free light-absorbing materials. Protection technology, in order not to release Pb from the Pb-based perovskite solar cell device, will be important

issue, which may learn from the CdTe solar cell industry. So far, 1000 h operation time has been guaranteed. However, this result is not enough to commercialize perovskite solar cells. Understanding the degradation mechanism as well as exploiting new materials and external encapsulation technologies should realize a more-than-20-years operation lifetime. The cost-effectiveness for materials and processes is a significant issue. The high throughput with reproducible materials and processes should be developed. Moreover, mechanical functionalities such as flexibility and stretchable properties will lead to making the perovskite solar cells more economically viable.

Acknowledgments

This work was supported by the National Research Foundation of Korea (NRF) grants funded by the Ministry of Science, ICT & Future Planning (MSIP) of Korea under contracts No. NRF-2010-0014992, NRF-2012M1A2A2671721, 2012M3A7B4049986 (Nano Material Technology Development Program) and NRF-2012M3A6A7054861 (Global Frontier R&D Program on Center for Multiscale Energy System).

- [1] D. Weber, *Z. Naturforsch.* **1978**, *33b*, 1443.
- [2] D. Weber, *Z. Naturforsch.* **1978**, *33b*, 862.
- [3] D. B. Mitzi, C. A. Feild, W. T. A. Harrison, A. M. Guloy, *Nature* **1994**, 369, 467.
- [4] A. Kojima, K. Teshima, Y. Shirai, T. Miyasaka, *J. Am. Chem. Soc.* **2009**, *131*, 6050.
- [5] A. Hagfeldt, G. Boschloo, L. Sun, L. Kloo, H. Pettersson, *Chem. Rev.* **2010**, *110*, 6595.
- [6] G. Chen, J. Seo, C. Yang, P. N. Prasad, *Chem. Soc. Rev.* **2013**, *42*, 8304.
- [7] J.-H. Im, C.-R. Lee, J.-W. Lee, S.-W. Park, N.-G. Park, *Nanoscale* **2011**, *3*, 4088.
- [8] H.-S. Kim, C.-R. Lee, J.-H. Im, K.-B. Lee, T. Moehl, A. Marchioro, S.-J. Moon, R. Humphry-Baker, J.-H. Yum, J. E. Moser, M. Grätzel, N.-G. Park, *Sci. Rep.* **2012**, *2*, 591.
- [9] F. G. Fumi, M. P. Tosi, *J. Chem. Phys.* **1960**, *33*, 1.
- [10] Y. Sakamoto, *J. Chem. Phys.* **1958**, *28*, 164.
- [11] D. Quane, *J. Chem. Educ.* **1970**, *47*, 396.
- [12] L. L. Hench, J. K. West *Principles of Electronic Ceramics* 1st Ed., A Wiley-Interscience Publication, New York **1990**, p.193.
- [13] W.-S. Xia, L.-X. Li, P.-F. Ning, Q.-W. Liao, *J. Am. Ceramic Soc.* **2012**, *95*, 2587.
- [14] R. E. Wasylissen, O. Knop, J. B. Macdonald, *Solid State Commun.* **1985**, *56*, 581.
- [15] A. Poglitsch, D. Weber, *J. Chem. Phys.* **1987**, *87*, 6373.
- [16] N. Onoda-Yamamura, *Doctoral Thesis*, Osaka University, **1990**.
- [17] W. Geng, L. Zhang, Y.-N. Zhang, W.-M. Lau, L.-M. Liu, *J. Phys. Chem. C* **2014**, DOI: 10.1021/jp504951h.
- [18] S. D. Wolf, J. Holovsky, S.-J. Moon, P. Löper, B. Niesen, M. Ledinsky, F.-J. Haug, J.-H. Yum, C. Ballif, *J. Phys. Chem. Lett.* **2014**, *5*, 1035.
- [19] C. C. Stoumpos, C. D. Malliakas, M. G. Kanatzidis, *Inorg. Chem.* **2013**, *52*, 9019.
- [20] F. Hao, C. C. Stoumpos, R. P. H. Chang, M. G. Kanatzidis, *J. Am. Chem. Soc.* **2014**, *136*, 8094.
- [21] T. Umebayashi, K. Asai, T. Kondo, A. Nakao, *Phys. Rev. B* **2003**, *67*, 155405.

- [22] E. Mosconi, A. Amat, M. K. Nazeeruddin, M. Grätzel, F. D. Angelis, *J. Phys. Chem. C* **2013**, *117*, 13902.
- [23] P. Umari, E. Mosconi, F. D. Angelis, *Sci. Rep.* **2014**, *4*, 4467.
- [24] N. Onoda-Yamamuro, T. Matsuo, H. Suga, *J. Phys. Chem. Solids* **1990**, *51*, 1383.
- [25] N. Onoda-Yamamuro, T. Matsuo, H. Suga, *J. Phys. Chem. Solids* **1992**, *53*, 935.
- [26] E. J. Juarez-Perez, R. S. Sanchez, L. Badia, G. Garcia-Belmonte, Y. S. Kang, I. Mora-Sero, J. Bisquert, *J. Phys. Chem. Lett.* **2014**, *5*, 2390.
- [27] *Principles of Electronic Ceramics*, Wiley, NY, USA, 1990.
- [28] K. Yamada, T. Matsui, T. Tsuritani, T. Okuda, S. Ichiba, *Z. Naturforsch.* **1990**, *45a*, 307.
- [29] K. Yamada, H. Kawaguchi, T. Matsui, T. Okuda, S. Ichiba, *Bull. Chem. Soc. Jpn.* **1990**, *63*, 3521.
- [30] G. Xing, N. Mathews, S. Sun, S. S. Lim, Y. M. Lam, M. Grätzel, S. Mhaisalkar, T. C. Sum, *Science* **2013**, *342*, 344.
- [31] S. D. Stranks, G. E. Eperon, G. Grancini, C. Menelaou, M. J. P. Alcocer, T. Leijtens, L. M. Herz, A. Petrozza, H. J. Snaith, *Science* **2013**, *342*, 341.
- [32] E. Edri, S. Kirmayer, A. Henning, S. Mukhopadhyay, K. Gartsman, Y. Rosenwaks, G. Hodes, D. Cahen, *Nano Lett.* **2014**, *14*, 1000.
- [33] Y. Zhao, A. M. Nardes, K. Zhu, *J. Phys. Chem. Lett.* **2014**, *5*, 490.
- [34] C. S. Ponseca Jr., T. J. Savenije, M. Abdellah, K. Zheng, A. Yartsev, T. Pascher, T. Harlang, P. Chabera, T. Pullerits, A. Stepanov, J.-P. Wolf, V. Sundstrom, *J. Am. Chem. Soc.* **2014**, *136*, 5189.
- [35] H.-S. Kim, I. Mora-Sero, V. Gonzalez-Pedro, F. Fabregat-Santiago, E. J. Juarez-Perez, N.-G. Park, J. Bisquert, *Nat. Commun.* **2013**, *4*, 2242.
- [36] V. Gonzalez-Pedro, E. J. Juarez-Perez, W.-S. Arsyad, E. M. Barea, F. Fabregat-Santiago, I. Mora-Sero, J. Bisquert, *Nano Lett.* **2014**, dx.doi.org/10.1021/nl404252e.
- [37] J.-W. Lee, T.-Y. Lee, P. J. Yoo, M. Grätzel, S. Mhaisalkar, N.-G. Park, *J. Mater. Chem. A* **2014**, *2*, 9251.
- [38] D.-Y. Son, J.-H. Im, H.-S. Kim, N.-G. Park, *J. Phys. Chem. C* **2014**, *118*, 16567.
- [39] G. S. Han, S. Lee, J. H. Noh, H. S. Chung, J. H. Park, B. S. Swain, J.-H. Im, N.-G. Park, H. S. Jung, *Nanoscale* **2014**, *6*, 6127.
- [40] J. T.-W. Wang, J. M. Ball, E. M. Barea, A. Abate, J. A. Alexander-Webber, J. Huang, M. Saliba, I. Mora-Sero, J. Bisquert, H. J. Snaith, R. J. Nicholas, *Nano Lett.* **2014**, *14*, 724.
- [41] G. S. Han, H. S. Chung, B. J. Kim, D. H. Kim, J. W. Lee, B. S. Swain, K. Mahmood, J. S. Yu, N.-G. Park, J. H. Lee, H. S. Jung, *J. Mater. Chem. A* **2014**, DOI: 10.1039/C4TA03684K.
- [42] H. Zhou, Q. Chen, G. Li, S. Luo, T.-B. Song, H.-S. Duan, Z. Hong, J. You, Y. Liu, Y. Yang, *Science* **2014**, *345*, 542.
- [43] H. Zhang, H. Azimi, Y. Hou, T. Ameri, T. Przybilla, E. Specker, M. Kraft, U. Scherf, C. J. Brabec, *Chem. Mater.* **2014**, *26*, 5190.
- [44] L. Etgar, P. Gao, Z. Xue, Q. Peng, A. K. Chandiran, B. Liu, M. K. Nazeeruddin, M. Grätzel, *J. Am. Chem. Soc.* **2012**, *134*, 17396.
- [45] W. A. Laban, L. Etgar, *Energy Environ. Sci.* **2013**, *6*, 3249.
- [46] S. Aharon, S. Gamliel, B. E. Cohen, L. Etgar, *Chem. Chem. Phys.* **2014**, *16*, 10512.
- [47] A. Mei, X. Li, L. Liu, Z. Ku, T. Liu, Y. Rong, M. Xu, M. Hu, J. Chen, Y. Yang, M. Grätzel, H. Han, *Science* **2014**, *345*, 295.
- [48] J.-Y. Jeng, Y.-F. Chiang, M.-H. Lee, S.-R. Peng, T.-F. Guo, P. Chen, T.-C. Wen, *Adv. Mater.* **2013**, *25*, 3727.
- [49] M. H. Kumar, N. Yantara, S. Dharani, M. Graetzel, S. Mhaisalkar, P. P. Boix, N. Mathews, *Chem. Commun.* **2013**, *49*, 11089.
- [50] H. Chen, X. Pan, W. Liu, M. Cai, D. Kou, Z. Huo, X. Fang, S. Dai, *Chem. Commun.* **2013**, *49*, 7277.
- [51] H.-S. Kim, J.-W. Lee, N. Yantara, P. P. Boix, S. A. Kulkarni, S. Mhaisalkar, M. Grätzel, N.-G. Park, *Nano Lett.* **2013**, *13*, 2412.
- [52] J. H. Heo, S. H. Im, J. H. Noh, T. N. Mandal, C.-S. Lim, J. A. Chang, Y. H. Lee, H.-J. Kim, A. Sarkar, M. K. Nazeeruddin, M. Grätzel, S. I. Seok, *Nat. Photonics* **2013**, *7*, 486.
- [53] J. Burschka, N. Pellet, S.-J. Moon, *Nature* **2013**, *499*, 316.
- [54] D. Bi, S.-J. Moon, L. Häggman, G. Boschloo, L. Yang, E. M. J. Johansson, M. K. Nazeeruddin, M. Grätzel, A. Hagfeldt, *RSC Adv.* **2013**, *3*, 18762.
- [55] N. J. Jeon, J. H. Noh, Y. C. Kim, W. S. Yang, S. Ryu, S. I. Seok, *Nat. Mater.* **2014**, *13*, 897.
- [56] J.-H. Im, I.-H. Jang, N. Pellet, M. Grätzel, N.-G. Park, *Nat. Nanotechnol.* **2014**, DOI: 10.1038/NNANO.2014.181.
- [57] K.-C. Wang, J.-Y. Jeng, P.-S. Shen, Y.-C. Chang, E. W.-G. Diau, C.-H. Tsai, T.-Y. Chao, H.-C. Hsu, P.-Y. Lin, P. Chen, T.-F. Guo, T.-C. Wen, *Sci. Rep.* **2014**, *4*, 4756.
- [58] O. Malinkiewicz, A. Yella, Y. H. Lee, G. M. Espallargas, M. Graetzel, M. K. Nazeeruddin, H. J. Bolink, *Nat. Photonics* **2014**, *8*, 128.
- [59] D. Liu, T. L. Kelly, *Nat. Photonics* **2014**, *8*, 133.
- [60] Z. Zhu, Y. Bai, T. Zhang, Z. Liu, X. Long, Z. Wei, Z. Wang, L. Zhang, J. Wang, F. Yan, S. Yang, *Angew. Chem.* **2014**, *126*, 1.
- [61] P. Qin, S. Tanaka, S. Ito, N. Tetreault, K. Manabe, H. Nishino, M. K. Nazeeruddin, M. Grätzel, *Nat. Commun.* **2014**, *5*, 3834.
- [62] J. A. Christians, R. C. M. Fung, P. V. Kamat, *J. Am. Chem. Soc.* **2014**, *136*, 758.
- [63] M. M. Lee, J. Teuscher, T. Miyasaka, T. N. Murakami, H. J. Snaith, *Science* **2012**, *338*, 643.
- [64] B. Conings, L. Baeten, C. D. Dobbelaere, J. D'Haen, J. Manca, H.-G. Boyen, *Adv. Mater.* **2013**, DOI: 10.1002/adma.201304803.
- [65] M. J. Carnie, C. Charbonneau, M. L. Davies, J. Troughton, T. M. Watson, K. Wojciechowski, H. Snaith, D. A. Worsley, *Chem. Commun.* **2013**, *49*, 7893.
- [66] M. Liu, M. B. Johnston, H. J. Snaith, *Nature* **2013**, *501*, 395.
- [67] B. Cai, Y. Xing, Z. Yang, W.-H. Zhang, J. Qiu, *Energy Environ. Sci.* **2013**, *6*, 1480.
- [68] E. Edri, S. Kirmayer, D. Cahen, G. Hodes, *J. Phys. Chem. Lett.* **2013**, *4*, 897.
- [69] S. Ryu, J. H. Noh, N. J. Jeon, Y. C. Kim, W. S. Yang, J. Seo, S. I. Seok, *Energy Environ. Sci.* **2014**, *7*, 2614.
- [70] E. Edri, S. Kirmayer, M. Kulbak, G. Hodes, D. Cahen, *J. Phys. Chem. Lett.* **2014**, *5*, 429.
- [71] J. H. Noh, S. H. Im, J. H. Heo, T. N. Mandal, S. I. Seok, *Nano Lett.* **2013**, *13*, 1764.
- [72] T. M. Koh, K. Fu, Y. Fang, S. Chen, T. C. Sum, N. Mathews, S. G. Mhaisalkar, P. P. Boix, T. Baikie, *J. Phys. Chem. C* **2014**, *118*, 16458.
- [73] G. E. Eperon, S. D. Stranks, C. Menelaou, M. B. Johnston, L. M. Herz, H. J. Snaith, *Energy Environ. Sci.* **2014**, *7*, 982.
- [74] J.-W. Lee, D.-J. Seol, A.-N. Cho, N.-G. Park, *Adv. Mater.* **2014**, *26*, 4991.
- [75] N. Pellet, P. Gao, G. Gregori, T.-Y. Yang, M. K. Nazeeruddin, J. Maier, M. Grätzel, *Angew. Chem. Int. Ed.* **2014**, *53*, 3151.
- [76] N. K. Noel, S. D. Stranks, A. Abate, C. Wehrenfennig, S. Guarnera, A. A. Haghhighirad, A. Sadhanala, G. E. Eperon, M. B. Johnston, A. M. Petrozza, L. M. Herz, H. J. Snaith, *Energy Environ. Sci.* **2014**, *7*, 3061.
- [77] F. Hao, C. C. Stoumpos, D. H. Cao, R. P. H. Chang, M. G. Kanatzidis, *Nat. Photonics* **2014**, *8*, 489.
- [78] Y. Ogomi, A. Morita, S. Tsukamoto, T. Saitho, N. Fujikawa, Q. Shen, T. Toyoda, K. Yoshino, S. S. Pandey, T. Ma, S. Hayase, *J. Phys. Chem. Lett.* **2014**, *5*, 1004.
- [79] J.-H. Im, H.-S. Kim, N.-G. Park, *APL Mater.* **2014**, *2*, 081510.
- [80] Y. Ma, L. Zheng, Y.-H. Chung, S. Chu, L. Xiao, Z. Chen, S. Wang, B. Qu, Q. Gong, Z. Wu, X. Hou, *Chem. Comm.* **2014**, DOI: 10.1039/c4cc01962h.
- [81] G. Juška, K. Arlauskas, M. Viliūnas, J. Kočka, *Phys. Rev. Lett.* **2000**, *84*, 4946.
- [82] M. Xiao, F. Huang, W. Huang, Y. Dkhissi, Y. Zhu, J. Etheridge, A. Gray-Weale, U. Bach, Y.-B. Cheng, L. Spiccia, *Angew. Chem.* **2014**, *126*, 10056.

- [83] Y. Wu, A. Islam, X. Yang, C. Qin, J. Liu, K. Zhang, W. Penga, L. Han, *Energy Environ. Sci.* **2014**, *7*, 2934.
- [84] C. Zuo, L. Ding, *Nanoscale* **2014**, *6*, 9935.
- [85] Q. Chen, H. Zhou, Z. Hong, S. Luo, H.-S. Duan, H.-H. Wang, Y. Liu, G. Li, Y. Yang, *J. Am. Chem. Soc.* **2014**, *136*, 622.
- [86] N. C. Greenham, R. H. Friend, D. D. C. Bradley, *Adv. Mater.* **1994**, *6*, 491.
- [87] N. C. Greenham, I. D. W. Samuel, G. R. Hayes, R. T. Phillips, Y.A.R.R. Kessener, S. C. Moratti, A. B. Holmes, R. H. Friend, *Chem. Phys. Lett.* **1995**, *241*, 89.
- [88] A. Sadhanala, F. Deschler, T. H. Thomas, S. E. Dutton, K. C. Goedel, F. C. Hanusch, M. L. Lai, U. Steiner, T. Bein, P. Docampo, D. Cahen, R. H. Friend, *J. Phys. Chem. Lett.* **2014**, *5*, 2501.
- [89] A. S. Subbiah, A. Halder, S. Ghosh, N. Mahuli, G. Hodes, S. K. Sarkar, *J. Phys. Chem. Lett.* **2014**, *5*, 1748.
- [90] V. Gonzalez-Pedro, E. J. Juarez-Perez, W.-S. Arsyad, E. M. Barea, F. Fabregat-Santiago, I. Mora-Sero, J. Bisquert, *Nano Lett.* **2014**, *14*, 888.
- [91] R. S. Sanchez, V. Gonzalez-Pedro, J.-W. Lee, N.-G. Park, Y. S. Kang, I. Mora-Sero, J. Bisquert, *J. Phys. Chem. Lett.* **2014**, *5*, 2357.
- [92] H. J. Snaith, A. Abte, J. M. Ball, G. E. Eperon, T. Leijtens, N. K. Noel, S. D. Stranks, J. T.-W. Wang, K. Wojciechowski, W. Zhang, *J. Phys. Chem. Lett.* **2014**, *5*, 1511.
- [93] H.-S. Kim, N.-G. Park, *J. Phys. Chem. Lett.* **2014**, *5*, 2927.
- [94] M. Kaltenbrunner, M. S. White, E. D. Glowacki, T. Sekitani, T. Someya, N. S. Sariciftci, S. Bauer, *Nat. Commun.* **2012**, *3*, 770.
- [95] D. J. Lipomi, Z. Bao, *Energy Environ. Sci.* **2011**, *4*, 3314.
- [96] P. Docampo, J. M. Ball, M. Darwich, G. E. Eperon, H. J. Snaith, *Nat. Commun.* **2013**, *4*, 2761.
- [97] J. You, Z. Hong, Y. Yang, Q. Chen, M. Cai, T.-B. Song, C.-C. Chen, S. Lu, Y. Liu, H. Zhou, Y. Yang, *ACS Nano* **2014**, *8*, 1674.
- [98] C. R. Carmona, O. Malinkiewicz, A. Soriano, G. M. Espallargas, A. Garcia, P. Reinecke, T. Kroger, M. I. Dar, M. K. Nazeeruddine, H. J. Bolink, *Energy Environ. Sci.* **2014**, *7*, 994.
- [99] B. J. Kim, D. H. Kim, Y.-Y. Lee, H.-W. Shin, G. S. Han, J. S. Hong, K. Mahmood, T. K. Ahn, Y.-C. Joo, K. S. Hong, N.-G. Park, S. Lee, H. S. Jung, *Energy Environ. Sci.* **2014**, DOI: 10.1039/C4EE02441A.
- [100] S. N. Habersreutinger, T. Leijtens, G. E. Eperon, S. D. Stranks, R. J. Nicholas, H. J. Snaith, *Nano Lett.* **2014**, dx.doi.org/10.1021/nl501982b.
- [101] W.-J. Yin, T. Shi, Y. Yan, *Adv. Mater.* **2014**, *26*, 4653.

Received: September 13, 2014

Revised: September 30, 2014

Published online: October 30, 2014

Sensitization of silicon by singlet exciton fission in tetracene

Markus Einzinger^{1,5}, Tony Wu^{1,5}, Julia F. Kompalla¹, Hannah L. Smith², Collin F. Perkins¹, Lea Nienhaus¹, Sarah Wieghold³, Daniel N. Congreve^{1,4}, Antoine Kahn², Moungi G. Bawendi¹ & Marc A. Baldo^{1*}

Silicon dominates contemporary solar cell technologies¹. But when absorbing photons, silicon (like other semiconductors) wastes energy in excess of its bandgap². Reducing these thermalization losses and enabling better sensitivity to light is possible by sensitizing the silicon solar cell using singlet exciton fission, in which two excited states with triplet spin character (triplet excitons) are generated from a photoexcited state of higher energy with singlet spin character (a singlet exciton)^{3–5}. Singlet exciton fission in the molecular semiconductor tetracene is known to generate triplet excitons that are energetically matched to the silicon bandgap^{6–8}. When the triplet excitons are transferred to silicon they create additional electron–hole pairs, promising to increase cell efficiencies from the single-junction limit of 29 per cent to as high as 35 per cent⁹. Here we reduce the thickness of the protective hafnium oxynitride layer at the surface of a silicon solar cell to just eight angstroms, using electric-field-effect passivation to enable the efficient energy transfer of the triplet excitons formed in the tetracene. The maximum combined yield of the fission in tetracene and the energy transfer to silicon is around 133 per cent, establishing the potential of singlet exciton fission to increase the efficiencies of silicon solar cells and reduce the cost of the energy that they generate.

Figure 1a shows how the absorption of photons in silicon wastes excess energy, and Fig. 1b displays the mechanism by which singlet exciton fission instead produces two electron–hole pairs¹⁰. As shown in Fig. 1c, photoexcitation of the 2.40-eV singlet exciton of tetracene in the blue or green region of the visible spectrum generates two triplet excitons with an energy of 1.25 eV each, which matches the bandgap of silicon at 1.11 eV almost perfectly^{11,12}. Energy transfer from tetracene to inorganic lead sulfide semiconductor nanocrystals has previously been demonstrated at high efficiencies^{13,14}. There have also been reports of triplet dissociation at silicon–tetracene heterojunctions¹⁵. However, experiments on hydrogen-passivated silicon with lithium fluoride interlayers have yielded no evidence of triplet transfer from tetracene to silicon^{16,17}. One reason might be the lack of a suitable bifunctional interlayer, which should allow transfer of charge carriers or excitons and provide sufficient passivation to prevent rapid recombination of charge carriers at the silicon surface^{18,19}. Passivation can be achieved through two methods: chemical passivation involves the reduction of recombination centres by saturating silicon dangling bonds, and field-effect passivation results from the repulsion of charge carriers, especially minority carriers, in response to an electric field present at the surface of the material. Most modern passivation layers rely on contributions from both approaches.

To permit tetracene charge carriers to tunnel into silicon, the silicon passivation interlayer should be a conformal dielectric grown with atomic control over its thickness, because the tunnelling probability decreases exponentially with the barrier width. We chose hafnium oxynitride (HfO_xN_y) for this purpose because it is insulating and can be grown on top of silicon wafers by atomic layer deposition²⁰. The atomic

concentrations of the elements for the interlayer were determined to be 57% hafnium, 22% nitrogen and 21% oxygen using X-ray photoelectron spectroscopy (see Supplementary Figs. 1–5). The bandgap was measured to be 4.28 eV using ultraviolet photoelectron spectroscopy and inverse photoemission spectroscopy; see Fig. 1d and Supplementary Figs. 6–9. Atomic force microscopy yielded a root-mean-square roughness of 150 pm (Extended Data Fig. 1). The overall structure is silicon– HfO_xN_y –tetracene, where the tetracene was thermally evaporated. The optimal thickness of HfO_xN_y was determined to be 8 Å, as discussed below. The tetracene thickness was kept constant at 30 nm.

Following a previously reported protocol²¹ we fabricate dopant-free interdigitated back-contacted silicon solar cells with aluminium/molybdenum oxide contacts for hole extraction and aluminium/lithium fluoride contacts for electron extraction. The solar cell device structure is shown in Fig. 2a and photographs of the devices are shown in Fig. 2b. See Methods and Extended Data Fig. 2 for further fabrication details. We subsequently protect the back contacts with a combination of polydimethylsiloxane (PDMS) and an additional piece of silicon, and perform a mild version of a Radio Corporation of America clean on the front surface of the silicon. We then fabricate the HfO_xN_y interlayer and tetracene film as described in Methods. We compare cells with 8-Å-thick HfO_xN_y interlayers to cells with 16-Å-thick HfO_xN_y interlayers. In these two devices, the optical properties are almost identical, but the thicker interlayer is expected to hinder charge and exciton tunnelling between tetracene and silicon, allowing us to isolate effects that stem from coupling at the interface. For characterization, we also fabricate samples without electrical back contacts that are otherwise identical to the samples described above. We henceforth refer to these samples as ‘photoluminescent’ after the detection methods used to characterize them.

The current–voltage characteristics of the solar cell devices with back contacts under AM1.5G solar spectrum illumination conditions are shown in Fig. 2c. The cell with the 16-Å-thick interlayer exhibits a short-circuit current of $I_{SC} = 4.6 \text{ mA cm}^{-2}$, an open-circuit voltage of $V_{OC} = 0.40 \text{ V}$, a fill factor of 48% and a power conversion efficiency of 0.9%. By contrast, the cell with the 8-Å-thick interlayer has $I_{SC} = 21.7 \text{ mA cm}^{-2}$, $V_{OC} = 0.46 \text{ V}$, a fill factor of 51% and a power conversion efficiency of 5.1%. This constitutes an almost fivefold increase in I_{SC} and an almost sixfold increase in power conversion efficiency, owing to the superior external quantum efficiency (EQE) of the 8-Å-thick HfO_xN_y device (Fig. 2d). Specifically, under a white-light bias, the EQE for the 8-Å-thick HfO_xN_y cell is higher than that of the 16-Å-thick HfO_xN_y cell by a factor of 6.6, at wavelengths longer than $\lambda = 560 \text{ nm}$. The cell with the thinner interlayer performs even better in the blue part of the spectrum, with a peak at $\lambda = 517 \text{ nm}$ (close to the tetracene absorption maximum at $\lambda = 524 \text{ nm}$), which represents an EQE 11.6 times greater than that of the 16-Å-thick interlayer cell. In fact, the shape of the relative improvement roughly matches the absorption of tetracene, but with notable broadening at longer wavelengths. The shape is analysed further below and compared to

¹Center for Excitonics, Massachusetts Institute of Technology (MIT), Cambridge, MA, USA. ²Department of Electrical Engineering, Princeton University, Princeton, NJ, USA. ³Department of Mechanical Engineering, Massachusetts Institute of Technology, Cambridge, MA, USA. ⁴Present address: The Rowland Institute at Harvard, Harvard University, Cambridge, MA, USA. ⁵These authors contributed equally: Markus Einzinger, Tony Wu. *e-mail: baldo@mit.edu

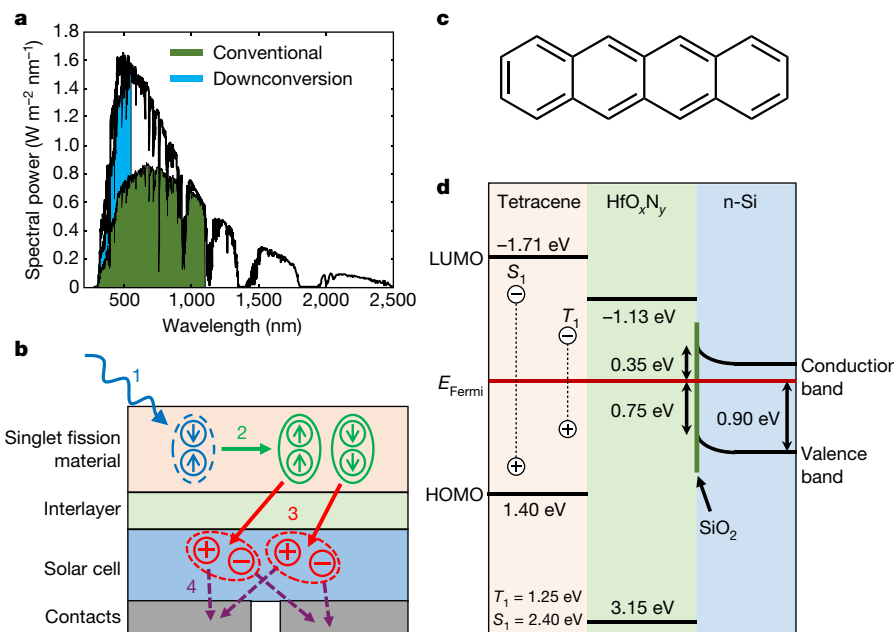


Fig. 1 | The concept of downconversion and the materials employed in this study. **a**, The solar spectrum. The green area indicates the power density that can be harvested in conventional silicon solar cells and the blue area indicates the possible gains from employing singlet-fission materials as downconverters. **b**, The downconversion process. 1, Light absorption; 2, singlet fission; 3, energy transfer; 4, hole and electron extraction. **c**, The molecular structure of tetracene.

The energetic structure of the system, as determined from ultraviolet photon spectroscopy (Supplementary Figs. 6–9). The vertical green line at the silicon surface indicates the location of a possible monolayer oxide coating formed immediately after surface cleaning. S_1 , singlet exciton energy; T_1 , triplet exciton energy; E_{Fermi} , Fermi energy of the system; LUMO, lowest unoccupied molecular orbital; HOMO, highest occupied molecular orbital; n-Si, phosphorus-doped silicon.

the photoluminescence excitation spectrum. The full spectral response including wavelengths greater than 640 nm is shown in Extended Data Fig. 3.

As summarized in Fig. 3a, we consider two possible causes for the enhancement in solar cell performance observed for the device with thinner HfO_xN_y interlayer. First, exciton dissociation at the interface between tetracene and silicon could cause charging of the interface and

thus electric-field-effect passivation. We note that such charging could be initiated by photoexcitation of either the tetracene or the silicon. Second, singlet fission in tetracene and the subsequent triplet energy transfer could enhance the photocurrent in the silicon.

To probe potential electronic or excitonic interactions between silicon and tetracene, we characterize the photoluminescent samples that do not have back contacts. As shown in Fig. 3b, we excite the

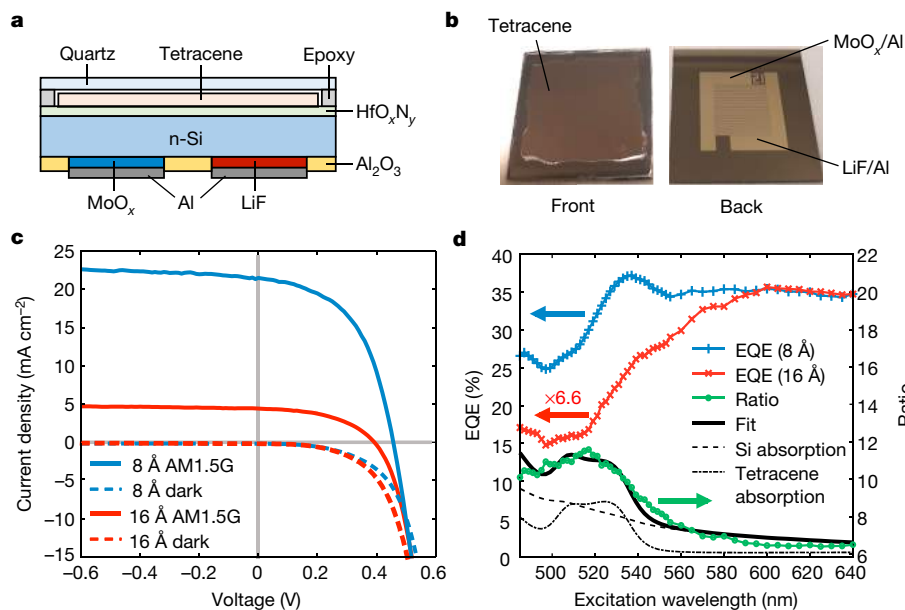


Fig. 2 | Photocurrent experiments. **a**, Device structure for a singlet-fission-sensitized silicon solar cell. **b**, Photograph of the solar cell with back contacts. **c**, Current–voltage characteristics for the solar cells with interlayer thicknesses of 8 Å (blue) and 16 Å (red). **d**, EQE spectra of solar cells with interlayer thicknesses of 8 Å and 16 Å. The EQE of the

16-Å-thick HfO_xN_y cell is scaled by 6.6 for comparison. The ratio of the EQE of the 8-Å-thick HfO_xN_y cell to that of the 16-Å-thick HfO_xN_y cell is shown in green and compared to a fit (black solid line) using the contributions of the silicon absorption (black dashed line) and tetracene absorption (black dash-dotted line).

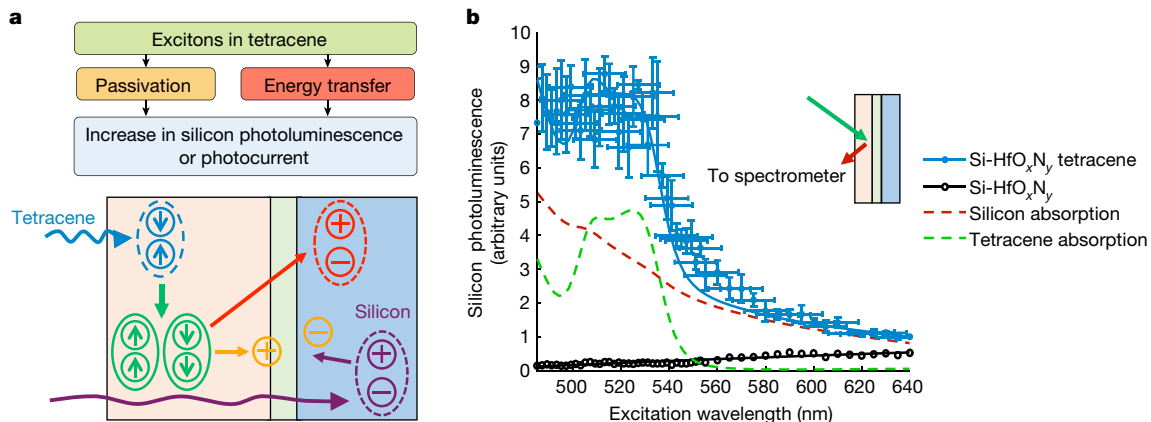


Fig. 3 | Photoluminescence experiments. **a**, Flow diagram summarizing the two pathways that increase silicon photoluminescence. Following photoexcitation of tetracene (blue) or silicon (dark purple), electric-field-effect passivation (orange charges) is caused by exciton dissociation at the interface or charge diffusion from the silicon. Additional electron-hole pairs in silicon can also be created by singlet exciton fission in tetracene (green) and triplet energy transfer (light red).

photoluminescent samples with and without tetracene (silicon-8-Å HfO_xN_y and silicon-8-Å HfO_xN_y-tetracene, respectively) using a variable-wavelength excitation source. We record their photoluminescence spectrum in the near infrared ($\lambda = 837\text{--}1,642\text{ nm}$), and additionally verify in Extended Data Fig. 4 that all of the photoluminescent samples show only emission from the silicon band-to-band transition, peaking at $\lambda = 1,144\text{ nm}$. The excitation spectra are shown in Fig. 3b. In this figure, the silicon photoluminescence of the photoluminescent sample without tetracene (black line with circles) increases with increasing wavelength. This trend is characteristic of surface recombination losses in silicon and is explained by the decreasing absorption coefficient of silicon at longer wavelengths (red dashed line in Fig. 3b). Charge carriers generated by longer-wavelength light are created deeper in the bulk of the wafer and have more time to radiatively recombine before they reach the interface.

We notice a stark difference when examining the excitation spectrum of the sample with the tetracene layer. The photoluminescence of the silicon in the sample is stronger at all wavelengths, increasing about eight times in the tetracene absorption region $\lambda < 550\text{ nm}$ compared

spectrum showing the beneficial influence of the tetracene coating on a photoluminescent silicon sample. The contributions of the silicon absorption (red dashed line) and the tetracene absorption (green dashed line) are shown. Vertical error bars are 1σ ; horizontal error bars are the spectral width of the excitation source at an intensity of e^{-2} ; $n = 1,600$. Inset, schematic of the measurement method.

to $\lambda = 640\text{ nm}$. Because fission and energy transfer are capable of at most a twofold enhancement, the data suggest an improvement in surface passivation during the illumination of tetracene. The behaviour is reversible when the wavelength is swept back and forth (Extended Data Fig. 5), and so we cannot attribute the effect to chemical passivation, for which we would expect a permanent modification. We instead explain this behaviour as an electric-field-effect passivation following generation of charge at the interface between the tetracene and the silicon. The excitation spectrum for $\lambda < 560\text{ nm}$ is proportional to the absorption spectrum of tetracene, and the tetracene absorption edge is clearly visible in Fig. 3b (blue solid line with circles and error bars). Similarly, the excitation spectrum for $\lambda > 560\text{ nm}$, where tetracene absorption is minimal, appears to be proportional to the absorption coefficient of silicon. We attribute this to the fact that more charge carriers are generated closer to the interface at higher absorption coefficients.

To further investigate the passivation properties of the silicon-HfO_xN_y-tetracene cell, we perform quasi-steady-state photoconductance decay measurements²². For an intrinsic silicon wafer passivated by 8-Å-thick layers of HfO_xN_y on both sides, the surface recombination

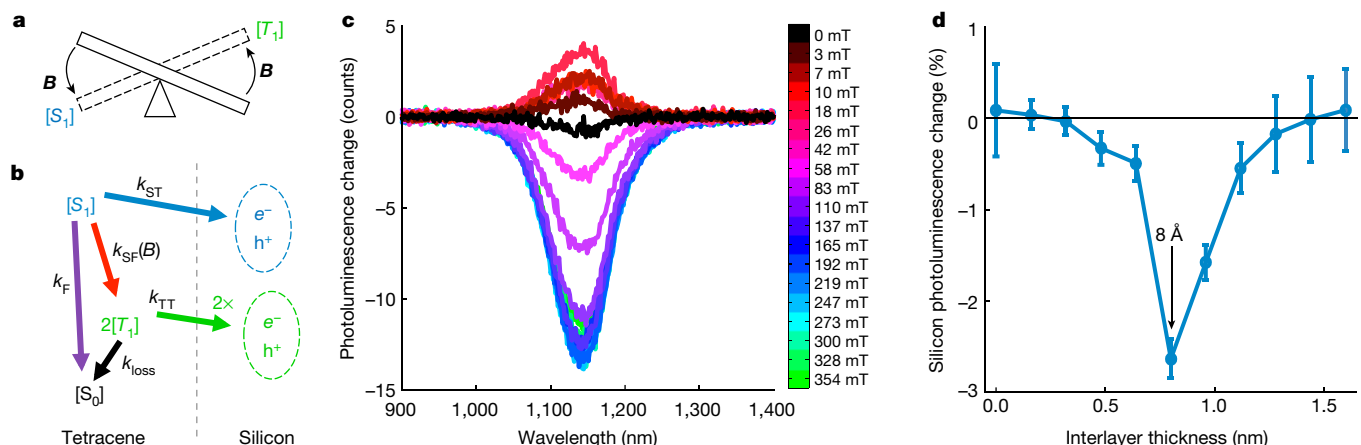


Fig. 4 | Effect of an applied magnetic field on the photoluminescence of silicon. **a**, Simplistic model of the effect of an applied magnetic field on singlet exciton fission. Application of a strong field ($B > 0.05\text{ T}$) increases the singlet exciton density, $[S_1]$, and decreases the triplet exciton density, $[T_1]$. **b**, Key processes at the tetracene–silicon interface. k_{ST} and k_{TT} are the rate constants of singlet and triplet exciton transfer, respectively; k_F is the tetracene fluorescence rate constant; k_{loss} is the rate constant of non-radiative triplet deactivation and $k_{SF}(B)$ is the net rate constant of

singlet exciton fission, which depends on the applied magnetic field B . e^- , electrons; h^+ , holes. **c**, The effect of a magnetic field on a silicon-8-Å-thick HfO_xN_y-tetracene photoluminescent sample excited at $\lambda = 532\text{ nm}$, measured as the change in photoluminescence for detection wavelengths between 900 and 1,400 nm. **d**, The effect of the applied magnetic field on photoluminescence depends on the thickness of the HfO_xN_y, with a clear peak at 8 Å. Error bars are 1σ ; $n = 4,000$.

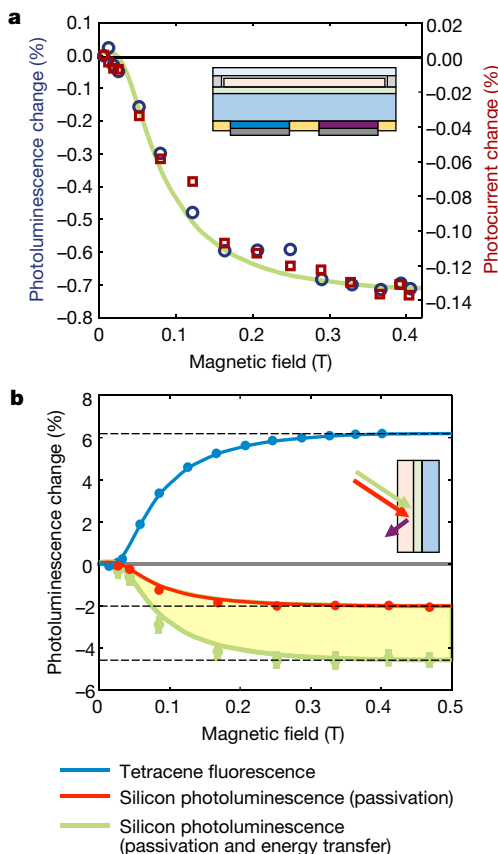


Fig. 5 | Exciton transfer yield. **a**, Effect of an applied magnetic field on sensitized solar cells. The negative trend demonstrates that singlet exciton fission in tetracene increases the efficiency of the solar cell. The effect on the photocurrent, however, is five times weaker than that on the photoluminescence. Inset, schematic of the solar cell, as in Fig. 2a. **b**, The effect of the applied magnetic field on the photoluminescence of photoluminescent samples photoexcited at $\lambda = 532$ nm. To quantify the electric-field-effect passivation we employ a second beam at $\lambda = 785$ nm that is sensitive to passivation changes but does not drive energy transfer from the tetracene. The solid lines in **a** and **b** are fits to the singlet fission characteristic in tetracene, as determined from the fluorescence. Error bars are 1σ ; $n = 4,000$ (silicon); $n = 216$ (tetracene). Inset, schematic of the bichromatic experiment with red and green lasers (see Methods section ‘Bichromatic experiment’).

velocity is $971 \pm 40 \text{ cm s}^{-1}$ with an effective lifetime of $15 \pm 1 \mu\text{s}$. With tetracene on the front surface, the effective lifetime increases to $27 \pm 1 \mu\text{s}$, corresponding to a velocity of $534 \pm 39 \text{ cm s}^{-1}$. After illumination with light of $\lambda = 460 \text{ nm}$ at 20 mW cm^{-2} for 60 s, the surface recombination velocity decreases to $173 \pm 34 \text{ cm s}^{-1}$ with an effective lifetime of $55 \pm 2 \mu\text{s}$, where the uncertainties are 1σ . We conclude that charge generation at the silicon–HfO_xN_y–tetracene interface shown in Fig. 3 causes electric-field-effect passivation and that it can be initiated by optically pumping tetracene or silicon. The same phenomena are observed in the solar cell excitation spectra in Fig. 2c. The ratio of the photocurrent in the 8-Å-thick and 16-Å-thick HfO_xN_y cells has equal contributions from tetracene and silicon, identical to the enhancement of photoluminescence seen in Fig. 3b, which confirms that the photoluminescence excitation spectrum represents the same interfacial processes as the device.

We perform magnetic-field-dependent spectroscopy to probe for the possible presence of triplet energy transfer in addition to the electric-field-effect passivation. The net singlet fission rate is the combination of forward and backward processes; the backward process can be manipulated by applying an external magnetic field^{23–25}.

For small magnetic fields, the overall singlet fission rate first increases, then decreases and plateaus, yielding a characteristic

dependence on the applied magnetic field. In Fig. 4a we show a simplistic model in which the presence of a strong magnetic field B shifts the balance in tetracene from triplets back to singlets, with a corresponding impact on the various processes that are shown in Fig. 4b. Experimentally, we place the sample between the poles of an electromagnet and excite it monochromatically at $\lambda = 532 \text{ nm}$. We show the silicon spectra in response to an external magnetic field in Fig. 4c, presented as a percentage change in the photoluminescence. We find that the silicon photoluminescence can be modulated by external magnetic fields, and our results agree well with the expected magnetic field dependence. At higher magnetic fields, we observe a corresponding decrease in silicon photoluminescence, demonstrating that triplet excitons are the dominant cause of the passivation effect on the silicon photoluminescent samples.

As shown in Fig. 4d, we measure the magnetic field dependence of the photoluminescence of silicon for several HfO_xN_y interlayer thicknesses between 0 nm and 1.6 nm at a resolution of 0.16 nm, where every data point corresponds to one additional atomic layer deposition cycle. For interlayers thinner than 0.8 nm, the effect of the magnetic field on photoluminescence, measured as a percentage change, decreases towards zero with decreasing interlayer thickness. We attribute this magnetic-field effect to a lack of chemical passivation. For interlayers thicker than 0.8 nm, the effect of the magnetic field on photoluminescence again decreases to zero. The fact that it is possible to turn this effect off by increasing the interlayer thickness suggests the presence of a tunnelling process.

We also determine the effect of the applied magnetic field on the photoluminescence and photocurrent I_{SC} of the 8-Å-thick HfO_xN_y cell. We find that triplet excitons positively contribute to both the photoluminescence in the solar cell and to the photocurrent (Fig. 5a), but we note that the effect on the cell’s photoluminescence is approximately five times stronger than the effect on the photocurrent through the cell. The photoluminescence and the photocurrent are probably generated at the front and back sides of the cell, respectively. Therefore, this difference indicates the losses in carrier collection from the front side. When we compare both measurements to those in the silicon–HfO_xN_y–tetracene structures that were not subjected to additional solar cell processing to create back contacts, we find that their photoluminescence modulation under a magnetic field is about seven times greater than that in the solar cells. Thus, our photoluminescent samples exhibit photoluminescence modulations about 35 times stronger than the photocurrent modulations in the solar cells. We conclude that the photoluminescent samples provide an excellent system in which to study triplet-state energy transfer.

To quantify the contributions of electric-field-effect passivation and possible exciton transfer in the photoluminescent samples, we perform bichromatic experiments in which we introduce a second probe beam at $\lambda = 785 \text{ nm}$ with a photon flux that is almost 18 times greater than that of the excitation beam at $\lambda = 532 \text{ nm}$. Because tetracene does not absorb light at 785 nm, this pump creates additional electron–hole pairs in silicon that are sensitive to electric-field-effect passivation but are not affected by the magnetic field, because they do not originate from tetracene. Therefore, this experiment is sensitive to effects resulting almost solely from passivation, whereas the monochromatic excitation experiment at $\lambda = 532 \text{ nm}$ also measures energy transfer. The behaviour can be reproduced using a variety of pump intensities across two orders of magnitude and also if the second probe beam is set at $\lambda = 632.8 \text{ nm}$ (Extended Data Figs. 6–9).

Using the data from the monochromatic and bichromatic photoluminescence measurements that are shown in Fig. 5b, we employ a model to quantify the exciton yields, defined as the number of excitons fully transferred into silicon divided by the number of singlet excitons created in tetracene (detailed in Supplementary Information sections C, D and Supplementary Figs. 10–16). By comparing the effects of the applied magnetic field on the photoluminescence of the samples, we obtain a peak total exciton yield of $133\% \pm 13\%$, which is composed of a singlet transfer yield of $56\% \pm 6\%$ and a triplet transfer yield of

76% ± 7%, demonstrating efficient triplet exciton transfer from tetracene to silicon.

As discussed in Supplementary Information, the dominant loss in the photoluminescent samples is from singlet transfer to silicon that bypasses exciton fission. Future work could employ exothermic singlet fission molecules with higher fission rates than tetracene. Additional spectroscopy studies will be required to identify and characterize the other dynamics, including the passivation and energy-transfer mechanisms. For example, triplet energy transfer may proceed via a Dexter process²⁶ with simultaneous transfer of electrons and holes, or it may be mediated by exciton dissociation. The energy level alignment at the silicon–HfO_xN_y–tetracene interface depicted in Fig. 1d suggests that triplet exciton dissociation is not energetically favoured; we suggest therefore that electric-field-effect passivation must be mediated by traps.

Looking towards the prospect of silicon solar cells operating beyond the single-junction limit, we note that the technological challenge is to achieve control over the thickness, stoichiometry and trap density of the passivation layer and the uppermost few atomic layers of the cell. The strong passivation effect observed in thin HfO_xN_y layers is a crucial advance because it alleviates the quenching of injected electron–hole pairs in silicon and also permits coupling between silicon and the triplet excited states in tetracene. The next step is to improve the efficiency of sensitized cells, which is at present limited by poor carrier collection from the front surface of the silicon. Thinner silicon and tighter control over materials, processing and fabrication will increase efficiency, with a corresponding improvement in the ratio between the effects of the magnetic field on the photoluminescence and the photocurrent of the cell.

Online content

Any methods, additional references, Nature Research reporting summaries, source data, extended data, supplementary information, acknowledgements, peer review information; details of author contributions and competing interests; and statements of data and code availability are available at <https://doi.org/10.1038/s41586-019-1339-4>.

Received: 13 July 2018; Accepted: 7 May 2019;

Published online 3 July 2019.

- Green, A. M. Commercial progress and challenges for photovoltaics. *Nat. Energy* **1**, 15015 (2016).
- Shockley, W. & Queisser, H. J. Detailed balance limit of efficiency of p–n junction solar cells. *J. Appl. Phys.* **32**, 510–519 (1961).
- Smith, M. B. & Michl, J. Singlet fission. *Chem. Rev.* **110**, 6891–6936 (2010).
- Smith, M. B. & Michl, J. Recent advances in singlet fission. *Annu. Rev. Phys. Chem.* **64**, 361–386 (2013).

- Yost, S. R. et al. A transferable model for singlet-fission kinetics. *Nat. Chem.* **6**, 492–497 (2014); corrigendum **6**, 649 (2014).
- Dexter, D. L. Two ideas on energy transfer phenomena: ion-pair effects involving the OH stretching mode, and sensitization of photovoltaic cells. *J. Lumin.* **18**–**19**, 779–784 (1979).
- Congreve, D. N. et al. External quantum efficiency above 100% in a singlet-exciton-fission-based organic photovoltaic cell. *Science* **340**, 334–337 (2013).
- Wu, T. C. et al. Singlet fission efficiency in tetracene-based organic solar cells. *Appl. Phys. Lett.* **104**, 193901 (2014).
- Rao, A. & Friend, R. H. Harnessing singlet exciton fission to break the Shockley–Queisser limit. *Nat. Rev. Mater.* **2**, 17063 (2017).
- Hanna, M. C. & Nozik, A. J. Solar conversion efficiency of photovoltaic and photoelectrolysis cells with carrier multiplication absorbers. *J. Appl. Phys.* **100**, 074510 (2006).
- Swenberg, C. E. & Stacy, W. T. Bimolecular radiationless transitions in crystalline tetracene. *Chem. Phys. Lett.* **2**, 327–328 (1968).
- Burdett, J. J., Gosztola, D. & Bardeen, C. J. The dependence of singlet exciton relaxation on excitation density and temperature in polycrystalline tetracene thin films: kinetic evidence for a dark intermediate state and implications for singlet fission. *J. Chem. Phys.* **135**, 214508 (2011).
- Tabachnyk, M. et al. Resonant energy transfer of triplet excitons from pentacene to PbSe nanocrystals. *Nat. Mater.* **13**, 1033–1038 (2014).
- Thompson, N. J. et al. Energy harvesting of non-emissive triplet excitons in tetracene by emissive PbS nanocrystals. *Nat. Mater.* **13**, 1039–1043 (2014).
- MacQueen, R. W. et al. Crystalline silicon solar cells with tetracene interlayers: the path to silicon-singlet fission heterojunction devices. *Mater. Horiz.* **5**, 1065–1075 (2018).
- Hayashi, T., Castner, T. G. & Boyd, R. W. Quenching of molecular fluorescence near the surface of a semiconductor. *Chem. Phys. Lett.* **94**, 461–466 (1983).
- Piland, G. B. et al. Dynamics of molecular excitons near a semiconductor surface studied by fluorescence quenching of polycrystalline tetracene on silicon. *Chem. Phys. Lett.* **601**, 33–38 (2014).
- Bonilla, R. S., Hoex, B., Hamer, P. & Wilshaw, P. R. Dielectric surface passivation for silicon solar cells: a review. *Phys. Status Solidi A* **214**, 1700293 (2017).
- Aberle, A. G. Surface passivation of crystalline silicon solar cells: a review. *Prog. Photovolt. Res. Appl.* **8**, 473–487 (2000).
- Becker, J. S., Kim, E. & Gordon, R. G. Atomic layer deposition of insulating hafnium and zirconium nitrides. *Chem. Mater.* **16**, 3497–3501 (2004).
- Um, H.-D. et al. Dopant-free all-back-contact Si nanohole solar cells using MoO_x and LiF films. *Nano Lett.* **16**, 981–987 (2016).
- Sinton, R. A. & Cuevas, A. Contactless determination of current–voltage characteristics and minority-carrier lifetimes in semiconductors from quasi-steady-state photoconductance data. *Appl. Phys. Lett.* **69**, 2510–2512 (1996).
- Geacintov, N., Pope, M. & Vogel, F. Effect of magnetic field on the fluorescence of tetracene crystals: exciton fission. *Phys. Rev. Lett.* **22**, 593–596 (1969).
- Merrifield, R. E., Avakian, P. & Groff, R. P. Fission of singlet excitons into pairs of triplet excitons in tetracene crystals. *Chem. Phys. Lett.* **3**, 386–388 (1969).
- Suna, A. Kinematics of exciton–exciton annihilation in molecular crystals. *Phys. Rev. B* **1**, 1716–1739 (1970).
- Dexter, D. L. A theory of sensitized luminescence in solids. *J. Chem. Phys.* **21**, 836–850 (1953).

Publisher's note: Springer Nature remains neutral with regard to jurisdictional claims in published maps and institutional affiliations.

© The Author(s), under exclusive licence to Springer Nature Limited 2019

METHODS

Device fabrication. For a schematic of the fabrication process, see Extended Data Fig. 2. We purchased silicon wafers from PureWafer (for details see Supplementary Table 3) and transferred them to a clean room. We then performed a standard Radio Corporation of America (RCA) clean as follows. First, organic contaminants were removed by immersing the sample in a 5:1:1 ratio solution of deionized water, aqueous ammonium hydroxide (29%), and aqueous hydrogen peroxide (30%) for 20 min at 80 °C. Second, the native oxide was removed by etching with aqueous hydrofluoric acid (1%) for 60 s. Third, metal-ion contaminants were removed from the wafer surface in a 5:1:1 ratio solution of deionized water, aqueous hydrochloric acid (37%), and aqueous hydrogen peroxide (30%) for 20 min at 80 °C. We then deposited 10 nm of aluminium oxide on both sides using atomic layer deposition. Using photolithography, we fabricated electron-selective contacts (aluminium/lithium fluoride) and hole-selective contacts (aluminium/molybdenum oxide) in an interdigitated fashion. We then diced the wafers into chips and protected the back side of the individual chips using PDMS and a second piece of encapsulating silicon to provide a seal. We experimentally verify in Extended Data Fig. 10 that a full RCA clean before HfO_xN_y deposition is not compatible with our solar cell fabrication because the protective rear PDMS seal decomposes in the presence of acids, and the monomers subsequently reattach to the front side by condensation^{27,28}. Consequently, to minimize contamination by PDMS in this process, we cleaned the front side using 10% aqueous hydrofluoric acid for 1 min and a 5:1:1 ratio solution of deionized water, aqueous ammonium hydroxide (29%) and aqueous hydrogen peroxide (30%) for 20 min at 60 °C. We fabricated the downconversion front side as detailed below and then peeled off the silicon protecting the back contacts (as shown in Extended Data Fig. 2).

Photoluminescent sample fabrication. The silicon wafers for the photoluminescent samples were purchased from EL-CAT (for details see Supplementary Table 3) and transferred to a clean room, and were then diced and cleaned using a standard RCA clean (see Methods section ‘Device fabrication’). We then fabricated the downconversion front side as detailed below.

Downconversion front-side fabrication. HfO_xN_y was deposited using atomic layer deposition in a Cambridge Nanotech Savannah deposition system²². We used tetrakis(dimethylamino)hafnium as the hafnium precursor and ammonia as the nitrogen precursor with residual oxygen in the chamber. The hafnium injection pulse duration was 30 ms and the ammonia injection pulse duration was 20 ms. The hafnium precursor was at an initial temperature of 95 °C, and the reaction chamber was heated to 150 °C during the growth of the HfO_xN_y. The base pressure at a nitrogen flow of 40 cm³ min⁻¹ was 0.4 torr. The samples were immediately transferred into a nitrogen glovebox. Finally, 30 nm of tetracene was deposited at a rate of 1 Å s⁻¹ by thermal evaporation in a vacuum chamber with base pressure <1 × 10⁻⁶ torr, directly connected to the glovebox. The tetracene used in this work was received from Sigma Aldrich (98% purity) and purified by sublimation in a tube furnace three consecutive times. Samples were packaged in a nitrogen glovebox using ultraviolet-curing epoxy and a quartz slide at oxygen and water concentrations below 5 p.p.m. The active area of the substrates was protected with aluminium foil during ultraviolet exposure.

Photoelectron spectroscopy. Ultraviolet photoelectron spectroscopy, X-ray photoelectron spectroscopy and inverse photoemission spectroscopy experiments were conducted in an ultrahigh-vacuum chamber with a base pressure of 5 × 10⁻¹⁰ torr. Ultraviolet photoelectron spectroscopy measurements were done with both the He I (21.22 eV) and He II (40.81 eV) photon lines generated by a discharge lamp. Non-monochromated aluminium K α X-rays with an energy of 1,486.6 eV were used for all X-ray photoelectron spectroscopy measurements. Inverse photoemission spectroscopy was performed in the isochromat mode with a setup described elsewhere²⁹. The nominal energy resolutions for ultraviolet photoelectron spectroscopy, X-ray photoelectron spectroscopy and inverse photoemission spectroscopy were 100 meV, 800 meV and 400 meV, respectively. A tetracene layer with a thickness of 4 nm was deposited on the HfO_xN_y–silicon surfaces in an ultrahigh-vacuum chamber connected to the analysis chamber by thermal evaporation at rates of about 1 Å s⁻¹.

Device experiments. Current–voltage characteristics were recorded using a precision semiconductor parameter analyser (Agilent 4156C) in voltage mode sweeping from −0.6 V to +0.6 V in 10 mV intervals. The sample was illuminated through a shadow mask using a calibrated solar simulator (Newport 69920) emitting an AM1.5G solar spectrum. The EQE data was collected using a broadband tunable laser (SuperK EXTREME supercontinuum) or a tungsten lamp with monochromator as the excitation source under a white-light bias.

Excitation spectrum. A broadband tunable laser (SuperK EXTREME supercontinuum laser) was focused onto the sample with 20-ps pulses at 78 MHz. The infrared emission from the sample was collected by a liquid-nitrogen-cooled InGaAs detector (Princeton Instruments OMA V). The excitation wavelength was varied from 485 nm to 640 nm, but the photon fluxes were kept constant,

corresponding to optical intensities of 458 mW cm⁻² to 344 mW cm⁻². This was achieved by adjusting the photon flux for every wavelength using a beam splitter, a photodetector and a software-based feedback loop. For a schematic of the setup see Supplementary Fig. 17.

Surface recombination velocity. Photoconductance decay measurements were performed using the silicon lifetime and wafer metrology system WCT-120 from Sinton Instruments (fully compliant with the industry standard SEMI PV-13)²². The optical constants were calculated taking into account the reflection and absorption of all layers on top of the silicon. Where applicable, the transfer matrix method was used. The measured effective lifetimes were then used to determine the surface recombination velocities (see Supplementary Information section F).

Monochromatic experiments. The samples were excited with a Coherent Genesis MX532-500 STM laser at 532 nm (8.2 mW cm⁻²). Infrared emission from the samples was collected with a liquid-nitrogen-cooled InGaAs detector (Princeton Instruments OMA V). A pulsed external magnetic field of varying strength was applied and the spectra were recorded continuously. The laser intensity was monitored using a 90:10 (transmission:reflection) beam splitter and a silicon photodetector (Newport 818-SL). For a schematic of the setup see Supplementary Fig. 18. In the experiment in which we performed photoluminescence and photocurrent measurements simultaneously, we excited the sample with a Coherent Verdi G laser at 532 nm (25 W cm⁻²) chopped at 313 Hz. The bias point was approximately 0.16 V. The silicon photoluminescence was measured with a germanium photodetector (Newport 818-IR) connected to a lock-in amplifier (SR830, Stanford Research Systems) and the photocurrent was measured as the current across a 50-Ω resistor, connected to a second lock-in amplifier (SR830, Stanford Research Systems).

Bichromatic experiment. The beams of two lasers (Coherent Genesis MX532-500 STM and Thorlabs LDM 785) at 532 nm and 785 nm were merged using a 90:10 beam splitter. The photon flux of the 785-nm beam was chosen to be almost 18 times stronger than that of the 532 nm pump. The optical intensities were 8.2 mW cm⁻² and 198 mW cm⁻² for the 532-nm and 785-nm beams, respectively. The tetracene emission was collected with a silicon photodetector (Newport 818-SL) connected to a lock-in amplifier (SR830, Stanford Research Systems). Otherwise, this measurement was identical to the monochromatic experiment described above. For a schematic of the setup see Supplementary Fig. 19.

Modelling. The model used to calculate the yield is described in Supplementary Information sections C, D and Supplementary Figs. 10–16. The model was implemented using a custom MATLAB code.

Data availability

The data that support the findings of this study are available from the corresponding author upon reasonable request.

Code availability

The custom code that supports the findings of this study is available from the corresponding author upon reasonable request.

- 27. Mata, A., Fleischman, A. J. & Roy, S. Characterization of polydimethylsiloxane (PDMS) properties for biomedical micro/nanosystems. *Biomed. Microdevices* **7**, 281–293 (2005).
- 28. Kim, Y.-K., Kim, G. T. & Ha, J. S. Simple patterning via adhesion between a buffered-oxide etchant-treated PDMS stamp and a SiO₂ substrate. *Adv. Funct. Mater.* **17**, 2125–2132 (2007).
- 29. Wu, C. I., Hirose, Y., Sirringhaus, H. & Kahn, A. Electron–hole interaction energy in the organic molecular semiconductor PTCDA. *Chem. Phys. Lett.* **272**, 43–47 (1997).

Acknowledgements This work was supported through the Center for Excitonics, an Energy Frontier Research Center, by the US Department of Energy, Office of Science, Office of Basic Energy Sciences under award number DE-SC0001088 (MIT). Surface characterization work at Princeton was supported in part by the U.S. Department of Energy, Office of Basic Energy Sciences, Division of Materials Sciences and Engineering under award DE-SC0012458 (A.K.) and the National Science Foundation Graduate Research Fellowship grant DGE-1656466 (H.L.S.). We thank T. Buonassisi for access to the silicon lifetime and wafer metrology system. We thank D.-G. Ha for help with the atomic force microscopy measurements.

Author contributions M.E. and T.W. fabricated the photoluminescent samples and measured the photoluminescent excitation spectra and the effect of the magnetic field on photoluminescence. M.E., T.W. and C.F.P. built the setup for the measurements of the effect of the magnetic field on photoluminescence. J.F.K. and M.E. fabricated the solar cells. M.E. and J.F.K. performed solar cell measurements (current–voltage and EQE measurements, and measurements of the effects of the magnetic field). M.E., L.N. and S.W. performed the photoconductance decay measurements. H.L.S. performed the ultraviolet photoelectron spectroscopy and inverse photoemission spectroscopy

measurements. H.L.S. and M.E. performed the X-ray photoelectron spectroscopy measurements. M.A.B., M.E., D.N.C. and T.W. conceived the project. A.K., M.G.B. and M.A.B. supervised the experiments. All authors discussed the results and commented on the manuscript.

Competing interests MIT has filed a provisional application for a US patent based on this technology that names M.E., T.W. and M.A.B. as inventors (serial number 62/678,818).

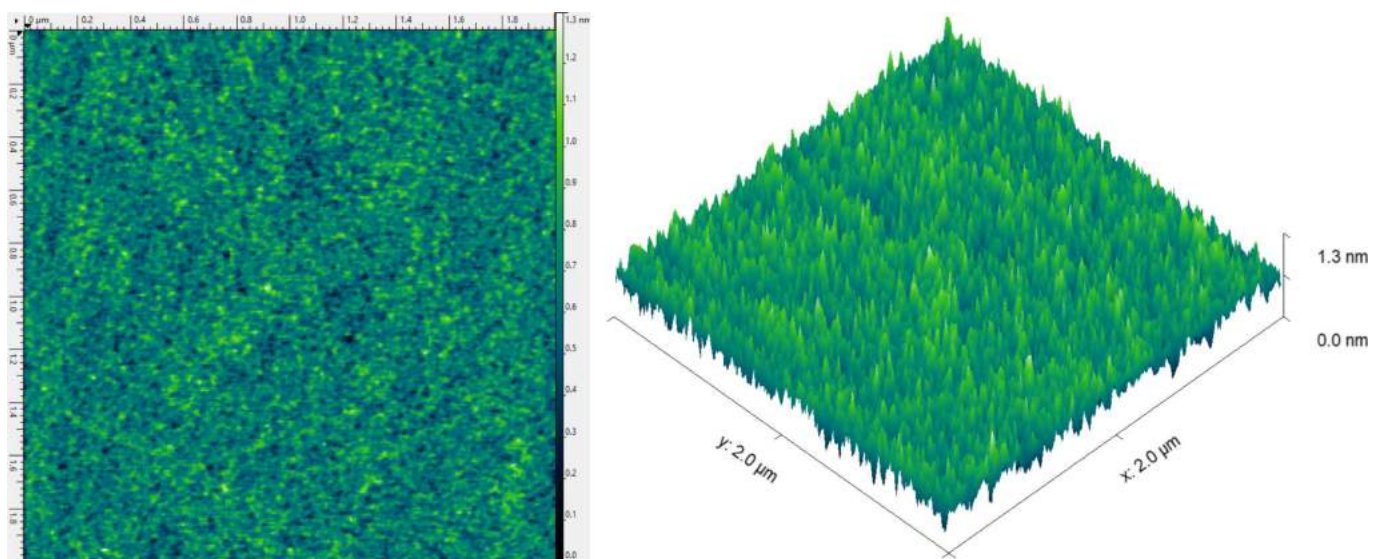
Additional information

Supplementary information is available for this paper at <https://doi.org/10.1038/s41586-019-1339-4>.

Correspondence and requests for materials should be addressed to M.A.B.

Peer review information *Nature* thanks Akshay Rao and the other anonymous reviewer(s) for their contribution to the peer review of this work.

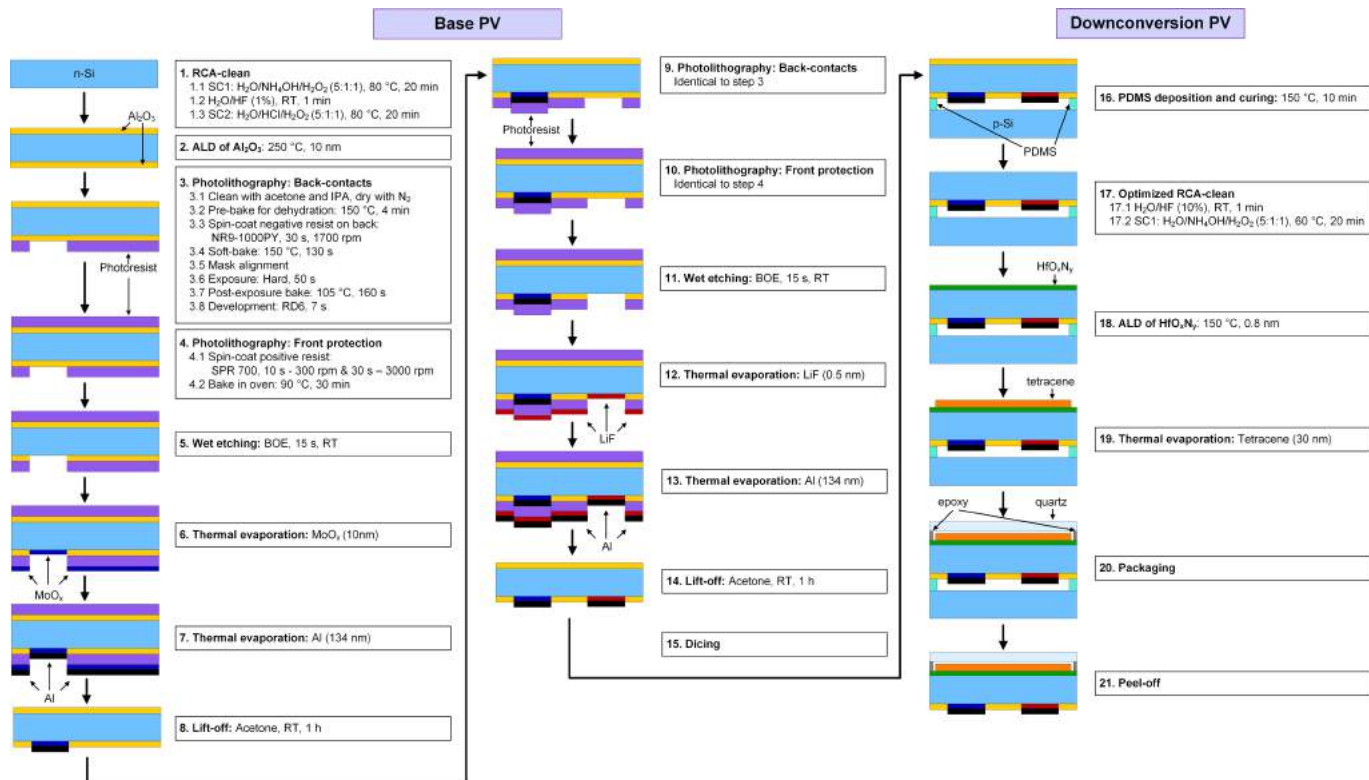
Reprints and permissions information is available at <http://www.nature.com/reprints>.



RMS roughness	150 pm
Mean roughness	120 pm
Excess kurtosis	0.00043

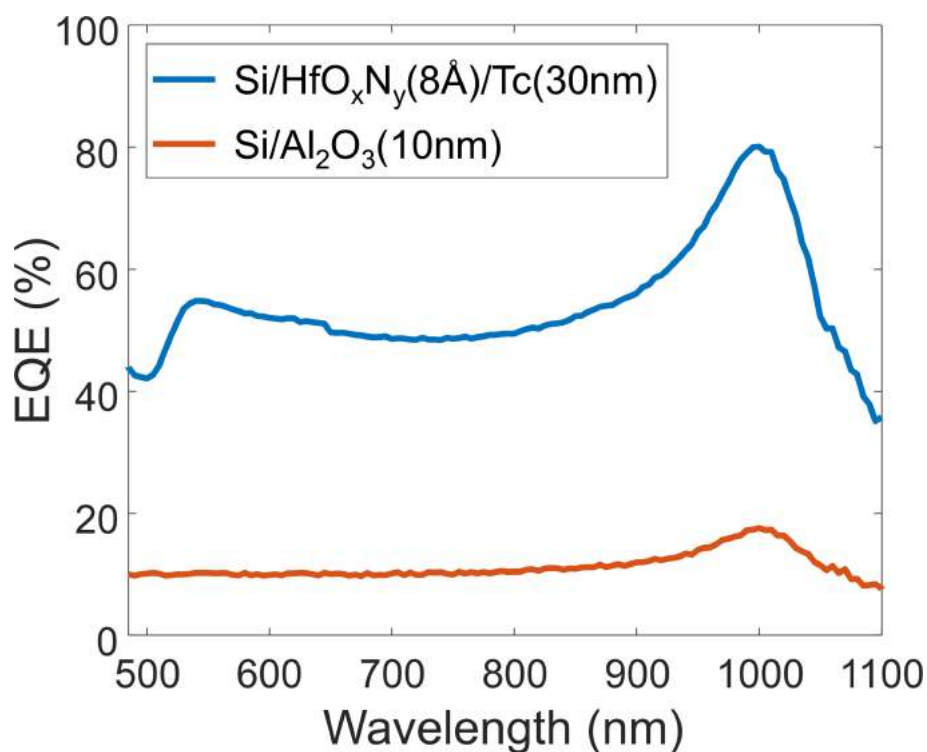
Extended Data Fig. 1 | Atomic force microscopy data of HfO_xN_y (8 Å, five atomic layer deposition cycles) on silicon. The film quality was monitored using atomic force microscopy (Veeco Metrology Nanoscope

V 3100 SPM; tip, HQ:NSC14/AL BS). The film thickness was monitored using ellipsometry (J. A. Woollam VASE ellipsometer). 500 cycles correspond to a thickness of 83 nm. RMS, root mean square.



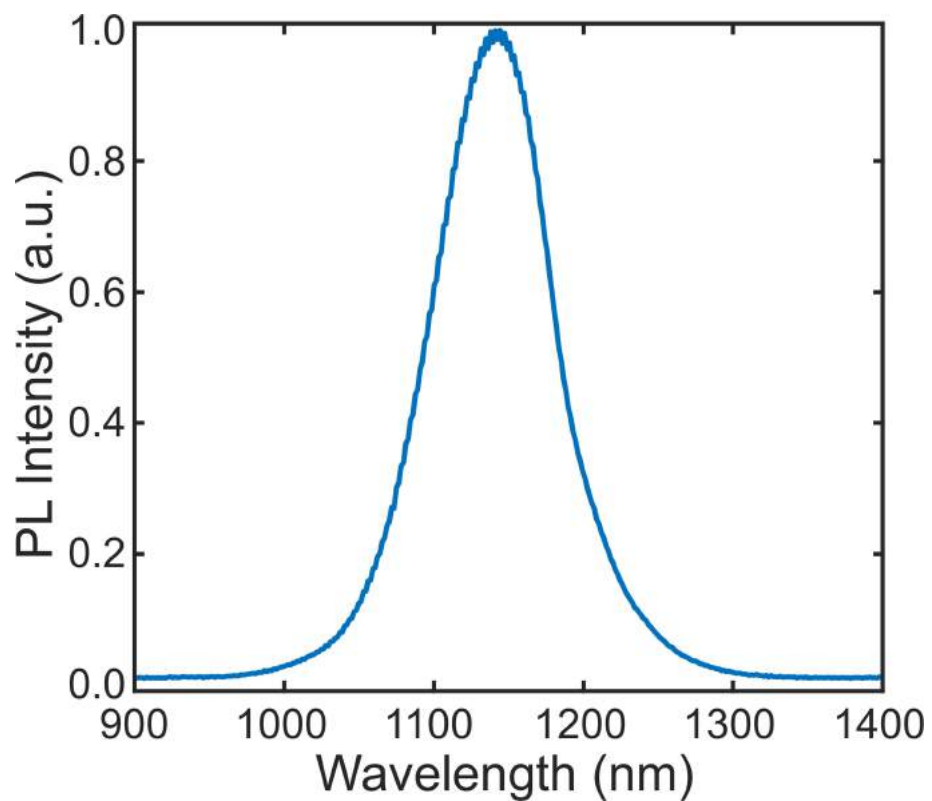
Extended Data Fig. 2 | Fabrication process of singlet-fission-enhanced silicon solar cells. Steps 1–14 are based on a previous work²¹. BOE, buffered oxide etch. RT, room temperature. ALD, atomic layer deposition; IPA, isopropylalcohol; NR9-1000PY; negative-tone photoresist designed

for 365 nm wavelength exposure; RD6, resist developer; SC1, RCA standard clean 1; SC2, RCA standard clean 2; PV, photovoltaic cell; p-Si, boron-doped silicon.

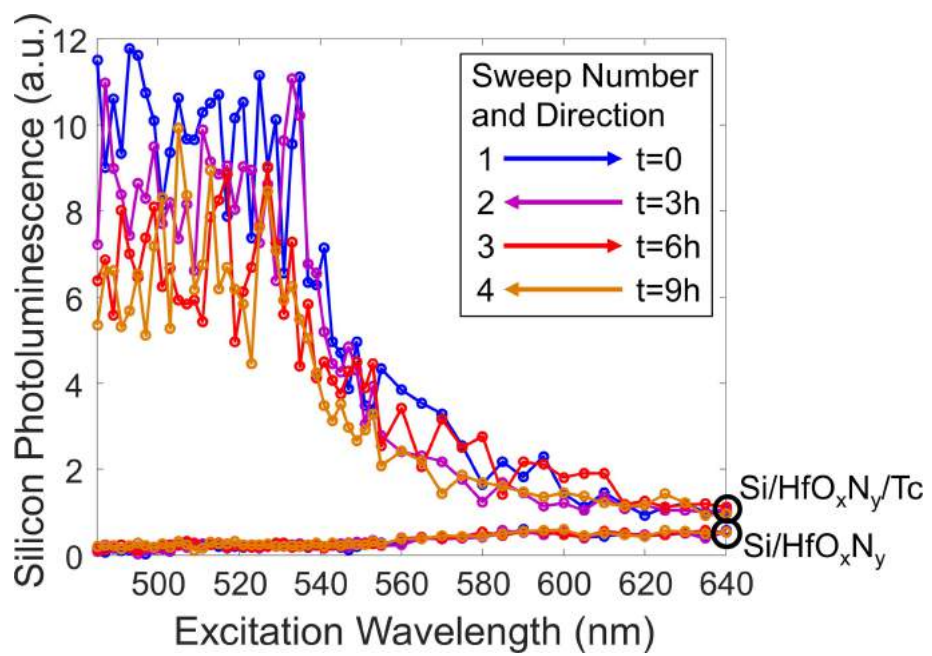


Extended Data Fig. 3 | Short-wavelength infrared EQE spectra for a tetracene-coated silicon solar cell (silicon-8-Å HfO_xN_y-30 nm tetracene) and a silicon solar cell without tetracene (silicon-10 nm aluminium oxide). Devices are fabricated using the procedures described in Methods and show increases in EQE at long wavelengths, potentially

due to poor carrier collection from the front of the cell. We note that in the absence of tetracene, there is ineffective thin-HfO_xN_y passivation. Silicon-8-Å-HfO_xN_y devices generate negligible photocurrent, in agreement with our measurements of the surface recombination velocity in the absence of tetracene. Tc, tetracene.

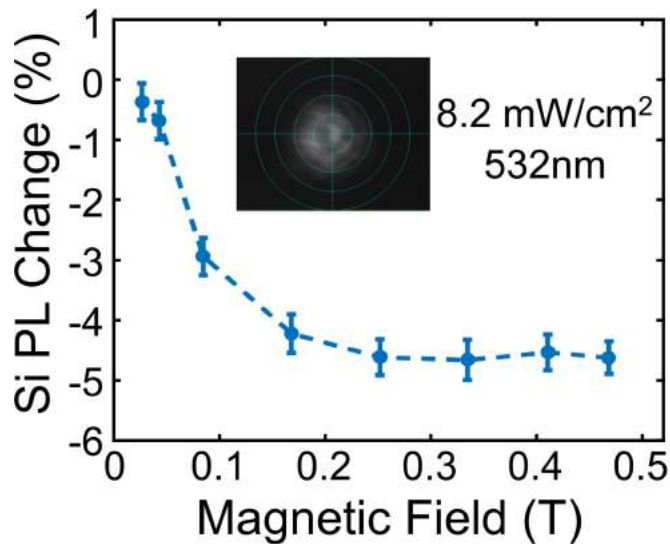


Extended Data Fig. 4 | Silicon photoluminescence (PL) spectrum corresponding to the band-to-band transition. The peak is at 1,144 nm (1.1 eV).

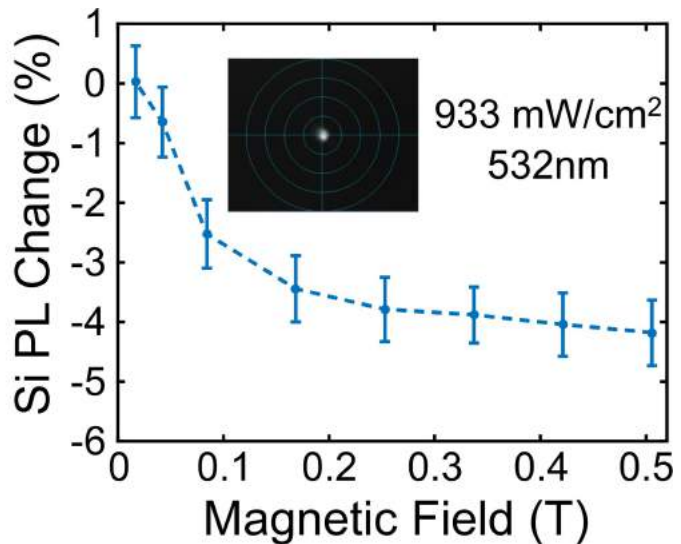


Extended Data Fig. 5 | Degradation for wavelength sweeps in the excitation spectrum. Arrows indicate the direction of the wavelength sweep (from short to long wavelengths or vice versa). The time t indicates

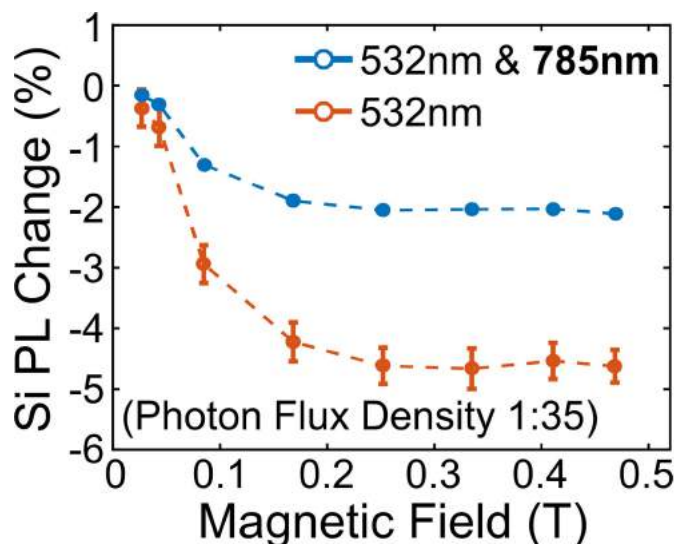
the start time of the sweep relative to the start of the entire measurement.
a.u., arbitrary units.



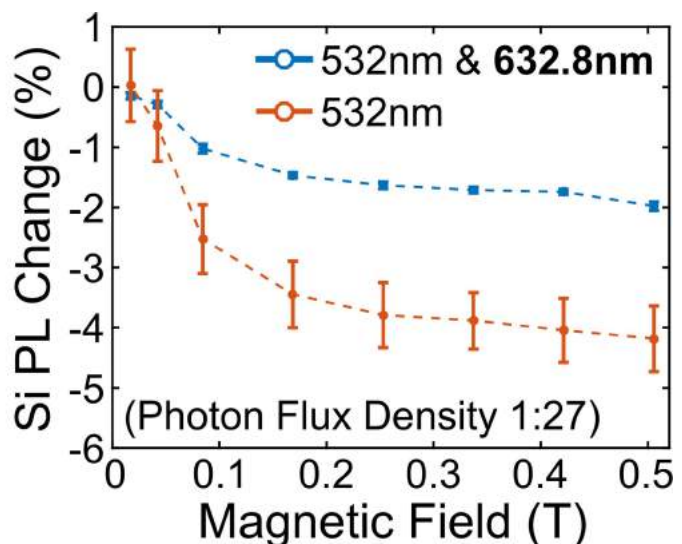
Extended Data Fig. 6 | Dependence of the change in photoluminescence from the applied magnetic field on the optical intensity (pump power density). Exciting the sample with vastly different intensities (left,



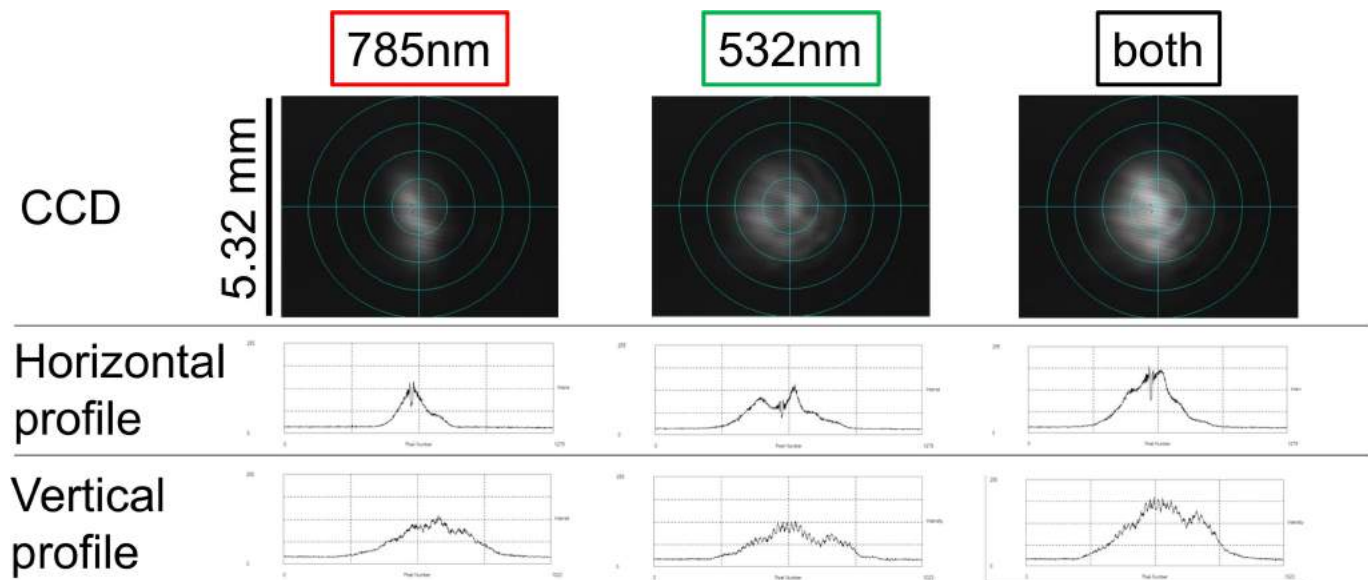
right, 933 mW cm^{-2}) yields a similar effect on the change in photoluminescence (-4.7% and -4.2% , respectively). Error bars are 1σ ; $n = 4,000$.



Extended Data Fig. 7 | Bichromatic experiments with different probe beam wavelengths. The choice of the second pump wavelength (left, 785 nm; right, 632.8 nm) has no influence on the change in photoluminescence from the application of the magnetic field (about -2.0% for both secondary wavelengths). This excludes the possibility that any effects resulting from the choice of the second pump beam impair

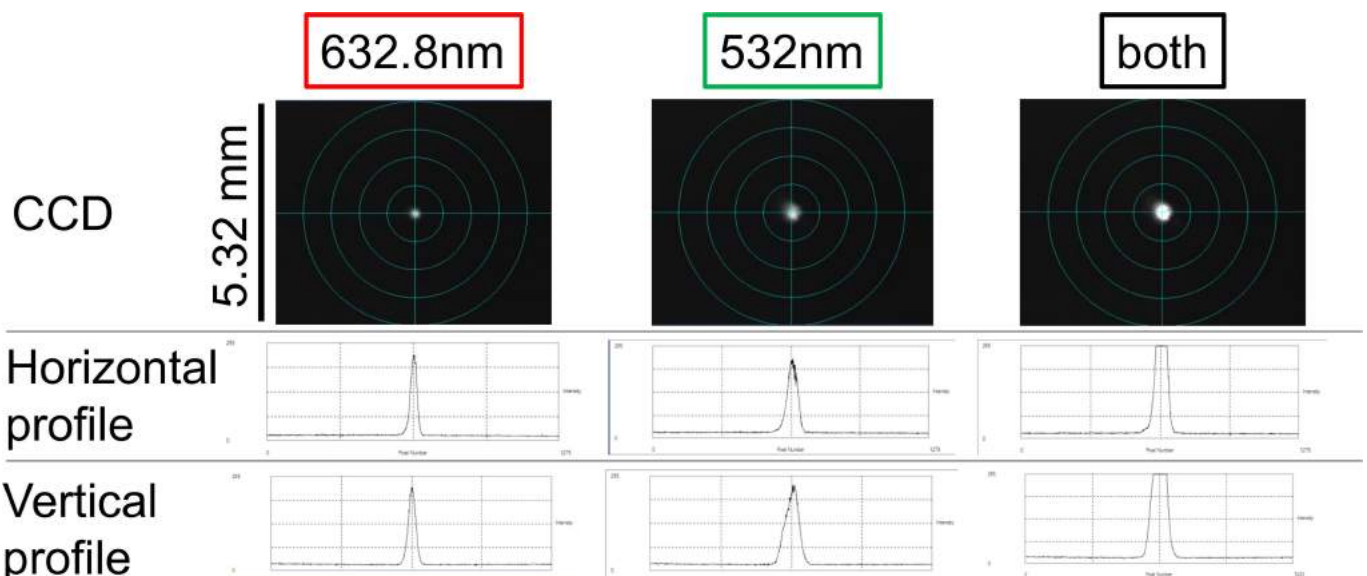


our determination of the exciton yield. The ratio of the flux density is calculated by comparing the number of incident photons per second from the two pump beams. The photon flux density of the 785 nm beam is 35 times larger than that of the 532 nm beam and the photon flux density of the 632.8 nm beam is 27 times larger than that of the 532 nm beam. Error bars are 1σ ; $n = 4,000$.



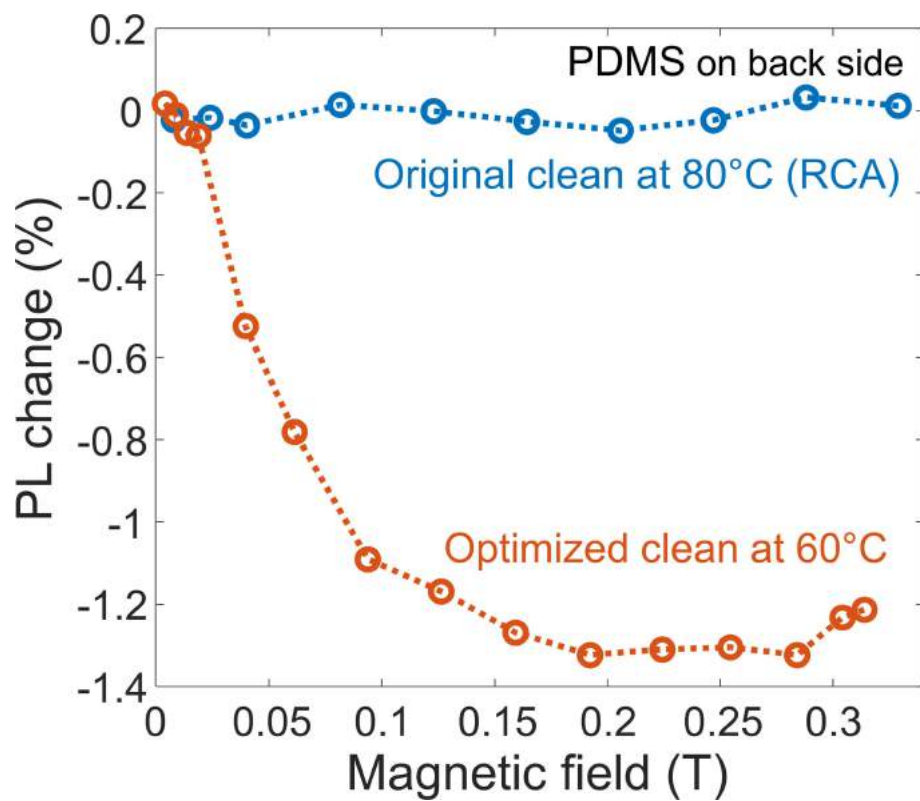
Extended Data Fig. 8 | Beam alignment for the bichromatic experiment with the second probe at 632.8 nm. The green beam (Genesis, 532 nm) influences the surface properties through passivation, and so must

cover the same area or a larger area than the red beam (Thorlabs HeNe, 632.8 nm). CCD, charge-coupled device.



Extended Data Fig. 9 | Beam alignment for the bichromatic experiment with the second probe at 785 nm. The green beam (Genesis, 532 nm) influences the surface properties through passivation, and so must

cover the same or a larger area than the red beam (Thorlabs photodiode, 785 nm).



Extended Data Fig. 10 | Back protection using PDMS. During device fabrication, we protect the back contacts using PDMS and an encapsulating piece of silicon to provide a seal during the front-side cleaning step. Here we show that the presence of PDMS on the back side can corrupt the integrity of the front surface. A full RCA clean of the front

surface at 80 °C shows no change in photoluminescence under an applied magnetic field. Using a milder version of the clean at 60 °C partly alleviates the issue but the change in photoluminescence from the applied magnetic field is not as large as in the samples processed without PDMS (see Fig. 5).

REVIEW

[View Article Online](#)
[View Journal](#) | [View Issue](#)



Cite this: *Energy Environ. Sci.*,
2016, 9, 281

Versatile ternary organic solar cells: a critical review

Qiaoshi An,^a Fujun Zhang,^{*a} Jian Zhang,^b Weihua Tang,^c Zhenbo Deng^a and Bin Hu^{*a}

The power conversion efficiency (PCE) of organic solar cells has been constantly refreshed in the past ten years from 4% up to 11% due to the contribution from the chemists on novel materials and the physicists on device engineering. For practical applications, a single bulk heterojunction structure may be the best candidate due to the cell with a high PCE, easy fabrication and low cost. Recently, ternary solar cells have attracted much attention due to enhanced photon harvesting by using absorption spectral or energy level complementary materials as the second donor or acceptor based on a single bulk heterojunction structure. For better promoting the development of ternary solar cells, we summarize the recent progress of ternary solar cells and try our best to concisely outline the scientific issues in preparing high performance ternary solar cells.

Received 27th August 2015,
Accepted 22nd October 2015

DOI: 10.1039/c5ee02641e

www.rsc.org/ees

Broader context

The fast growth of global energy demand and environmental pollution caused by excessive exploitation and consumption of mineral materials require ideal clean and renewable energy resources to meet the needs of economic and social development. Organic solar cells (OSCs), as one promising energy conversion technology, have attracted much attention due to their unique properties of low cost, easy fabrication, large scale, light weight, flexibility and abundant raw materials. Over the past ten years, the significant improvement of OSCs has been achieved by developing low bandgap materials with high charge carrier mobility and adopting the diversified strategies on the active layers and interfacial layers. However, further improvement of performance of single-junction OSCs is still limited by insufficient photon harvesting of active layers due to the relatively narrow absorption window (~ 100 nm) of organic semiconductors. The ternary solar cells combine the advantages of improved photon harvesting in tandem solar cells and simple fabrication technology of single bulk heterojunction OSCs, showing great potential for obtaining high-performance OSCs with bright application prospects.

1 Introduction

Due to excessive exploitation and consumption of mineral materials, energy shortage and environmental pollution have become the major problems in human development. The development of photovoltaic technology has brought a series of clean and renewable energy resources to solve energy and environmental problems. Organic solar cells (OSCs) as one of the most potential photovoltaic technologies have attracted enormous attention because of their easy fabrication, large area, light weight, flexibility and abundant raw materials.^{1–5} In particular, OSCs have the advantage over all photovoltaic technologies that the possible

manufacturing speed is very high and the thermal budget is low as no high temperatures are needed.^{6,7} OSCs have the smallest ecological footprint and the shortest energy payback time possible, it means that OSCs need the shortest time required to produce the energy invested during their life cycle.^{8,9} In recent years, the power conversion efficiency (PCE) of bulk heterojunction (BHJ) OSCs has been improved by over 10% based on novel low bandgap materials for better matching with the solar spectrum to increase the short circuit density (J_{SC}) and with the highest occupied molecular orbital (HOMO) level to enhance the open circuit voltage (V_{OC}).^{10–14} The BHJ structure is considered as the most effective strategy for obtaining high performance of solar cells due to the bi-continuous interpenetrating network for better exciton dissociation and charge carrier transport in the active layers.^{15–20} The key processes determining the performance of solar cells can be summarized as: (i) photon harvesting ability and the range of the active layers to generate more excitons;^{21–25} (ii) appropriate donor/acceptor phase separation trend for efficient exciton dissociation and charge transport

^a Key Laboratory of Luminescence and Optical Information, Ministry of Education, Beijing Jiaotong University, 100044, China. E-mail: fjzhang@bjtu.edu.cn, bhu@utk.edu

^b Department of Material Science and Technology, Guangxi Key Laboratory of Information Materials, Guilin University of Electronic Technology, 541004, China

^c Key Laboratory of Soft Chemistry and Functional Materials, Ministry of Education, Nanjing University of Science and Technology, 210094, China

(low recombination loss);^{26–30} and (iii) interfacial engineering for charge carrier collection by individual electrodes.^{31–34} Therefore, chemical and physical engineering should be simultaneously carried out for PCE improvement. The PCE of solar cells is proportional to the J_{SC} , the V_{OC} and the fill factor (FF), as given by eqn (1):

$$\text{PCE} = \frac{J_{SC} \times V_{OC} \times \text{FF}}{P_{in}} \times 100\% \quad (1)$$

where P_{in} is the incident light power. The J_{SC} is defined as the current density without an external load. The V_{OC} is defined as the voltage which compensates the current flow through the external circuit. The FF characterizes how “square” the current density–voltage (J – V) curve is and it represents how “difficult” or how “easy” the photogenerated carriers can be extracted out from a photovoltaic device.³⁵ For high efficiency OSCs, the FF is usually larger than 60% exhibiting an efficient charge carrier transport and collection. Meanwhile, the FF exhibits a rapidly decreasing trend along with the increase of the active area due to insufficient charge carrier collection by an individual electrode. The PCE improvement of OSCs strongly depends on the simultaneous enhancement of the V_{OC} , the J_{SC} and the FF by employing appropriate materials, film fabrication and post-treatment technology and interfacial engineering.

It is generally believed that the J_{SC} is proportional to the number of absorbed photons, which strongly depends on the absorption intensity and the absorption range of the active layer materials. A series of excellent low bandgap materials were successfully synthesized to improve the performance of solar cells by using benzodithiophene (BDT), dithienosilole (DTS), or indacenodithiophene (IDT), thienothiophene (TT), benzodithiophene (BDT), as well as BDT- and *N*-alkylthieno-[3,4-*c*]pyrrole-4,6-dione (TPD) donor units and benzothiadiazole (BT), thienopyrroledione (TPD), or thiazolothiazole (TTz) acceptor units.^{36–41} Optimized morphology, phase separation and crystallinity of the active layer also should play the key role in obtaining high performance solar cells. The effective strategy on adjusting properties of active layers can be summarized as: thermal annealing treatment, solvent additive, solvent vapor treatment, mixed solvents, hot solvents and casting solvent.^{42–52} Ma *et al.* first reported thermal annealing treatment on the active layer to improve the PCE up to 5% for OSCs with poly(3-hexylthiophene) (P3HT) and [6,6]-phenyl-C₆₁-butyric acid methyl ester (PCBM) as active layers, which is attributed to the improved nanoscale morphology and crystallinity of active layers.⁵³ Hou *et al.* reported that optimized PCE 7.4% OSCs based on P3HT as the donor and indene-C-70 bisadduct (IC₇₀BA) as the acceptor was obtained by using 3 vol% high boiling point solvent additive of 1-chloronaphthalene (CN), *N*-methyl pyrrolidone (NMP), 1,8-octanedithiol (OT) or 1,8-diiodooctane (DIO) with solvent annealing, which is due to the optimized P3HT/IC₇₀BA interpenetrating network and enhanced absorption of the active layer by using solvent additive treatment.¹⁸ Zhao *et al.* reported the enhanced PCE of P3HT:PCBM-based OSCs *via* 1,2-dichlorobenzene (DCB) vapor treatment and thermal annealing treatment, which is beneficial to P3HT self-organizing assisted by DCB vapor

treatment to enhance absorption and hole mobility.⁵⁴ During the solvent vapor treatment, PCBM molecules begin to diffuse into aggregates and together with the ordered P3HT phase form bicontinuous pathways in the entire layer for efficient charge separation and transport. Ye *et al.* reported a two-step strategy to improve the performance of OSCs: (i) tuning the volume ratio of binary solvents (DCB and CF) and (ii) adding DIO solvent into the optimized binary solvents.⁵⁵ Xiao *et al.* developed a method using solvent fluxing to form graded bulk heterojunction active layers with more uniform PCBM distribution, resulting in higher charge carrier collection efficiency.⁵⁶ For better charge carrier collection, an ultrathin interfacial buffer layer was commonly inserted between the active layer and the electrode to form a quasi Ohmic contact. Poly(styrene sulfonic acid) doped poly(3,4-ethylenedioxothiophene) (PEDOT:PSS) is the commonly used conducting polymer as an anode buffer layer.⁵⁷ As substitutes of PEDOT:PSS, metal oxidations were selected due to their appropriate work function, good hole-transporting and electron-blocking properties, such as MoO₃, NiO, V₂O₅ and WO₃.^{58–60} For the cathode buffer layers, some low work function metal or inorganic materials were adapted to modify the Al cathode to improve electron extraction from active layers, such as Ca, LiF, TiO_x, ZnO, Cs₂CO₃, and α -ZrAcac.^{61–65} Recently, cross-linkable water or alcohol soluble conjugated polymers were used as a cathode buffer layer, such as polyethylenimine (PEI), polyethylenimine ethoxylated (PEIE) and poly[(9,9-bis(3'-(*N,N*-dimethylamino)propyl)-2,7-fluorene)-*alt*-2,7-(9,9-diethylfluorene)] (PFN) and poly[3-(6-trimethylammoniumhexyl)thiophene] (PTMAHT), which can avoid intermixing between the active layer and the subsequently deposited interlayer.^{66,67} Zhang *et al.* reported the PCE improvement by using poly(ethylene oxide) (PEO) as the cathode interfacial layer mainly due to an increase in V_{OC} .⁶⁸ Sun *et al.* reported that the PCE of OSCs with PTB7-Th:PCBM as the active layers was increased from 6.13% to 8.69% by using a two-step strategy preparing PFN interfacial layers, 4 min methanol soaking the active layers and then directly spin-coating PFN methanol solution on the active layers.⁶⁹

Over the past ten years, significant PCE improvement of OSCs has been achieved by developing novel low bandgap materials, adopting the diversified strategy on phase separation and using interfacial layers for charge carrier collection. However, further improvement of performance for single-junction OSCs is still limited by insufficient photon harvesting of active layers containing one donor and one acceptor material due to the relatively narrow absorption window (~ 100 nm) of organic materials.⁷⁰ Furthermore, another limitation recognized by Shockley and Queisser showed that the trade-off between photocurrent and photovoltage in single-junction OSCs, with the efficiency of broad spectrum absorbers being reduced by the thermalization of above-bandgap excitations, named as thermalization loss.⁷¹ Efficient strategies for performance improvement of OSCs should rely on full utilization of solar light in a broad coverage and circumventing the standard single-junction Shockley–Queisser efficiency limit. Compared with the single-junction OSCs, tandem configuration solar cells can not only improve light absorption but also reduce thermalization loss of photonic

Published on 27 October 2015. Downloaded by CASE WESTERN RESERVE UNIVERSITY on 5/7/2020 4:52:19 AM.

energy by stacking two or more sub-cells with complementary absorption range, harvesting high and low energy photons in the separated sub-cells.^{72–76} The sub-cells in tandem solar cells work independently without any energy or charge carrier transfer between each other, which can be connected either in series or in parallel by adjusting the interconnecting scheme. The series connection is the most widely adopted model with two terminals. The intermediate connection layer should allow the recombination of holes coming from one sub-cell with electrons coming from the other cell.^{77,78} To maximize the utilization of solar light, the high and low bandgap polymers based sub-cells are usually used as front and rear cells, respectively. The active layer thickness of sub-cells should be optimized according to their absorption coefficient and bandgap to obtain the maximum J_{SC} because the J_{SC} of tandem solar cells is determined by the minimum J_{SC} of sub-cells. The V_{OC} of the tandem solar cell is the sum of the two sub-cells.^{79,80} The simulation proposed by Brabec *et al.* indicates that one cell donor should have a high bandgap of 1.6 eV and the other cell donor should have a low bandgap of 1.3 eV to achieve 15% PCE in a tandem solar cell, both cells have a flat external quantum efficiency (EQE) of 65% under this assumption.⁸¹ In fact, the wide applicability of tandem solar cells may be hampered due to the complex technology, such as using solution processing to accurately control the thickness of active layers for achieving photocurrent balance between the front and back cells, designing and optimizing the intermediate layers between the sub-cells to realize efficient charge carriers collection. Furthermore, processing tandem solar cells with two or more stacked sub-cells may increase the cost and decrease the yield, which is in contrast to the attractive simplicity of the single-step solution processing for inexpensive solar cells. The great challenge is to fabricate the middle terminal for in parallel tandem solar cells with three terminals.^{82,83}

Recently, ternary solar cells as one of the promising candidates exhibit great potential to obtain high performance, which enjoy both the enhanced photon harvesting by incorporating multiple organic materials in tandem solar cells and simplicity of fabrication conditions that is used in single bulk heterojunction solar cells. Meanwhile, all the strategies for optimizing the performance of single bulk heterojunction solar cells can be also effectively applied in ternary solar cells. The key parameters, V_{OC} , J_{SC} and FF, can be simultaneously or individually optimized to their maximum values by adjusting the donor or acceptor doping ratios, selecting materials for optimized absorption complementary, adjusting phase separation and adopting interfacial layers. Inspiringly, the PCE values of ternary solar cells have exceeded 10%, showing great potential for obtaining high performance ternary solar cells.^{84,85} For further improvement, some fundamental physical issues are needed to be clarified for further investigation, as there is no clear set of structure–function relationships for component selection and the operating mechanism for ternary solar cells. It should be highlighted that several excellent reviews by Brabec's group,⁸⁶ Yu's group,⁸⁷ Thompson's group,⁸⁸ Lin's group,⁸⁹ You's group,⁹⁰ and Zhan's group⁹¹ have summarized the progress in ternary solar cells based on their unique insights. The authors have great

chemistry background, especially in the synthesis of efficient photovoltaic materials. In this review, based on our research experiences in organic optoelectronics device physics, we will try our best to present a comprehensive view of the recent progress and argument on ternary solar cells from different perspectives compared with the early excellent reviews. We first pay more attention on the fundamental physical principles that govern the photovoltaic process in ternary solar cells and the corresponding characterization techniques, such as charge transfer, energy transfer, and parallel-linkage or alloy model. We then discuss and summarize the advantages of ternary solar cells according to the latest literature studies, like efficient strategies for enhanced photon harvesting, phase and morphology adjustment, crystallinity forming and device stability. The current challenges and further prospects on ternary solar cells are also briefly analyzed in the last section.

2 Fundamental principles of ternary solar cells

In general, ternary solar cells contain three components in the active layers: the dominating donor:acceptor (D:A) system and the third component, where the third component can be a polymer, a small molecule, a dye, or a nanoparticle.^{87,92–97} Ternary solar cells can also be classified into three categories according to the function of the third component: two donors/one acceptor ($D_1/D_2/A$),^{98–101} one donor/two acceptors ($D/A_2/A_1$),^{102–105} and donor/nonvolatile additive/acceptor (D/NA/A).^{106–109} The ternary solar cells inherit the major advantages of single junction binary solar cells and tandem configuration solar cells. As shown in Fig. 1, the ternary solar cells based on the $D_1/D_2/A$ system show the advantages of a simple device structure and a wide photon harvesting range. The mechanism that governs the photovoltaic process in ternary solar cells are very different from that of the conventional binary solar cells, which is more than a simple superposition of the photovoltaic process of the individual solar cells. There are four fundamental principles in ternary solar cells: charge transfer, energy transfer, and parallel-linkage or alloy structure, which are closely related to the location of the third component in the ternary active layer (Fig. 1(c)). The third component could: (i) be fully embedded in a donor; (ii) be fully embedded in an acceptor; (iii) locate at the donor/acceptor interface; or (iv) form its own channels. The interactions and intermixing among the three components, the correlation between the location of the third component and fundamental principles, and the relevant characterization methods will be discussed in detail in the following sections according to the latest literature studies.

2.1 Charge transfer

The charge transfer and transport in ternary solar cells are different from those of binary solar cells, which are governed by various mechanisms, such as the content of the third component, electronic energy levels and the bandgap of the three components, and the third component location in the

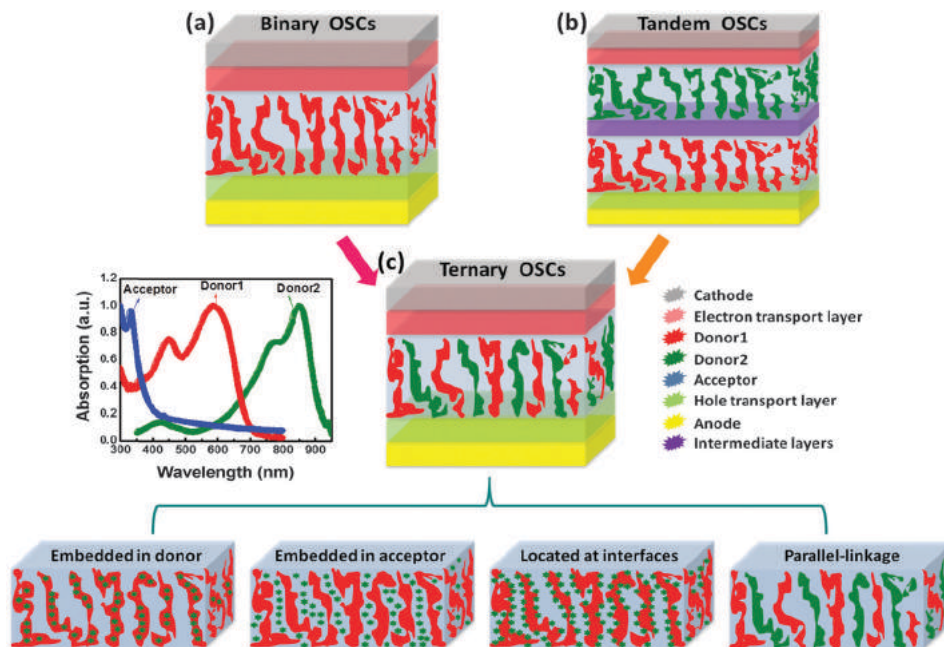


Fig. 1 The schematic configuration of the (a) conventional binary OSCs, (b) tandem OSCs, and (c) ternary OSCs with four possible active layer morphologies according to the location of the third component.

active layer as well as the final microstructure of the active layers. In the case of charge transfer mechanism, since the third component depends on the dominating D:A system to form percolating pathways for charge transfer and transport, the third component molecule should be located at the interface between that of the dominating donor and acceptor (Fig. 1(c)). The selection of the third component is also required that the third component should have suitable energy levels to avoid forming excitons and charge traps in the active layers. For instance, the highest occupied molecular orbital (HOMO) and the lowest unoccupied molecular orbital (LUMO) energy levels of the third component molecule are appropriately located between the corresponding energy levels of the dominating donor and acceptor to form the cascade energy level alignment, respectively.^{110–112} As shown in Fig. 2(a), the excitons generated in donors (D_1 or D_2) can be dissociated into charge carriers at the D_1/A or D_2/A interfaces in the ternary solar cells based on two donors, respectively. These holes can effectively travel to

the anode mainly through the channel formed by one of the donors, and electrons only transport *via* the acceptor domain to the cathode. Furthermore, the charge transfer may occur between donors due to the different energy level alignment. For $D/A_2/A_1$ ternary solar cells (Fig. 2(b)), the electrons on the LUMO energy levels of A_2 can be transferred to the LUMO energy levels of A_1 and then collected by the cathode. Meanwhile, holes can transport *via* the donor channels to the anode.

The location of the third component in the ternary active layer is a crucial factor for the charge transfer mechanism. Only when the third component is located at the interface between the donor and acceptor, the holes or electrons generated in the third component can be efficiently collected by the corresponding electrode through the dominating charge carrier transport channels, as described in Fig. 2. Ohkita *et al.* reported that the third component location in ternary blends is strongly dependent on the surface energy and crystallinity of the dominating system.^{113,114} For the P3HT:PCBM matrix with silicon

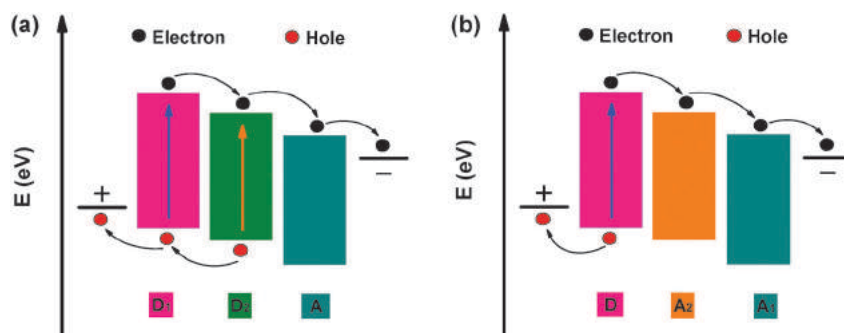


Fig. 2 Schematic of the charge transfer in ternary solar cells based on (a) $D_1/D_2/A$ and (b) $D/A_2/A_1$ systems, the arrows indicate the possible charge carrier transfer and transport pathway.

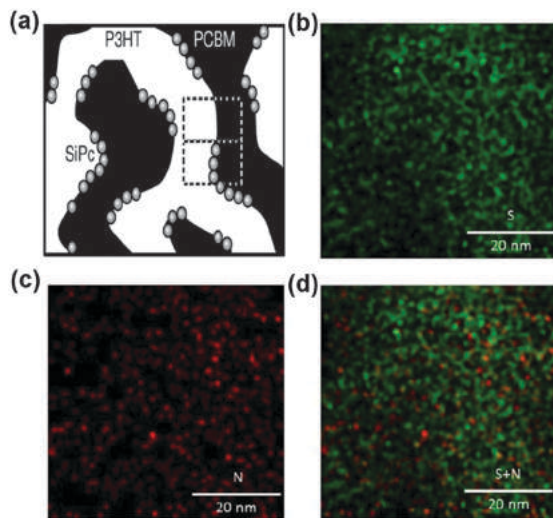


Fig. 3 (a) Schematic of the SiPc at P3HT:PCBM interfaces, highlighted by the dashed rectangles. Reprinted with permission from ref. 114. Copyright 2011 American Chemical Society. TEM energy dispersive X-ray elemental mapping of (b) sulphur indicating P3HT, (c) nitrogen indicating SQ, and (d) sulphur and nitrogen. Reprinted with permission from ref. 115. Copyright 2013, Nature Publishing Group.

phthalocyanine bis(trihexylsilyl oxide) (SiPc) as the third component, the SiPc molecules are likely to be located at the P3HT:PCBM interface due to different surface energy of three components and crystallization of P3HT phases (Fig. 3(a)). The surface energy of SiPc is 23 mJ m^{-2} estimated from the contact angle of pure water on SiPc films, which is close to that of P3HT (20 mJ m^{-2}) rather than that of PCBM (29 mJ m^{-2}). This result suggests that SiPc molecules tend to locate in disordered P3HT domains at the interfaces. Furthermore, the increased crystallinity of P3HT after thermal or solvent annealing can push SiPc from P3HT domains to D/A interfaces. Taylor *et al.* also studied the surface energy of P3HT, PCBM and 2,4-bis[4-(*N,N*-diisobutylamino)-2,6-dihydroxyphenyl] squaraine (SQ) to verify the location of SQ in the ternary system.¹¹⁵ The surface energy of SQ shows an intermediate value (41.5 mJ cm^{-2}) between those of P3HT (27.5 mJ m^{-2}) and PCBM (47.9 mJ m^{-2}), which is

similar to the phenomenon reported by Ohkita *et al.* The SQ location was further affirmed by measuring the transmission electron microscopy (TEM) energy dispersive X-ray elemental mapping of SQ in P3HT:PCBM films. As shown in Fig. 3(b) and (c), the green and red dots indicate sulphur and nitrogen signals, representing P3HT and SQ, respectively. The sulphur map clearly reveals the interconnecting network of P3HT, while the nitrogen map indicates the SQ scattered distribution in the ternary films. Interestingly, the nitrogen signals almost appear adjacent to the sulphur ones, showing that most SQ molecules are situated next to P3HT.

The charge transfer between the donor and the acceptor in ternary solar cells is similar to that in binary solar cells, while the charge transfer between two donors or two acceptors need to be further investigated to clarify the contribution on the performance of ternary solar cells. Photoluminescence (PL) measurement is a convenient tool to probe charge transfer or energy transfer between different materials. Generally, if energy transfer exists between two different bandgap donors, one would expect increased emission intensity for the relatively low bandgap donor with decreased emission intensity for the other donor, considering that the quantum yields of the two donors are similar. On the other hand, if charge transfer occurs between two donors, the emission intensity of one donor would be quenched without increased emission intensity for the other donor. The PL spectra of P3HT:SMPV1 blend films with different SMPV1 doping ratios were investigated to further clarify the charge transfer or energy transfer between P3HT and SMPV1.¹¹⁶ As shown in Fig. 4(a), the P3HT and SMPV1 emission intensity are substantially reduced along with the increase of SMPV1 doping ratios in donors, which indicates that charge carrier transfer occurs between P3HT and SMPV1. Expectedly, the PL spectra of P3HT:SMPV1 blend solutions exhibit a similar varying tendency compared with the PL spectra of blend films with different doping ratios. Zhang *et al.* first proposed another convenient way to verify the charge transfer between two donors by investigating the *J-V* curves of solar cells with two donors as active layers (without the acceptor). The J_{SC} of the solar cells with P3HT:SMPV1 (1 : 1) as the active layers is much larger than that of P3HT-based or SMPV1-based cells, which should be attributed

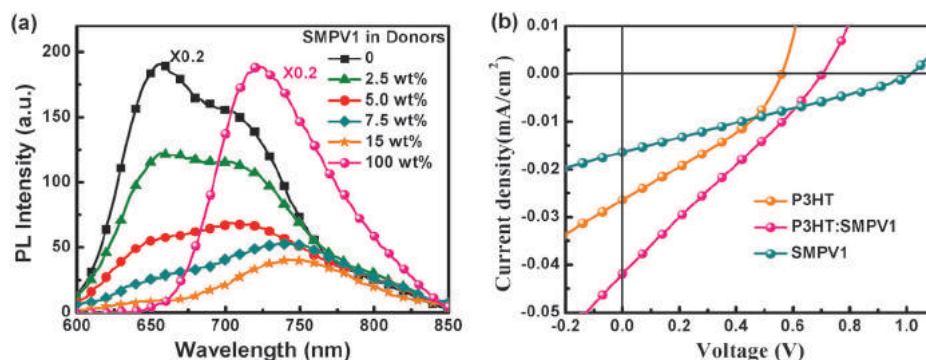


Fig. 4 (a) PL spectra of P3HT:SMPV1 films with different SMPV1 doping ratios under 490 nm wavelength light excitation; (b) *J-V* curves of OSCs with P3HT, SMPV1, and P3HT:SMPV1 (1 : 1) as active layers (without PC₇₁BM) under AM 1.5G illumination at 100 mW cm^{-2} . Reprinted with permission from ref. 116. Copyright 2015 American Chemical Society.

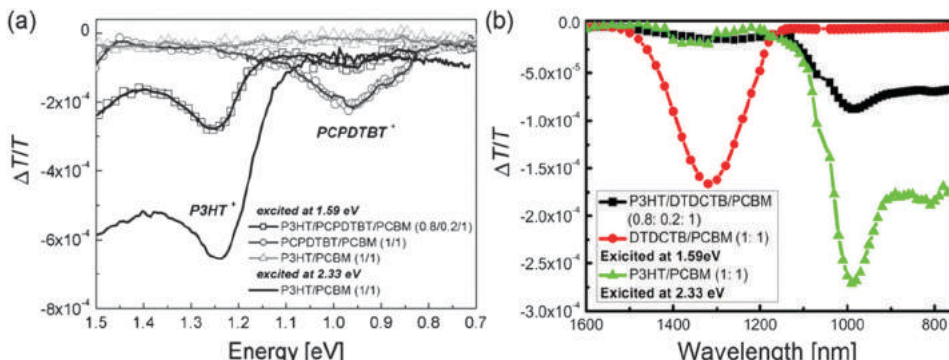


Fig. 5 PIA spectra of annealed thin films of (a) P3HT/PCPDTBT/PCBM (0.8/0.2/1), PCPDTBT/PCBM (1/1) and P3HT/PCBM (1/1), which were all excited at 1.59 eV. P3HT/PCBM (1/1), excited at 2.33 eV, serves as a reference for the spectroscopic position of the P3HT polaron. Reprinted with permission from ref. 118. Copyright 2010 Wiley-VCH. (b) PIA spectra of thin films of P3HT/DTDCTB/PCBM (0.8 : 0.2 : 1) and DTDCTB/PCBM (1 : 1) which were all excited with the pump wavelength of 780 nm and P3HT/PCBM (1 : 1) excited with the pump wavelength of 532 nm serving as a reference for the spectroscopic position of the P3HT polaron. Reprinted with permission from ref. 119. Copyright 2014 American Chemical Society.

to the effective charge carrier transfer between P3HT and SMPV1 (Fig. 4(b)). Yu *et al.* also fabricated a solar cell using only two donors to prove the charge transfer at the donor interfaces, exhibiting a relatively low PCE of 0.051%, and the corresponding low $J_{SC} = 0.192 \text{ mA cm}^{-2}$, $V_{OC} = 0.65 \text{ V}$ and FF = 40.8%.¹¹⁷

Koppe *et al.* employed steady-state photoinduced absorption (PIA) measurement to investigate the charge carrier dynamics in ternary solar cells with P3HT and low bandgap polymer poly-[2,6-(4,4-bis(2-ethylhexyl)-4H-cyclopenta[2,1-*b*;3,4-*b'*]dithiophene)-*alt*-4,7-(2,1,3-benzothiadiazole)] (PCPDTBT) as donors and PCBM as the acceptor.¹¹⁸ Fig. 5(a) shows the PIA spectra of binary blend P3HT/PCBM (1/1) PCPDTBT/PCBM (1/1) and ternary blend P3HT/PCPDTBT/PCBM (0.8/0.2/1) films with different pump energy. The PCPDTBT/PCBM films under the pump energy of 1.59 eV excitation results in the formation of PCPDTBT radical cations. The P3HT/PCBM films cannot be excited by 1.59 eV, while exciting the film at 2.33 eV yields the typical polaron peak of P3HT at 1.25 eV. Interestingly, P3HT/PCPDTBT/PCBM (0.8/0.2/1) films exhibit a pronounced absorption peak at around 1.25 eV under the excitation of 1.59 eV, which suggests that a significant

density of P3HT polaron is generated by photoexcitation of PCPDTBT. In addition, the intensity of the PCPDTBT polaron peak in ternary films is much lower than that of the P3HT polaron peak and the PCPDTBT polaron peak in PCPDTBT/PCBM films. These observations indicate that positive polaron in PCPDTBT can be transferred onto P3HT in ternary solar cells. Xu *et al.* also observed a similar phenomenon in ternary solar cells based on the same materials, as described in Fig. 5(b).¹¹⁹

Furthermore, the charge dynamics in ternary solar cells based on P3HT:PCBM as the dominating system and the low bandgap polymer [(4,4'-bis(2-ethylhexyl)dithieno[3,2-*b*:2',3'-*d*]silole)-2,6-diyl-*alt*-(4,7-bis(2-thienyl)-2,1,3-benzothiadiazole)-5,5'-diyl] (Si-PCPDTBT) as the third component was also systematically studied by Koppe and co-workers.¹¹² Fig. 6 shows the pump-probe spectra of binary blend Si-PCPDTBT/PCBM (1/1) and ternary blend P3HT/Si-PCPDTBT/PCBM (0.7/0.3/1) films during the first 4 picoseconds after selective photoexcitation of Si-PCPDTBT at 785 nm. The pump-probe spectra of binary blend films recorded at 0.2 ps are very similar to that of ternary blend films. In the pump-probe spectra of binary and

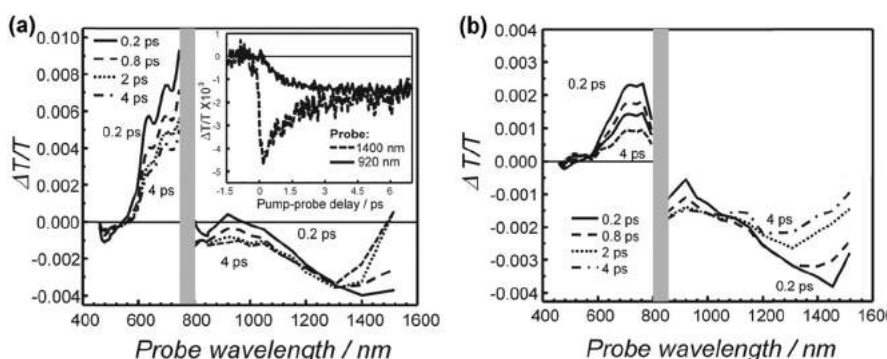


Fig. 6 Pump–probe spectra of (a) binary blend Si-PCPDTBT/PCBM (1/1) and (b) ternary blend P3HT/Si-PCPDTBT/PCBM (0.7/0.3/1) films after pumping at 785 nm. The spectra in the NIR spectral region were obtained by pumping with pulse energies of $7 \mu\text{J cm}^{-2}$. The spectra in the visible region were excited using pulse energies of $70 \mu\text{J cm}^{-2}$. They are normalized to the NIR traces in the overlap region. Inset of (a): Time traces at 920 nm and 1400 nm. Reprinted with permission from ref. 112. Copyright 2013 Wiley-VCH.

the ternary blend films, the PIA band at 1400 nm and the positive band at 900 nm disappear within 4 ps. Both pump-probe spectra of blend films show a PIA band at around 1300 nm after 4 ps. In addition, an additional smaller PIA band at around 1000 nm can be observed from the pump-probe spectra of ternary blend films, which is well known as the $D_2 \leftarrow D_0$ polaron absorption of P3HT films. These observations indicate that the quenching of the Si-PCPDTBT exciton occurs within approximately one picosecond in the both blend films to form a polaron. A significant portion of P3HT and Si-PCPDTBT polaron is formed in even less than 0.2 ps. Subsequently, the positive polaron on Si-PCPDTBT rapidly transfers to P3HT, leading to the depletion of the hole population on the Si-PCPDTBT within few hundreds of picoseconds after the pump pulse. At excitation densities corresponding to steady state conditions under one sun, the efficiency of hole transfer (predicted by model) from the lower bandgap polymer to the higher bandgap polymer exceeds 90%, which well explains why the J_{SC} monotonously increases upon addition of Si-PCPDTBT while the V_{OC} remains constant.

Ameri *et al.* investigated the charge dynamic process in ternary solar cells through transient absorption (TA) spectroscopy experiments.¹²⁰ There are two possible models of charge generation in P3HT:PCPDTBT:PCBM-based ternary solar cells upon exciting PCPDTBT. Fig. 7(a) shows the proposed mechanism of charge separation in ternary films with diffusion in PCPDTBT domains. Initially, the excitons are generated in PCPDTBT, and then the electrons are transferred from PCPDTBT to PCBM, followed by a diffusion of holes in the PCPDTBT domains to PCPDTBT/P3HT interfaces, finally, holes in PCPDTBT are transferred to P3HT, as described in Fig. 7(b). In Fig. 7(c), no diffusion of holes in the PCPDTBT domains is involved in the charge-generation process. In this model, the electrons are transferred from PCPDTBT to PCBM and the holes in the PCPDTBT domains are directly transferred to P3HT without the process of hole diffusion to the PCPDTBT/P3HT interfaces. The two proposed mechanisms of charge separation are confirmed by the results of TAS experiments. One the one hand, hole transfer starts at time faster than 1 ps, which supports the mechanism of direct hole transfer. On the other hand, hole transfer extends, nevertheless, throughout the investigated timescale of 7500 ps containing a dominant component of 140 ps. This observation is consistent with the mechanism of hole transfer upon diffusion.

2.2 Energy transfer

The energy transfer in ternary blend films should be a competing process compared with the charge transfer among the materials.¹¹⁸ It is known that the energy transfer mechanism involved either a dipole-induced coulombic interaction between materials (Förster resonance energy transfer for electrofluorescence) or an electron-exchange interaction between them (Dexter energy transfer for electrophosphorescence).¹²¹ Substantial overlapping of the one material emission spectrum and the other material absorption spectrum was desirable for an efficient energy transfer. The third component could be the “energy donor” or the “energy acceptor” in the ternary solar cells. When the third component only acts as the “energy donor”, all holes are only generated in the dominating donor and the third component works just as a sunlight absorber. The additional absorbers can harvest more photons and transfer these extra photogenerated excited states to the “energy acceptor”, which has been well explained and summarized by You and co-workers.⁹⁰ The location of the “energy donor” only needs to be close to the “energy acceptor” due to the limited radius of energy transfer. However, when the third component works as an “energy acceptor”, it should not only be located near the “energy donor” but should also make contact with a donor or an acceptor to dissociate excitons generated in the “energy acceptor”. Fig. 8 shows the schematic of the energy transfer in ternary solar cells for the third component (D_2 or A_2) as an “energy acceptor”, the arrows indicate a possible charge transfer and transport pathway, and the lightning bolts indicate the potential energy transfer pathway. For ternary solar cells based on the $D_1/D_2/A$ system, exciton energy in D_1 can be transferred to D_2 via the Förster or Dexter energy transfer, and excitons generated in D_2 can be dissociated into charge carriers at the interfaces of D_2/A (Fig. 8(a)). The electrons transport to the cathode through the channels formed by the acceptor and the holes at D_2 can directly transport to the anode or transfer to D_1 and then transport to the anode through the channels formed by D_1 .

The energy transfer can also occur between two acceptors, as reported by Cnops *et al.*¹²² A series of planar heterojunction solar cells were fabricated with α -sexithiophene (α -6T) as a donor and boron subnaphthalocyanine chloride (SubNc) and boron subphthalocyanine chloride (SubPc) as acceptors. Fig. 8(b) presents the pathway of energy transfer, charge transfer and

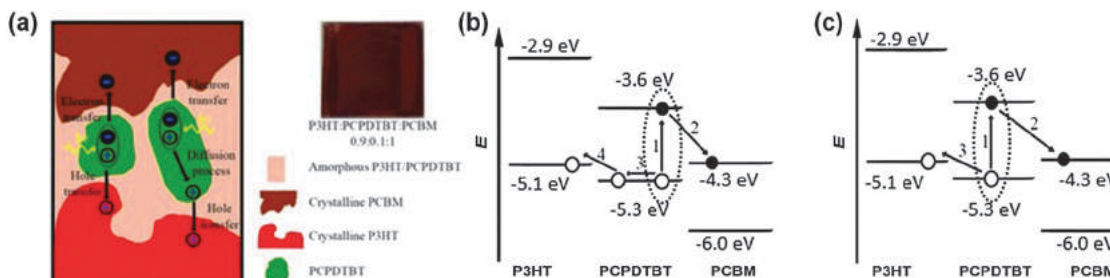


Fig. 7 (a) Schematic diagram of the charge dynamic process in ternary solar cells with a P3HT:PCPDTBT:PCBM matrix; (b) proposed mechanism of charge separation in ternary films with diffusion in PCPDTBT domains; and (c) proposed mechanism of charge separation in ternary films without diffusion in PCPDTBT domains. Reprinted with permission from ref. 120. Copyright 2013 Wiley-VCH.

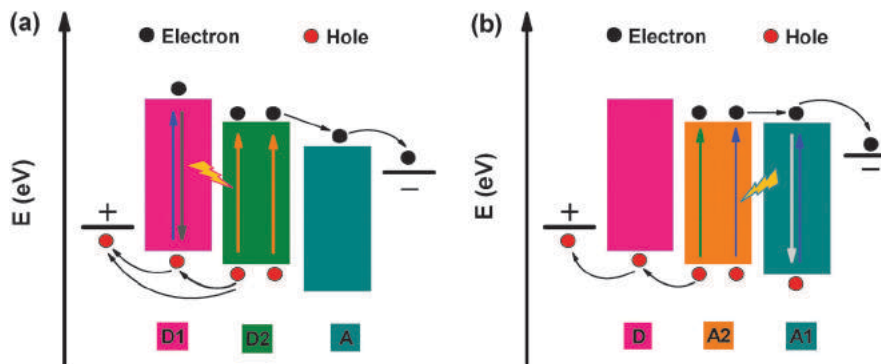


Fig. 8 Schematic of the energy transfer in ternary solar cells based on (a) $D_1/D_2/A$ and (b) $D/A_1/A_2$ system, the arrows indicate the possible charge transfer and transport pathway, and the lightning bolts indicate the potential energy transfer pathway.

transport for the α -6T/SubNc/SubPc ternary solar cells. Excitons generated in the SubPc acceptor can be transferred to the middle SubNc layer and consequently dissociated at the interface of α -6T/SubNc. The holes transfer from SubNc to α -6T and then travel to the anode through α -6T channels. Meanwhile, the electrons in SubNc transfer to SubPc and then are collected by the cathode. In this system, the SubNc layer simultaneously serves as an energy acceptor for excitons generated in the SubPc layer, and as a charge acceptor at the interface with α -6T.

As aforementioned, the energy transfer and charge transfer between two materials can be distinguished through measuring the PL spectra of their blend solutions or individual neat solution. As shown in Fig. 9(a), the PL spectra of P3HT:SQ blend solutions are measured to verify the energy transfer between P3HT and SQ molecules.¹²³ The emission intensity of P3HT significantly decreases while SQ emission intensity continuously increases along with the increasing SQ doping ratios. The emission intensity of the neat SQ solution is weak under 490 nm light excitation, indicating that direct photoexcitation of SQ molecules has hardly occurred. The relatively strong emission intensity of SQ should be attributed to the efficient energy transfer from P3HT to SQ molecules. A similar phenomenon was also observed in the PL spectra of SMPV1:SQ blend solutions and individual neat solutions (Fig. 9(b)).¹²⁴ The neat SMPV1 solution has strong emission intensity with a relatively wide PL emission spectral range from 600 nm to 750 nm, corresponding to an emission peak at 670 nm. The neat SQ solution shows a narrow PL emission spectral range from 660 nm to 690 nm with an emission peak at 680 nm. According to the PL spectra of blend solutions, SMPV1 emission intensity in the range from 600 nm to 650 nm is markedly quenched and emission intensity at 680 nm emission is enhanced along with the increase of SQ doping ratios in donors. The 680 nm emission intensity of blend solutions is much stronger than that of the neat SQ solution under the same excitation conditions, suggesting an efficient energy transfer from SMPV1 to SQ molecules. A series of cells were also fabricated with SMPV1, SQ or SMPV1:SQ as the active layers (without an acceptor), respectively. The J_{SC} of SMPV1:SQ-based solar cells is rather low, even lower than that of SMPV1-based solar cells, suggesting that charge transfer between SMPV1 and SQ should be negligible.

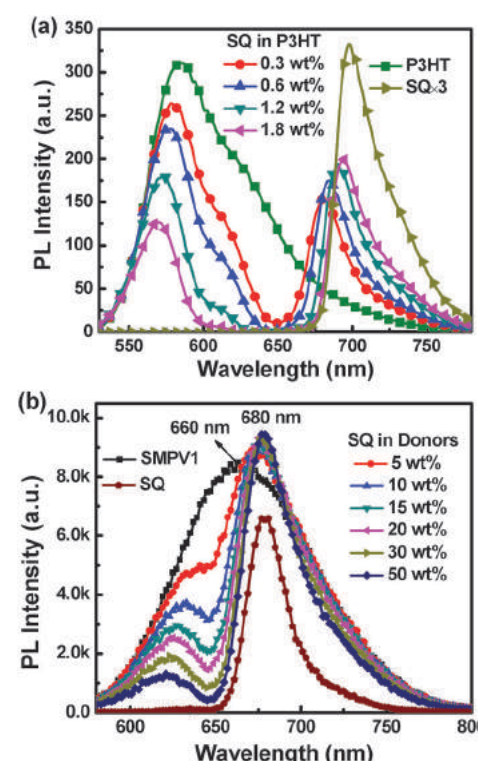


Fig. 9 (a) PL spectra of neat P3HT solution, neat SQ solution and P3HT:SQ co-solutions with different SQ doping ratios under 490 nm light excitation. Reprinted with permission from ref. 123. Copyright 2014 American Chemical Society. (b) PL spectra of SMPV1:SQ solutions with different SQ doping ratios under 500 nm light excitation. Reprinted with permission from ref. 124. Copyright 2015 Royal Society of Chemistry.

The theory of Förster resonance energy transfer (FRET) predicts a decrease in the excited-state lifetime of the FRET donor with increasing FRET acceptor concentrations, as FRET introduces an additional relaxation pathway for the donor excited-states in the ternary blends. The efficiency (η) of energy transfer can be calculated using the formula:¹²⁵

$$\eta = 1 - \frac{\tau_{DA}}{\tau} \quad (2)$$

where τ_{DA} and τ are the lifetimes of the donor in the absence and presence of an acceptor, respectively. The energy transfer between P3HT and SQ was also studied by Taylor and co-workers through the femtosecond fluorescence upconversion technique to measure the lifetime of P3HT and P3HT:SQ blend films (Fig. 10(a)).¹¹⁵ The average lifetime of P3HT was 223 ps for a neat P3HT film and was decreased to 52.4 ps for P3HT:SQ blend films with the addition of 1 wt% SQ, and further to 9.9 ps for P3HT:SQ blend films with 5 wt% SQ. According to formula (2), the energy transfer efficiency reaches up to 77% for the blend films with 1 wt% SQ and 96% for the blend films with 5 wt% SQ. The time-resolved transient photoluminescence (TRTPL) spectra of SMPV1:SQ blend films were also measured by Zhang and co-workers (Fig. 10(b)). The energy transfer efficiency is about 56% or 67% for blend films SMPV1:SQ with a weight ratio of 9:1 or 1:1, respectively. The spectral overlap between SMPV1 emission and SQ absorption also indicates that energy transfer from SMPV1 to SQ should be favourable (Fig. 10(b), inset). The efficient energy transfer can well support the increased EQE values in the short wavelength range for the ternary solar cells with low SQ doping ratios in donors.

Taylor *et al.* further employed TA spectroscopy to simultaneously probe photophysical processes of P3HT and SQ. Fig. 11(a) shows the TA spectra of neat P3HT and P3HT:SQ with 1 wt% SQ and 5 wt% SQ films. For neat P3HT films, the negative signal represents the ground-state bleach (GSB) of P3HT which contains

three peaks at 520, 560 and 610 nm at early times (<10 ps), corresponding to P3HT absorption with $\langle 0-2 \rangle$, $\langle 0-1 \rangle$ and $\langle 0-0 \rangle$ vibrational transitions, respectively. The positive signal (blue in color) at 650 nm represents the photoinduced absorption of the excited states in the P3HT. Another negative signal beyond 700 nm should be associated with stimulated emission of P3HT. For the TA spectra of P3HT:SQ blend films with 1 or 5 wt% SQ, the color at 665 nm is changed from blue to green, suggesting a sign change of the TA signal. This negative signal is identified as the GSB of SQ, indicating that the SQ is being excited. Because the SQ absorption at 500 nm is very weak, the excitation of SQ is almost certainly not caused by the pumping wavelength but by the excited P3HT. Meanwhile, signals of the photoinduced absorption and stimulated emission in P3HT both substantially decayed to zero. These observations suggest that the excitation energy is successfully transferred from P3HT to SQ molecules. A similar phenomenon was also observed in co-evaporated films with 2,4-bis-[*N,N*-diisobutylamino]-2,6-dihydroxyphenyl]-4-(4-diphenyliminio) squaraine (ASSQ) and SQ as active layers.¹²⁶ The GSB of SQ can be observed almost immediately after excitation (~1 ps), which reveals that the energy transfer of excitons from P3HT to SQ is very rapid. This was further confirmed by evaluating the TA dynamics with a global fitting procedure *via* singular-value decomposition (Fig. 11(b)). At early times, both samples with SQ show positive amplitude coefficients (at 2.8 ps for 1 wt% SQ and at 0.6 ps for 5 wt% SQ) at 665 nm, indicating a rise of the SQ GSB feature. The negative values in the region from 500 to 620 nm indicate the decay in the P3HT excited-state population. This result is also linked to energy transfer from P3HT to SQ molecules. Gupta also reported a similar phenomenon in ternary solar cells with two polymers as donors by measuring the TA spectra of neat and blend films.¹²⁷

Zhang *et al.* also proposed an efficient strategy to clarify the energy transfer from SMPV1 to SQ molecules based on three kinds of planar heterojunction solar cells,¹²⁴ as follows:

- Cells A: ITO/PEDOT:PSS/SMPV1/PCBM/Al;
- Cells B: ITO/PEDOT:PSS/SQ/PCBM/Al;
- Cells C: ITO/PEDOT:PSS/SMPV1/SQ/PCBM/Al.

The thickness of SMPV1 films prepared by the spin-coating method, and SQ and PCBM films prepared by thermal evaporation is about 40 nm, 20 nm and 20 nm, respectively. The elaborate control of each layer thickness is to investigate the energy or charge transfer between SMPV1 and SQ due to the limited exciton diffusion distance (~10 nm). The excitons in cells A or B can be dissociated at the SMPV1/PCBM interface or SQ/PCBM interface, respectively. For cells C, excitons generated in SQ can be directly dissociated at the interfaces of SQ/PCBM. Whereas, excitons generated in SMPV1 only can be transferred to SQ by FRET and then dissociated at SQ/PCBM interfaces because of exciton dissociation at SMPV1/SQ interfaces can be negligible, as marked in Fig. 12(a). The energy transfer from SMPV1 to SQ molecules can be further confirmed by comparing the EQE spectra of three kinds of cells. The EQE values in the range from 300 nm to 500 nm are mainly attributed to the contribution of SMPV1 and PCBM, which can be certified by the absorption spectra of each material,

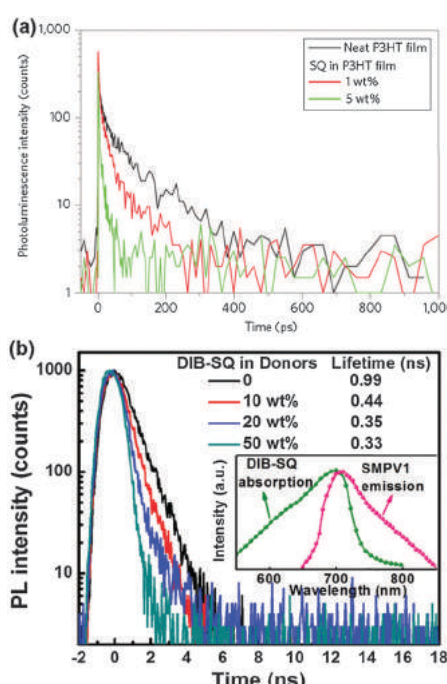


Fig. 10 (a) Time-resolved transient photoluminescence (TRPL) spectra of neat P3HT film, and P3HT:SQ blend films with 1 and 5 wt% SQ. Reprinted with permission from ref. 115. Copyright 2013, Nature Publishing Group. The TRPL spectra of (b) SMPV1:SQ films with different SMPV1 doping ratios (monitored at 705 nm), inset: the absorption spectrum of SQ film and the emission spectrum of SMPV1 film. Reprinted with permission from ref. 124. Copyright 2015 Royal Society of Chemistry.

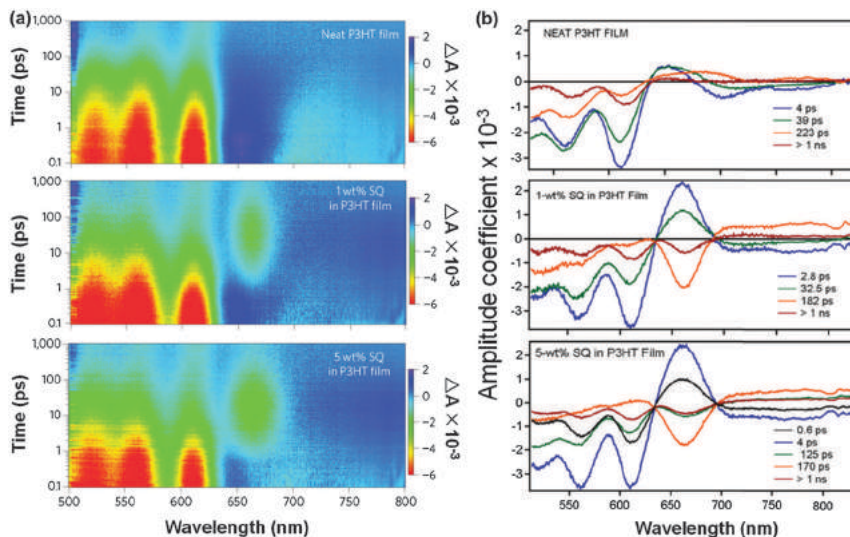


Fig. 11 (a) Transient absorption (TA) spectra of neat P3HT, P3HT:SQ with 1 wt% SQ and 5 wt% SQ, the pumping wavelength was 500 nm with a fluence of 8 mJ cm^{-2} ; (b) amplitude coefficient spectra from global fit of TA spectra of P3HT:SQ films. Reprinted with permission from ref. 115. Copyright 2013, Nature Publishing Group.

as shown in Fig. 12(b). The EQE values of cells C are relatively larger than that of cells B in this short wavelength range from 300 nm to 500 nm, suggesting the efficient energy transfer from SMPV1 to SQ molecules and then further exciton dissociation at the interfaces between SQ and PCBM molecules.

Based on the planar heterojunction ternary solar cells, Cnops *et al.* presented a strategy with a three-layer structure based on α -6T/SubNc/SubPc to certify the energy transfer from

SubPc to SubNc.¹²² A high bandgap material 4,40-bis(*N*-carbazolyl)-1,10-biphenyl (CBP) was used as the spacer layer to spatially separate the donor and the acceptor. The exciton quenching caused by direct charge transfer at the interface should be suppressed due to the existence of a spacer layer, while the long-range energy transfer across the transparent spacer layer is still possible. The energy transfer efficiency can be evaluated from the PL quenching for different spacer thicknesses. Fig. 13 shows the PL spectra of organic layer stacks with different spacer layer thicknesses. The emission spectrum of SubPc consists of two distinct peaks centered at 620 nm and 710 nm. The small molecule C_{60} is used as a quenching layer, and the energy transfer from SubPc to C_{60} is negligible due to limited overlap between the C_{60} absorption and SubPc emission, which is used as the expected control structure. It is obvious that the SubPc PL signal can be substantially quenched by a SubNc layer compared with a C_{60} quenching layer. This result suggests that the energy transfer from SubPc to SubNc is very efficient and long-range interlayer exciton transfer is also possible. Furthermore, the PL signal can be still effectively quenched by SubNc for the spacer layers up to 35 nm.

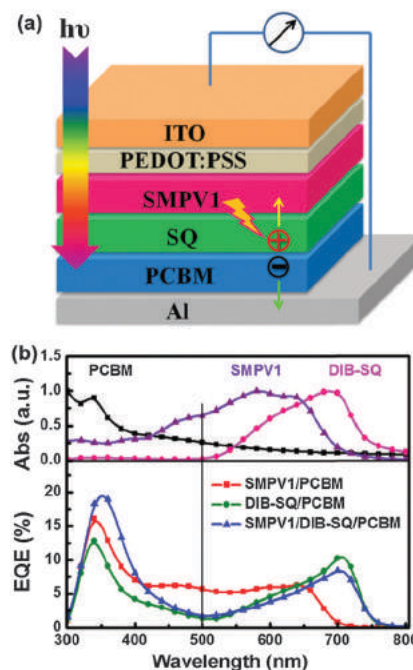


Fig. 12 (a) Schematic diagram of planar heterojunction solar cells and (b) the EQE spectra of planar heterojunction solar cells and the absorption spectra of neat PCBM, SMPV1 and SQ films. Reprinted with permission from ref. 124. Copyright 2015 Royal Society of Chemistry.

2.3 Parallel-linkage or the alloy model

The parallel-linkage mechanism of ternary solar cells is significantly different from the charge transfer and energy transfer mechanisms, which does not require accurate engineering of locations, energy levels and band gaps of all involved materials (including the dominating donor and acceptor, as well as the third component), to ensure efficient charge transfer or energy transfer. For $D_1/D_2/A$ ternary solar cells with the parallel-linkage mechanism, the excitons generated in each individual donor domain would migrate to the respective donor/acceptor interface and then dissociate into free electrons and holes. As shown in Fig. 14(a), these generated holes are transported through

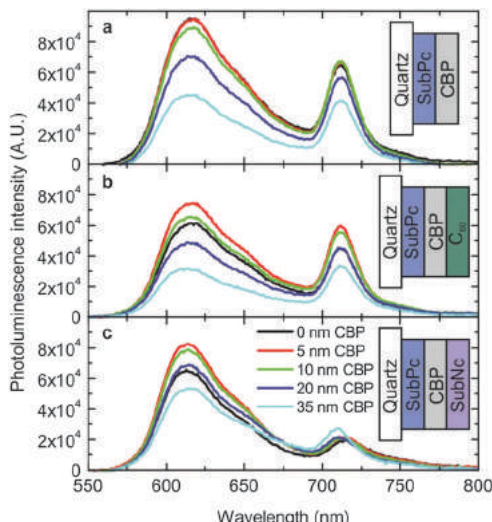


Fig. 13 PL spectra of organic layer stacks deposited on quartz substrates for different spacer layer thicknesses (x nm BCP). (a) 20 nm SubPc/ x nm CBP, (b) 20 nm SubPc/ x nm CBP/10 nm C_{60} , and (c) 20 nm SubPc/ x nm CBP/10 nm SubNc. Reprinted with permission from ref. 122. Copyright 2013, Nature Publishing Group.

their corresponding donor channels to the anode and electrons still transport *via* the acceptor channels to the cathode as in normal binary solar cells. For the ternary solar cells with two acceptors (Fig. 14(b)), the excitons generated in the donor domain can be dissociated into free electrons and holes at the D/A₁ or D/A₂ interfaces. The holes should be transported

only *via* the donor channels to the anode and electrons should be transported to the cathode through the two parallel channels formed by the two acceptors. In the parallel-linkage ternary solar cells, either energy transfer or charge transfer is absent between two donors or two acceptors, equivalent to a parallel connection of two individual binary solar cells.

The parallel-linkage mechanism in ternary solar cells can also be verified from the PL spectra of the corresponding neat films or blend films. Fig. 15(a) presents the PL spectra of poly{4,8-bis[(2-ethylhexyl)-oxy]benzo[1,2-*b*:4,5-*b*]dithiophene-2,6-diyl-*alt*-3-fluoro-2-[(2-ethylhexyl)carbonyl]thieno[3,4-*b*]thiophene-4,6-diyl} (PTB7) and PBDT-TS1 blend films with different PBDT-TS1 doping ratios (excited at 660 nm). Emission intensity of PTB7:PBDT-TS1 blend films can be gradually enhanced in the range from 750 nm to 850 nm along with the increase of PBDT-TS1 doping ratios in donors. The emission peak of the blend films is located between that of neat PTB7 and PBDT-TS1 film, which indicates neither charge transfer nor energy transfer exists between PTB7 and PBDT-TS1 molecules. Fig. 15(b) shows the *J-V* curves of solar cells with PTB7, PBDT-TS1 or PTB7:PBDT-TS1 (1 : 1) as active layers (without acceptors). The J_{SC} of PTB7:PBDT-TS1 is in between that of PTB7-based or PBDT-TS1-based solar cells, suggesting that the charge transfer between PTB7 and PBDT-TS1 molecules should be negligible. The limited spectral overlap between PTB7 emission and PBDT-TS1 absorption (or PTB7 absorption and PBDT-TS1 emission) further indicates the energy transfer between PTB7 and PBDT-TS1 molecules can be negligible.

The parallel-linkage ternary solar cells was first reported by You and co-workers.¹²⁸ Two groups of polymers were selected to demonstrate the parallel-linkage mechanism of ternary solar cells: (1) poly(benzodithiophene-dithienylbenzotriazole) (TAZ) and poly(benzodithiophene-dithienylbenzothiadiazole) (DTBT) and (2) poly(benzodithiophene-dithienylthiadiazolopyridine) (DTPyT) and poly-(benzodithiophene-dithienyldifluorobenzothiadiazole) (DTffBT). Each group contains two polymers with different bandgaps and energy levels. For the purpose of comparison, the thicknesses of active layers were fixed as 100 nm for all ternary solar cells (TAZ/DTBT/PCBM = 0.5 : 0.5 : 1 and DTffBT/DTPyT/PCBM = 0.5 : 0.5 : 1) and 50 nm for all binary solar cells (polymer/PCBM = 1 : 1). It is obvious that the absorption spectra of ternary films are essentially linear combinations of the spectra of their corresponding two binary solar cells (Fig. 16(a) and (b)). For better understanding, 50 nm thick binary solar cells were named as “sub-cells”. Interestingly, the ternary films exhibit much broader absorption width than the absorption of high bandgap donor-based “sub-cells” and significantly increased absorption strength in the low-wavelength regions relative to the low bandgap donor-based “sub-cells”. As shown in Fig. 16(c) and (d), the EQE spectra of the ternary solar cells are approximately the sum of the individual “sub-cells” in the short wavelength range, where both donors contribute to the formation of excitons as well as photocurrent. This result suggests that most of the free charge carriers generated in each “sub-cell” of the ternary solar cells can be successfully collected by the respective electrodes. In the long-wavelength range,

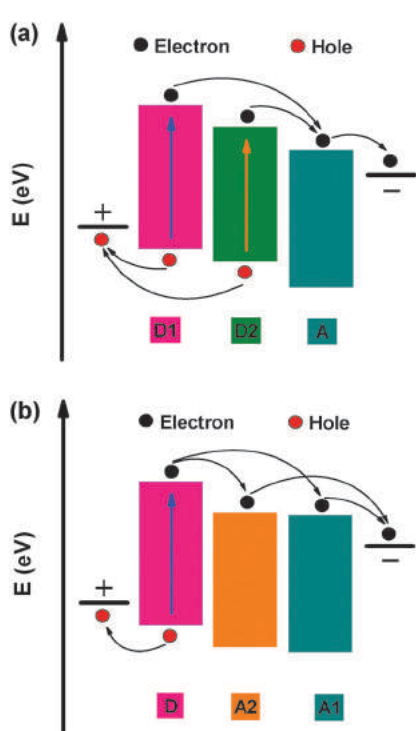


Fig. 14 Schematic of the parallel-linkage mechanism in ternary solar cells based on (a) $D_1/D_2/A$ and (b) $D/A_1/A_2$ systems, the arrows indicate the possible charge transfer and transport pathway.

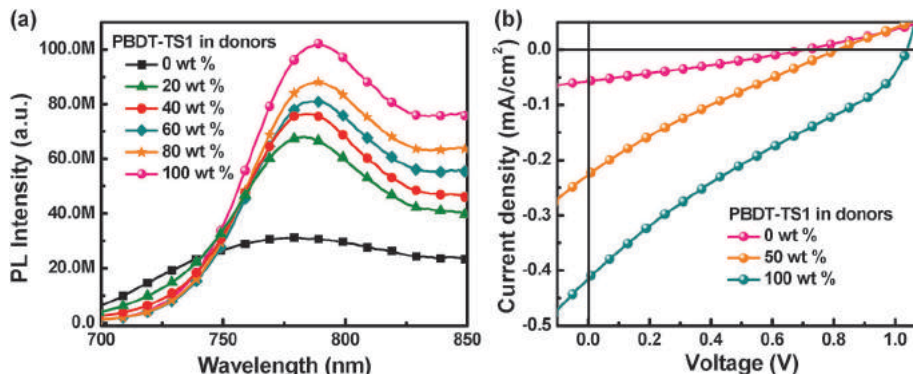


Fig. 15 (a) PL spectra of PTB7:PBDT-TS1 films with different PBDT-TS1 doping ratios under 660 nm wavelength light excitation and (b) J - V curves of solar cells with PTB7, PBDT-TS1, and PTB7:PBDT-TS1 (1:1) as active layers (without PC₇₁BM) under AM 1.5G illumination at 100 mW cm⁻².

the EQE of ternary solar cells is higher than the sum of EQE of the larger bandgap “subcell” and the lower bandgap “subcell”, which should attribute to an additional charge transport channel served by the larger bandgap donor in ternary solar cells. The EQE spectra of both ternary solar cells are markedly enhanced (over 40% across a width of over 400 nm) compared with their corresponding single “sub-cells”. As a result, the J_{SC} values of the ternary solar cells are significantly increased and almost equal to the sum of those for the two single “sub-cells” (Fig. 16(e) and (f)). The V_{OC} values of the parallel-linkage ternary solar cells are in between the measured value for the individual “sub-cells”, which are much different from that in ternary solar cells with the charge transfer or energy transfer mechanism, where the observed V_{OC} is close to the smaller V_{OC} of the corresponding “sub-cells”. In the ternary solar cells with the charge transfer or energy transfer mechanism, the hole transport and collection are mainly through the channels formed by the donor with the highest HOMO level. Therefore, the V_{OC} of parallel-linkage ternary solar cells is determined by the highest HOMO level. For parallel-linkage ternary solar cells, neither the energy transfer nor the charge transfer is dominant between different donor materials. The holes generated from the individual donor mainly travel to the anode *via* their corresponding channels, similar to the parallel connection of two single-junction binary solar cells. Consequently, the observed J_{SC} combines those from each “sub-cells”, whereas the V_{OC} is in between that of the single “sub-cells”, both of which clearly indicate parallel-linkage ternary solar cells.

Yang *et al.* reported a series of ternary solar cells based on a pool of donors with different absorption ranges, including P3HT, PTB7, poly[4,8-bis-substitutedbenzo[1,2-*b*:4,5-*b*]dithiophene-2,6-diyl-*alt*-4-substituted-thieno[3,4-*b*]thiophene-2,6-diyl] (PBDTTT-C), poly{2,6-4,8-di(5-ethylhexylthienyl)benzo[1,2-*b*;3,4-*b*]dithiophene-*alt*-5-dibutyloctyl-3,6-bis(5-bromothiophene-2-yl)pyrrole[3,4-*c*]-pyrrole-1,4-dione} (PBDTT-DPP) and poly{2,6'-4,8-di(5-ethylhexylthienyl)benzo[1,2-*b*;3,4-*b*]dithiophene-*alt*-2,5-bis(2-butylcetyl)-3,6-bis(selenophene-2-yl)pyrrolo[3,4-*c*]pyrrole-1,4-dione} (PBDTT-SeDPP).¹²⁹ The study clearly shows that the compatible donors (similar molecular orientation to the substrate, crystallinity and domain size) can coexist harmoniously in ternary

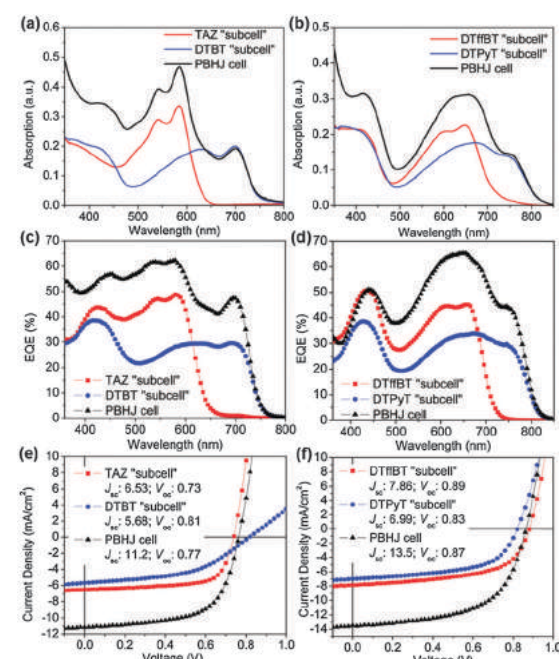


Fig. 16 Absorption spectra of the parallel-linkage ternary solar cells based on (a) TAZ/DTBT and (b) DTffBT/DTPyT, and their “sub-cells”; EQEs of the parallel-linkage ternary solar cells based on (c) TAZ/DTBT and (d) DTffBT/DTPyT, and their “sub-cells”; characteristic J - V curves of the parallel-linkage ternary solar cells based on (e) TAZ/DTBT and (f) DTffBT/DTPyT, and their “sub-cells”. Reprinted with permission from ref. 128. Copyright 2012 American Chemical Society.

solar cells and contribute to an improved performance, but use of two blended donors with incompatible physical natures leads to severe molecular disorder and limited device performance. For instance, the ternary solar cells with P3HT:PBDTT-DPP:PC₇₁BM or P3HT:PBDTT-SeDPP:PC₇₁BM as the active layer present much broader photocurrent response, but do not produce an overall enhanced photocurrent compared with that of the corresponding binary solar cells. Additionally, the FF values of the ternary solar cells are much lower than that of binary solar cells. In other words, additional absorption has no contribution to the performance of ternary solar cells. These results mainly ascribe to the

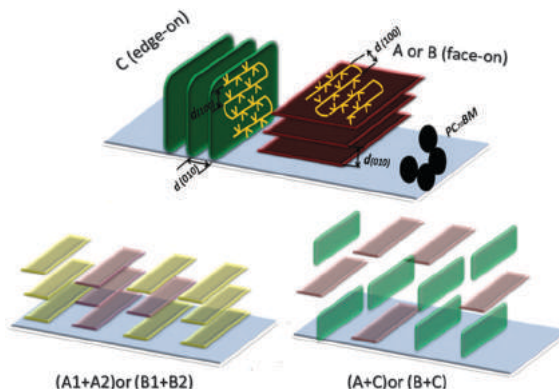


Fig. 17 Schematic diagram of local molecular packing in different polymer blending systems. Reprinted with permission from ref. 129. Copyright 2015, Nature Publishing Group.

incompatible physical natures between P3HT and PBDTT-DPP or P3HT and PBDTT-SeDPP. It is well known that the P3HT tends to form edge-on lamellae in P3HT:PCBM blend films and the low bandgap donors, PBDTTT-C, PBDTT-DPP, PTB7 and PBDTT-SeDPP, generally show face-on molecular orientation due to their similar molecular structures. As shown in Fig. 17, when two donors with different molecular orientation are mixed, such as the P3HT:PBDTT-DPP blend system, the non-conductive side chain of one donor prefers to be close to the conductive conjugated backbone of the other donor. This unfavourable molecular pattern produces 'morphological traps', and then

reduces the crystalline length, disrupts long-range charge transport and lowers the charge carrier mobility of the blended film. The compatible donors show the same molecular orientation and can coexist harmoniously. As expected, the ternary solar cells based on two compatible donors can provide excellent device performance even under relatively large doping ratios for donors.

The grazing incidence wide angle X-ray scattering (GIWAXS) was employed by Yang and co-workers to explore the correlation between electronic properties and structural information of the compatible donors. The GIWAXS is sensitive to the crystalline parts and provide unique insights on the crystal structure and the orientation of the crystalline regions in the active layers.¹³⁰ As shown in Fig. 18, the compatible donors, PBDTTT-C, PBDTT-DPP, PTB7 and PBDTT-SeDPP, show face-on molecular orientation and P3HT show edge-on orientation. When two compatible donors are mixed together, such as PBDTTT-C:PBDTT-DPP blend films, the molecular ordering can be well maintained in the blend films. However, the molecular ordering of both in-plane direction and the vertical direction may be significantly disturbed for the blend films with incompatible donors (P3HT:PBDTT-DPP or P3HT:PBDTTSeDPP). The molecular disorder introduced by mixing of incompatible polymers is very likely one of the key physical origins of electronic traps and recombination centres, and then limits the device performance of ternary solar cells. The resonant soft X-ray scattering (RSoSXS) profiles of compatible and incompatible ternary blend films were measured to clarify the influence

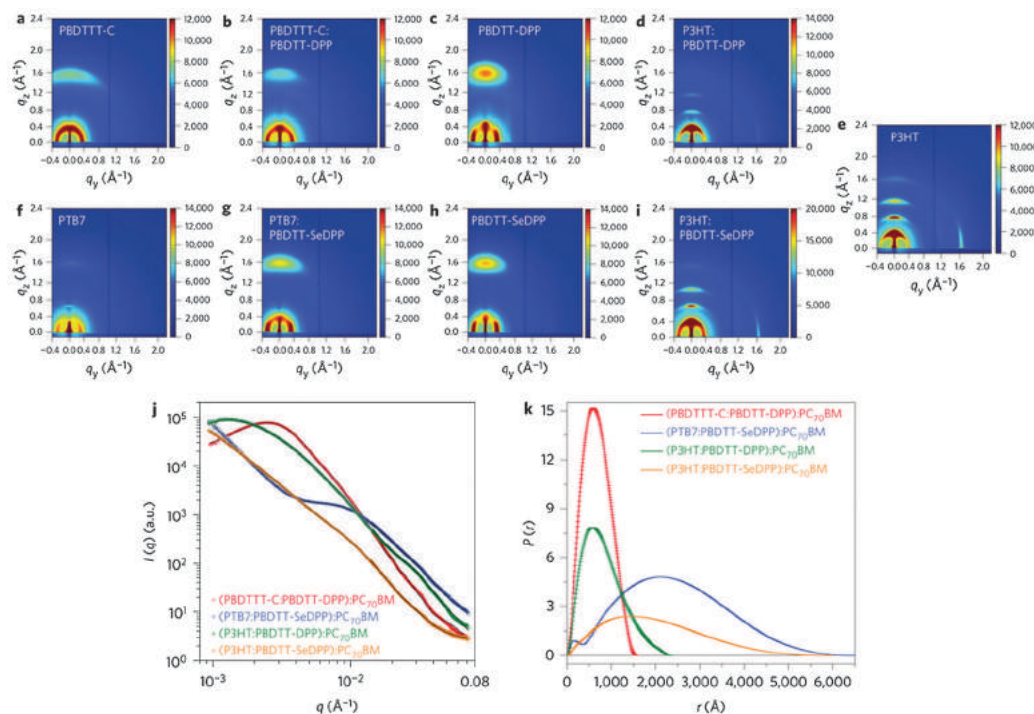


Fig. 18 GIWAXS patterns of (a) PBDTTT-C, (b) PBDTTT-C:PBDTT-DPP, (c) PBDTT-DPP, (d) P3HT:PBDTT-DPP, (e) P3HT, (f) PTB7, (g) PTB7:PBDTT-SeDPP, (h) PBDTT-SeDPP, and (i) P3HT:PBDTT-SeDPP. Each color scale is a measure of intensity, in units of counts. (j) RSoSXS profiles (open symbols) and calculated $I(q)$ (solid lines). (k) Corresponding $P(r)$ of PBDTTT-C:PBDTT-DPP:PC₇₀BM, PTB7:PBDTT-SeDPP:PC₇₀BM, P3HT:PBDTT-DPP:PC₇₀BM and P3HT:PBDTT-SeDPP:PC₇₀BM. Reprinted with permission from ref. 129. Copyright 2015, Nature Publishing Group.

of molecular crystals and aggregates on device performance. As indicated in Fig. 18(j) and (k), the compatible ternary blend films (P3HT:PBDTT-DPP:PC₇₁BM and P3HT:PBDTT-SeDPP:PC₇₁BM) exhibit much larger domain sizes than that of incompatible blend films, which correlate with their unsatisfactory device performance, especially their low J_{SC} . The best performing PTB7:PBDTT-SeDPP:PC₇₁BM-based ternary solar cells show the smallest domains than those in other ternary blended films, which has direct relation to the enhanced exciton dissociation and photocurrent. Taken together, the GIWAXS and RSoXS results suggest that mixing of compatible donors has no significant effect on the molecular stacking preferences, and even the crystallite size and the domain structure can be well retained. The electronic properties of the donors can be well preserved in the ternary solar cells and two different donors can coexist in harmony and contribute to an improved photovoltaic performance by broadening the photon harvesting range and enhancing the photon harvesting ability of ternary active layers.

Thompson *et al.* proposed another model to explain the phenomenon that was observed in parallel-linkage ternary solar cells (improved J_{SC} and tunable V_{OC}), named as the alloy model.^{131–135} Instead of each component forming its own independent charge carrier transport network illustrated by the parallel-linkage mechanism, the alloy model means that two electronically similar components in the ternary active layers (two donors or two acceptors) form an electronic alloy with the same frontier orbital (HOMO and LUMO) energies based on the average composition of these two components, similar to the variation of valence and conduction band energies with composition in inorganic semiconductor alloys (Fig. 19). However, the optical absorption of the exciton states cannot reflect the average composition in the ternary films, but retains the individual molecular properties of the two donors or two acceptors across the blend composition. This difference mainly results from the highly localized molecular nature of the exciton and the more delocalized intermolecular nature of electrons and holes that reflect the average composition of the alloy states between two donors or two acceptors. As a result, the V_{OC} of the ternary solar cells varies gradually as the composition of donors or acceptors changes, while the J_{SC} can be increased due to the complementary absorption of the used donors or acceptors in the ternary active layers. The alloy model generally requires the donors or acceptors with good miscibility and compatibility for obtaining high efficiency ternary solar cells, which will be discussed in more detail in Section 3.2: adjusting open circuit voltage.

As discussed above, the fundamental mechanisms of ternary solar cells, charge transfer, energy transfer, and the parallel-linkage or alloy model, are distinctly different from each other. There may be one or more mechanisms that govern the photovoltaic process in one ternary solar cell. More importantly, each mechanism has its own advantages and limitations. For the charge transfer mechanism, a cascade energy level alignment is necessary to reduce the charge transfer barrier within the active layer, and to ensure efficient exciton dissociation and charge transport to the corresponding electrodes. The charge transport

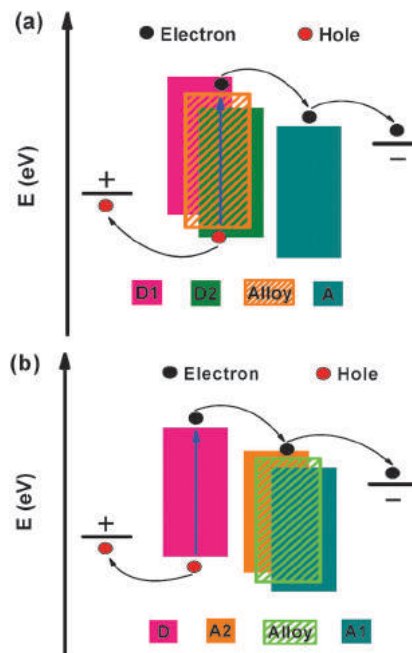


Fig. 19 Schematic of the alloy model in ternary solar cells based on (a) D₁/D₂/A and (b) D/A₁/A₂ systems, the rectangle included sparse diagonal represents a new charge transfer state and the arrows indicate the possible charge transfer and transport pathway.

mainly relies on the pathways formed by the dominating system, the amount of the third components is generally less than 20% in most systems to avoid forming exciton or charge traps. Thus, the third components should have a high absorption coefficient to ensure harvest enough photons with limited content. The energy transfer may occur between different bandgap materials due to their energy level alignment. The third component can act as the “energy donor” or the “energy acceptor” in the ternary solar cells dominated by the energy transfer mechanism. The exciton energy generated in large bandgap materials can be transferred to the low bandgap materials and excitons dissociate at the low bandgap donor/acceptor interface. The charge transport in ternary solar cells governed by energy transfer also relies on the dominating system. The efficient energy transfer between two components generally requires substantial overlap of the one material emission spectrum and another material absorption spectrum, while the overlap of two kinds of spectra is not the sufficient condition for the energy transfer to occur. For example, Lu *et al.* demonstrated that although the emission of the third component matches well with the absorption of the primary donor polymer, the dominating mechanism is charge transfer but not energy transfer for the ternary solar cells.¹¹⁷ For the parallel-linkage or alloy model, the ternary solar cells may realize an increased J_{SC} and an intermediate, composition-dependent V_{OC} compared with the corresponding binary solar cells.^{136,137} The third component doping ratios can arrive to relatively high levels for efficiently harvesting different energy photons, regardless of their energy level alignment. The trade-off photon harvesting in the whole spectral range is the key issue for performance improvement of ternary solar cells according

to the absorption coefficient and absorption range of materials. In order to form parallel-linkage or alloy ternary solar cells, the two donors or two acceptors should have similar chemical and physical natures for good compatibility and miscibility.

3 Key functions of the third component

As aforementioned, there are mainly five fundamental physical processes occurring in OSCs: (i) photon harvesting and exciton generation; (ii) exciton diffusion to the D/A interface; (iii) exciton dissociation at the D/A interface to form free charge carriers; (iv) charge carrier transport; and (v) charge carrier collection by the individual electrode. The number of photons harvested by the active layer is mainly determined by the absorption coefficient and the absorption range of the used materials and the thickness of the active layers. Typical organic semiconducting materials generally have higher absorption coefficient (*ca.* 10^{-4} – 10^{-5} cm $^{-1}$) than that of the conventional inorganic semiconducting materials.¹³⁸ Whereas, the narrow molecular orbital energy level of organic semiconductors makes it very difficult to realize broad plateau absorption coverage with a single organic semiconductor. Normally, the full width at half maximum of the absorption spectrum is about 100 nm for the common organic materials. It is known that the broad and strong absorption spectrum of the active layers should be beneficial to harvesting more photons from the sunlight. Only the photons with energies higher than the bandgap of organic semiconducting materials can be harvested by the materials and then an oppositely charged electron–hole pair is created. Because of a relatively small dielectric constant of the organic semiconducting materials, the electron–hole pairs are strongly bound as a result of their mutual Coulomb interaction, and termed as excitons. The binding energy of the excitons is substantially larger than the thermal energy (about 26 meV at room temperature), implying that the spontaneous dissociation of the exciton could not occur under room temperature conditions. The exciton can be dissociated at donor/acceptor interfaces by energetic driving force which is attributed from the difference between the LUMO or the HOMO energy levels of the donor and the acceptor. In fact, excitons have a diffusion process in the active layers. However, the exciton diffusion length is rather short (about 10 nm), if excitons cannot diffuse to donor/acceptor interfaces, which will not make any contribution on the performance of solar cells.¹³⁹ The exciton diffusion length, the D/A interface area and the energy level offset are of great significance for exciton dissociation efficiency. After exciton dissociation at the D/A interface, electrons are transferred into the acceptor phase and then transported to the cathode *via* the channels formed by acceptors through the hopping mechanism. The holes remain in the donor domains and then transport to the anode through the channels formed by donors. The transport of charge carriers in the active layers strongly depends on the phase separation degree, trap density and domain size, the difference between the work function of anode and cathode provides the driving force for the charge carrier

transport in the active layers. The charge carrier collection strongly relies on the properties of contact between the active layers and electrodes. Thus, the surface topography of the active layers and interfacial layers also plays a vital role in obtaining high performance OSCs. The interfacial engineering is one of the key physical issues in thin film organic electronic devices.

Each of the fundamental process occurring in OSCs could become a bottleneck to limit the efficiency of solar cells. Thus elegant strategies need to be developed to optimize these processes for developing high performance OSCs. It has been commonly demonstrated that the ternary strategy plays an essential role in achieving high performance OSCs (Table 1), which combines the benefits of the extended light absorption range in tandem solar cells and simplicity of processing technology used in single-junction OSCs. In addition, the cascade energy level alignment in ternary solar cells can facilitate charge transport and collection, as well as nanomorphology of the active layer also can be optimized by ternary strategy with a rational design. Among the successful cases, the selection of the third component is rather wide open (Fig. 20), which offers considerable opportunities for solar cell optimization. More detailed discussion about the effect of ternary strategy on the performance of the OSC cells will be presented in the following sections.

3.1 Enhancing short circuit current (J_{SC})

A broader and stronger absorption of the active layer is beneficial to harvest more photons from the solar light, which is a crucial prerequisite for obtaining high efficiency OSCs. Minnaert *et al.* reported that the single-junction OSCs have potential to reach a PCE of 15.2% by expanding the absorption spectrum to an optimistic width of 400 nm.¹⁵⁰ However, the intrinsic narrow absorption width of the organic materials limits the improvement on the efficiency of OSCs. A wide absorption spectrum of the active layer could be achieved by employing ternary strategy with absorption spectral complementary materials. The J_{SC} can be calculated from the EQE spectrum and the AM 1.5G solar spectrum using the equation:

$$J_{SC} = \frac{q}{hc} \int_{\lambda_1}^{\lambda_2} \text{EQE}(\lambda) \cdot P_{in}(\lambda) \cdot \lambda d\lambda \quad (3)$$

where q is the elementary charge, h is Plank's constant, c is the speed of light, λ_1 and λ_2 are wavelength limits of the EQE spectrum, $\text{EQE}(\lambda)$ is the external quantum efficiency as a function of wavelength (λ), and $P_{in}(\lambda)$ is spectral irradiance under standard AM 1.5G solar illumination. The J_{SC} values that are calculated from the EQE and the $J-V$ results support each other in the same experiments. Furthermore, the contribution of the enhanced photon harvesting by the third component to the photocurrent can be further confirmed from the EQE spectra of ternary solar cells.

In 2010, Koppe *et al.* incorporated a low bandgap polymer PCPDTBT into the dominating P3HT:PCBM system to extend the spectroscopic response into the near infrared region (NIR).¹¹⁸

Table 1 Non-exhaustive survey of reports about the ternary solar cells, and summary of the key photovoltaic parameters of representative ternary and binary solar cells under AM 1.5G illumination at 100 mW cm⁻²

Binary blend [D:A]	Photovoltaic parameters (binary)					Ratio [D:TC:A]	Photovoltaic parameters (ternary)				
	J_{SC} [mA cm ⁻²]	V_{OC} [V]	FF [%]	PCE [%]	The third component (TC)		J_{SC} [mA cm ⁻²]	V_{OC} [V]	FF [%]	PCE [%]	Ref.
PTB7-Th:PC ₇₁ BM	17.53	0.805	65.26	9.2	P-DTS(FBTTH ₂) ₂ :PC ₇₁ BM	0.85:0.15:1.1	18.44	0.755	75.27	10.5	85
P-DTS(FBTTH ₂) ₂ :PC ₇₁ BM	12.63	0.711	59.74	5.40							
PTB7-EFT:PC ₇₁ BM	17.11	0.786	65.1	8.75	PDVT-10	1:0.005:1.5	18.73	0.780	69.0	10.08	84
PTB7-Th:PC ₇₁ BM	14.92	0.75	70.3	7.88	PID2	0.8:0.2:1.5	16.68	0.78	70.8	9.20	140
PID2:PC ₇₁ BM	5.29	0.86	44.3	2.01							
PTB7:PC ₇₁ BM	14.7	0.731	63.5	6.8	PCDTBT	0.7:0.3:2	17.1	0.795	65.4	8.9	127
PTB7:PC ₇₁ BM	14.99	0.701	68.8	7.35	ICBA	1:0.225:1.275	16.68	0.735	71.2	8.88	141
PTB7:ICBA	10.84	0.873	50.1	4.83							
PTB7:PC ₇₁ BM	15.1	0.72	66.3	7.2	PBDTT-SeDPP	0.5:0.5:2	18.7	0.69	67.4	8.7	129
PBDTT-SeTDP:PC ₇₁ BM	16.9	0.68	62.9	7.2							
α -6T/SubPc	7.46	1.09	57.9	4.69	SubNc		14.55	0.96	61.0	8.40	122
α -6T/SubNc	12.04	0.94	53.9	6.02							
PBDTTPD-HT:PC ₇₁ BM	11.79	0.990	58.14	6.85	BDT-3TCNCOO	0.6:0.4:1	12.17	0.969	71.23	8.40	142
BDT-3TCNCOO:PC ₇₁ BM	10.11	0.968	72.63	7.48							
PTB7:PC ₇₁ BM	15.0	0.72	67.1	7.25	PID2	0.9:0.1:1.5	16.8	0.72	68.7	8.22	117
PID2:PC ₇₁ BM	5.27	0.86	44.4	2.01							
LP2:PC ₇₁ BM	11.80	0.97	0.64	7.32	LP4	0.5:0.5:3	13.88	0.94	0.62	8.09	70
LP4:PC ₇₁ BM	13.15	0.90	0.56	6.63							
SMPV1:PC ₇₁ BM	9.22	0.92	69	5.85	SQ	0.9:0.1:1	11.18	0.92	72	7.40	124
SQ:PC ₇₁ BM	4.50	0.90	28	1.13							
DTffBT:PCBM	12.2	0.91	56.5	6.26	DTPyT	0.5:0.5:1	13.7	0.87	58.9	7.02	128
DTPyT:PCBM	12.8	0.85	58.1	6.30							
ASSQ/C ₆₀	7.46	0.97	58.3	4.22	SQ	1:2/C ₆₀	10.05	0.87	70.3	6.15	126
SQ/C ₆₀	9.05	0.81	63.5	4.65							
P3HT75-co-EHT25:PCBM	7.96	0.675	59	3.16	P3HTT-DPP-10%	0.9:0.1:1.1	15.05	0.603	61	5.51	132
P3HTT-DPP-10%:PCBM	14.38	0.57	62	5.07							
PBTADN:PC ₇₁ BM	6.9	0.83	53.1	3.0	BantHBT	1:0.2:4	11	0.91	56.4	5.6	143
P3HT:PCBM	7.1	0.57	63	2.5	PCPDTBT	0.8:0.2:1	8.02	0.62	55.4	2.8	118
P3HT:PCBM	8.6	0.57	63.6	3.1	Si-PCPDTBT	0.6:0.4:1	11	0.59	62.1	4.0	144
P3HT:ICBA	7.9	0.82	60.1	3.9	Si-PCPDTBT	0.8:0.2:1	10	0.79	64.9	5.1	145
P3HT:PCBM	10.3	0.59	53	3.27	SQ	1:0.01:1	11.6	0.60	64.8	4.51	115
P3HT:PCBM	9.69	0.55	66	3.5	SiPc	1:0.048:1	11.1	0.58	65	4.2	113
PCDTBT:PC ₇₁ BM	10.79	0.86	68	6.3	Ag NPs (40 nm)	1:0.01:4	11.61	0.88	69	7.1	146
PTB7:PC ₇₁ BM	16.71	0.732	68.03	8.31	Au:BCNT	—	18.50	0.743	72.61	9.98	147
CH ₃ NH ₃ Pb _{3-x} Cl _x	19.3	0.98	72.9	13.8	DOR3T-TBDT:PC ₇₁ BM	—	21.2	0.99	67.9	14.3	148
CH ₃ NH ₃ Pb _{3-x} Cl _x	18.1	0.89	60.4	9.7	PBDTT-SeDPP:PC ₇₁ BM	—	20.6	0.94	62.0	12.0	
CH ₃ NH ₃ PbI ₃	13.09	0.90	80.33	9.46	PDPP3T:PCBM	—	13.93	0.88	71.78	8.80	149
PDPP3T:PCBM	8.82	0.67	67.07	3.96		—					

The intensity of the absorption spectra in the region from 650 nm to 900 nm was gradually enhanced with the concentration of PCPDTBT increasing, whereas, the absorption of the P3HT does not change obviously upon dilution with PCPDTBT. In the region between 650 nm and 900 nm, the EQE was significantly enhanced due to the PCPDTBT sensitization of the NIR photoresponse, which has similar varying tendency with the absorption spectra. Ameri *et al.* also carried out a series of excellent research studies on the ternary solar cells.^{86,144,145,151} The low bandgap polymer Si-PCPDTBT was used as the complementary material for the binary dominating system of P3HT/PCBM at different doping ratios. The EQE spectra of P3HT/PCBM and ternary solar cells with 10 wt%, 20 wt%, 30 wt% and 40 wt% Si-PCPDTBT in donors, as shown in Fig. 21(a), indicate that the response region of the absorption spectra was expended to 850 nm by adding Si-PCPDTBT. By adding 40% Si-PCPDTBT into the P3HT/PCBM, the average EQE was improved to 35% in the range from 650 nm to 800 nm (Si-PCPDTBT absorption) and the average EQE from the P3HT absorbing region is still maintained at 50%. As a result, the J_{SC} of the P3HT/PCBM cells was improved from 8.6 mA cm⁻² to

11 mA cm⁻² and 13 mA cm⁻² by adding 40 wt% and 70 wt% Si-PCPDTBT respectively. Compared with the binary solar cells, the PCE of the ternary solar cells arrived to 4% with adding 30–40 wt% Si-PCPDTBT, while the FF is kept still higher than 60 wt%. The high FF values of the ternary solar cells demonstrated that the dominating system P3HT/PCBM is not destroyed by addition of Si-PCPDTBT, as proved by the AFM images. To simultaneously overcome the two main limitations of OSCs (narrow absorption window of polymers and low V_{OC} of PCBM-based cells), Ameri *et al.* introduced Si-PCPDTBT into the dominating system of P3HT and indene-C₆₀ bisadduct (ICBA) to increase the lower energy photon harvesting of the active layer. In this work, the donors (Si-PCPDTBT and P3HT) to the ICBA ratio were maintained at 1:1 (w/w). The EQE values of the ternary solar cells with 20 wt% Si-PCPDTBT in donors, presented in Fig. 21(b), show an obvious enhancement in the range of 650 nm to 850 nm compared with those of the binary cells. At the same time, the EQE values of ternary solar cells between 350 nm and 660 nm are more or less identical to the P3HT/ICBA cells. It is indicated that the absorption spectra of the P3HT/ICBA active layer could be

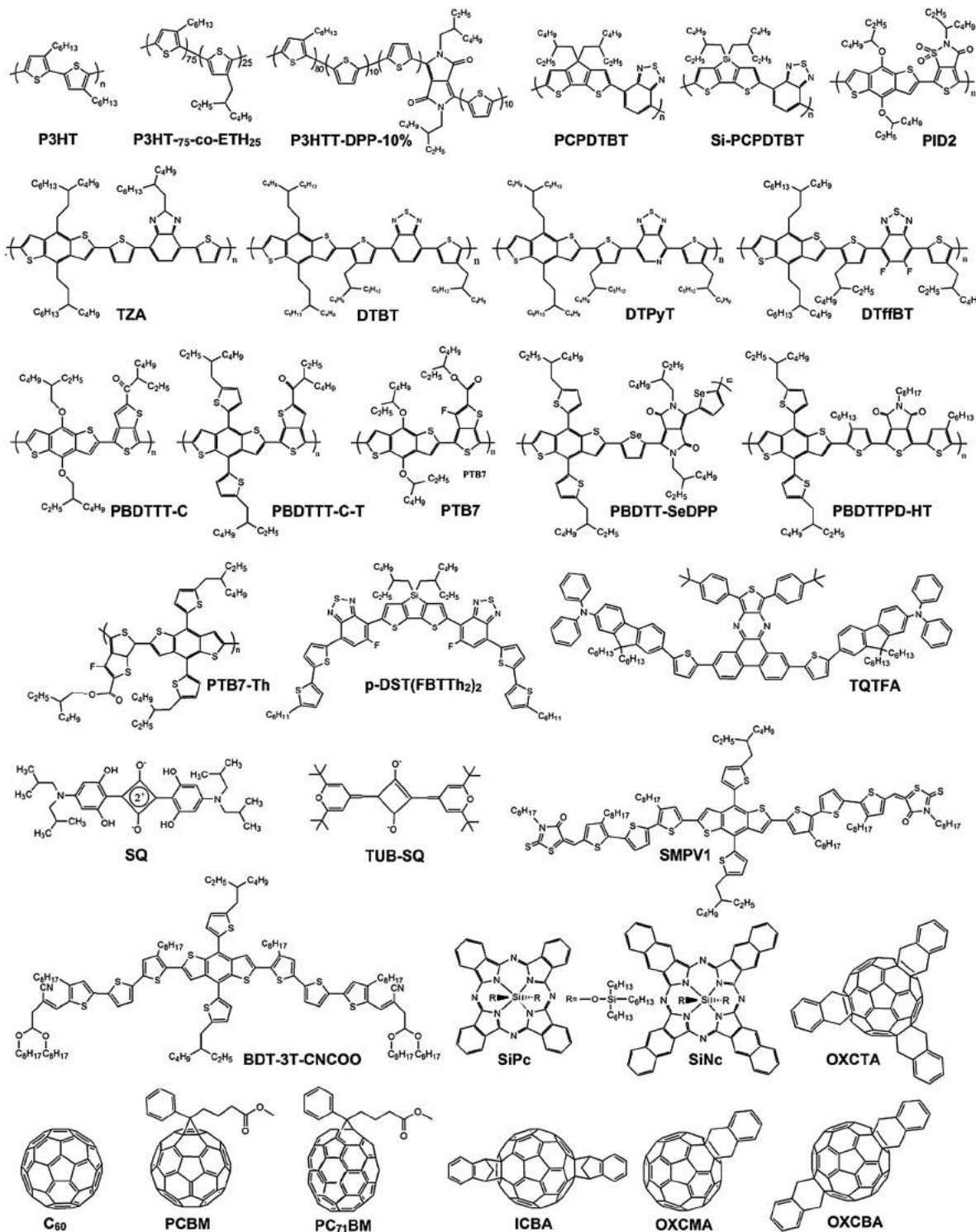


Fig. 20 Chemical structures of representative organic materials used in ternary solar cells.

expanded to 850 nm by adding Si-PCPDTBT, which is also demonstrated by the absorption spectra. Upon addition of 20 wt% Si-PCPDTBT into the binary system, the J_{SC} increased from 7.9 mA cm^{-2} to 10 mA cm^{-2} , which corresponds to 26% J_{SC} enhancement. The champion PCE of 5.1% with a $J_{SC} = 10 \text{ mA cm}^{-2}$, $V_{OC} = 0.79 \text{ V}$ and FF = 66% was achieved for

P3HT/Si-PCPDTBT/ICBA ternary cells, which is much higher than the PCE values of the P3HT/ICBA cells (3.9%), Si-PCPDTBT/ICBA cells (1.6%) and Si-PCPDTBT/PCBM cells (4.4%).

Before 2014, most of the research studies on the ternary solar cells were based on P3HT as the dominating donor, resulting in a relatively low PCE compared with binary solar

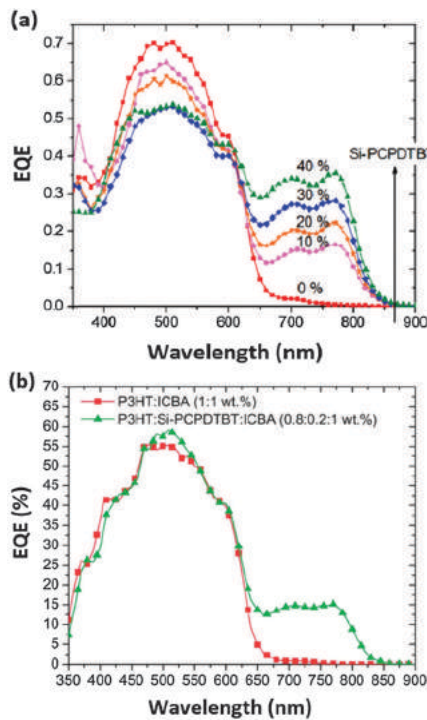


Fig. 21 The EQE spectra of (a) P3HT:PCBM (1:1) and ternary cells with concentrations of 10 wt%, 20 wt%, 30 wt% and 40 wt% Si-PCPDTBT in donors. Reproduced with permission from ref. 144. Copyright 2012 Wiley-VCH. (b) The EQE spectra of the P3HT:ICBA (1:1) and ternary cells with a concentration of 20 wt% Si-PCPDTBT in donors. Reproduced with permission from ref. 145. Copyright 2013 Royal Society of Chemistry.

cells based on low bandgap materials.^{16,152–158} Recently, a series of parallel-linkage ternary solar cells with compatible polymers as donors were reported by Yang *et al.*¹²⁹ The used polymers in this study, PBDTTT-C, PBDTT-DPP, PTB7 and PBDTT-SeDPP, all have the rigid planar BDT unit in their backbone and their preferred orientation is face-on with respect to the substrate in the deposited active layers. Fig. 22 presents the EQE of the PBDTTT-C:PBDTT-DPP:PC₇₁BM-based and PTB7:PBDTT-SeDPP:PC₇₁BM-based ternary solar cells as well as their corresponding binary solar cells. The EQE spectrum of

the ternary solar cells based on PBDTTT-C:PBDTT-DPP:PC₇₁BM distinctively shows a wider photoresponse than that of PBDTTT-C:PC₇₁BM-based solar cells and a higher photoresponse in the range from 300 nm to 700 nm than that of PBDTT-DPP:PC₇₁BM-based solar cells. As a result, the J_{SC} of ternary solar cells was increased to 15.7 mA cm⁻², surpassing that of the individual binary solar cells. The EQE spectrum of PTB7:PBDTT-SeDPP:PC₇₁BM-based ternary solar cells also shows the combined photoresponse of PTB7 and PBDTT-SeDPP, corresponding J_{SC} is as high as 18.7 mA cm⁻². The PCE of the ternary solar cells (8.7%) is much higher than those of PTB7:PC₇₁BM-based (7.8%) and PBDTT-SeDPP:PC₇₁BM-based (7.7%) solar cells, which mainly attributes to increased J_{SC} . The ternary solar cells with PBDTTT-C:PBDTT-DPP:PC₇₁BM or PTB7:PBDTT-SeDPP:PC₇₁BM as an active layer also show reasonably good performances compared to their binary solar cells. All of the ternary solar cells were found to outperform the binary cells at certain blending ratios (1:1). Furthermore, the solar cells with four polymers as donors (PBDTTT-C, PBDTT-DPP, PTB7 and PBDTT-SeDPP) show a PCE of 7.8%, with EQE values close to those of the constituent polymers. These results conceptually indicate that the compatibility of the materials used in the ternary solar cells is a decisive factor for achieving high performance.

Interestingly, Yu *et al.* incorporated a high bandgap polymer, poly-3-oxothieno[3,4-*d*]isothiazole-1,1-dioxide/benzodithiophene (PID2), as a complementary donor material into the PTB7:PC₇₁BM dominating system for improving the utilization efficiency of photon energy in short wavelength coverage.¹¹⁷ As presented in Fig. 23(a), the absorption is gradually enhanced in the range from 450 nm to 650 nm along with the increase of the PID2 content while absorption from 650 nm to 750 nm is simultaneously decreased, consistent with the fact that the absorption maximum of PID2 is at 610 nm and PTB7 has its maximum absorption at 683 nm. The EQE spectra of PTB7:PID2:PC₇₁BM ternary solar cells with various PID2 contents are shown in Fig. 23(b). It is obvious that the EQE values were enhanced over the whole wavelength region by incorporating 10 wt% PID2 into the PTB7:PC₇₁BM matrix, resulting in an increased J_{SC} of 16.8 mA cm⁻² and a PCE of 8.2% for ternary solar cells. The enhancement in EQE was not entirely the same trend with that

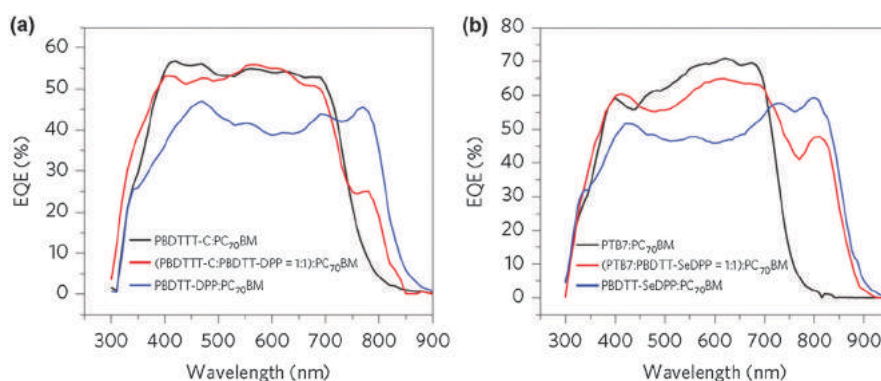


Fig. 22 EQE of (a) PBDTTT-C:PBDTT-DPP:PC₇₁BM and (b) PTB7:PBDTT-SeDPP:PC₇₁BM ternary solar cells. Reprinted with permission from ref. 129. Copyright 2015, Nature Publishing Group.

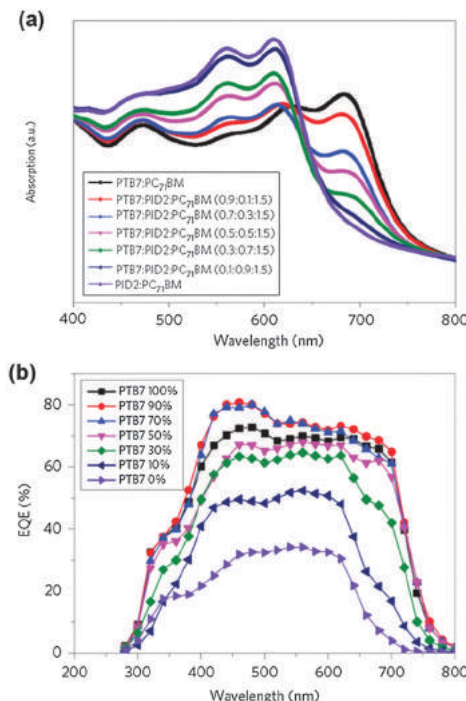


Fig. 23 (a) Absorption spectra of PTB7:PID2:PC₇₁BM films with various blend ratios of donors. (b) EQE of PTB7:PID2:PC₇₁BM ternary solar cells with various blend ratios of donors. Reprinted with permission from ref. 117. Copyright 2014, Nature Publishing Group.

observed in the absorption spectra because of the ternary film with 10 wt% PID2 only show better absorption from 500 nm to 620 nm while the most enhanced EQE is in the spectral range from 400 nm to 550 nm. The enhancement of EQE in the range from 400 nm to 550 nm for low PID2 content should be attributed to the effective extraction of holes from PC₇₁BM because of the cascade HOMO energy levels formed by PID2 doping into PTB7. The high bandgap polymer PID2 was also incorporated into poly[4,8-bis(5-(2-ethylhexyl)thiophen-2-yl)benzo[1,2-*b*:4,5-*b'*]dithiophene-*co*-3-fluorothieno[3,4-*b*]-thiophene-2-carboxylate] (PTB7-Th) and the PC₇₁BM blend system.¹⁴⁰

The optimized ternary solar cells achieve a PCE as high as 9.20% by incorporating 20 wt% PID2 into the PTB7-Th:PC₇₁BM matrix without further device engineering. These results demonstrate that the use of ternary strategy helps to re-evaluate the potential of many low-performance donor polymers, which may provide a promising way towards developing high performance ternary solar cells.

The small molecule materials as the third component have also been investigated in the ternary solar cells by many groups.^{159–161} In the early stages, the small molecules were also incorporated into the P3HT:PCBM matrix, exhibiting a relatively low PCE of ternary solar cells.^{162–165} Wei *et al.* combined the advantages of the conjugated polymer and small molecules by ternary strategy. The ternary solar cell contains a D-A polymer (PBDTPD-HT) and a novel small molecule (BDT-3T-CNCOO) as donors and PC₇₁BM as an acceptor.¹⁴² Selecting PBDTPD-HT and BDT-3T-CNCOO as donors is because PBDTPD-HT-based solar cells exhibit a high *V_{OC}* (~1.0 V) and BDT-3T-CNCOO show high crystallinity in blend films. Furthermore, the three used materials exhibit a complementary absorption in the range from 300 nm to 700 nm. As shown in Fig. 24(a), the absorption intensity of the optimized PBDTPD-HT:BDT-3T-CNCOO:PC₇₁BM (0.6:0.4:1) film is higher than that of the BDT-3T-CNCOO-based binary blend film at the short wavelength range and higher than that of the PBDTPD-HT-based binary blend film at the long wavelength range. Accordingly, the EQE spectra of the ternary solar cells are consistent with the corresponding absorption spectra (Fig. 24(b)). The *J_{SC}* of optimized ternary solar cells is higher than that of corresponding binary solar cells, and the *V_{OC}* and FF of optimized ternary solar cells are close to the higher values between two binary solar cells, resulting in a high PCE of 8.40%.

Recently, Zhang *et al.* reported an efficient ternary solar cell based on three small molecules which contain SMPV1 and SQ as donors as well as PC₇₁BM as an acceptor. Fig. 25(a) presents the absorption spectra of SMPV1:SQ blend films with different SQ doping ratios. The absorption spectra of SMPV1 and SQ films exhibit an apparent complementary absorption in the range from 400 nm to 800 nm. The SQ has a strong absorption in the range from 550 nm to 800 nm, which can be considered

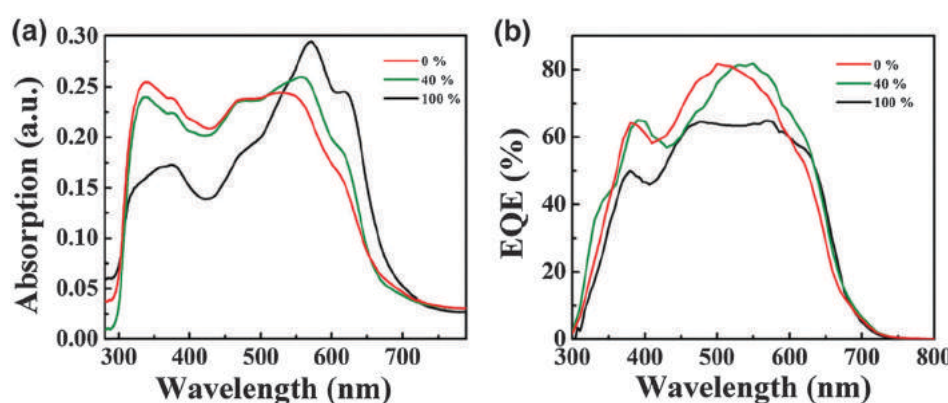


Fig. 24 (a) Absorption spectra of the ternary and binary blend films and (b) EQE spectra of the ternary and binary solar cells. Reprinted with permission from ref. 142. Copyright 2015 Wiley-VCH.

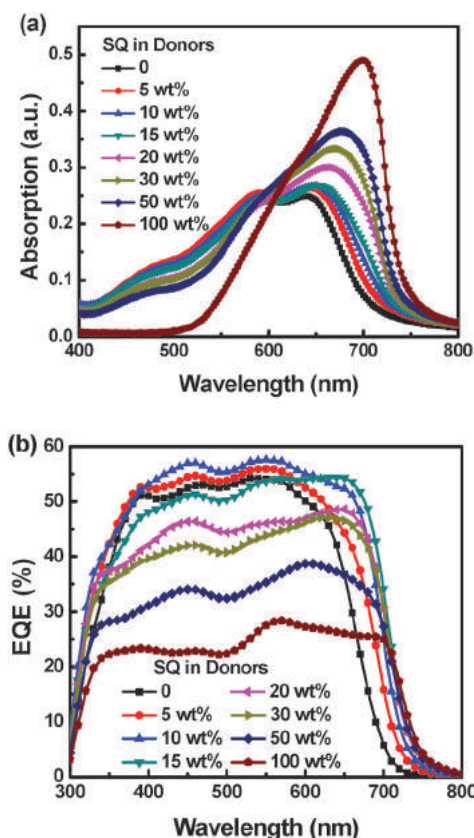


Fig. 25 (a) Absorption spectra of SMPV1:SQ blend films with different SQ doping ratios and (b) EQE spectra of binary or ternary solar cells with different SQ doping ratios in donors. Reprinted with permission from ref. 124. Copyright 2015 Royal Society of Chemistry.

as an excellent complementary donor material to harvest more photons in the longer wavelength region for SMPV1-based solar cells. For the blend films, the absorption intensity is gradually enhanced in the range from 600 nm to 700 nm along with the increase of SQ doping ratios, while the absorption intensity of blend films is reduced from 400 nm to 600 nm due to the relatively decreased SMPV1 content. The EQE spectra of the ternary cells with different SQ doping ratios are shown in Fig. 25(b). There are two interesting phenomena in EQE spectra compared with the corresponding absorption spectra. The EQE values of ternary solar cells are markedly increased in the long wavelength range for the SQ doping ratios up to 15 wt%, which should be attributed to the increase of photon harvesting by SQ molecules. However, the EQE values in this spectral range are clearly decreased for further increase of SQ doping ratios, suggesting inefficient exciton dissociation, charge carrier transport and collection although the increase of photon harvesting by the more SQ content in the blend films. For the ternary solar cells with SQ doping ratios less than 15 wt%, the relatively high EQE values in the long wavelength range suggests an efficient hole (generated from exciton dissociation at the SQ/PC₇₁BM interface) transfer from SQ to SMPV1 and then transport along the channels formed by SMPV1 molecules. However, the efficient hole transport channels formed by SMPV1 will be disrupted

along with the increase of SQ doping ratios, which can be demonstrated from the decreased J_{SC} and FF of ternary solar cells with a high SQ doping ratio. Another interesting phenomenon should be highlighted that the EQE values of ternary solar cells with lower SQ doping ratios (≤ 10 wt%) are slightly increased in the spectral range from 400 nm to 650 nm where SMPV1 exhibits lower absorption than that of the neat SMPV1 film. The EQE improvement in this spectral range is mainly attributed to the efficient energy transfer from SMPV1 to SQ, which provide a new route to increase SMPV1 exciton dissociation efficiency. The optimized ternary solar cells showed the higher PCE and J_{SC} than that of the binary system, resulting from the synergistic effect of the enhanced photon harvesting and exciton dissociation efficiency.

Cnops *et al.* presented a simple planar heterojunction ternary solar cell with two non-fullerene acceptors (SubNc and SubPc) and α -6T as a donor.¹²² The absorption spectra of the three used materials are shown in Fig. 26(a). The three materials have a high absorption coefficient of $3.5 \times 10^5 \text{ cm}^{-1}$ at their peak wavelength and show complementary absorption in the broad spectral range from 300 nm to 800 nm. It is apparent that both layers contribute to the photocurrent due to their different photon harvesting range, which can be confirmed from the measured EQE spectra of the planar heterojunction ternary solar cells (Fig. 24(b)). In the planar ternary solar cell, the excitons generated in acceptors only can be dissociated at the D/A interface. The excitons generated in the outer SubPc acceptor can be transferred to the middle SubNc layer and consequently dissociated at the interface of α -6T/SubNc. Therefore, the EQE of ternary show high values in the range from 450 nm to 650 nm where SubNc have strong absorption. The J_{SC} of the ternary solar cells is 14.55 mA cm^{-2} , which is much higher than that of α -6T/SubNc-based (12.04 mA cm^{-2}) and α -6T/SubPc-based (7.46 mA cm^{-2}) solar cells. The PCE of ternary solar cells is

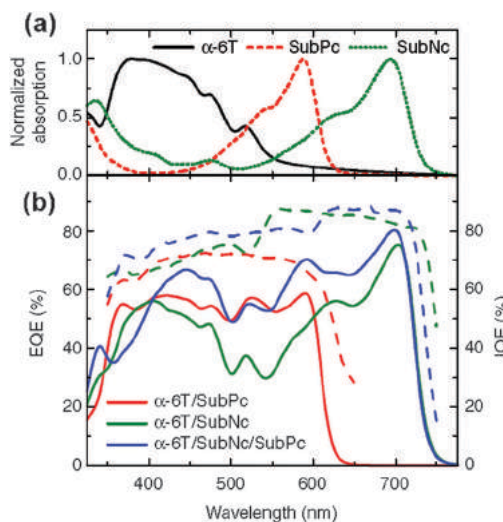


Fig. 26 (a) Absorption spectra of the three active materials complementing each other to effectively harvest solar light. (b) The measured EQE (solid lines) and IQE (dashed lines) spectra show efficient photocurrent generation by all three absorbing materials. Reprinted with permission from ref. 122. Copyright 2014 Nature Publishing Group.

as high as 8.4%, surpassing the 4.69% and 6.02% of the individual α -6T:SubPc-based and α -6T:SubNc-based solar cells. Taylor *et al.* also reported a planar heterojunction ternary solar cell by co-evaporating two different squaraine SQ and ASSQ as donor layers as well as C_{60} as an acceptor layer.¹²⁶ The ASSQ show strong absorption in the range from 450 nm to 600 nm and its absorption peak locates at about 543 nm, which exhibits good complementary with the absorption spectrum of SQ (peak at 695 nm). Thus, the ASSQ/SQ blend films show a broader absorption range compared with the individual ASSQ or SQ films. At the optimized doping ratio of ASSQ to SQ (1:2), the ternary solar cells achieve a PCE of 6.15% due to the increased J_{SC} compared with the corresponding binary solar cells. The improvement of J_{SC} is mainly attributed to the broader absorption range of the ternary active layer and enhanced exciton dissociation efficiency through energy transfer, meanwhile the charge carrier recombination can be effectively limited in the planar heterojunction active layers.

Low bandgap organic dyes have also been used for the more photon harvesting of the active layers in ternary solar cells.^{99,113,166} Ohkita *et al.* selected the dye SiPc as a complementary material to incorporate with the P3HT:PCBM matrix for harvesting more photons from the long wavelength range. The SiPc has a narrow absorption from 650 nm to 700 nm and the absorption peak is located at 676 nm for the solvent-annealed ternary blend films. The contribution of SiPc to the photocurrent of ternary solar cells can be confirmed from the EQE spectra (Fig. 27(a)). The EQE spectrum of ternary solar cells with 4.8 wt% SiPc shows higher values in the range from 400 nm to 800 nm than those of the binary solar cells. The improvement of EQE values in the range from 400 nm to 600 nm (P3HT absorption) is ascribed to the efficient energy transfer from P3HT to SiPc, and the improvement from 600 nm to 800 nm is ascribed to the direct absorption of SiPc. When the doping ratio of SiPc is 17 wt%, EQE values slightly decreased in the range from 400 nm to 600 nm and remained constant from 600 nm to 800 nm for the solvent-annealed ternary solar cells. The excess SiPc molecules could overflow into P3HT domains and thus quench P3HT excitons, resulting in EQE decrease at the absorption band of P3HT. Consequently, the optimized

ternary solar cells with 4.8 wt% SiPc exhibited an increase of 15% in J_{SC} (from 9.69 mA cm⁻² to 11.1 mA cm⁻²) and ~5% increase in V_{OC} (from 0.55 V to 0.58 V), resulting in the increase of PCE from 3.5% to 4.2%. Furthermore, Ohkita *et al.* reported a quaternary solar cell with two dyes as complementary donors.¹⁶⁶ The response range of EQE spectra for P3HT:PCBM:SiPc ternary solar cells was further extended by the dye silicon naphthalocyanine bis(trihexylsilyl oxide) (SiNc). As shown in Fig. 27(b), the EQE of the quaternary solar cell exhibited sharp and intense absorption bands at around 670 nm and 780 nm, which is mainly attributed by the direct photon harvesting by SiPc and SiNc molecules. Owing to enhanced photon harvesting, the quaternary solar cells based on P3HT:PCBM:SiPc:SiNc as the active layers achieve the highest PCE (4.3%) than that of ternary or binary solar cells.

Perovskite solar cells are attracting global attention and interest due to their outstanding performance. Perovskite materials have many unique advantages as light absorbers for high performance solar cells, such as direct bandgap, long exciton diffusion lengths, high absorption coefficient, low exciton binding energy and high charge carrier mobility.^{92,167–169} The most efficient perovskite absorbers, such as $CH_3NH_3PbI_3$ and $CH_3NH_3Pb_{3-x}Cl_x$, show onset light response at ~800 nm due to their optical bandgap of 1.55 eV, which limits the quantity of photon harvesting and further improvement of PCE. Making the most of solar light below 800 nm and broadening the light absorption range into NIR should be effective strategies to further enhance the performance of perovskite solar cells. Recently, Yang *et al.* designed and fabricated an integrated perovskite/BHJ solar cell with $CH_3NH_3Pb_{3-x}Cl_x$ as the perovskite absorber and DOR3T-TBDT:PC₇₁BM as the BHJ layer.¹⁴⁸ Fig. 28(a) presents the absorption spectra of perovskite/DOR3T-TBDT and perovskite/DOR3T-TBDT:PC₇₁BM films and the EQE spectra of the perovskite/DOR3T-TBDT-based and perovskite/DOR3T-TBDT:PC₇₁BM-based solar cells. Both perovskite/DOR3T-TBDT-based and perovskite/DOR3T-TBDT:PC₇₁BM-based solar cells show photocurrent response in the range from 300 to 800 nm, which is consistent with their absorption spectra. The integrated solar cell based on perovskite/DOR3T-TBDT:PC₇₁BM shows higher EQE values than that of perovskite/DOR3T-TBDT-based solar cells between 520 to 740 nm, indicating the efficient

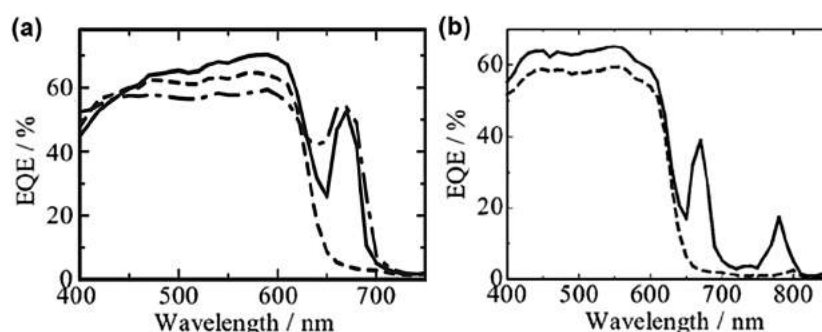


Fig. 27 (a) EQE spectra of a P3HT:PCBM:SiPc ternary blend with 4.8 wt% SiPc (solid lines) and 17 wt% SiPc (dashed-dotted lines) and P3HT:PCBM (1:1) binary blend solar cells (broken lines) after solvent annealing. Reprinted with permission from ref. 113. Copyright 2011 Wiley-VCH. (b) EQE spectra of P3HT:PCBM:SiPc:SiNc-based (solid lines) and P3HT:PCBM-based (broken lines) solar cells. Reprinted with permission from ref. 166. Copyright 2010 Royal Society of Chemistry.

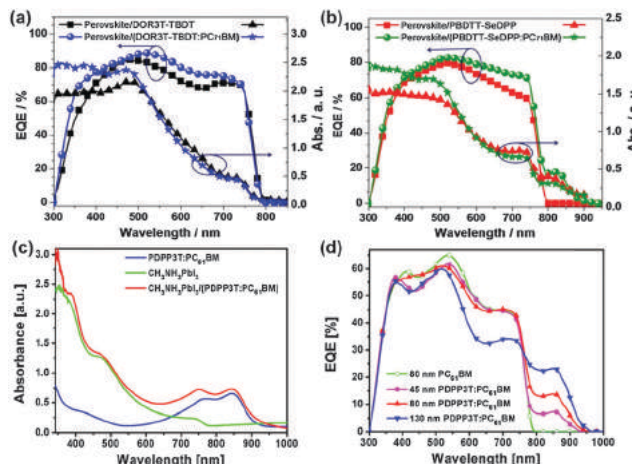


Fig. 28 Absorption spectra of HTL and BHJ film on glass/TiO₂/perovskite and EQE spectra of perovskite/HTL and integrated perovskite/BHJ solar cells. (a) DOR3T-TBDT as HTL and DOR3T-TBDT:PC₇₁BM as the BHJ layer and (b) PBDTT-SeDPP as HTL and PBDTT-SeDPP:PC₇₁BM as the BHJ layer. Reprinted with permission from ref. 148. Copyright 2014 American Chemical Society. (c) Absorption spectra of the PDPP3T:PCBM (1 : 2) blend film, CH₃NH₃PbI₃ film and CH₃NH₃PbI₃/PDPP3T:PCBM (1 : 2) bilayer film. (d) EQE spectra of perovskite solar cells with 80 nm PCBM and the integrated perovskite/BHJ solar cells. Reprinted with permission from ref. 149. Copyright 2015 Royal Society of Chemistry.

photoresponse of DOR3T-TBDT:PC₇₁BM films. As a result, the integrated perovskite solar cell shows a J_{SC} of 21.2 mA cm⁻², which is higher than that of the perovskite/DOR3T-TBDT-based device (19.3 mA cm⁻²), resulting in a higher PCE of 14.3%. In order to investigate the origin of enhanced photocurrent, a low bandgap polymer PBDTT-SeDPP as the hole transporting layer (HTL) for perovskite solar cells and a donor in BHJ film are further studied by the authors. As shown in Fig. 28(b), in addition to the characteristic absorption band of perovskite, both perovskite/PBDTT-SeDPP and perovskite/PBDTT-SeDPP:PC₇₁BM films show good absorption in the range from 800 nm to 900 nm, which is attributed to the low bandgap polymer PBDTT-SeDPP. Interestingly, there is no photocurrent response in the range from 800 nm to 900 nm for photovoltaic solar cells with PBDTT-SeDPP as HTL, while the integrated perovskite/BHJ solar cells with PBDTT-SeDPP as the donor not only shows improved photoresponse from 500 nm to 800 nm but also a notable EQE response up to 900 nm. These results indicate that the HTL in traditional perovskite solar cells, even with good light absorption capability, have no contribution to the overall device photocurrent, unless this HTL becomes a BHJ layer (by adding an acceptor material like PCBM). Ding *et al.* also reported integrated perovskite/BHJ solar cells with CH₃NH₃PbI₃ as the perovskite absorber and PDPP3T:PCBM as the BHJ layer.¹⁴⁹ It is obvious that the absorption spectrum of CH₃NH₃PbI₃/PDPP3T:PCBM films shows good accumulation of the respective absorption of CH₃NH₃PbI₃ films and PDPP3T:PCBM films (Fig. 26(c)). As described in Fig. 26(d), the EQE spectra of integrated perovskite/BHJ solar cells show a broader response range than that of the CH₃NH₃PbI₃-based solar cells. When the thickness

of the BHJ layer is 80 nm, the perovskite/BHJ solar cell gives a J_{SC} of 13.93 mA cm⁻², which is higher than that of CH₃NH₃PbI₃-based solar cells due to the additional photocurrent contribution from the PDPP3T:PCBM layer. According to the examples, integrating the perovskite and BHJ solar cells may be an efficient way to further improve the device performance.

Photon harvesting also can be enhanced by incorporating inorganic nanoparticles (NPs) with the dominating system.¹⁷⁰ Among NPs, noble metal NPs, such as Au and Ag NPs, generally can enhance the light absorption of the active layer due to their localized surface plasmon resonance (LSPR).^{171–179} LSPR interacts strongly with the incident light and thus enhances the local absorption within the vicinity of the plasmonic structure. Furthermore, the incident light can be reflected and scattered by the embedded metal NPs, thereby increasing the optical path length in the active layer. Heeger *et al.* demonstrated the positive effects of Ag NPs on the performance of the poly[N-9'-hepta-decanyl-2,7-carbazole-*alt*-5,5-(4',7'-di-2-thienyl-2',1',3'-benzothiadiazole)] (PCDTBT):PC₇₁BM solar cells.¹⁴⁶ As shown in Fig. 29(a), the ternary film with 1 wt% 40 nm-sized Ag NPs presents increased absorption at around 350 nm to 550 nm compared with that of the binary film, which originates in light scattering of the Ag clusters. The schematic of the light trapping and optical reflection caused by the scattering from the Ag clusters is described in the inset of Fig. 29(a). The EQE spectra of the binary and ternary solar cells are shown in the inset of Fig. 29(b). The ternary solar cell shows the relatively high EQE values even up to 75% near 450 nm. Moreover, the EQE enhancement can be apparently observed in the range from 350 nm to 550 nm for the ternary active layers, which is consistent with the tendency of the corresponding absorption spectra of used materials. Consequently, the PCE was increased from 6.3% to 7.1%, which should be mainly attributed to the increase of J_{SC} from 10.79 mA cm⁻² to 11.61 mA cm⁻² by doping appropriate metal NPs in the active layers.

3.2 Adjusting open circuit voltage (V_{OC})

The second advantage of the third component is to obtain continuously tunable V_{OC} of ternary solar cells for optimized performance, which have been confirmed experimentally by many independent studies.^{88,116,180,181} As we know, the V_{OC} is determined by the quasi-Fermi levels for electrons and holes as per the following equation:

$$V_{OC} = \frac{E_{fn} - E_{fp}}{q} \quad (4)$$

where q is the elementary charge, and E_{fn} and E_{fp} are electron and hole quasi-Fermi levels under steady-state illumination under open-circuit conditions, respectively. In conventional binary solar cells with ohmic contacts, the quasi-Fermi levels are limited by the HOMO level of the donor and the LUMO level of the acceptor. It is generally recognized that the V_{OC} of the binary solar cell is mainly determined by the difference between the HOMO energy level of the donor and the LUMO

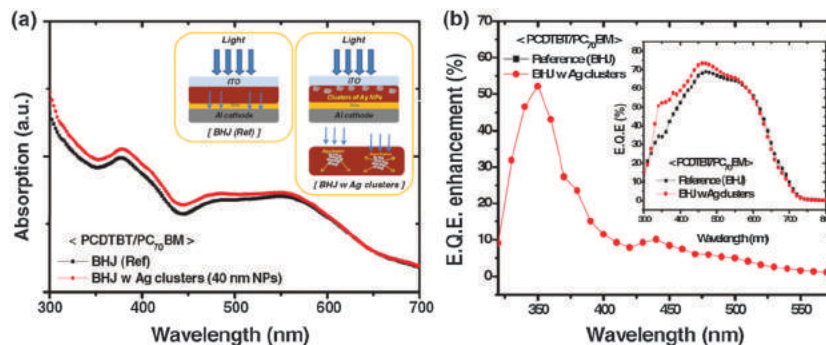


Fig. 29 (a) Absorption spectra of the PCDTBT:PC₇₁BM binary film and the ternary film based on PCDTBT:PC₇₁BM:AgNPs with 40 nm-sized NP based Ag clusters (1 wt%). The inset schematic figures show the light trapping and optical reflection by the scattering and excitation of localized surface plasmons. (b) EQE enhancement spectra of the devices from the ternary film with 40 nm-sized NP based Ag clusters (1 wt%). The inset figure shows measured EQE of binary and ternary solar cells (with Ag clusters). Reprinted with permission from ref. 146. Copyright 2011 Wiley-VCH.

energy level of the acceptor:

$$V_{OC} = \frac{1}{q}(E_{LUMO}^A - E_{HOMO}^D - \Delta E) \quad (5)$$

where E_{LUMO}^A is the LUMO energy level of the acceptor, and E_{HOMO}^D is the HOMO of the donor. ΔE represents an empirical factor, which normally owns a value of about 0.3 eV. If the ΔE is larger than the empirical value, excitons can be effectively dissociated into free charge carriers at the D/A interfaces. In the ternary system with two donors or two acceptors, the V_{OC} open-circuit voltage becomes increasingly complicated and cannot be predicted simply by eqn (5). The tunable V_{OC} in the ternary solar cells was dominantly interpreted by the more favourable ratios of charge generation to charge recombination. It is well known that V_{OC} can be expressed as:

$$V_{OC} = \frac{n k T}{q} \ln \left(\frac{J_{SC}}{J_{SO}} \right) + \frac{\Delta E_{DA}}{2q} \quad (6)$$

where n is the diode ideality factor, k is the Boltzmann constant, T is the Kelvin temperature, and ΔE_{DA} is the interfacial energy gap between the donor and the acceptor. The magnitude of J_{SO} depends on a number of material properties that determine the carrier generation and recombination rate, independent of the energy barrier, ΔE_{DA} .^{143,182}

In 2011, Thompson *et al.* first demonstrated that the V_{OC} of the ternary solar cells with P3HT/ICBA/PCBM as an active layer could be tuned across the full composition range of the components by varying the proportion of ICBA in acceptors as well as high FF and J_{SC} were maintained.¹³¹ In this ternary system, the overall proportion of donor (P3HT) to acceptor (ICBA and PCBM) was maintained at 1:1, while the proportion of the ICBA and PCBM in acceptors was varied. The chemical structures and corresponding HOMO and LUMO energy levels of used materials are shown in Fig. 30(a). The two acceptors have a similar chemical structure and excellent miscibility with P3HT, resulting in similar donor/acceptor ratios and processing conditions for achieving optimized performance. As shown in Fig. 30(b), the V_{OC} of the ternary solar cells increased from 0.605 V to 0.844 V with increasing ICBA doping ratios in acceptors. The ternary solar cells with various proportions of

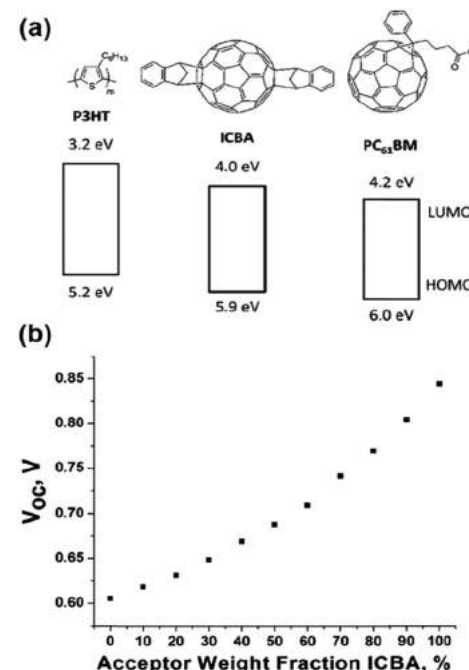


Fig. 30 (a) Chemical structures and corresponding HOMO and LUMO energy levels of P3HT, ICBA, and PCBM and (b) V_{OC} of the ternary cells as a function of the proportion of ICBA in acceptors. Reprinted with permission from ref. 131. Copyright 2011 American Chemical Society.

ICBA in acceptors have high FF values, which is attributed to favorable morphology and charge carrier transport. The J_{SC} of ternary solar cells showed a slightly decreased trend along with the increase of ICBA doping ratios in acceptors because the absorption strength of ICBA is significantly less than that of PCBM in the visible light range. These results indicate that the V_{OC} of ternary solar cells is not limited to the smaller V_{OC} value but can be adjusted between the extreme V_{OC} values of the corresponding binary blend solar cells without significant effect on the J_{SC} or FF.

Wang *et al.* also reported a ternary solar cell with P3HT as the donor and mixed PCBM and ICBA acceptors by using the layer-by-layer (LL) process.¹⁸³ The $J-V$ characteristics of the

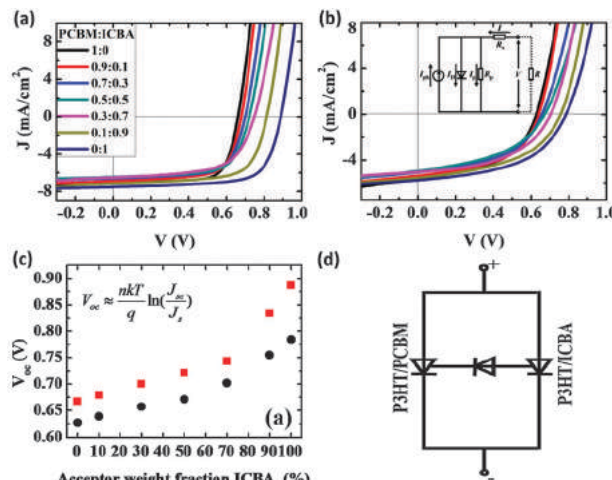


Fig. 31 J - V curves of the solar cells with (a) and without (b) annealed treatment; dependences of V_{oc} (c) on the proportion of ICBA in acceptors; and (d) three-diode model of the ternary solar cells. Reprinted with permission from ref. 183. Copyright 2012 American Institute of Physics.

ternary solar cells with various PCBM/ICBA doping weight ratios are shown in Fig. 31(a) (active layers with annealed treatment) and Fig. 31(b) (active layers without annealed treatment). An interesting finding is that both V_{oc} values of ternary solar cells with and without annealing treatment exhibit similar tendency with the change in ICBA proportions in acceptors. The V_{oc} was gradually increased from 0.667 V to 0.887 V along with the increased proportion of ICBA, while the changes in J_{sc} and FF were not significant. The V_{oc} dependence on the proportions of ICBA in acceptors is described in Fig. 31(c). It is apparent that with increasing proportions of ICBA in acceptors, V_{oc} increases slowly at the beginning. Only when the proportion of ICBA in acceptors was more than 70%, the increase of V_{oc} speeds up. This indicates that the V_{oc} is mainly dominated by PCBM rather than by ICBA. Such as in ternary solar cells with annealed treatment, the V_{oc} is significantly reduced from 0.887 to 0.834 V with 10 wt% PCBM in the acceptors, while the V_{oc} only increases from 0.667 to 0.679 V with 10 wt% ICBA in the acceptors. These results indicate that the ternary solar cells should include two types of binary solar cells: P3HT/PCBM and P3HT/ICBA cells. In the ternary solar cells, P3HT collects photo-generated holes and transports them to the anode. The acceptors, PCBM and ICBA, collect the photo-generated electrons and transport them to the cathode. Although the two kinds of cells are parallel in the ternary system, they are not completely independent. The photo-generated electrons transported by ICBA could drop onto PCBM when they are near the PCBM/ICBA interface due to the LUMO of ICBA is about 0.2 eV higher than that of PCBM. However, electrons transported by PCBM hardly jump onto the LUMO level of ICBA because of this 0.2 eV LUMO barrier between PCBM and ICBA molecules.

A three-diode model was proposed to analyze the tunable behavior of V_{oc} in ternary solar cells, as shown in Fig. 31(d), which may be applied to all ternary systems. The third diode model indicates that the photocurrent of P3HT/ICBA solar cells

could leak into P3HT/PCBM cells, while not the other way around. The leak current of ternary solar cells generally was ascribed to energy loss, such as each electron flows from the LUMO of ICBA to the LUMO of PCBM, the corresponding energy loss is 0.2 eV. When an exciton dissociates at the interface of P3HT/PCBM, the electron on the LUMO of the P3HT drops to the LUMO of PCBM, and there is an energy loss of 1.1 eV. However, the lost energy is 0.9 eV if the electron from exciton dissociates at the P3HT/ICBA interface drops from the P3HT to the ICBA. Compared to the lower-LUMO level of PCBM, the relatively high-LUMO level of ICBA could reduce energy loss by collecting electrons from P3HT. The ICBA plays a key role for saving energy in the ternary solar cells. The more ICBA, the more energy will be saved and then more energy will be gathered by the solar cells, which is conducive to enhance the V_{oc} . It is difficult to ignore that a portion of saved energy will be handy because the electrons flowed from ICBA to PCBM, this might be the reason for the V_{oc} increasing slowly when the proportions of ICBA in acceptors are small. In this case, a P3HT/PCBM diode dominates the ternary system, most energy saved by ICBA is eventually lost again through the third diode. When proportions of ICBA in acceptors are large enough and the P3HT/ICBA diode dominates the ternary system, energy loss will be significantly suppressed and then the V_{oc} becomes increasingly faster, as shown in Fig. 31(c). A similar phenomenon was also reported by Zhan and co-workers in the ternary solar cells based on the PTB7:ICBA:PC₇₁BM matrix.¹⁸⁴

Kim *et al.* observed a different tunable behavior of V_{oc} in the ternary solar cells with P3HT and an *o*-xylenyl C₆₀ mono-adduct (OXCMA) as the dominating system, and either the *o*-xylenyl C₆₀ bisadduct (OXCBA) or the *o*-xylenyl C₆₀ trisadduct (OXCTA) as the second acceptor.¹⁸⁵ In the ternary solar cells, W_{OXCBA} is the doping ratio of OXCBA in acceptors (OXCMA:OXCBA). The V_{oc} of the P3HT:OXCMA:OXCBA-based ternary solar cells can be continuously increased from 0.634 to 0.843 V along with the increase of W_{OXCBA} doping ratios in acceptors, which is consistent with that of the P3HT:PCBM:ICBA ternary solar cells (Fig. 32(a)). Unlike the observation in the previous section, as the W_{OXCTA} doping ratios in acceptors increased, the V_{oc} values show a nonlinear transformation trend in the ternary solar cells with P3HT:OXCMA:OXCTA as active layers. The V_{oc} can be increased by incorporating a small amount of OXCTA into the P3HT:OXCMA-based binary solar cells (W_{OXCTA} < 0.3), while the V_{oc} of ternary solar cells is dramatically decreased when the W_{OXCTA} values are over 0.7 in acceptors. For instance, the V_{oc} value increased from 0.634 to 0.674 V when the ternary solar cell is at W_{OXCTA} = 0.3, which mainly results from the higher LUMO level of OXCTA. Consequently, the ternary solar cells at W_{OXCTA} = 0.3 show a higher PCE (4.03%) than those of the corresponding P3HT:OXCMA-based (3.61%) and P3HT:OXCTA-based (1.31%) binary solar cells (Fig. 32(b)). In contrast, the V_{oc} and PCE values of the ternary solar cells are lower than those of the two binary solar cells when OXCTA is the major fullerene component in the ternary device (W_{OXCTA} = 0.8–0.9). These results indicate that the OXCTA can enhance the V_{oc} and PCE values in the P3HT:OXCMA:OXCTA-based ternary solar cells by

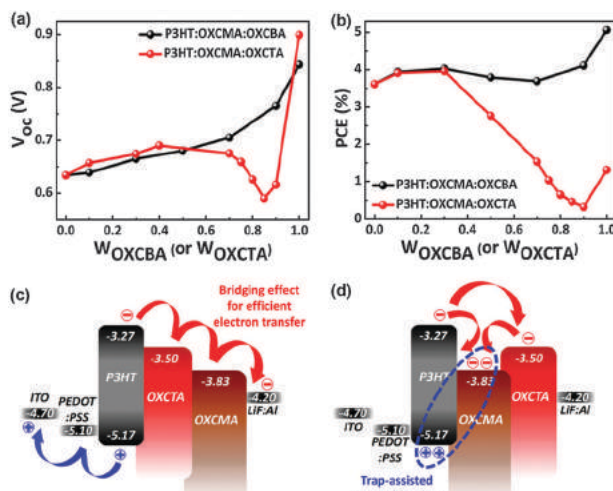


Fig. 32 The variation of (a) PCE and (b) V_{oc} as a function of the W_{OXCBA} or W_{OXCTA} in ternary solar cells. The energy levels (eV) of electrodes and used materials in the ternary solar cells. The LUMO energy levels of the fullerene multiadducts (OXCMA: -3.83 eV, OXCBA: -3.66 eV, and OXCTA: -3.50 eV) were estimated by CV measurements. Two different bridging and trapping effects on the performance of P3HT:OXCMA:OXCTA-based solar cells were observed to be dependent on the W_{OXCTA} values: (c) bridging effect of OXCTA for the case of $W_{OXCTA} = 0.1\text{--}0.3$ and (d) trapping effect by OXCMA for $W_{OXCTA} = 0.7\text{--}0.9$. Reprinted with permission from ref. 185. Copyright 2013 American Chemical Society.

forming synergistic bridges between the P3HT and OXCMA domains (Fig. 32(c)) when W_{OXCTA} doping ratios in acceptors are small (<0.3). As shown in Fig. 32(d), OXCMA act as charge-trapping sites in the ternary solar cells when $W_{OXCTA} > 0.7$ in acceptors, thus preventing efficient charge transport and promoting trap-assisted recombination. For the ternary solar cells with P3HT:OXCMA:OXCBA as the active layer, this trapping does not occur and the V_{oc} gradually increases with composition but more steeply for a higher OXCBA ratio. The different change trends in V_{oc} of the two ternary solar cells are likely related to the larger offset of the LUMO levels of OXCMA and OXCTA (0.33 eV) than between OXCMA and OXCBA (0.17 eV).

The tunable behavior of V_{oc} in the ternary solar cells based on the D₁/D₂/A system was also demonstrated by Thompson *et al.*

The V_{oc} of the ternary solar cells with two donors (P3HT75-*co*-EHT25 and P3HTT-DPP-10%) could be tuned between the limited V_{oc} values of the corresponding P3HT75-*co*-EHT25:PCBM and P3HTT-DPP-10%:PCBM solar cells, as was shown for the case of the ternary solar cells with two acceptors.^{132,134} As shown in Fig. 33(a), the three used materials have a broad and strong absorption in the region from 300 nm to 830 nm, which should provide a higher J_{sc} of ternary solar cells than that of either binary blend solar cells. Meanwhile, the different HOMO energy levels of P3HT75-*co*-EHT25 (5.4 eV) and P3HTT-DPP-10% (5.2 eV) should enable V_{oc} tunability in the ternary blend solar cells at different polymer doping ratios. Fig. 33(b) shows V_{oc} of ternary solar cells as a function of the proportion of P3HT75-*co*-EHT25 in donors. It can be observed that by incorporating P3HT75-*co*-EHT25 into the P3HTT-DPP-10%/PCBM matrix, the V_{oc} rapidly increased by 29 mV. With the proportion of P3HT75-*co*-EHT25 increased in the donors, the V_{oc} of the ternary solar cells with individually optimized at each polymer:polymer ratio increased linearly from 0.603 V to 0.646 V. When the overall donor/acceptor proportion in the ternary system was not individually optimized but rather kept constant, the V_{oc} decreased significantly and deviated from linearity. When the proportion of the donors:PCBM was kept in 1:1.1 in the ternary system, the V_{oc} increased linearly with the proportion of P3HT75-*co*-EHT25 from 20% to 90%, which was the optimal overall D:A proportion. It is obvious that V_{oc} values of ternary solar cells with donors:PCBM remaining 1:1.1 were lower than that of the individually optimized ternary solar cells. A nonlinear dependence of V_{oc} on the proportion of P3HT75-*co*-EHT25 was observed for the ratio of donors:PCBM remaining 1:1. In this case, the V_{oc} increased linearly with the proportion of P3HT75-*co*-EHT25 below 50%, which was followed by almost constant V_{oc} with the proportion of P3HT75-*co*-EHT25 up to 80% and then an increased V_{oc} at higher proportion of P3HT75-*co*-EHT25. The authors emphasized that it is necessary to individually optimize the overall composition at each donor/donor proportion for achieving maximum performance of ternary solar cells and the V_{oc} of the solar cells could be significantly increased by introducing even small amounts of a donor with a lower HOMO energy level.

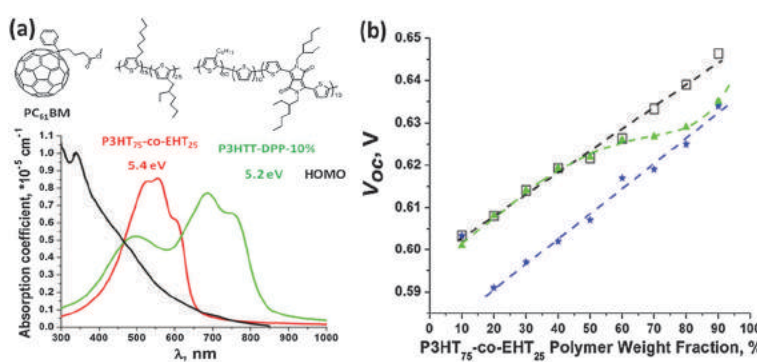


Fig. 33 (a) Chemical structures, HOMO energy levels and absorption spectra of PCBM, P3HT75-*co*-EHT25, and P3HTT-DPP-10%; (b) the V_{oc} of the ternary solar cells with individually optimized (□) and cells with fixed overall donor/PCBM ratios of 1/1.1 (blue ★) and 1/1.0 (green ▲). Reprinted with permission from ref. 132. Copyright 2012 American Chemical Society.

The alloy model was proposed by Thompson and co-workers to explain how the tunable V_{OC} in the ternary solar cells occurs.¹³³ The V_{OC} could be adjusted continuously with various compositions of donors or acceptors, which has been described in the previous section. The V_{OC} of OSCs is determined by the energy of interface bandgap (E_{GI}) minus the quasi-Fermi energies, where the E_{GI} is the energy difference value between the HOMO energy level of the donor and the LUMO energy level of the acceptor. The reason for continuous change in V_{OC} is the corresponding change in the HOMO or LUMO energy level, it is possible that the effect reflects the change in the quasi-Fermi energies. The photocurrent spectral response (PSR) of the ternary solar cells was measured to explore the electronic states and then to confirm the continuous change in the HOMO or LUMO energy level (Fig. 34). The PSR experimental results provide some information about the electronic states by measuring the optical absorption of active layer transitions that generate charge carriers in the solar cells. It was reported that when the energy is below the optical bandgap of each material, the PSR spectrum results from direct excitation at the interface from the donor HOMO to the acceptor LUMO (Fig. 34(a) inset) and measures the optical absorption of the heterojunction interface. The excitation is generally considered as the charge-transfer (CT) state. Fig. 34(a) shows the PSR spectrum of the P3HT/ICBA/PCBM ternary solar cells. Previous investigations confirm that the E_{GI} corresponds to a photocurrent of $\sim 10^{-4}$ of the peak value, and where the shape of the PSR spectrum changes from an exponential at lower energy to a broader band at higher energy.¹⁸⁶ The E_{GI} energy at

photocurrent values of 0.1 and 0.01 (dashed lines in Fig. 34(a)) and the V_{OC} of ternary solar cells are summarized in Fig. 34(b). It is evident that the V_{OC} is ~ 0.55 V smaller than the E_{GI} , which is similar to the expected quasi-Fermi energies. The results indicate that the change in the E_{GI} was accurately measured by V_{OC} and that E_{GI} changes continuously with the composition of two-component acceptors. The composition dependence of the bandgap for an alloy is often described by the following equation,

$$E_{GI}(x) = (1 - x)E_{G1} + xE_{G2} - bx(1 - x) \quad (7)$$

Here b is the bowing factor, and E_{G1} and E_{G2} are the bandgaps of the corresponding materials. This model fits the measured data very well, as shown in Fig. 34(b). The analogous data for ternary solar cells based on the P3HT75-*co*-EHT25/P3HTT-DPP-10%/PCBM system are shown in Fig. 34(c) and (d). The HOMO energy levels of two donors are slightly different (5.2 eV for P3HTT-DPP-10% and 5.4 eV for P3HT75-*co*-EHT25) but optical bandgaps have big difference (1.5 and 1.9 eV, respectively). In the two donor system, the V_{OC} also can be continuously changed along with different proportions of two donors, but the change is smaller than that of the system with two acceptors. These results indicate that either two donors or two acceptors form an electronic alloy with HOMO and LUMO energies based on the average composition of two-component donors or acceptors, resulting in variation of V_{OC} with composition in these two components. The same group further studied the effect of different miscibility between the used materials on the

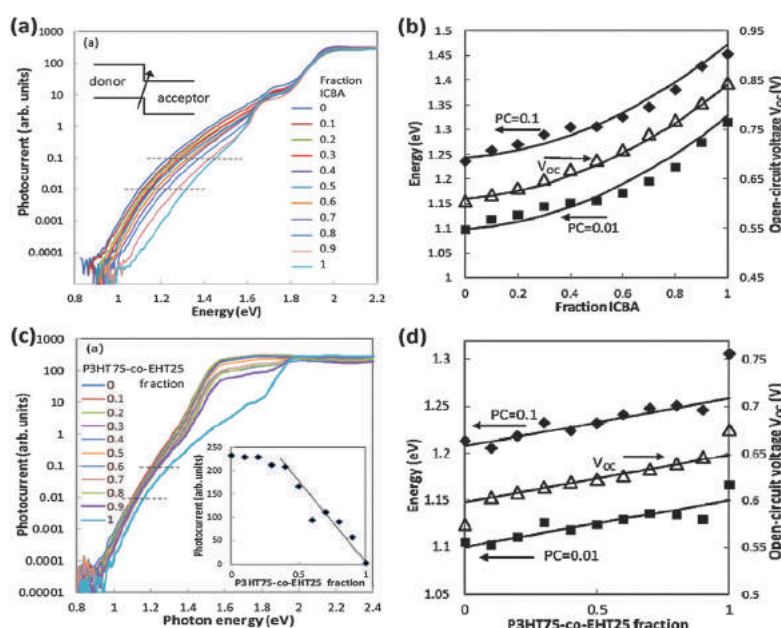


Fig. 34 (a) PSR spectrum of the ternary solar cells based on the P3HT/ICBA/PCBM system with various proportions of ICBA in acceptors. The inset represents the E_{GI} or CT transition; (b) the estimated E_{GI} energy defined by PSR at photocurrent values of 0.1 and 0.01 compared to the values of V_{OC} for P3HT/ICBA/PCBM ternary solar cells. The solid lines are the model of eqn (8) with the same bowing parameter b ; (c) PSR spectrum of the ternary solar cells based on P3HTT-DPP-10%/P3HT75-*co*-EHT25/PCBM with various proportions of P3HT75-*co*-EHT25 in donors. The inset represents the photocurrent signal at 1.6 eV with a proportion of P3HT75-*co*-EHT25 in donors and (d) plot of the estimated E_{GI} energy defined by PSR at photocurrent values of 0.1 and 0.01 compared to the values of V_{OC} (open triangles), as a function of P3HT75-*co*-EHT25 fraction for the mixed donor system. Solid lines are linear fits to the data with the same slope ($b = 0$). Reprinted with permission from ref. 133. Copyright 2013 American Chemical Society.

alloy behavior. The polymer PCDTBT as the third component was incorporated with the P3HTT-DPP-10%:PCBM system. The HOMO energy levels of P3HTT-DPP-10% and PCDTBT are 5.2 eV and 5.4 eV, respectively, which translates to the V_{OC} of 0.582 V for P3HTT-DPP-10%:PCBM-based and 0.924 V for PCDTBT:PCBM-based binary solar cells. Unlike the continuous change in the V_{OC} with composition that was observed in the P3HT:PCBM:ICBA system and the P3HTT-DPP-10%:P3HT75-co-EHT25:PCBM system, the V_{OC} of P3HTT-DPP-10%:PCDTBT:PCBM-based solar cells changes by only 23 mV going (from 0.582 V to 0.605 V) along with the increase of PCDTBT from 0 to 95%. Thus, only 5% of P3HTT-DPP-10% in ternary solar cells pins the V_{OC} to the smallest V_{OC} value of the two limiting binary blend solar cells. These results indicate that alloy formation between polymers does not occur in the P3HTT-DPP-10%:PCDTBT:PCBM system, as even 95% of PCDTBT in the polymer fraction has little effect on the V_{OC} , which is demonstrated by the PSR and EQE measurements. Furthermore, the ternary solar cells with a high PCDTBT content show lower J_{SC} , FF, and PCE than the corresponding binary solar cells. These results mainly ascribe to the lack of miscibility between the polymers, which facilitates preferential location of the P3HTT-DPP-10% away from the PCBM interface with high PCDTBT contents and does not allow CT state averaging or effective hole transport. The authors further proposed the use of the surface energy of the used materials in the ternary solar cells as a figure of merit to predict the formation of an organic alloy and compositional dependence of the V_{OC} of ternary solar cells. Similar surface energy should facilitate material mixing and formation of an alloy state, while large difference in the surface energy should result in demixing, preventing alloying state formation and causing significant performance decrease of the ternary solar cell. As such, miscibility among materials is a necessary attribution for forming the alloy state between different materials. However, it is not clear that if miscibility is sufficient for alloy formation and future work need to focus on other effects, such as HOMO energy, relative crystallinity, and compatibility of the used materials.

Zhang and co-workers also reported the tunable behaviour of V_{OC} in the ternary solar cells with P3HT:SMPV1:PC₇₁BM as active layers.¹¹⁶ The V_{OC} of the ternary solar cells can be monotonically improved along with the increase of SMPV1 doping ratios in donors. The photoemission spectroscopy (UPS) was employed to investigate the HOMO energy levels of P3HT, SMPV1 and P3HT:SMPV1 films due to the direct relationship between V_{OC} and the alloy HOMO energy levels of electron donors, and then to clarify the effect of SMPV1 doping ratios on V_{OC} of ternary solar cells. The HOMO energy level can be calculated according to the following equation,

$$E_{HOMO} = h\nu - (E_{onset} - E_{cutoff}) \quad (8)$$

where $h\nu$ is the incident photon energy of 36 eV; E_{cutoff} is defined as the lowest kinetic energy of the measured electrons and E_{onset} is the HOMO energy onset, generally referred to as the high kinetic energy onset.^{187,188} The E_{cutoff} and E_{onset} locations of P3HT, P3HT:SMPV1 (1:1), and SMPV1 films are

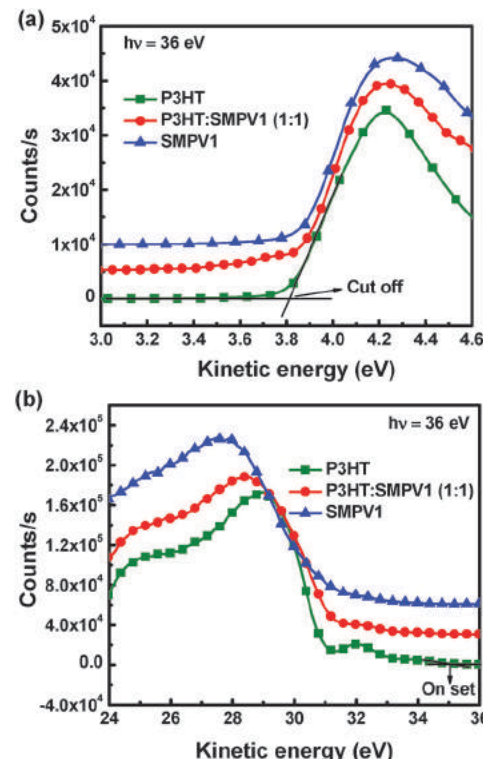


Fig. 35 UPS spectra of the inelastic cutoff region (a) and the HOMO region (b) of P3HT, P3HT:SMPV1 (1:1) and SMPV1 films (photon energy is 36 eV), measured under ultrahigh vacuum (10^{-9} Pa) conditions. Reprinted with permission from ref. 116. Copyright 2015 American Chemical Society.

marked in Fig. 35(a) and (b), respectively. According to Fig. 35 and the above equation, the calculated HOMO energy levels are -4.82 eV for P3HT, -4.97 eV for P3HT:SMPV1 and -5.26 eV for SMPV1. The V_{OC} of the OSCs is increased from 0.59 V to 0.64 V for the cells with 15 wt% SMPV1 and even to 0.73 V for the cells with 50 wt% SMPV1. The monotonically increased V_{OC} of ternary solar cells can be well explained by the decreased alloyed HOMO energy levels of P3HT:SMPV1 along with the increase of SMPV1 doping ratios in donors. This result suggests that P3HT and SMPV1 should have excellent miscibility to form an electronic alloy with the varied HOMO energy levels along with different SMPV1 doping ratios in donors.

Instead of the alloy model demonstrated by Thompson and co-workers, You *et al.* proposed the parallel-linkage mechanism to explain the tunable behaviour of V_{OC} in ternary solar cells. In this scenario, the holes generated in different donors mainly transport through their corresponding donor-linked channels to the anode, while electrons still transport *via* the acceptor domain to the cathode, equivalent to a parallel connection of two binary solar cells. It means that two donors can independently work with the acceptor. Consequently, the V_{OC} is co-determined by the two HOMO energy levels of the donors.⁹⁰

Janssen *et al.* further proposed a two-state CT model to explain the tunable behaviour of V_{OC} in ternary solar cells with a semiconducting biphenyl-dithienyldiketopyrrolopyrrole copolymer (PDPP2TBP) as the donor and two different fullerene (PCBM and ICBA) acceptors.¹⁸⁰ The ternary solar cells show a gradual

increase in V_{OC} from 0.81 to 1.07 V with increasing doping ratios of ICBA, which mainly originates from the changing electronic structure of the ternary blend with various ratios. To study the tunable V_{OC} as the function of PCBM/ICBA ratios, the EQE spectra were measured and performed in a semi-logarithmic plot as a function of the photon energy (Fig. 36(a)). It is obvious that the contribution of the CT-state absorption to the EQE mainly located at the range from 1.35 to 1.65 eV (950 nm to 750 nm) is below the onset of PDPP2TBP absorption. The low-energy shoulder gradually disappears along with the increase of ICBA doping ratios, which indicates that the CT-state contribution shifts to higher energies in the EQE spectra of the solar cells. The EQE data are modeled in two different ways by the authors for further understanding the changes in the EQE data as a function of composition: the alloy CT-state model and the two CT-state model. The modeled EQE curves of the alloy CT-state model and the two CT-state model are shown in Fig. 36(b) and (c), respectively. By comparing two models with the experimental EQE data, the two CT-state model fits better with the experiment than the alloy CT-state model, which can be better seen from Fig. 36(d) that plots the photon energy at a normalized EQE = 10^{-3} . The authors further modeled the $J-V$ curves of the ternary solar cells as a parallel bulk heterojunction that is consistent with the two CT-state model. The modeled V_{OC} is more sublinear than the measured values, while the two-state CT model still does not explain the sub-linear behaviour of the V_{OC} as a function of the blend composition.

There is another controversy whether the tunable V_{OC} relies on the blend composition of donors for parallel-linkage ternary solar cells. As mentioned above, many groups have

experimentally confirmed that the V_{OC} of ternary solar cells can be continuously tuned between the V_{OC} values of corresponding binary solar cells as an approximately linear function of the blend composition of each donor (x):

$$V_{OC} = \frac{x_1}{x_1 + x_2} V_{OC1} + \frac{x_2}{x_1 + x_2} V_{OC2} \quad (9)$$

where V_{OC1} and V_{OC2} refer to the open circuit voltages of the binary solar cells with $D_1:A$ and $D_2:A$ as the active layer, respectively. The linear dependence of densities of states (DOS) on the weight fraction of each component can be accurately captured by eqn (9), while it fails to account for the possibility of differential light absorption in the two materials, which will generally affect the occupation probabilities in each band. For example, a ternary solar cell contains a low bandgap donor (1.0 eV), a high bandgap donor (3.0 eV), and a typical acceptor. In this blend, assuming the high bandgap donor has a negligible absorption coefficient, virtually all of the light would be absorbed by the low bandgap donor, yet eqn (9) would predict the V_{OC} as though the high bandgap donor valence band possessed half the photogenerated holes. Thus eqn (9) generally overestimates V_{OC} in cases where a low-voltage strongly absorbing $D_1:A$ combination is paired with a high-voltage weakly absorbing $D_2:A$ blend. This incorrect limiting behavior can be corrected by weighting each component's voltage contribution by its current production:

$$V_{OC} = \frac{J_1}{J_1 + J_2} V_{OC1} + \frac{J_2}{J_1 + J_2} V_{OC2} \quad (10)$$

where $J_i = \frac{q}{hc} \int_{\lambda_1}^{\lambda_2} \text{EQE}(\lambda) \cdot P_{in}(\lambda) \cdot \lambda d\lambda$ is the current generated from an equal thickness reference binary solar cells composed

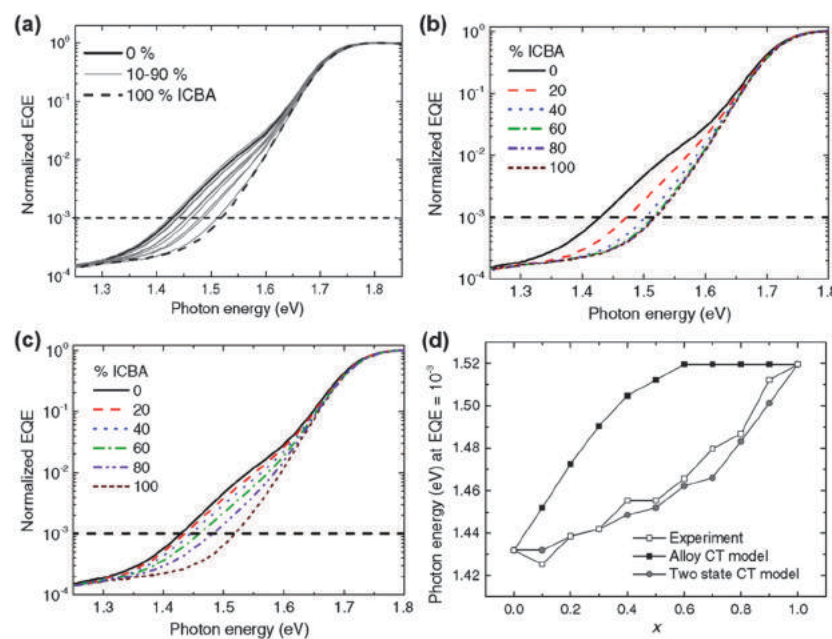


Fig. 36 (a) Normalized EQE as a function of photon energy for experimental data. Modeled EQE curves for different relative ratios of ICBA (x): (b) the alloy CT-state model and (c) the two CT-state model. (d) Photon energy at a normalized EQE = 10^{-3} for PDPP2TBP:PCBM:ICBA ternary solar cells as a function of the relative ratio of ICBA (x). The experimental data (open squares) are compared to two models: the alloy CT-state model (solid squares) and the two CT-state model (solid circles). Reprinted with permission from ref. 180. Copyright 2015 SPIE.

of D₁:A, under short circuit conditions.¹⁸¹ Eqn (10) reproduces the linear dependence observed experimentally for donors that absorb similar amounts of light, while also recovering the appropriate limiting behavior when the two donors have disparate absorption features.

Given the above discussion, the V_{OC} of the ternary solar cells can be continuously tuned with composition of donor or acceptor changes, which allows a higher V_{OC} in the ternary solar cells than that of the corresponding binary solar cells, providing the ternary strategy as a platform for highly efficient next generation organic solar cells. However, there are still some arguments about the tunable V_{OC} in the ternary solar cells. Therefore, further investigation on the intriguing V_{OC} is certainly required to verify the underlying mechanisms for high efficiency ternary solar cells.

3.3 Versatile function of the third component

In addition to enhanced photon harvesting and tunable energy level, the ternary solar cells also show more efficient exciton dissociation, charge transport and extraction, as well as better stability, phase separation and crystallinity of the active films by optimizing the morphology. The V_{OC} of the OSCs can be increased by incorporating a second donor with a lower HOMO energy level (D₂) or a second acceptor with a higher LUMO energy level (A₂) as the third component. The J_{SC} has a good relationship with photon harvesting, exciton dissociation, charge carrier transport and extraction, which can be well optimized by the versatile ternary strategy. The FF is a very sensitive parameter, which is determined by the competition

between sweep-out of the photoinduced charge carriers and the recombination of charge carriers to the ground state. The ternary strategy can increase FF by balancing charge carrier transport and reducing charge carrier recombination. In the following section, we mainly focus on the multiple advantages of ternary solar cells.

Wei *et al.* demonstrated a high efficiency ternary solar cell by employing a high-performance polymer PTB7-Th and a high-crystalline small molecule 7,7-(4,4-bis(2-ethylhexyl)-4H-silolo[3,2-b:4,5-b']dithiophene-2,6-diyl)bis(6-fluoro-4(5'-hexyl-[2,2'-bithiophen]-5-yl)benzo-[c] [1,2,5]thiadiazole) (p-DTS(FBTTH₂)₂) as two donors, and PC₇₁BM as an acceptor.⁸⁵ The optimized ternary solar cells with 15 wt% p-DTS(FBTTH₂)₂ achieved a higher average PCE of 10.5% due to the substantial improvement in FF and a slight J_{SC} increase. The FF (75.27%) of the optimized ternary solar cells is much higher than that of the PTB7-Th:PC₇₁BM-based (65.26%) and p-DTS(FBTTH₂)₂:PC₇₁BM-based (59.74%) binary solar cells, which have a close connection with crystallinity and molecular orientation of the active layer. The molecular stacking and orientation of the active layer was probed and studied by the GIWAXS. As described in Fig. 37, the PTB7-Th molecules have a preferential face-on orientation and the p-DTS(FBTTH₂)₂ molecules show a edge-on orientation with respect to the substrate. The face-on orientation is beneficial to reduce the recombination of charge carrier during the transport and collection process. Compared with the PTB7-Th:PC₇₁BM blend film, the face-on π - π stacking peak of the ternary blend film with a low p-DTS(FBTTH₂)₂ content (≤ 15 wt%) becomes more remarkable in the 2D images and sharper in out-of-plane direction, thus indicating an increased

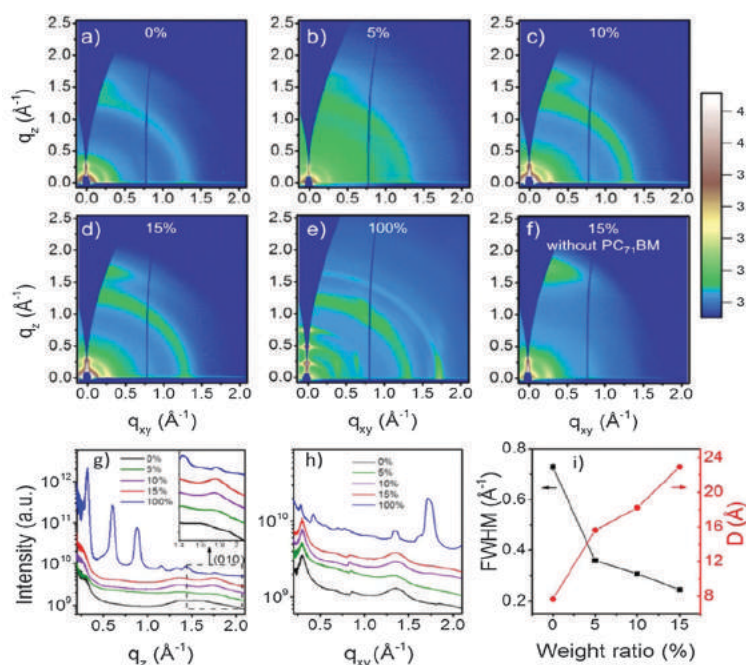


Fig. 37 Two-dimensional GIWAXS patterns of PTB7-Th:p-DTS(FBTTH₂)₂:PC₇₁BM active layer films. The weight ratio of p-DTS(FBTTH₂)₂ in donors is (a) 0, (b) 5%, (c) 10%, (d) 15%, (e) 100%, and (f) 15% (without PC₇₁BM). The out-of-plane (g) and in-plane (h) cuts of the corresponding 2D GIWAXS patterns. (010) diffraction peak is enlarged in the inset profile. (i) Peak full-width half-maximum (FWHM) of the (010) peak (black symbols) and the correlation length of the π - π stacking (red symbols). Reprinted with permission from ref. 85. Copyright 2015 American Chemical Society.

ratio of face-on oriented molecules. Furthermore, there is no aggregation of small molecules either on the top surface or the bottom of the ternary blend films when p-DTS(FBTTH₂)₂ weight ratios are less than 15%. This result indicates that the small amount of p-DTS(FBTTH₂)₂ can be well mixed in the PTB7-Th rich phase and has almost no influence on the bicontinuous phase separation in ternary solar cells. As shown in Fig. 37(i), the correlation length of the π - π stacking is increased from ~ 8 Å to ~ 23 Å along with the increase of p-DTS-(FBTTH₂)₂ from 0 wt% to 15 wt%, which helps to enhance charge carrier mobility and charge collection efficiency. The presence of p-DTS(FBTTH₂)₂ further is beneficial to purify PTB7-Th domains, which facilitates the charge transport and reduces charge carrier recombination in ternary solar cells. Thus, the high FF of ternary solar cells mainly results from the high degree of ordering, face-on π - π stacking, short π - π stacking distance, and relatively pure domains.

Yan *et al.* investigated the effect of high-mobility conjugate polymers as the third component on the performance of the ternary solar cells.⁸⁴ The ternary solar cells with PTB7:PC₇₁BM as the dominating system and high-mobility polymer alkylidiketopyrrolopyrrole and dithienylthieno[3,2-*b*]thiophene (DPP-DTT) as additives achieve an average PCE of 8.33%, which is much higher than the PTB7:PC₇₁BM-based (7.58%) and DPP-DTT:PC₇₁BM-based (2.3%) solar cells. The improvement of the performance is mainly attributed to increased hole mobility. As shown in Fig. 38(a), the hole mobility is gradually increased along with the increase of the DPP-DTT ratio, which is reasonable due to the high hole mobility of DPP-DTT. However, the electron mobility decreases with the increase of the DPP-DTT percentage and shows a close value of hole mobility when the DPP-DTT percentage is around 1 wt% (Fig. 38(c)). It is well known that more balance of carrier mobility between electrons and holes is favourable for charge carrier transport and collection of OSCs, which well accords with the highest PCE obtained at 1 wt% DPP-DTT. Furthermore, choosing a suitable high-mobility polymer with similar HOMO levels to the dominating donor as complementary materials is a key issue for improving the performance of ternary solar cells. The PCE of ternary solar cells is promoted to 10.08% by employing PBDTTT-EFT:PC₇₁BM as the dominating system and a high mobility polymer poly[2,5-bis(alkyl)pyrrolo[3,4-*c*]pyrrole-1,4(2H,5H)-dione-*alt*-5,50-di(thiophene-2-yl)-2,20-(*E*)-2-(2-thiophen-2-yl)vinyl]thiophene] (PDVT-10) as the third component.

The nonvolatile, crystalline and conducting P3HT, as an effective morphology control agent, was incorporated into the PCPDTBT:PCBM matrix by Chang and co-workers.¹⁸⁹ As shown in Fig. 39, the root-mean-square (RMS) roughness of the surface is about 4.6 nm for PCPDTBT:PCBM thin films, increased to 5.4 nm for ternary blend films with 1 wt% P3HT, and then further increased to 26.7 nm by adding 3 vol% DIO into the ternary blend films. This result indicates that P3HT truly acts as a morphology modulator to control the morphology of the active layers. The ternary blend films with 1 wt% P3HT shows larger and longer domain size of the separated phase than that of PCPDTBT:PCBM-based films, as can be seen from the TEM images. The size and length of the separated domains of the

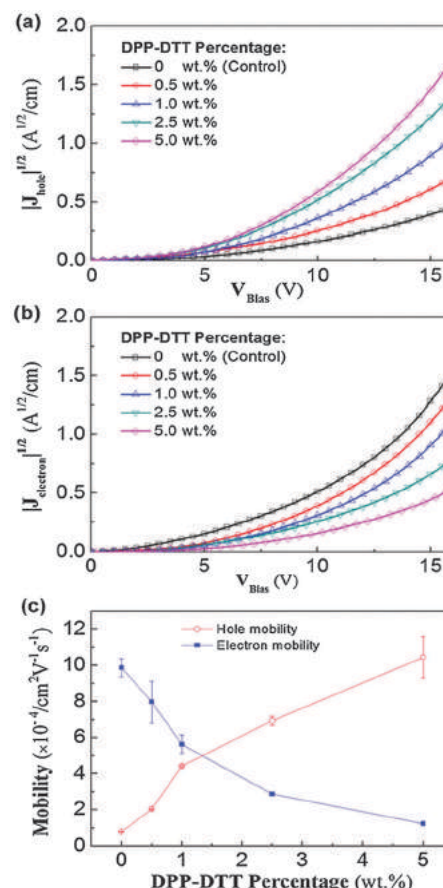


Fig. 38 (a) Square root of hole current densities versus bias voltage of ITO/PEDOT:PSS/PTB7:DPP-DTT:PC₇₁BM/Au devices with various DPP-DTT percentage. (b) Square root of electron current densities versus bias voltage of the ITO/ZnO/PTB7:DPP-DTT:PC₇₁BM/Al devices with various DPP-DTT percentage. (c) Electron and hole mobilities calculated from the SCLCs. Reprinted with permission from ref. 84. Copyright 2015 Royal Society of Chemistry.

ternary blend films is further increased by adding 3 vol% DIO, which is beneficial to the charge transport in the active layers. The ternary blend films with 1 wt% P3HT also shows increased scattering intensity than the binary films, which indicates an improved phase separation for the better exciton dissociation and charge transport (Fig. 39(b)). The PCE of PCPDTBT:PCBM-based solar cells can be improved 20% by adding 1 wt% P3HT into the blend films. Moreover, the 17% improvement of PCE can be further obtained by incorporation of 3 vol% DIO into the ternary blend films. The increased performance mainly attributes to the favourable bi-continuous phase separation and appropriate domain size of each phase in the ternary active layers.

In addition to increase the phase separation, ternary strategy also can prevent the clustering of crystalline molecules. It is well known that the highly symmetric molecule ICBA generally results in serious horizontal phase separation of the active layer, which reduces the V_{OC} and J_{SC} of solar cells. Lin *et al.* also employed a conjugate polymer PVK with high carrier mobility as an additive to disperse the ICBA clustering in the

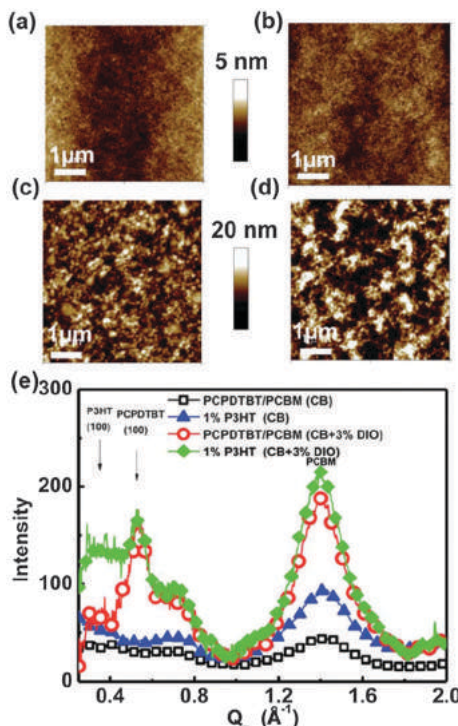


Fig. 39 AFM images of (a) PCPDTBT/PCBM and (b) PCPDTBT/PCBM/P3HT (1 wt%), (c) PCPDTBT/PCBM with 3 vol% DIO and (d) PCPDTBT/PCBM/P3HT (1 wt%) with 3 vol% DIO films. (e) The corresponding out-of-plane GIXRD profiles of the four thin films. Reprinted with permission from ref. 189. Copyright 2013 Royal Society of Chemistry.

P3HT:ICBA matrix.¹⁹⁰ As shown in Fig. 40, PVK can be effective to avoid the ICBA aggregation into the island and shunt path, which was also demonstrated by surface morphology according to the AFM images. The active layer film shows uniform morphology by adding 13 wt% PVK in P3HT:ICBA, resulting in simultaneously optimized J_{SC} and V_{OC} of ternary solar cells. The PCE of ternary solar cells is further improved to 4.5% by selecting CuO_x as the hole transport layer. Zhang *et al.* incorporated a low bandgap polymer PBDTTT-C into the P3HT:ICBA matrix to increase the photon harvesting of the active layer and tailor the miscibility between P3HT and ICBA.¹⁰⁰ The ternary solar cell with 1 minute 150 °C annealing treatment shows a PCE of 4.38%, which is much higher than that of P3HT:ICBA-based solar cells (3.32%).

In order to study the effect of the third component on the microstructure of the ternary active layers, Sellinger *et al.* utilized GIWAXS technology to clarify the role of a *tert*-butyl-functionalized silicon 2,3-naphthalocyanine bis(trihexylsilyloide) (*t*-butyl SiNc) in enabling higher dye doping ratios in P3HT:PCBM to harvest more photons in the longer wavelength range.¹⁹¹ Fig. 41 shows X-ray scattering images for P3HT:PCBM films, both as-cast and annealed (Fig. 41(a) and (b)), along with images for ternary blends of P3HT:PCBM with 20 wt% *t*-butyl SiNc (unannealed in Fig. 41(c) and annealed in Fig. 41(d)) and 20 wt% unfunctionalized SiNc (unannealed in Fig. 41(e) and annealed in Fig. 41(f)). The GIWAXS images of ternary films containing the *t*-butyl SiNc

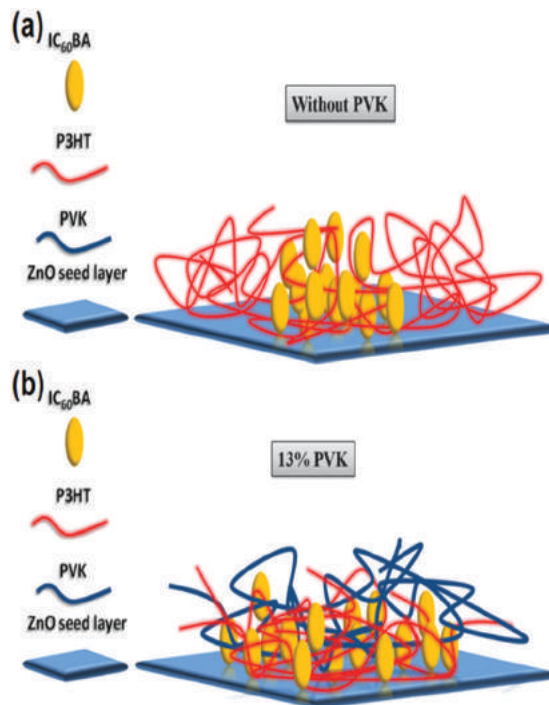


Fig. 40 Schematic structure of molecular chain distribution in the active layer is blended with the following (a) 0% and (b) 13% PVK, which dispersed ICBA aggregation cluster by the PVK molecular chain. Reprinted with permission from ref. 190. Copyright 2013 Elsevier.

closely resemble the binary P3HT:PCBM blend films, where the typical (100) and (010) peaks of the P3HT and characteristic ring of the PC60BM are clearly visible along with a few rings of moderate intensity that are likely due to scattering from the *t*-butyl SiNc molecules. This would be a scattering pattern that is commensurate with either a lightly disordered *t*-butyl SiNc phase or mixing of *t*-butyl SiNc molecules within a disordered P3HT, disordered PCBM, or mixed P3HT:PCBM amorphous phase. In contrast, the ternary blends containing the unfunctionalized SiNc show significant scattering intensity from peaks not associated with either the P3HT or PCBM, indicating a highly ordered and textured SiNc phase within the ternary blend film. This pattern would be commensurate with a film morphology that has relatively large volumes of ordered SiNc phase and low fractions of SiNc molecules contained within an amorphous mixed phase between the P3HT and PCBM. These data, taken with the efficiency and EQE data, suggest that the morphological differences are the key reasons behind the capability to incorporate higher volumes of *t*-butyl SiNc into the P3HT:PCBM blend film without disruption of the optimal BHJ microstructure and resulting in the decrease of PCE of ternary solar cells.

Brabec *et al.* also reported that the effect of low bandgap polymer analogues of C- and Si-bridged PCPDTBT as near IR sensitizers on the morphology of ternary active layers based on the main systems of P3HT:PCBM or P3HT:ICBA.^{192,193} The binary blend system contains crystalline P3HT and PCBM parts embedded in an amorphous matrix of both components.¹⁹⁴ Addition of 20 wt% C-PCPDTBT decreases the crystallinity of

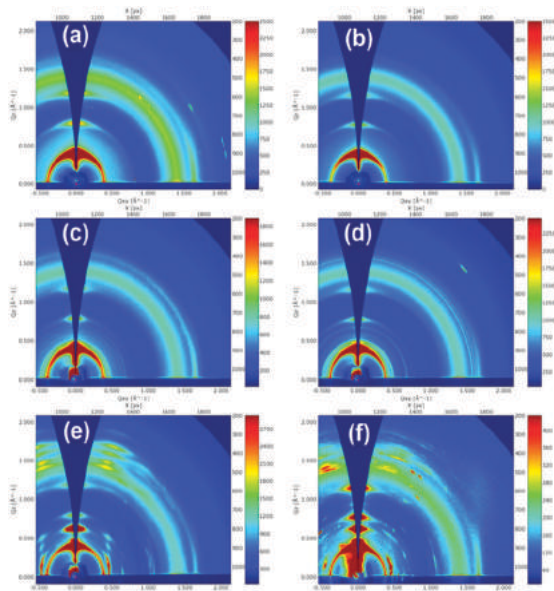


Fig. 41 Two-dimensional X-ray scattering patterns of P3HT:PCBM films with the following dye additions and thermal treatments: (a) no dye, unannealed; (b) no dye, annealed; (c) 20 wt% t-butyl SiNc, unannealed; (d) 20 wt% t-butyl SiNc, annealed; (e) 20 wt% unfunctionalized SiNc, unannealed; and (f) 20 wt% unfunctionalized SiNc, annealed. Reprinted with permission from ref. 191. Copyright 2014 American Chemical Society.

PCBM as observed from GIWAXS patterns. Since the impact on P3HT crystallinity is relatively small, it is concluded that C-PCPDTBT is dominantly embedded in the amorphous part of P3HT. With higher amounts of C-PCPDTBT, the crystallinity of PCBM is strongly damaged and hardly recognizable with GIWAXS measurements. Furthermore, the P3HT crystallinity is diminished as compared to that of the binary blend. At this high C-PCPDTBT concentration, the amorphous part from all three materials becomes the main phase with small inclusions of P3HT and PCBM crystals. Adding high content of C-PCPDTBT mainly influences the semi-crystallinity (aggregation) of the PCBM and reduces the electron mobility, but Si-PCPDTBT impacts mainly the P3HT ordering and, in turn, deteriorates the hole mobility. These findings show that the disruption of the fullerene semi-crystalline domains is more detrimental to the device performance than the disruption of the polymer domains. The GIWAXS experimental results provide further investigation on the device performance dependence on the morphology or microstructure of the ternary active layers.

The ternary strategy has been proven a viable strategy for not only accommodating the phase separation of the active layer, but also optimizing photoconductivity in the OSCs by choosing an appropriate third component. According to the conducting properties, semiconductors can be classified as p-type or n-type materials exhibiting different charge carrier transport ability. The balance of charge carrier transport in the active layers is one of the key issues for obtaining high performance solar cells. p-Type or n-type materials have been selected as the third component to balance the charge carrier transport and simultaneously increase photon harvesting. Nguyen *et al.* reported high

performance ternary solar cells with a widely used fluorinated molecular p-type dopant, 2,3,5,6-tetrafluoro-7,7,8,8-tetracyanoquinodimethane (F4-TCNQ) as the third component and PCDTBT:PC₇₁BM as the dominating system.¹⁹⁵ By controlling the doping concentration of F4-TCNQ/PCDTBT at 1/250, the ternary solar cells achieve a PCE of 7.94%, which is much higher than that of the PCDTBT:PC₇₁BM-based solar cells (6.41%). The performance improvement mainly attribute to the increase of charge carriers due to background carriers induced by F4-TCNQ and the enhancement of tail absorption by the active layer. The transient photoconductivity measurements were performed to study how the molecular doping influenced the charge transport kinetics. As presented in Fig. 42(a), the ternary solar cells exhibit a greater number of initial mobile carriers than the binary solar cell, which is beneficial to the efficient charge carrier collection. Moreover, the normalized curves of the ternary solar cells are identical to each other, suggesting that the different concentration of F4-TCNQ in the ternary solar cells have the predominant effect of altering the absorption spectrum, and not the rates of charge carrier sweep-out/recombination in the ternary active layers. This result is evident that the increase in dark carrier density does not significantly increase charge carrier recombination. Fig. 42(b) shows a 20–25% increase of the total extracted charge carrier, which is consistent with the performance improvement of ternary solar cells.

It has been demonstrated that the electrical properties of the semiconducting polymers can be modified *via* molecular doping with charge transfer between the host material and dopant molecules.¹⁹⁶ However, the choices of the dopant molecules used in polymeric materials are limited, as it requires good compatibility in solubility and efficient charge transfer. Tetrafluoro-tetracyanoquinodimethane (F4-TCNQ) has been confirmed as an effective p-type molecular dopant contributing

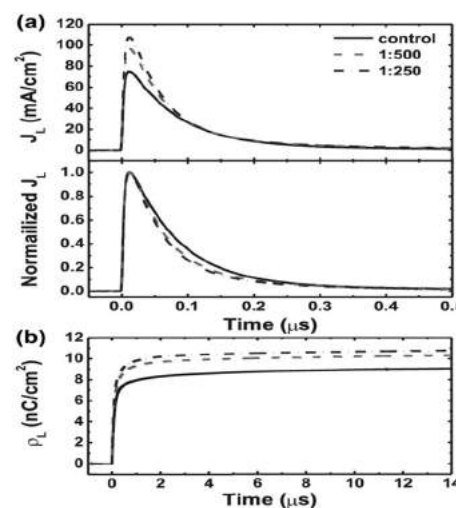


Fig. 42 (a) Decays of the photocurrent density J_L (upper panel) and normalized J_L (lower panel) of PCDTBT:PC₇₁BM solar cells without and with F4-TCNQ when measured at zero bias under 590 nm excitation. (b) Total swept-out charge carrier density (ρ_L) as a function of decay time for PCDTBT:PC₇₁BM solar cells. Reprinted with permission from ref. 195. Copyright 2013 Wiley-VCH.

to an increased photoconductivity and a resultant improved PCE.^{197,198} Recently, a new dopant bis(trifluoromethanesulfonyl)-amide (TFSA) has also been reported as a p-type dopant for carbonaceous materials (carbon nanotubes and graphene) due to its strong electron affinity. Graphene-based Schottky junction solar cells doped with TFSA exhibited a PCE of 8.6%.¹⁹⁹ Xu *et al.* reported that hole mobility was increased with the reduced series resistance in ternary solar cells based on PCDTBT:PCBM matrices doping appropriate TFSA.²⁰⁰ The p-doping effect of TFSA was confirmed by photoemission spectroscopy that the Fermi level of doped PCDTBT shifts downward to the HOMO level and it results in a larger internal electrical field at the donor/acceptor interface for more efficient charge transfer. By controlling the doping concentration (0.2–0.8 wt%, TFSA to PCDTBT), the V_{OC} was increased from 0.85 V to 0.91 V, the FF was increased from 60.7% to 67.3% and an enhanced PCE from 5.39% to 6.46% was further achieved by doping 0.4 wt% TFSA. Molecular doping with extra carriers would lead to lower resistance in PV devices. Fig. 43(a) shows the Nyquist curves of the impedance spectra for undoped and doped PCDTBT:PC₇₁BM cells measured under the open circuit voltage conditions. An apparent change is observed in the doped devices. The real impedance is decreased from 1011 Ω to 918 Ω, 352 Ω and 701 Ω as doping concentrations are increased from 0.2 wt% to 0.6 wt%, respectively. This can be attributed to the contribution of both carrier concentration and carrier mobility. To explore the doping effect of TFSA on PCDTBT, the UPS measurements were carried out at various concentrations and the results are shown in Fig. 43(b). The cut-off energy level of TFSA doped PCDTBT shifts from 15.90 eV to lower binding energy level of 15.85 eV at 0.2% and saturates at 15.73 eV for the rest of the doping concentrations (0.4% to 0.8%), suggesting an increase of work function from 5.32 to 5.37 eV and 5.49 eV, respectively. Because the HOMO level of PCDTBT is at around 5.5 eV, it clearly shows that after doping with TFSA, the Fermi level of PCDTBT shifts downward effectively and leads to a larger effective bandgap at the donor/acceptor interface, and the enlarged effective bandgap should be one of the reasons for the increased open circuit voltage.

N-doped multiwall carbon nanotubes (N-MCNTs) as complementary materials were incorporated into the PTB7:PC₇₁BM matrix by Yu and co-workers, achieving an improved performance of 8.6%.²⁰¹ The incorporation of N-MCNTs leads to not only increased nanocrystallite sizes but also smaller phase-separated domain sizes of both PTB7 and PC₇₁BM, which can be demonstrated by X-ray scattering techniques. As shown in 2D GIWAXS patterns, an in-plane arc-like scattering is observed at $q = 0.3\text{--}0.4 \text{ \AA}^{-1}$ which arises from the Bragg diffraction of periodic PTB7 lamellae, suggesting that PTB7 molecules mainly remain in the face-on orientation with respect to the substrate. The molecular stacking of PTB7 molecules are enhanced after incorporating N-MCNTs into the PTB7:PC₇₁BM matrix. In addition, compared with the binary blend film, the ternary blend film shows stronger scattering intensities of both PTB7 and PC₇₁BM. According to the Scherrer equation, the narrower FWHMs of both the scattering peaks for PTB7 and PC₇₁BM in ternary blend film than that in binary film indicates the increase in

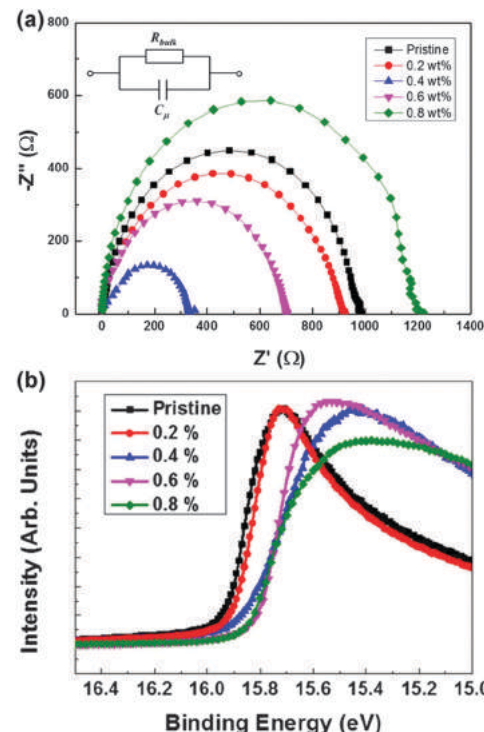


Fig. 43 (a) Nyquist plots of impedance spectra for PCDTBT:PC₇₁BM solar cells with various TFSA concentrations and measured under the V_{OC} condition under dark. Inset shows the equivalent circuits of the devices, where R_{bulk} is the bulk resistance and C_μ the chemical capacitance. (b) UPS spectra of pristine and TFSA-doped PCDTBT film as concentrations vary from 0.2% to 0.8%. Reprinted with permission from ref. 200. Copyright 2015 American Chemical Society.

nanocrystallite sizes of both PTB7 and PC₇₁BM in the ternary film, implying the enhancement of local ordering and thus the increase in crystallinity. The RSoXS profiles of the binary and ternary blend films are shown in Fig. 44(e). The profile of the binary blend film exhibits a diffuse scattering at $q \sim 0.003\text{--}0.02 \text{ \AA}^{-1}$, while that of the ternary blend film shows a well-defined peak within the same q range but centered a larger q value of $\sim 0.006 \text{ \AA}^{-1}$. This illustrates that the ternary blend film has smaller domain sizes than those of binary blend films. These smaller domains would increase the area of interfaces between PTB7 and PC₇₁BM, thereby facilitating exciton dissociation. The effects of NMCNTs in the ternary solar cells can be summarized as: (i) enhancing light absorption of the active layer; (ii) facilitating exciton dissociation in the active layer; and (iii) improving charge collection efficiency of ternary solar cells.

As mentioned above, the LSPR of noble metal NPs, such as Au and Ag NPs, is an effective route to improve the performance of OSCs. Kim *et al.* merged the advantages of metal NPs and carbon nanotubes (CNTs) in ternary solar cells, achieving synergistic enhancements of charge generation, dissociation, and transport.¹⁴⁷ As described in Fig. 45(a), these functional groups mediate strong electrostatic forces or coordinate interaction with N- or B-doped sites at CNTs. The high-resolution transmission electron microscopy (HR-TEM) image (Fig. 45(b)) of Au:BCNT films presents lattice fringes for the (111) planes of

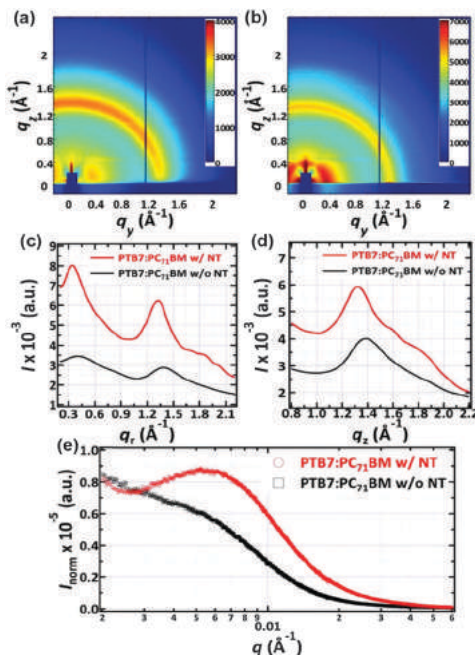


Fig. 44 (a-d) 2D GIWAXS patterns of PTB7:PC₇₁BM blend films without (a) and with (b) N-MCNTs on PEDOT:PSS-modified Si substrates and their in-plane (qr) (c) and out-of-plane (qz) (d) line cuts. (e) RSoXS profiles of the PTB7:PC₇₁BM blend films without (black) and with (red) N-MCNTs. Reproduced with permission from ref. 201. Copyright 2013 American Chemical Society.

Au NPs (0.23 nm) and graphite stacking of BCNTs (0.34 nm). The SEM image of Au:BCNT film in Fig. 45(c) demonstrates that Au NPs are substantially bound along BCNT strands. The incorporation of CNTs with Au NPs does not influence the LSPR behavior of NPs since the ternary films with Au NPs show stronger absorption in the range from 400 to 600 nm than other films, as can be seen in Fig. 45(d). The multiple effect of Au:CNTs for the performance enhancement of solar cells can be summarized in Fig. 45(e): (i) the LSPR effect enhances additional exciton generation; (ii) NP-exciton coupling promotes exciton dissociation; (iii) heteroatom-doped CNTs encourage charge selective transport and avoid charge recombination; and (iv) crystallinity enhancement of ternary films for improved exciton dissociation and charge transport. By incorporating Au NP-decorated nitrogen (N)-doped CNTs (Au:NCNTs) into the PTB7:PC₇₁BM matrix, the ternary solar cells achieved a higher PCE (9.45%) than that of PTB7:PC₇₁BM-based solar cells (8.31%). The ternary solar cells with Au NP-decorated boron (B)-doped CNTs (Au:BCNTs) also show an increased PCE of 9.81%. Introducing Au NPs into the hole transport layer, the performance of the ternary solar cells with Au:BCNTs was further improved to 9.98%.

In addition to the efficiency improvement of OSCs, the device stability is also a key evaluation criterion for its commercialization, such as the 10–10 targets (10% PCE and 10 years of stability) proposed by Krebs *et al.*^{202–204} Crosslinking is a promising approach to maintain long-term thermal stability for the OSCs by “locking” the as-cast morphology. Furthermore, parts

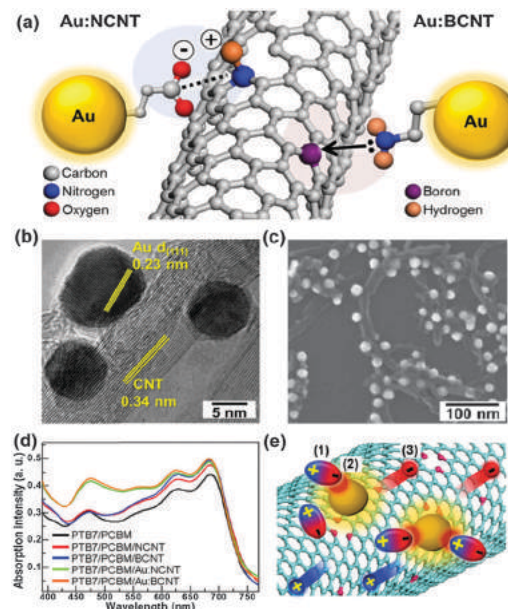


Fig. 45 (a) Schematic chemical interactions for Au:NCNT (left) and Au:BCNT (right) hybrids. (b) HR-TEM image of a Au:BCNT with an interval distance of the BCNT (0.34 nm) and (111) lattice spacing of Au NPs (0.23 nm). (c) Nanometer-scale morphology of Au:BCNTs by SEM. (d) UV-vis absorption spectra of PTB7:PC₇₁BM films with NCNT, BCNT, Au:NCNT and Au:BCNT. (e) Schematic summary of synergistic effects of Au:CNTs: (i) additional exciton generation by LSPR; (ii) promoted exciton dissociation by NP-exciton coupling and (iii) charge-selective fast charge transport along CNT. Reproduced with permission from ref. 147. Copyright 2015 Wiley-VCH.

of crosslinkers also show positive additive effect to boost the efficiency of solar cells by optimizing the microstructure of the active layer film. Rumer *et al.* exploited the advantages of both the small molecule crosslinking and additive concepts for simultaneous enhancement of PCE and stability of OSCs by incorporating a small molecule crosslinker bis-azide 1,6-diazidohexane (DAZH) into polysilaindacenodithiophene-benzothiadiazole (with *N*-octyl side-chains) (SiIDT-BT) and the PC₇₁BM matrix.²⁰⁵ Ternary solar cells exhibited a PCE of 6.8% and 7.0%, for 5 wt% and 10 wt% DAZH, respectively, both which are higher than the efficient SiIDT-BT:PC₇₁BM-based solar cells. The efficient improvement with DAZH as the third component is attributed to the improved FF, which may result from the optimized morphology yielding increased exciton dissociation and improved charge carrier transport. Under 85 °C inert atmospheric conditions (industry standard for realistic solar cell testing), ternary solar cells show better stability, achieving up to >80% retention of PCE after ageing for 130 h (compared to <60% for the binary solar cells). The effects of crosslinking and additive can be proved by Fig. 46. It is obvious that the fullerene crystallization is greatly suppressed by adding bis-azide DAZH, even with the omission of the UV curing step, due to thermal activation of the cross-linker. In addition, the ternary film exhibits more of a fibrillar character as observed by AFM, indicating improved ordering and packing of the polymer backbones. It is concluded that the DAZH acts not only as a stabilizing cross-linker but also as an

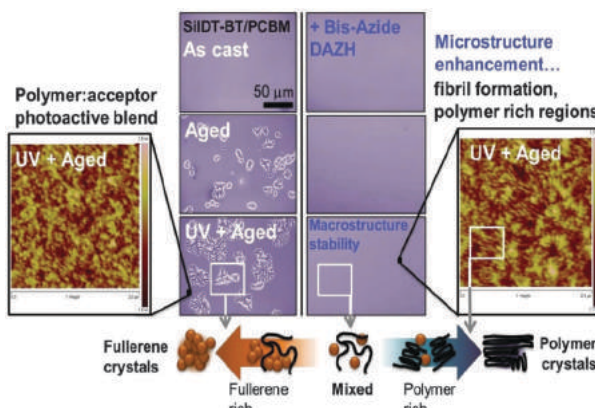


Fig. 46 Crosslinking and thermal ageing morphology: small molecule additives confer macrostructure thermal stability, through suppressed fullerene crystallization (central optical microscopy images), with the bis-azide DAZH additionally enhancing the microstructure through fibril formation (flanking AFM images). Such a “double” picture of morphology highlights the various donor–acceptor phases in BHJ and the microstructure basis of stability. Reprinted with permission from ref. 205. Copyright 2014 Wiley-VCH.

additive in the ternary solar cells, resulting in improved device performance and stability.

The cascade energy level alignment has shown unique effects for achieving high performance ternary solar cells, which has been demonstrated by many groups based on various systems. Groves *et al.* employed a kinetic Monte Carlo model to examine the effect of cascade energy level alignment on geminate charge separation in OSCs.²⁰⁶ It has been demonstrated that the energy cascades can lead to substantial improvement of exciton dissociation efficiency and reductions in charge recombination, resulting in the performance improvement of the solar cells. Zhan *et al.* utilized the advantages of cascade energy level alignment to achieve a highly efficient ternary solar cell with a PTB7:ICBA:PC₇₁BM matrix.¹⁸⁴ Compared to the charge transfer (one route) in binary PTB7:PC₇₁BM solar cells, there are three routes for charge transfer in ternary solar cells. As presented in Fig. 2(b), the excitons generated in PTB7 can be dissociated at both the PTB7/PC₇₁BM and PTB7/ICBA interfaces, and then electrons transport to the cathode through the channels of PC₇₁BM or ICBA, respectively. Meanwhile, the electrons on the LUMO of ICBA can be transferred to the LUMO of PC₇₁BM due to lower energy orbital of PC₇₁BM, which can facilitate charge transfer from PTB7 to ICBA. The PCE of ternary solar cells with 15 wt% ICBA in acceptors reaches 8.24%, which is the highest reported value for ICBA-based ternary solar cells. Recently, the same group improved the PCE to 8.88% by employing the method of diluting concentrated solution.¹⁴¹ Huang *et al.* also reported a ternary solar cell with ICBA and PC₇₁BM as acceptors and small molecule (2Z,2'E)-dioctyl3,3'-(5'',5''''-(4,8-bis(5-octyl-thiophen-2-yl)benzo[1,2-b:5,4-b']dithiophene-2,6-diyl)bis(3,4',4''-triocetyl-[2,2':5',2''-terthiophene]-5'',5-diyl))bis(2-cyanoacrylate) (BDT6T) as a donor.¹⁰⁴ Similarly, the ternary solar cell reached a PCE of 6.36% by incorporating a 15 wt% ICBA relative to PC₇₁BM, which is much higher than both that of BDT6T:PC₇₁BM-based (5.74%) and BDT6T:ICBA-based (2.97%) solar cells.

4 Challenges and outlooks for ternary solar cells

According to the above discussion, the ternary strategy should be a simple, effective and promising way to further improve the performance of OSCs. However, there are still some challenges and limitations for the development of ternary solar cells. The fundamental working mechanisms of ternary solar cells are much more complicated due to the incorporation of the third component than the traditional binary device, which need further investigation for better selection of the active layer materials. The arguments about the tunable V_{OC} in the ternary solar cells are required to further verification for better utilization of the ternary strategy, such as the alloy CT-state model and the two CT-state model. The thickness of the active layer is still a problem for ternary solar cells, which are commonly limited to the same thickness as the corresponding binary devices. The organic photovoltaic materials with long exciton diffusion length and high charge carrier mobility need further research and development. The understanding and controlling of the morphology and crystallinity of the ternary film are also big challenges for ternary solar cells, which are closely related to the compatibility and miscibility. It should be noted that the physical compatibility of the used materials is not the sole decisive factor for good morphology of the ternary blend film. For example, for PTB7:PID2:PC₇₁BM-based solar cells reported by Yu and co-workers, although preferential orientations of PTB7 and PID2 are different (edge-on for PID2 and face-on for PTB7), the morphology of the ternary blend film was actually improved.¹¹⁷ The photophysical interactions between two donors or acceptors play important roles in determining the performance of the ternary solar cells, which is required to better understanding and utilization. Moreover, the competition of the overlap absorption for the photons in the active layer is also a meaningful subject need to be addressed.

According to the fundamental mechanisms, advantages and challenges, the complementary absorption spectra, good compatibility and miscibility, high absorption coefficient, high charge carrier mobility and cascade energy level alignment of active materials are needed to fabricate high efficiency ternary solar cells. Furthermore, the V_{OC} values of these ternary solar cells are essentially located between the V_{OC} of their corresponding binary cells. To get a high V_{OC} in ternary solar cells, the two donors in the D₁/D₂/A system should have similar HOMO energy levels or similar LUMO energy levels in the D/A₂/A₁ system. It should be highlighted that enhancing photon harvesting not only need to improve the light absorption in the NIR, the photon energy in the short wavelength also should be fully utilized. It is encouraging that a series of excellent high bandgap materials have been reported very recently. For instance, poly{dithieno[2,3-d:2',3'-d']benzo[1,2-b:4,5-b']dithiophene-co-1,3-bis(thiophen-2-yl)-benzo-[1,2-c:4,5-c']dithiophene-4,8-dione} (PDBT-T1), PPDT2FBT, PM6 and so on show high performance (PCE > 9%) with a narrow absorption range (300–700 nm).^{207–210} It is reasonable to believe that the realization of a PCE beyond 12% or even 15% might be possible by employing

suitable materials in ternary solar cells, as well as in tandem solar cells. Savoie *et al.* made a significant prediction about the efficiency for different types of ternary solar cells.¹⁸¹ As described in Fig. 47, the predicted efficiencies of parallel-linkage or alloy ternary solar cells are several percentage points above those of other types of devices due to the unique capability of simultaneously collecting carriers from each individual “sub-cells”, resulting in reduced thermalization losses and broad spectral absorption. However in practice, the thickness (~ 100 nm) of active layers has restricted the potential of parallel-linkage or alloy ternary solar cells for improving the performance. It is predicted that sensitized and parallel-linkage architectures are capable of increasing efficiency of $\approx 40\%$ and $\approx 20\%$, respectively, over equal thickness solar cells. If parallel-linkage ternary solar cells are to significantly exceed the performance of their binary sub-cells, means of fabricating thicker devices with well charge carrier transport and collection must be developed, like poly[(5,6-difluoro-2,1,3-benzothiadiazol-4,7-diyl)-*alt*-(3,3'''-di(2-octyldodecyl)-2,2';5',2'';5'',2'''-quaterthiophen-5,5'''-diyl)] (PffBT4T-2OD), poly[(2,5-bis(2-hexyldecyloxy)phenylene)-*alt*-(5,6-difluoro-4,7-di(thiophen-2-yl)benzo[c]-[1,2,5]thiadiazole)] (PPDT2FBT), DT-PDPP2T-TT and so on.^{14,211,212}

In addition to the optimal complementary materials for ternary solar cells, the performance improvement of ternary solar cells strongly depends on further understanding of the working mechanism, especially for the morphology of ternary active layers. Now, the commonly used characterization techniques on surface or bulk morphology of active layers include AFM, SEM, TEM and water contact angle technologies. Very recently, a combination of synchrotron techniques are employed

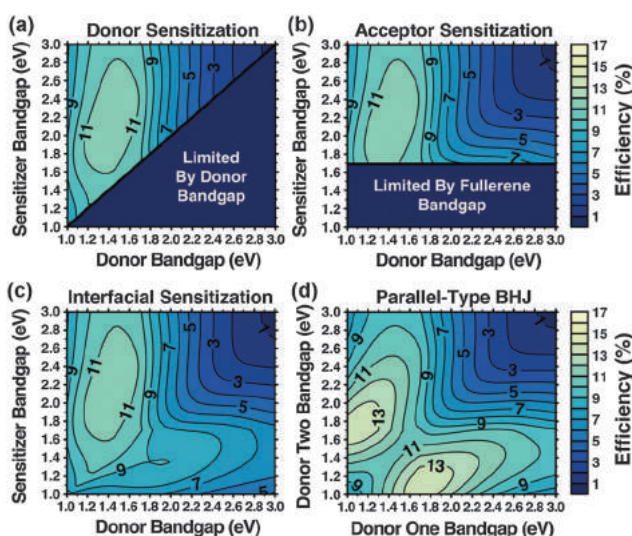


Fig. 47 Predicted PCE in organic photovoltaic D:A blends as a function of the donor bandgap and (a) the donor sensitizer bandgap, (b) acceptor sensitizer, (c) interfacial sensitizer, and (d) second donor in the parallel-linkage architecture. The parallel-linkage architecture possesses the highest potential efficiency and also the sharpest efficiency maximum. This behavior arises in part from the voltage gains returned by the third percolating component. Reprinted with permission from ref. 181. Copyright 2014 Wiley-VCH.

including surface-sensitive near-edge X-ray absorption fine structure (NEXAFS) spectroscopy, bulk-sensitive GIWAXS and RSoXS to investigate the phase separation and domain size of active layers in OSCs.^{213–216} NEXAFS spectroscopy was employed to study the molecular orientation and chemical composition of the blend interfaces which measures X-ray absorption due to the resonant transitions from core states to antibonding states. The intensity of the resonant transition is strongly dependent on the orientation of the transition dipole moment (TDM) relative to the polarization of the incident X-ray beam.^{217,218} By acquiring NEXAFS spectra as a function of X-ray angle of incidence the orientation of π bonds (and hence orientation of the conjugated backbone) can be determined. Three different signals can be recorded during each NEXAFS scan. Partial electron yield (PEY) data (recorded using a Channeltron) have a surface sensitivity of ≈ 1 nm while total electron yield (TEY) data (measured by recording the drain current to the sample) have a surface sensitivity of ≈ 3 nm.²¹⁹ Fluorescence yield (FY) data were also recorded by measuring the X-ray fluorescence from the sample and is bulk sensitive. The GIWAXS pattern provides complementary information regarding crystalline portions of the film. X-rays at an incident angle very slightly above the critical angle of the polymer film but below the critical angle of the silicon substrate optimize the scattering signal from the thin film. The scattered X-rays are detected by the critical angle of the silicon substrate optimizing the scattering signal from the thin film. The scattered X-rays detected by relative crystallinity, polymer orientation and coherence length are straightforward to extract from the 2D scattering pattern *via* the peak area, peak position and FWHM, respectively.²²⁰ The investigations making use of NEXAFS, GISAXS and/or GIWAXS on materials and films used in OSC research are increasing. According to the experimental results from NEXAFS, GISAXS and GIWAXS, valuable information for an in-depth understanding of the complex morphologies and their effects in organic solar cells has already been achieved, although the methods are still developing in the characterization on organic films. It is foreseeable that the use of these new technologies will further increase for further investigation on the effect of phase separation on the performance of OSCs, which is extremely helpful for correlating the structure and function of these devices.¹³⁰ Since the structures are very sensitive to the actual preparation protocol and the used materials in the case of conjugated polymer based solar cells, the new technologies will become the essential tools for structure characterization and should be routinely applied for structure determination. With the latest generation of powerful laboratory X-ray sources, GISAXS and GIWAXS on OSC relevant structures have become feasible in laboratory experiments. These new technologies should provide efficient and deep analysis to clarify the working mechanism of ternary solar cells.

Along with an in-depth investigation on the working mechanism of ternary solar cells, the PCE values of OSCs should be constantly improved due to the unremitting efforts from chemists, physicists and engineers. From practical application in solving the problem of energy and environment, the key parameter, energy payback time, should be further shortened for better satisfying the sustainable development. Krebs *et al.* has analyzed the short energy payback

time due to the material inventory and lower process energy associated with low-temperature roll-to-roll processing and flexible choice in plastic substrates. The large requirements on energy and monetary cost in the ITO sputtering were clearly identified as dominating material cost for OSCs. It is reasonably believed that the energy payback time can be shortened using ITO free plastic substrates. Darling *et al.* also reported the long-term sustainability advantages of organics when compared to silicon and other photovoltaic technologies in terms of energy payback time and global warming potential.⁸ It was preliminarily reported that energy payback times of OSCs are about from 1.35 to 2.02 years corresponding to 3% or 2% PCE, respectively.²¹⁷ The state-of-the-art efficiencies of ternary cells have already been comparable to the best results for either binary or tandem cells. The bright prospects of binary or ternary bulk heterojunction solar cells have appeared in our minds, which inspires the scientists and engineers to make the most of their creativity from chemistry and device physics to promote the development of organic solar cells, especially for ternary solar cells.

5 Conclusions

Ternary organic solar cells enjoy the advantages of enhanced photon harvesting by incorporating multiple organic materials into tandem solar cells and simplicity of processing conditions that is used in single bulk heterojunction solar cells. An appropriate design can offer multiple benefits and synergistic effects, such as optimizing modifying film morphology, crystallinity and improving charge carrier mobility as well as device stability, to obtain high efficiency ternary solar cells. Moreover, all of strategies for optimizing the performance of single bulk heterojunction solar cells can also be effectively applied in ternary solar cells. There is no doubt that the parallel-linkage or alloy model has tremendous potential to improve the performance of OSCs due to unique capability of simultaneously collecting carriers from each sub-component at different chemical potentials, which can be used to reduce thermalization losses while achieving broad spectral coverage. It should also be highlighted that the advantages of charge transfer and energy transfer mechanisms cannot be ignored, one of the donors as the primary charge (hole) transport channel while both donors serve as light absorbers, which could fully utilize the advantages of one donor (high V_{OC} and high charge carrier mobility) and circumvent the disadvantages in another donor. The PCE values of ternary solar cells have been improved to over 10%, showing great potential for obtaining high performance and realizing industrialization production. However, there are still some fundamental physical issues and arguments need to be further clarified for selecting the third component. Based on the research and analysis of the previous reports in the literature, some fundamental issues and development direction probably deserve further investigation: (i) synthesizing novel materials with high absorption coefficient and charge carrier mobility to fully utilize the solar light, such as PDBT-T1, PPDT2FBT, PffBT4T-2OD, and DT-PDPP2T-TT;

(ii) investigating molecular interactions and the photovoltaic process in ternary solar cells to further understand and utilize the third component functions; (iii) employing the optimization techniques in the ternary solar cells to further improve the performance; and (iv) improving the stability of ternary solar cells for its potential application. Though the detailed specific working mechanism and process remain to be further investigated, ternary solar cells provide a new avenue to develop high-performance OSCs with bright application prospects.

Acknowledgements

This work was supported by Fundamental Research Funds for the Central Universities (2015YJS178), the National Natural Science Foundation of China (61377029) and the Beijing Natural Science Foundation (2122050).

Notes and references

- 1 J. S. Wu, S. W. Cheng, Y. J. Cheng and C. S. Hsu, *Chem. Soc. Rev.*, 2015, **44**, 1113–1154.
- 2 A. J. Heeger, *Adv. Mater.*, 2014, **26**, 10–27.
- 3 W. R. Cao and J. G. Xue, *Energy Environ. Sci.*, 2014, **7**, 2123–2144.
- 4 L. Lu, T. Zheng, Q. Wu, A. M. Schneider, D. Zhao and L. Yu, *Chem. Rev.*, 2015, DOI: 10.1021/acs.chemrev.5b00098.
- 5 Y. Lin, Y. Li and X. Zhan, *Chem. Soc. Rev.*, 2012, **41**, 4245–4272.
- 6 N. Espinosa, M. Hosel, D. Angmo and F. C. Krebs, *Energy Environ. Sci.*, 2012, **5**, 5117–5132.
- 7 N. Espinosa, M. Hosel, M. Jorgensen and F. C. Krebs, *Energy Environ. Sci.*, 2014, **7**, 855–866.
- 8 S. B. Darling and F. Q. You, *RSC Adv.*, 2013, **3**, 17633–17648.
- 9 B. Azzopardi, C. J. M. Emmott, A. Urbina, F. C. Krebs, J. Mutale and J. Nelson, *Energy Environ. Sci.*, 2011, **4**, 3741–3753.
- 10 Y. Liu, C. C. Chen, Z. Hong, J. Gao, Y. M. Yang, H. Zhou, L. Dou, G. Li and Y. Yang, *Sci. Rep.*, 2013, **3**, 3356–3363.
- 11 J. You, L. Dou, K. Yoshimura, T. Kato, K. Ohya, T. Moriarty, K. Emery, C. C. Chen, J. Gao, G. Li and Y. Yang, *Nat. Commun.*, 2013, **4**, 1446–1455.
- 12 J. You, C. C. Chen, Z. Hong, K. Yoshimura, K. Ohya, R. Xu, S. Ye, J. Gao, G. Li and Y. Yang, *Adv. Mater.*, 2013, **25**, 3973–3978.
- 13 Z. C. He, B. Xiao, F. Liu, H. B. Wu, Y. L. Yang, S. Xiao, C. Wang, T. P. Russell and Y. Cao, *Nat. Photonics*, 2015, **9**, 174–179.
- 14 Y. Liu, J. Zhao, Z. Li, C. Mu, W. Ma, H. Hu, K. Jiang, H. Lin, H. Ade and H. Yan, *Nat. Commun.*, 2014, **5**, 5293.
- 15 Z. He, C. Zhong, X. Huang, W. Y. Wong, H. Wu, L. Chen, S. Su and Y. Cao, *Adv. Mater.*, 2011, **23**, 4636–4643.
- 16 L. Bian, E. Zhu, J. Tang, W. Tang and F. Zhang, *Prog. Polym. Sci.*, 2012, **37**, 1292–1331.

- 17 F. Zhang, X. Xu, W. Tang, J. Zhang, Z. Zhuo, J. Wang, J. Wang, Z. Xu and Y. Wang, *Sol. Energy Mater. Sol. Cells*, 2011, **95**, 1785–1799.
- 18 X. Guo, C. Cui, M. Zhang, L. Huo, Y. Huang, J. Hou and Y. Li, *Energy Environ. Sci.*, 2012, **5**, 7943–7949.
- 19 G. Li, R. Zhu and Y. Yang, *Nat. Photonics*, 2012, **6**, 153–161.
- 20 G. Yu, J. Gao, J. Hummelen, F. Wudl and A. Heeger, *Science*, 1995, **270**, 1789–1790.
- 21 Y. Liu, F. Zhang, H. Dai, W. Tang, Z. Wang, J. Wang, A. Tang, H. Peng, Z. Xu and Y. Wang, *Sol. Energy Mater. Sol. Cells*, 2013, **118**, 135–140.
- 22 X. Guo, N. Zhou, S. J. Lou, J. Smith, D. B. Tice, J. W. Hennek, R. P. Ortiz, J. T. L. Navarrete, S. Li and J. Strzalka, *Nat. Photonics*, 2013, **7**, 825–833.
- 23 J. B. You, L. T. Dou, Z. R. Hong, G. Li and Y. Yang, *Prog. Polym. Sci.*, 2013, **38**, 1909–1928.
- 24 J. B. You, C. C. Chen, Z. R. Hong, K. Yoshimura, K. Ohya, R. Xu, S. L. Ye, J. Gao, G. Li and Y. Yang, *Adv. Mater.*, 2013, **25**, 3973–3978.
- 25 X. Fan, S. S. Guo, G. J. Fang, C. M. Zhan, H. Wang, Z. G. Zhang and Y. F. Li, *Sol. Energy Mater. Sol. Cells*, 2013, **113**, 135–139.
- 26 Z. Guo, D. Lee, R. D. Schaller, X. B. Zuo, B. Lee, T. F. Luo, H. F. Gao and L. B. Huang, *J. Am. Chem. Soc.*, 2014, **136**, 10024–10032.
- 27 J. Kim, M. H. Yun, G. H. Kim, J. Lee, S. M. Lee, S. J. Ko, Y. Kim, G. K. Dutta, M. Moon, S. Y. Park, D. S. Kim, J. Y. Kim and C. Yang, *ACS Appl. Mater. Interfaces*, 2014, **6**, 7523–7534.
- 28 T. K. An, I. Kang, H. J. Yun, H. Cha, J. Hwang, S. Park, J. Kim, Y. J. Kim, D. S. Chung, S. K. Kwon, Y. H. Kim and C. E. Park, *Adv. Mater.*, 2013, **25**, 7003–7009.
- 29 Z. Q. Guan, J. S. Yu, J. Huang and L. Zhang, *Sol. Energy Mater. Sol. Cells*, 2013, **109**, 262–269.
- 30 H. Y. Chen, S. H. Lin, J. Y. Sun, C. H. Hsu, S. Lan and C. F. Lin, *Nanotechnology*, 2013, **24**, 484009.
- 31 L. Y. Lu and L. P. Yu, *Adv. Mater.*, 2014, **26**, 4413–4430.
- 32 M. J. Tan, S. Zhong, J. Li, Z. K. Chen and W. Chen, *ACS Appl. Mater. Interfaces*, 2013, **5**, 4696–4701.
- 33 N. K. Elumalai, C. Vijila, R. Jose, K. Z. Ming, A. Saha and S. Ramakrishna, *Phys. Chem. Chem. Phys.*, 2013, **15**, 19057–19064.
- 34 Z. A. Tan, S. S. Li, F. Z. Wang, D. P. Qian, J. Lin, J. H. Hou and Y. F. Li, *Sci. Rep.*, 2014, **4**, 4691.
- 35 B. Y. Qi and J. Z. Wang, *Phys. Chem. Chem. Phys.*, 2013, **15**, 8972–8982.
- 36 Y. Y. Liang and L. P. Yu, *Acc. Chem. Res.*, 2010, **43**, 1227–1236.
- 37 Y. F. Li, *Acc. Chem. Res.*, 2012, **45**, 723–733.
- 38 Y. Y. Liang, Y. Wu, D. Q. Feng, S. T. Tsai, H. J. Son, G. Li and L. P. Yu, *J. Am. Chem. Soc.*, 2009, **131**, 56–57.
- 39 C. Piliego, T. W. Holcombe, J. D. Douglas, C. H. Woo, P. M. Beaujuge and J. M. J. Fréchet, *J. Am. Chem. Soc.*, 2010, **132**, 7595–7596.
- 40 Y. Y. Liang, D. Q. Feng, Y. Wu, S. T. Tsai, G. Li, C. Ray and L. P. Yu, *J. Am. Chem. Soc.*, 2009, **131**, 7792–7799.
- 41 J. H. Hou, H. Y. Chen, S. Q. Zhang, R. I. Chen, Y. Yang, Y. Wu and G. Li, *J. Am. Chem. Soc.*, 2009, **131**, 15586–15587.
- 42 S. Alem, J. P. Lu, R. Movileanu, T. Kololuoma, A. Dadvand and Y. Tao, *Org. Electron.*, 2014, **15**, 1035–1042.
- 43 X. Liu, Q. D. Li, Y. C. Li, X. Gong, S. J. Su and Y. Cao, *J. Mater. Chem. A*, 2014, **2**, 4004–4013.
- 44 N. Shin, L. J. Richter, A. A. Herzing, R. J. Kline and D. M. DeLongchamp, *Adv. Energy Mater.*, 2013, **3**, 938–948.
- 45 E. J. Zhou, J. Z. Cong, K. Hashimoto and K. Tajima, *Macromolecules*, 2013, **46**, 763–768.
- 46 B. Gholamkhass and P. Servati, *Org. Electron.*, 2013, **14**, 2278–2283.
- 47 D. J. Kim, B. M. Lee and S. Y. Nam, *Thin Solid Films*, 2013, **546**, 431–435.
- 48 X. N. Yang, J. Loos, S. C. Veenstra, W. J. H. Verhees, M. M. Wienk, J. M. Kroon, M. A. J. Michels and R. A. J. Janssen, *Nano Lett.*, 2005, **5**, 579–583.
- 49 G. Li, Y. Yao, H. Yang, V. Shrotriya, G. Yang and Y. Yang, *Adv. Funct. Mater.*, 2007, **17**, 1636–1644.
- 50 F. C. Chen, H. C. Tseng and C. J. Ko, *Appl. Phys. Lett.*, 2008, **92**, 103316.
- 51 F. C. Chen, C.-J. Ko, J.-L. Wu and W.-C. Chen, *Sol. Energy Mater. Sol. Cells*, 2010, **94**, 2426–2430.
- 52 Y. F. Wang, X. G. Zhao and X. W. Zhan, *J. Mater. Chem. C*, 2015, **3**, 447–452.
- 53 W. Ma, C. Yang, X. Gong, K. Lee and A. J. Heeger, *Adv. Funct. Mater.*, 2005, **15**, 1617–1622.
- 54 Y. Zhao, Z. Xie, Y. Qu, Y. Geng and L. Wang, *Appl. Phys. Lett.*, 2007, **90**, 043504.
- 55 L. Ye, S. Zhang, W. Ma, B. Fan, X. Guo, Y. Huang, H. Ade and J. Hou, *Adv. Mater.*, 2012, **24**, 6335–6341.
- 56 Z. Xiao, Y. Yuan, B. Yang, J. VanDerslice, J. Chen, O. Dyck, G. Duscher and J. Huang, *Adv. Mater.*, 2014, **26**, 3068–3075.
- 57 M. De Jong, L. Van IJzendoorn and M. De Voigt, *Appl. Phys. Lett.*, 2000, **77**, 2255–2257.
- 58 D. Zhao, S. Tan, L. Ke, P. Liu, A. Kyaw, X. Sun, G. Lo and D. Kwong, *Sol. Energy Mater. Sol. Cells*, 2010, **94**, 985–991.
- 59 F. Zhang, D. Zhao, Z. Zhuo, H. Wang, Z. Xu and Y. Wang, *Sol. Energy Mater. Sol. Cells*, 2010, **94**, 2416–2421.
- 60 X. Tu, F. Wang, C. Li, Z. a. Tan and Y. Li, *J. Phys. Chem. C*, 2014, **118**, 9309–9317.
- 61 M. F. Xu, Y. J. Liao, F. S. Zu, J. Liang, D. X. Yuan, Z. K. Wang and L. S. Liao, *J. Mater. Chem. A*, 2014, **2**, 9400–9404.
- 62 S. S. Li, M. Lei, M. L. Lv, S. E. Watkins, Z. A. Tan, J. Zhu, J. H. Hou, X. W. Chen and Y. F. Li, *Adv. Energy Mater.*, 2013, **3**, 1569–1574.
- 63 Q. Xu, F. Z. Wang, Z. A. Tan, L. J. Li, S. S. Li, X. L. Hou, G. Sun, X. H. Tu, J. H. Hou and Y. F. Li, *ACS Appl. Mater. Interfaces*, 2013, **5**, 10658–10664.
- 64 Z. A. Tan, L. J. Li, C. H. Cui, Y. Q. Ding, Q. Xu, S. S. Li, D. P. P. Qian and Y. F. Li, *J. Phys. Chem. C*, 2012, **116**, 18626–18632.
- 65 Z. A. Tan, W. Q. Zhang, D. P. Qian, C. H. Cui, Q. Xu, L. J. Li, S. S. Li and Y. F. Li, *Phys. Chem. Chem. Phys.*, 2012, **14**, 14217–14223.
- 66 K. Zhang, Z. C. Hu, C. H. Duan, L. Ying, F. Huang and Y. Cao, *Nanotechnology*, 2013, **24**, 484003.

- 67 Y.-M. Chang and C.-Y. Leu, *J. Mater. Chem. A*, 2013, **1**, 6446–6451.
- 68 F. Zhang, M. Ceder and O. Inganäs, *Adv. Mater.*, 2007, **19**, 1835–1838.
- 69 Q. Q. Sun, F. J. Zhang, J. Wang, Q. S. An, C. Zhao, L. L. Li, F. Teng and B. Hu, *J. Mater. Chem. A*, 2015, **3**, 18432–18441.
- 70 K. Yao, Y.-X. Xu, F. Li, X. Wang and L. Zhou, *Adv. Opt. Mater.*, 2015, **3**, 321–327.
- 71 W. Shockley and H. J. Queisser, *J. Appl. Phys.*, 1961, **32**, 510–519.
- 72 Z. M. Beiley, M. G. Christoforo, P. Gratia, A. R. Bowring, P. Eberspacher, G. Y. Margulis, C. Cabanetos, P. M. Beaujuge, A. Salleo and M. D. McGehee, *Adv. Mater.*, 2013, **25**, 7020–7026.
- 73 T. Kim, H. Kim, J. Park, H. Kim, Y. Yoon, S. M. Kim, C. Shin, H. Jung, I. Kim, D. S. Jeong, H. Kim, J. Y. Kim, B. Kim, M. J. Ko, H. J. Son, C. Kim, J. Yi, S. Han and D. K. Lee, *Sci. Rep.*, 2014, **4**, 7154.
- 74 H. P. Lu, A. N. Bartynski, M. J. Greaney, M. E. Thompson and R. L. Brutchez, *ACS Appl. Mater. Interfaces*, 2014, **6**, 18306–18311.
- 75 O. Adebajo, P. P. Maharjan, P. Adhikary, M. T. Wang, S. F. Yang and Q. Q. Qiao, *Energy Environ. Sci.*, 2013, **6**, 3150–3170.
- 76 T. Ameri, G. Dennler, C. Lungenschmied and C. J. Brabec, *Energy Environ. Sci.*, 2009, **2**, 347–363.
- 77 D. Zhao, X. Sun, C. Jiang, A. Kyaw, G. Lo and D. Kwong, *Appl. Phys. Lett.*, 2008, **93**, 083305.
- 78 X. Sun, D. Zhao, L. Ke, A. Kyaw, G. Lo and D. Kwong, *Appl. Phys. Lett.*, 2010, **97**, 053303.
- 79 J. You, L. Dou, Z. Hong, G. Li and Y. Yang, *Prog. Polym. Sci.*, 2013, **38**, 1909–1928.
- 80 K. S. Chen, H. L. Yip, J. F. Salinas, Y. X. Xu, C. C. Chueh and A. K. Y. Jen, *Adv. Mater.*, 2014, **26**, 3349–3354.
- 81 G. Dennler, M. C. Scharber, T. Ameri, P. Denk, K. Forberich, C. Waldauf and C. J. Brabec, *Adv. Mater.*, 2008, **20**, 579–583.
- 82 A. B. Yusoff, D. Kim, H. P. Kim, F. K. Shneider, W. J. da Silva and J. Jang, *Energy Environ. Sci.*, 2015, **8**, 303–316.
- 83 C. C. Chen, W. H. Chang, K. Yoshimura, K. Ohya, J. You, J. Gao, Z. Hong and Y. Yang, *Adv. Mater.*, 2014, **26**, 5670–5677.
- 84 S. Liu, P. You, J. Li, J. Li, C.-S. Lee, B. S. Ong, C. Surya and F. Yan, *Energy Environ. Sci.*, 2015, **8**, 1463–1470.
- 85 J. Zhang, Y. Zhang, J. Fang, K. Lu, Z. Wang, W. Ma and Z. Wei, *J. Am. Chem. Soc.*, 2015, **137**, 8176–8183.
- 86 T. Ameri, P. Khoram, J. Min and C. J. Brabec, *Adv. Mater.*, 2013, **25**, 4245–4266.
- 87 L. Lu, M. A. Kelly, W. You and L. Yu, *Nat. Photonics*, 2015, **9**, 491–500.
- 88 P. P. Khlyabich, B. Burkhardt, A. E. Rudenko and B. C. Thompson, *Polymer*, 2013, **54**, 5267–5298.
- 89 Y. C. Chen, C. Y. Hsu, R. Y. Lin, K. C. Ho and J. T. Lin, *ChemSusChem*, 2013, **6**, 20–35.
- 90 L. Yang, L. Yan and W. You, *J. Phys. Chem. Lett.*, 2013, **4**, 1802–1810.
- 91 P. Cheng and X. W. Zhan, *Mater. Horiz.*, 2015, **2**, 462–485.
- 92 Z. Hu, S. Tang, A. Ahlvers, S. I. Khondaker and A. J. Gesquiere, *Appl. Phys. Lett.*, 2012, **101**, 053308.
- 93 M. Zhang, F. Zhang, Q. An, Q. Sun, J. Wang, L. Li, W. Wang and J. Zhang, *Sol. Energy Mater. Sol. Cells*, 2015, **141**, 154–161.
- 94 B. H. Lessard, J. D. Dang, T. M. Grant, D. Gao, D. S. Seferos and T. P. Bender, *ACS Appl. Mater. Interfaces*, 2014, **6**, 15040–15051.
- 95 M. M. Mandoc, F. B. Kooistra, J. C. Hummelen, B. de Boer and P. W. M. Blom, *Appl. Phys. Lett.*, 2007, **91**, 263505.
- 96 Y. G. Zhen, H. Tanaka, K. Harano, S. Okada, Y. Matsuo and E. Nakamura, *J. Am. Chem. Soc.*, 2015, **137**, 2247–2252.
- 97 C.-H. Chen, C.-H. Hsieh, M. Dubosc, Y.-J. Cheng and C.-S. Hsu, *Macromolecules*, 2010, **43**, 697–708.
- 98 H. C. Hesse, J. Weickert, C. Hundschell, X. Feng, K. Müllen, B. Nickel, A. J. Mozer and L. Schmidt-Mende, *Adv. Energy Mater.*, 2011, **1**, 861–869.
- 99 S. Honda, T. Nogami, H. Ohkita, H. Benten and S. Ito, *ACS Appl. Mater. Interfaces*, 2009, **1**, 804–810.
- 100 Q. An, F. Zhang, L. Li, Z. Zhuo, J. Zhang, W. Tang and F. Teng, *Phys. Chem. Chem. Phys.*, 2014, **16**, 16103–16109.
- 101 Q. Sun, F. Zhang, J. Hai, J. Yu, H. Huang, F. Teng and W. Tang, *Electron. Mater. Lett.*, 2015, **11**, 236–240.
- 102 S.-J. Ko, W. Lee, H. Choi, B. Walker, S. Yum, S. Kim, T. J. Shin, H. Y. Woo and J. Y. Kim, *Adv. Energy Mater.*, 2015, **5**, 1401687.
- 103 Y. Santo, I. Jeon, K. Sheng Yeo, T. Nakagawa and Y. Matsuo, *Appl. Phys. Lett.*, 2013, **103**, 073306.
- 104 T.-Y. Huang, D. Patra, Y.-S. Hsiao, S. H. Chang, C.-G. Wu, K.-C. Ho and C.-W. Chu, *J. Mater. Chem. A*, 2015, **3**, 10512–10518.
- 105 W. L. Leong, S. R. Cowan and A. J. Heeger, *Adv. Energy Mater.*, 2011, **1**, 517–522.
- 106 Y.-J. Cheng, C.-H. Hsieh, P.-J. Li and C.-S. Hsu, *Adv. Funct. Mater.*, 2011, **21**, 1723–1732.
- 107 Q. Wei, T. Nishizawa, K. Tajima and K. Hashimoto, *Adv. Mater.*, 2008, **20**, 2211–2216.
- 108 F. Bonaccorso, N. Balis, M. M. Stylianakis, M. Savarese, C. Adamo, M. Gemmi, V. Pellegrini, E. Stratatakis and E. Kymakis, *Adv. Funct. Mater.*, 2015, **25**, 3870–3880.
- 109 Z. Zhuo, F. Zhang, J. Wang, J. Wang, X. Xu, Z. Xu, Y. Wang and W. Tang, *Solid-State Electron.*, 2011, **68**, 83–88.
- 110 Q. An, F. Zhang, J. Zhang, W. Tang, Z. Wang, L. Li, Z. Xu, F. Teng and Y. Wang, *Sol. Energy Mater. Sol. Cells*, 2013, **118**, 30–35.
- 111 J.-H. Huang, M. Velusamy, K.-C. Ho, J.-T. Lin and C.-W. Chu, *J. Mater. Chem.*, 2010, **20**, 2820–2825.
- 112 M. Koppe, H.-J. Egelhaaf, E. Clodic, M. Morana, L. Lüer, A. Troeger, V. Sgobba, D. M. Guldi, T. Ameri and C. J. Brabec, *Adv. Energy Mater.*, 2013, **3**, 949–958.
- 113 S. Honda, H. Ohkita, H. Benten and S. Ito, *Adv. Energy Mater.*, 2011, **1**, 588–598.
- 114 S. Honda, S. Yokoya, H. Ohkita, H. Benten and S. Ito, *J. Phys. Chem. C*, 2011, **115**, 11306–11317.
- 115 J. S. Huang, T. Goh, X. K. Li, M. Y. Sfeir, E. A. Bielinski, S. Tomasulo, M. L. Lee, N. Hazari and A. D. Taylor, *Nat. Photonics*, 2013, **7**, 480–486.

- 116 Q. S. An, F. J. Zhang, L. L. Li, J. Wang, Q. Q. Sun, J. Zhang, W. H. Tang and Z. B. Deng, *ACS Appl. Mater. Interfaces*, 2015, **7**, 3691–3698.
- 117 L. Y. Lu, T. Xu, W. Chen, E. S. Landry and L. P. Yu, *Nat. Photonics*, 2014, **8**, 716–722.
- 118 M. Koppe, H.-J. Egelhaaf, G. Dennler, M. C. Scharber, C. J. Brabec, P. Schilinsky and C. N. Hoth, *Adv. Funct. Mater.*, 2010, **20**, 338–346.
- 119 L. Ye, H.-H. Xu, H. Yu, W.-Y. Xu, H. Li, H. Wang, N. Zhao and J.-B. Xu, *J. Phys. Chem. C*, 2014, **118**, 20094–20099.
- 120 H. Loslein, T. Ameri, G. J. Matt, M. Koppe, H. J. Egelhaaf, A. Troeger, V. Sgobba, D. M. Guldi and C. J. Brabec, *Macromol. Rapid Commun.*, 2013, **34**, 1090–1097.
- 121 F. J. Zhang, Z. Xu, S. L. Zhao, L. Liu, W. W. Jiang, B. Sun, D. Liu, J. Z. Huang and J. Pei, *J. Lumin.*, 2007, **122**, 727–729.
- 122 K. Cnops, B. P. Rand, D. Cheyns, B. Verreet, M. A. Empl and P. Heremans, *Nat. Commun.*, 2014, **5**, 3406.
- 123 Q. An, F. Zhang, L. Li, J. Wang, J. Zhang, L. Zhou and W. Tang, *ACS Appl. Mater. Interfaces*, 2014, **6**, 6537–6544.
- 124 Q. An, F. Zhang, Q. Sun, J. Wang, L. Li, J. Zhang, W. Tang and Z. Deng, *J. Mater. Chem. A*, 2015, **3**, 16653–16662.
- 125 J. R. Lakowicz, *Principles of fluorescence spectroscopy*, Springer Science & Business Media, 2007.
- 126 T. Goh, J.-S. Huang, E. A. Bielinski, B. A. Thompson, S. Tomasulo, M. L. Lee, M. Y. Sfeir, N. Hazari and A. D. Taylor, *ACS Photonics*, 2015, **2**, 86–95.
- 127 V. Gupta, V. Bharti, M. Kumar, S. Chand and A. J. Heeger, *Adv. Mater.*, 2015, **27**, 4398–4404.
- 128 L. Yang, H. Zhou, S. C. Price and W. You, *J. Am. Chem. Soc.*, 2012, **134**, 5432–5435.
- 129 Y. Yang, W. Chen, L. Dou, W.-H. Chang, H.-S. Duan, B. Bob and G. Li, *Nat. Photonics*, 2015, **9**, 190–198.
- 130 P. Muller-Buschbaum, *Adv. Mater.*, 2014, **26**, 7692–7709.
- 131 P. P. Khlyabich, B. Burkhardt and B. C. Thompson, *J. Am. Chem. Soc.*, 2011, **133**, 14534–14537.
- 132 P. P. Khlyabich, B. Burkhardt and B. C. Thompson, *J. Am. Chem. Soc.*, 2012, **134**, 9074–9077.
- 133 R. A. Street, D. Davies, P. P. Khlyabich, B. Burkhardt and B. C. Thompson, *J. Am. Chem. Soc.*, 2013, **135**, 986–989.
- 134 P. P. Khlyabich, A. E. Rudenko, B. C. Thompson and Y.-L. Loo, *Adv. Funct. Mater.*, 2015, **25**, 5557–5563.
- 135 P. P. Khlyabich, A. E. Rudenko, R. A. Street and B. C. Thompson, *ACS Appl. Mater. Interfaces*, 2014, **6**, 9913–9919.
- 136 H. J. Chun, E. S. Kim and B. R. Cho, *Scanning*, 2014, **36**, 462–464.
- 137 L. Q. Yang, H. X. Zhou, S. C. Price and W. You, *J. Am. Chem. Soc.*, 2012, **134**, 5432–5435.
- 138 B. Xiao, H. Wu and Y. Cao, *Mater. Today*, 2015, DOI: 10.1016/j.mattod.2015.02.016.
- 139 F. Liu, Y. Gu, X. B. Shen, S. Ferdous, H. W. Wang and T. P. Russell, *Prog. Polym. Sci.*, 2013, **38**, 1990–2052.
- 140 L. Lu, W. Chen, T. Xu and L. Yu, *Nat. Commun.*, 2015, **6**, 7327.
- 141 P. Cheng, W. Ma, C. Yan, Y. Li and X. Zhan, *Energy Environ. Sci.*, 2015, 2357–2364.
- 142 Y. Zhang, D. Deng, K. Lu, J. Zhang, B. Xia, Y. Zhao, J. Fang and Z. Wei, *Adv. Mater.*, 2015, **27**, 1071–1076.
- 143 H. Cha, D. S. Chung, S. Y. Bae, M.-J. Lee, T. K. An, J. Hwang, K. H. Kim, Y.-H. Kim, D. H. Choi and C. E. Park, *Adv. Funct. Mater.*, 2013, **23**, 1556–1565.
- 144 T. Ameri, J. Min, N. Li, F. Machui, D. Baran, M. Forster, K. J. Schottler, D. Dolfin, U. Scherf and C. J. Brabec, *Adv. Energy Mater.*, 2012, **2**, 1198–1202.
- 145 T. Ameri, T. Heumüller, J. Min, N. Li, G. Matt, U. Scherf and C. J. Brabec, *Energy Environ. Sci.*, 2013, **6**, 1796–1801.
- 146 D. H. Wang, K. H. Park, J. H. Seo, J. Seifter, J. H. Jeon, J. K. Kim, J. H. Park, O. O. Park and A. J. Heeger, *Adv. Energy Mater.*, 2011, **1**, 766–770.
- 147 J. M. Lee, J. Lim, N. Lee, H. I. Park, K. E. Lee, T. Jeon, S. A. Nam, J. Kim, J. Shin and S. O. Kim, *Adv. Mater.*, 2015, **27**, 1519–1525.
- 148 Y. Liu, Z. Hong, Q. Chen, W. Chang, H. Zhou, T. B. Song, E. Young, Y. M. Yang, J. You, G. Li and Y. Yang, *Nano Lett.*, 2015, **15**, 662–668.
- 149 C. Zuo and L. Ding, *J. Mater. Chem. A*, 2015, **3**, 9063–9066.
- 150 B. Minnaert and M. Burgelman, *Prog. Photovoltaics*, 2007, **15**, 741–748.
- 151 N. Li, T. Stubhan, N. A. Luechinger, S. C. Halim, G. J. Matt, T. Ameri and C. J. Brabec, *Org. Electron.*, 2012, **13**, 2479–2484.
- 152 A. Kokil, A. M. Poe, Y. Bae, A. M. Della Pelle, P. J. Homnick, P. M. Lahti, J. Kumar and S. Thayumanavan, *ACS Appl. Mater. Interfaces*, 2014, **6**, 9920–9924.
- 153 C.-S. Ho, W.-C. Hsu, Y.-N. Lai, C.-S. Lee, W.-M. Chen, E. L. Huang, E.-P. Yao and C.-W. Wang, *Appl. Phys. Express*, 2013, **6**, 042301.
- 154 Y. Lou, Z. Wang, S. Naka and H. Okada, *Appl. Phys. Lett.*, 2011, **99**, 033305.
- 155 G. Adam, A. Pivrikas, A. M. Ramil, S. Tadesse, T. Yohannes, N. S. Sariciftci and D. A. M. Egbe, *J. Mater. Chem.*, 2011, **21**, 2594–2600.
- 156 P. Cheng, Q. Q. Shi and X. W. Zhan, *Acta Chim. Sin.*, 2015, **73**, 252–256.
- 157 W. Liu, H. Shi, W. Fu, L. Zuo, L. Wang and H. Chen, *Org. Electron.*, 2015, **25**, 219–224.
- 158 M. C. Chen, D. J. Liaw, Y. C. Huang, H. Y. Wu and Y. Tai, *Sol. Energy Mater. Sol. Cells*, 2011, **95**, 2621–2627.
- 159 X. Xiao, G. Wei, S. Wang, J. D. Zimmerman, C. K. Renshaw, M. E. Thompson and S. R. Forrest, *Adv. Mater.*, 2012, **24**, 1956–1960.
- 160 B. Ananda Rao, M. Sasi Kumar, G. Sivakumar, S. P. Singh, K. Bhanuprakash, V. J. Rao and G. D. Sharma, *ACS Sustainable Chem. Eng.*, 2014, **2**, 1743–1751.
- 161 L. Ye, H. Xia, Y. Xiao, J. Xu and Q. Miao, *RSC Adv.*, 2014, **4**, 1087–1092.
- 162 Y. J. Cho, J. Y. Lee, B. D. Chin and S. R. Forrest, *Org. Electron.*, 2013, **14**, 1081–1085.
- 163 S. S. Sharma, G. D. Sharma and J. A. Mikroyannidis, *Sol. Energy Mater. Sol. Cells*, 2011, **95**, 1219–1223.
- 164 J. Peet, A. B. Tamayo, X. D. Dang, J. H. Seo and T. Q. Nguyen, *Appl. Phys. Lett.*, 2008, **93**, 163306.
- 165 J. Lee, M. H. Yun, J. Kim, J. Y. Kim and C. Yang, *Macromol. Rapid Commun.*, 2012, **33**, 140–145.

- 166 S. Honda, H. Ohkita, H. Benten and S. Ito, *Chem. Commun.*, 2010, **46**, 6596–6598.
- 167 S. D. Stranks and H. J. Snaith, *Nat. Nanotechnol.*, 2015, **10**, 391–402.
- 168 K. Wang, C. Liu, P. C. Du, J. Zheng and X. Gong, *Energy Environ. Sci.*, 2015, **8**, 1245–1255.
- 169 D. Zhao, M. Sexton, H.-Y. Park, G. Baure, J. C. Nino and F. So, *Adv. Energy Mater.*, 2015, **5**, 1401855.
- 170 J. M. Lee, B. H. Kwon, H. I. Park, H. Kim, M. G. Kim, J. S. Park, E. S. Kim, S. Yoo, D. Y. Jeon and S. O. Kim, *Adv. Mater.*, 2013, **25**, 2011–2017.
- 171 F.-X. Xie, W. C. H. Choy, C. C. D. Wang, W. E. I. Sha and D. D. S. Fung, *Appl. Phys. Lett.*, 2011, **99**, 153304.
- 172 X. Li, W. C. H. Choy, H. Lu, W. E. I. Sha and A. H. P. Ho, *Adv. Funct. Mater.*, 2013, **23**, 2728–2735.
- 173 H. A. Atwater and A. Polman, *Nat. Mater.*, 2010, **9**, 205–213.
- 174 X. Li, W. C. Choy, L. Huo, F. Xie, W. E. Sha, B. Ding, X. Guo, Y. Li, J. Hou, J. You and Y. Yang, *Adv. Mater.*, 2012, **24**, 3046–3052.
- 175 F. C. Chen, J. L. Wu, C. L. Lee, Y. Hong, C. H. Kuo and M. H. Huang, *Appl. Phys. Lett.*, 2009, **95**, 013305.
- 176 J. L. Wu, F. C. Chen, Y. S. Hsiao, F. C. Chien, P. L. Chen, C. H. Kuo, M. H. Huang and C. S. Hsu, *ACS Nano*, 2011, **5**, 959–967.
- 177 Q. Q. Gan, F. J. Bartoli and Z. H. Kafafi, *Adv. Mater.*, 2013, **25**, 2385–2396.
- 178 E. Stratakis and E. Kymakis, *Mater. Today*, 2013, **16**, 133–146.
- 179 C. H. Chou and F. C. Chen, *Nanoscale*, 2014, **6**, 8444–8458.
- 180 S. Kouijzer, W. Li, M. M. Wienk and R. A. J. Janssen, *J. Photonics Energy*, 2014, **5**, 057203.
- 181 B. M. Savoie, S. Dunaisky, T. J. Marks and M. A. Ratner, *Adv. Energy Mater.*, 2015, **5**, 1400891.
- 182 M. D. Perez, C. Borek, S. R. Forrest and M. E. Thompson, *J. Am. Chem. Soc.*, 2009, **131**, 9281–9286.
- 183 H. Li, Z.-G. Zhang, Y. Li and J. Wang, *Appl. Phys. Lett.*, 2012, **101**, 163302.
- 184 P. Cheng, Y. Li and X. Zhan, *Energy Environ. Sci.*, 2014, **7**, 2005–2011.
- 185 H. Kang, K. H. Kim, T. E. Kang, C. H. Cho, S. Park, S. C. Yoon and B. J. Kim, *ACS Appl. Mater. Interfaces*, 2013, **5**, 4401–4408.
- 186 R. Street, K. Song, J. Northrup and S. Cowan, *Phys. Rev. B: Condens. Matter Mater. Phys.*, 2011, **83**, 165207.
- 187 T. B. Yang, M. Wang, C. H. Duan, X. W. Hu, L. Huang, J. B. Peng, F. Huang and X. Gong, *Energy Environ. Sci.*, 2012, **5**, 8208–8214.
- 188 F. J. Zhang, A. Vollmer, J. Zhang, Z. Xu, J. P. Rabe and N. Koch, *Org. Electron.*, 2007, **8**, 606–614.
- 189 S.-Y. Chang, H.-C. Liao, Y.-T. Shao, Y.-M. Sung, S.-H. Hsu, C.-C. Ho, W.-F. Su and Y.-F. Chen, *J. Mater. Chem. A*, 2013, **1**, 2447–2452.
- 190 C. Hsin-Yi, S. Lan, P.-C. Yang, S.-H. Lin, J.-Y. Sun and C.-F. Lin, *Sol. Energy Mater. Sol. Cells*, 2013, **113**, 90–95.
- 191 B. Lim, J. T. Bloking, A. Ponec, M. D. McGehee and A. Sellinger, *ACS Appl. Mater. Interfaces*, 2014, **6**, 6905–6913.
- 192 T. Ameri, P. Khoram, T. Heumuller, D. Baran, F. Machui, A. Troeger, V. Sgobba, D. M. Guldi, M. Halik, S. Rathgeber, U. Scherf and C. J. Brabec, *J. Mater. Chem. A*, 2014, **2**, 19461–19472.
- 193 F. Machui, S. Rathgeber, N. Li, T. Ameri and C. J. Brabec, *J. Mater. Chem.*, 2012, **22**, 15570–15577.
- 194 C. Muller, T. A. M. Ferenczi, M. Campoy-Quiles, J. M. Frost, D. D. C. Bradley, P. Smith, N. Stingelin-Stutzmann and J. Nelson, *Adv. Mater.*, 2008, **20**, 3510–3515.
- 195 Y. Zhang, H. Zhou, J. Seifter, L. Ying, A. Mikhailovsky, A. J. Heeger, G. C. Bazan and T. Q. Nguyen, *Adv. Mater.*, 2013, **25**, 7038–7044.
- 196 Y. H. Zhou, C. Fuentes-Hernandez, J. Shim, J. Meyer, A. J. Giordano, H. Li, P. Winget, T. Papadopoulos, H. Cheun, J. Kim, M. Fenoll, A. Dindar, W. Haske, E. Najafabadi, T. M. Khan, H. Sojoudi, S. Barlow, S. Graham, J. L. Bredas, S. R. Marder, A. Kahn and B. Kippelen, *Science*, 2012, **336**, 327–332.
- 197 X. Y. Han, Z. W. Wu and B. Q. Sun, *Org. Electron.*, 2013, **14**, 1116–1121.
- 198 A. V. Tunc, A. De Sio, D. Riedel, F. Deschler, E. Da Como, J. Parisi and E. von Hauff, *Org. Electron.*, 2012, **13**, 290–296.
- 199 X. C. Miao, S. Tongay, M. K. Petterson, K. Berke, A. G. Rinzler, B. R. Appleton and A. F. Hebard, *Nano Lett.*, 2012, **12**, 2745–2750.
- 200 Y. B. Xiao, H. Wang, S. Zhou, K. Y. Yan, Z. Q. Guan, S. W. Tsang and J. B. Xu, *ACS Appl. Mater. Interfaces*, 2015, **7**, 13415–13421.
- 201 L. Y. Lu, T. Xu, W. Chen, J. M. Lee, Z. Q. Luo, I. H. Jung, H. I. Park, S. O. Kim and L. P. Yu, *Nano Lett.*, 2013, **13**, 2365–2369.
- 202 F. C. Krebs, *Sol. Energy Mater. Sol. Cells*, 2009, **93**, 1636–1641.
- 203 F. C. Krebs, J. E. Carlé, N. Cruys-Bagger, M. Andersen, M. R. Lilliedal, M. A. Hammond and S. Hvilstedt, *Sol. Energy Mater. Sol. Cells*, 2005, **86**, 499–516.
- 204 F. C. Krebs, N. Espinosa, M. Hösel, R. R. Søndergaard and M. Jørgensen, *Adv. Mater.*, 2014, **26**, 29–39.
- 205 J. W. Rumer, R. S. Ashraf, N. D. Eisenmenger, Z. G. Huang, I. Meager, C. B. Nielsen, B. C. Schroeder, M. L. Chabiny and I. McCulloch, *Adv. Energy Mater.*, 2015, **5**, 1401426.
- 206 C. Groves, *Energy Environ. Sci.*, 2013, **6**, 1546.
- 207 B. Kan, M. Li, Q. Zhang, F. Liu, X. Wan, Y. Wang, W. Ni, G. Long, X. Yang, H. Feng, Y. Zuo, M. Zhang, F. Huang, Y. Cao, T. P. Russell and Y. Chen, *J. Am. Chem. Soc.*, 2015, **137**, 3886–3893.
- 208 L. Huo, T. Liu, X. Sun, Y. Cai, A. J. Heeger and Y. Sun, *Adv. Mater.*, 2015, **27**, 2938–2944.
- 209 M. Zhang, X. Guo, W. Ma, H. Ade and J. Hou, *Adv. Mater.*, 2015, **27**, 4655–4660.
- 210 H. Li, J. Cao, Q. Zhou, L. Ding and J. Wang, *Nano Energy*, 2015, **15**, 125–134.
- 211 W. Li, K. H. Hendriks, W. S. Roelofs, Y. Kim, M. M. Wienk and R. A. Janssen, *Adv. Mater.*, 2013, **25**, 3182–3186.
- 212 T. L. Nguyen, H. Choi, S. J. Ko, M. A. Uddin, B. Walker, S. Yum, J. E. Jeong, M. H. Yun, T. J. Shin, S. Hwang,

- J. Y. Kim and H. Y. Woo, *Energy Environ. Sci.*, 2014, **7**, 3040–3051.
- 213 W. C. Huang, E. Gann, L. Thomsen, C. K. Dong, Y. B. Cheng and C. R. McNeill, *Adv. Energy Mater.*, 2015, **5**, 1401259.
- 214 H. Y. Wang, Y. M. Ding, Y. B. Lai, Z. W. Sun, Y. Liu, B. Jiang, M. Chen, J. Yao, F. Liu and T. P. Russell, *J. Mater. Chem. A*, 2015, **3**, 12972–12981.
- 215 C. Guo, Y.-H. Lin, M. D. Witman, K. A. Smith, C. Wang, A. Hexemer, J. Strzalka, E. D. Gomez and R. Verduzco, *Nano Lett.*, 2013, **13**, 2957–2963.
- 216 C. Guo, D. R. Kozub, S. V. Kesava, C. Wang, A. Hexemer and E. D. Gomez, *ACS Macro Lett.*, 2013, **2**, 185–189.
- 217 N. Espinosa, R. Garcia-Valverde, A. Urbina and F. C. Krebs, *Sol. Energy Mater. Sol. Cells*, 2011, **95**, 1293–1302.
- 218 D. M. DeLongchamp, R. J. Kline, D. A. Fischer, L. J. Richter and M. F. Toney, *Adv. Mater.*, 2011, **23**, 319–337.
- 219 L. L. Chua, M. Dipankar, S. Sivaramakrishnan, X. Y. Gao, D. C. Qi, A. T. S. Wee and P. K. H. Ho, *Langmuir*, 2006, **22**, 8587–8594.
- 220 J. Rivnay, S. C. B. Mannsfeld, C. E. Miller, A. Salleo and M. F. Toney, *Chem. Rev.*, 2012, **112**, 5488–5519.